

Lawrence Berkeley National Laboratory

Recent Work

Title

PICOSECOND TIME-RESOLVED EMISSION STUDIES. I. REAL-TIME MEASUREMENTS OF SOLVENT-SOLUTE INTERACTIONS. II. KINETICS OF ENERGY FLOW IN A PHOTOSYNTHETIC ANTENNA SYSTEM

Permalink

<https://escholarship.org/uc/item/2d81d6v9>

Author

Yeh, S.W.

Publication Date

1985-11-01



Lawrence Berkeley Laboratory

UNIVERSITY OF CALIFORNIA

CHEMICAL BIODYNAMICS DIVISION

PICOSECOND TIME-RESOLVED EMISSION STUDIES.
I. REAL-TIME MEASUREMENTS OF SOLVENT-SOLUTE INTERACTIONS. II. KINETICS OF ENERGY FLOW IN A PHOTOSYNTHETIC ANTENNA SYSTEM.

S.W. Yeh
(Ph.D. Thesis)

November 1985

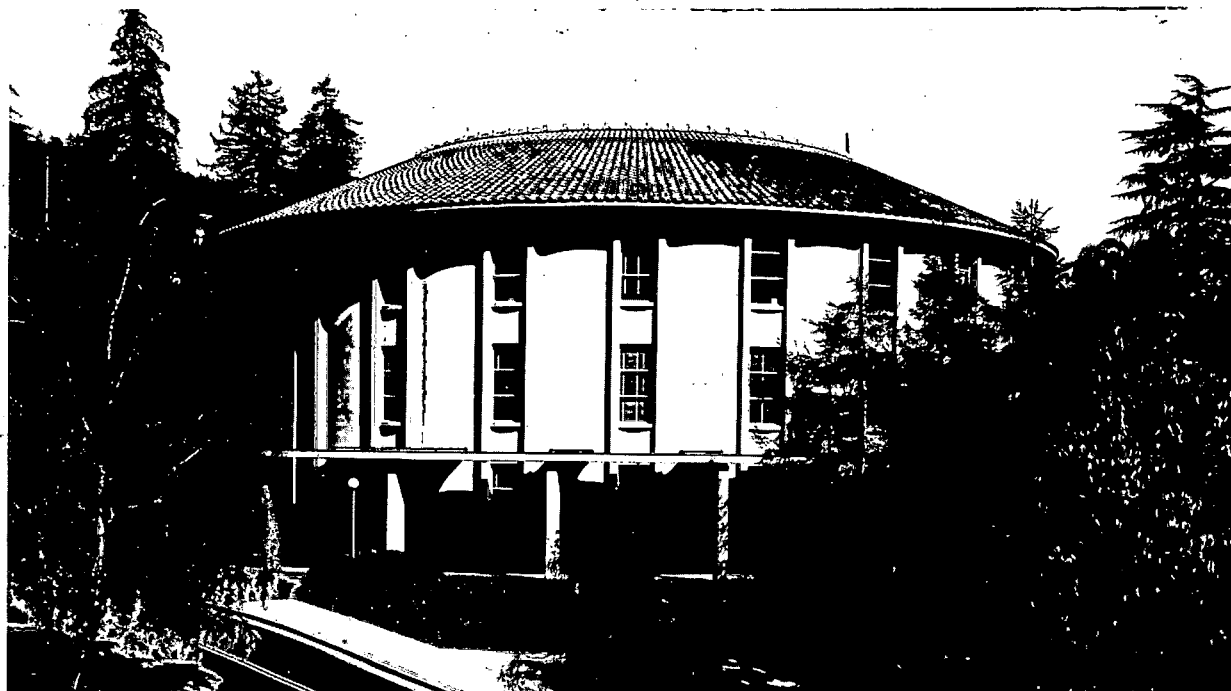
RECEIVED
LAWRENCE
BERKELEY LABORATORY

JAN 31 1986

LIBRARY AND
DOCUMENTS SECTION

For Reference

Not to be taken from this room



LBL-20662
c.1

DISCLAIMER

This document was prepared as an account of work sponsored by the United States Government. While this document is believed to contain correct information, neither the United States Government nor any agency thereof, nor the Regents of the University of California, nor any of their employees, makes any warranty, express or implied, or assumes any legal responsibility for the accuracy, completeness, or usefulness of any information, apparatus, product, or process disclosed, or represents that its use would not infringe privately owned rights. Reference herein to any specific commercial product, process, or service by its trade name, trademark, manufacturer, or otherwise, does not necessarily constitute or imply its endorsement, recommendation, or favoring by the United States Government or any agency thereof, or the Regents of the University of California. The views and opinions of authors expressed herein do not necessarily state or reflect those of the United States Government or any agency thereof or the Regents of the University of California.

Picosecond Time-Resolved Emission Studies.

I. Real-Time Measurements of Solvent-Solute Interactions.

II. Kinetics of Energy Flow in a Photosynthetic Antenna System.

Sheila Walsh Yeh
Ph.D. Thesis

Lawrence Berkeley Laboratory
University of California
Berkeley, California 94720

November 1985

The United States Department of Energy has the right to use
this thesis for any purpose whatsoever including the right
to reproduce all or any part thereof.

Picosecond Time-Resolved Emission Studies

I. Real-Time Measurements of Solvent-Solute Interactions

II. Kinetics of Energy Flow in a Photosynthetic Antenna System

Copyright © 1985

Sheila Walsh Yeh

Picosecond Time-Resolved Emission Studies

I. Real-Time Measurements of Solvent-Solute Interactions

II. Kinetics of Energy Flow in a Photosynthetic Antenna System

Sheila Walsh Yeh

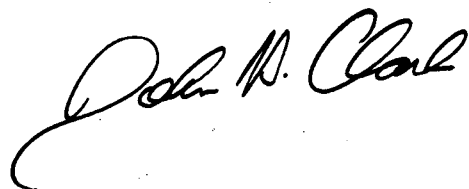
Abstract

A novel picosecond time-resolved fluorimeter is described in this work. The application of this fluorimeter to two distinctly different physical systems yields fundamentally new results for both. The picosecond fluorimeter is based on an actively and passively modelocked, Nd:YAG laser as the excitation source and an ultrafast streak camera as the detector. The system has a temporal resolution as short as 6 ps. The sensitivity of the system allows detection of extremely weak emission signals with full retention of temporal resolution.

Using the picosecond fluorimeter, the dynamics of solvation of electronically excited 4-aminophthalimide in a variety of solvents is measured. The solvation process is manifested by a time-dependent red shift in the emission spectrum in certain solvents. This red shift is time-resolved using the streak camera system. The time constant of the relaxation is found to correlate strongly with the longitudinal dielectric relaxation rate of the solvent. The correlation holds for changes in solvent, for isotopic substitution of a solvent, and for changes in temperature. Never before have direct measurements of excited-state solvation dynamics been shown to correlate with dielectric relaxation over such a wide range of experimental conditions.

Emission from certain photosynthetic antenna complexes, phycobilisomes, and from the building blocks of phycobilisomes, phycobiliproteins, has also been studied using the streak camera system. Both the rising and falling portions of the time-resolved emission profiles of the fluorescing chromophores in these structures are studied. The

rates of energy transfer between structural domains of the antenna complex and within the isolated biliprotein complexes are deduced from these studies. Comparisons of emission profiles from a series of structurally distinct phycobilisomes isolated from three related strains of cyanobacteria have provided new insights into the correlation of the energy transfer function and macromolecular structure in these light-harvesting antenna systems.

A handwritten signature in black ink, reading "John W. Clark". The signature is written in a cursive style with a large, sweeping initial "J" and a long, horizontal flourish extending to the right.

Dedication

I dedicate this thesis to:

my mother, Mary Elizabeth Walsh, for whom life was too short, and

my father, Michael John Walsh, who patiently and lovingly raised

three children alone.

Acknowledgments

I have worked hard to complete three projects, descriptions of which fill the pages of this thesis. However, the better part of the labor that this document represents was borne by others. There are a multitude of people who have supported me and taught me throughout my life, and I would like to take a few lines to acknowledge gratefully their invaluable contributions.

The most substantial contributors are my parents, Michael and Mary Walsh. First, their lifelong examples of hard work have taught me the value of effort. My father did not have the opportunity to obtain very much education, and so knew from unhappy experience the value an education has. Throughout her life, my mother encouraged my brother, sister, and me to excel. Because of the sacrifices of both of my parents, I have always been free to continue my education. My education has been important to me, but its value is even greater to my parents. Their support has always been a source of strength and encouragement.

During the course of my education I have benefitted from the lessons of many teachers, far too many to list here. The one who contributed most significantly and most directly to the work in this thesis is John Clark, whose imagination and enthusiasm helped make most of the hard work bearable, and helped immensely in the initial stages of all the projects. Alex Glazer's inspired suggestions of experiments on phycobilisomes brought that entire project into existence. I am looking forward to our future collaborations.

The people that I have had the opportunity to work with while in graduate school are also due my deep appreciation. Steve Webb's continual contributions to the construction of the streak camera system, Howard Nathel's, Doug Anthon's and Dennis Guthals' development of the tunable source, and Cindy Buhse's and Ward Brown's construction of the steady-state fluorimeter made the experiments described in this thesis possible. These are just a few of the many contributions of people from the Clark group. Thoughts

of the many friends I have made while in graduate school (both in the Clark group and beyond it) will last much longer than any thoughts about the work described here.

In addition, there are many people outside of graduate school who have assisted me with warmth and friendship. These include the "Gang", whose entirely pleasant gatherings have punctuated the last fifteen years of my education(—hard to believe, isn't it?). My in-laws, Mom and Pop, are also included with warm thoughts of their acceptance and support.

The last person to be mentioned is my dear Francis. Without his unending help, patience, and support, this work would never have been finished. His job has been very difficult, as he endured my long working hours and my periods of poor temper with warmth and love. He holds a majority share in this degree.

Research support for the solvation project was from the Gas Research Institute Basic Coal Sciences Program under Contract 5081-260-568. Work on the photosynthetic antenna systems was supported by the Office of Energy Research, Office of Basic Energy Sciences, Chemical Sciences Division of the Department of Energy under Contract DE-AC03-76SF00098. In addition, I have received support of a National Science Foundation Pre-Doctoral Fellowship (1980-83) and an Amy Bowles Johnson Memorial Fellowship (1983-84). I have spent the last year as a Procter and Gamble Fellow (1984-85). This generous financial support is gratefully acknowledged.

Table of Contents

	Page
Abstract	1
Dedication	i
Acknowledgments	ii
Table of Contents	iv
List of Figures	vii
List of Tables	xi
Chapter 1	
Introduction	1
Chapter 2	
Picosecond Time-Resolved Emission Studies	5
A. Introduction	5
B. Streak Camera Fluorimetry	5
1. Introduction	5
2. Laser System	6
3. Physical Layout of System	9
4. Data Processing Software	17
5. Calibrations and Corrections	18
6. Temporal Resolution of the Streak Camera System	24
C. Data Handling	30
1. Determining Temporal Parameters	30
2. Generating Emission Spectra at Discrete Times	37
D. Sample Preparation	40
1. Excited-State Solvation Studies	40

2. Photosynthetic Antenna System Studies	43
E. References for Chapter 2	44
Chapter 3	
I. Real-Time Measurements of Solvent-Solute Interactions	45
A. Introduction	45
B. Experimental Approach—Dynamic Stokes' Shifts	46
C. Previous Applications of Time-Resolved Stokes' Shifts	51
D. Results from a Picosecond Fluorimeter	60
1. 4AP in 1-Propanol	65
2. 4AP in Toluene	79
3. 4AP in Acetonitrile	79
4. 4AP in an Assortment of Other Solvents	91
E. Relaxation of Excited-States 4AP in a Series of Linear Alcohols	97
1. Solvation and Dielectric Relaxation of the Solvent	113
2. Dielectric Relaxation Under the Conditions of Constant Charge	115
3. Molecular Mechanisms for Dielectric Relaxation of Alcohols	118
F. Using Dielectric Relaxation As a Predictive Model of Excited-State Solvation Dynamics	120
1. 4AP in non-Alcoholic Solvents	120
2. Solvation and Temperature Variations	121
3. Isotope Effects on the Photophysics of 4AP	123
4. Solvation of a Different Solute in Linear Alcohols	140
G. Studies of the Rotational Diffusion of 4AP	150
H. Conclusions	154
I. Future Directions	159
J. References for Chapter 3	161

Chapter 4

II. Kinetics of Energy Flow in a Photosynthetic Antenna System.....	166
A. Introduction	166
B. Photosynthetic Antenna Systems.....	166
C. Phycobilisomes and Phycobiliproteins	168
1. Morphology	168
2. Spectroscopy	171
D. Experimental Approach	176
E. Power Considerations.....	181
F. Emission Rise Times of Phycobiliproteins	193
G. Time-Resolved Emission of Intact Phycobilisomes	206
H. Kinetic Modelling of the WT6701 Phycobilisomes	220
1. General Background	220
2. Phycobilisome Rods	225
3. Phycobilisome Core	227
I. Kinetic Modelling of Other Phycobilisomes	229
J. Conclusions	233
K. References for Chapter 4.....	234

Chapter 5

Conclusions.....	237
------------------	-----

Appendix

A. Kinetic Modelling of Phycobilisome Rods.....	241
B. Kinetic Modelling of Phycobilisome Cores	243

List of Figures

Figure	Page
2.1 Diagram of Picosecond Laser Oscillator Cavity	7
2.2 Diagram of Ultrafast Streak Camera Time-Resolved Emission Apparatus	10
2.3 Flowchart of Time-Resolved Emission Data Acquisition Process	15
2.4 Etalon Traces, Summed But Uncorrected	19
2.5 Normalized Etalon Spacing as a Function of Photodiode Array Channel Number	21
2.6 Etalon Traces, Summed and Corrected	25
2.7 Excitation Pulse Width vs. Streak Camera System Instrument Response Function	28
2.8 Decay of Emission from 3AP in 1-Propanol	32
2.9 Double-Exponential Decay Determination	35
2.10 Initial Profile of Emission from 4AP in 1-Propanol—Rise Time Sensitivity ...	38
2.11 Time-Resolved Emission Spectra	41
3.1 Potential Energy Diagram for Solute-Solvent Interaction	49
3.2 The Structure of 4-(N,N'-Dimethylamino)-benzotrile (DMABN)	54
3.3 The Structure of the Aminophthalimides	57
3.4 Emission from 4AP in 1-Propanol—Fluorescence Lifetime at 650 and 480 nm	61
3.5 Emission from 4AP in 1-Propanol—Initial Temporal Profiles at 650 and 480 nm	63
3.6 Time-Resolved Emission Spectrum for 4AP in 1-Propanol—Initial Profiles ...	66
3.7 Emission Spectra for 4AP in 1-Propanol at Selected Times	72
3.8 Emission Maximum as a Function of Time for 4AP in 1-Propanol	75

3.9	Semi-logarithmic Plot of Emission Maximum as a Function of Time for 4AP in 1-Propanol	77
3.10	Steady-State Emission and Absorption Spectra of 4AP in 1-Propanol and Toluene	80
3.11	Time-Resolved Emission of 4AP in Toluene—Initial Temporal Profile	81
3.12	Steady-State Emission and Absorption Spectra of 4AP in Acetonitrile and 1-Propanol	85
3.13	Time-Resolved Emission of 4AP in Acetonitrile—Initial Temporal Profiles ...	87
3.14	Steady-State Spectra of 4AP in DMSO, Acetone and 1-Propanol	92
3.15	Diagram of Charge-Transfer Character of 4AP Excited-State	98
3.16	Emission Spectra for 4AP in Ethanol at Selected Times	100
3.17	Emission Spectra for 4AP in 2-Propanol at Selected Times	102
3.18	Emission Spectra for 4AP in 1-Butanol at Selected Times	104
3.19	Emission Spectra for 4AP in 1-Pentanol at Selected Times	106
3.20	Peak Positions as a Function of Time for 4AP in a Number of Simple Alcohols	108
3.21	Semi-logarithmic Plot of the Peak Positions as a Function of Time for 4AP in a Number of Simple Alcohols	110
3.22	Steady-State Emission Spectra of 4AP in 1-Propanol at T=0, 20 and 40°C ..	124
3.23	Time-Resolved Emission from 4AP in 1-Propanol at T=0, 20, and 40°C Detected at 650 nm	126
3.24	Time-Resolved Emission from 4AP in 1-Propanol at T=0, 20, and 40°C Detected at 480 nm	128
3.25	Semi-logarithmic Plot of Peak Positions as a Function of Time for 4AP in 1-Propanol at T=0, 20, 40°C	130
3.26	Emission from 4AP in Methanol and Methanol-d—Fluorescence Lifetimes ..	137

3.27	Emission from 4-AP in 2-Propanol and 2-Propanol-d—Initial Profiles of Low Energy Emission	141
3.28	Steady-State Emission and Absorption Spectra for 3AP in 1-Propanol and 4AP in 1-Propanol	144
3.29	Time-Resolved Emission from 3-AP in 1-Propanol and 4AP in 1-Propanol— Initial Profiles	147
3.30	Time-Resolved Fluorescence Polarization Anisotropy for 4AP in 1-Butanol..	152
3.31	Rotational Reorientation Times for 4AP in a Series of Linear Alcohols as a Function of Viscosity	156
4.1	Schematic Diagram of Phycobilisome Structure	169
4.2	Absorption Spectrum of an Isolated R-Phycoerythrin Complex	173
4.3	Steady-state Spectra of the <i>Synechocystis</i> 6701 Family of Phycobilisomes ...	177
4.4	Emission Profiles of R-Phycoerythrin Isolated from <i>Gastroclonium coulteri</i> as a Function of Excitation Intensity	183
4.5	Phycobiliprotein Emission Profiles from R-Phycoerythrin as a Function of Excitation Intensity	185
4.6	Initial Profiles of Emission Profiles from R-Phycoerythrin as a Function of Input Intensity	188
4.7	Relative Quantum Yields of Emission as a Function of Excitation Intensity for R-Phycoerythrin	191
4.8	R-Phycoerythrin Rise Times as a Function of Excitation Wavelength	196
4.9	Allophycocyanin Rise Times as a Function of Excitation Wavelength.....	200
4.10	Relative Quantum Yield as a Function of Excitation Wavelength for Allophycocyanin Complexes	204
4.11	Time-Resolved Emission from Intact and Dissociated WT6701 Phycobilisomes.....	208

4.12	Short Time Scale Emission from Intact WT6701 Phycobilisomes	210
4.13	Excitation Distributions for WT6701 and CM25 Phycobilisomes with Excitation at 570 nm	213
4.14	Time-Resolved Emission for WT6701 and CM25 Phycobilisomes	216
4.15	Excitation Distributions for WT6701 and CM25 Phycobilisomes with Excitation at 620 nm	218
4.16	Time-Resolved Emission from CM25 and UV16 Phycobilisomes and from Nile Blue A Laser Dye	221

List of Tables

Table	Page
3.1 Parameters of Fits to 4AP in 1-Propanol Spectrally- and Temporally-Resolved Data	70
3.2 Parameters of Fits for Spectrally- and Temporally-Resolved Data for 4AP in Four Alcohols	95
3.3 Solvation Times for 4AP in Five Alcohols	112
3.4 Solvation Times for 4AP in a Series of Solvents, with Dielectric Data for the Solvents	114
3.5 Dielectric Relaxation Times for a Series of non-Alcoholic Solvents	122
3.6 Parameters of Fits to 4AP in 1-Propanol Spectrally- and Temporally-Resolved Data at T=0, 20, and 40°C	132
3.7 Solvation Times for 4AP in 1-Propanol at Three Different Temperatures, with Dielectric Relaxation Times	134
3.8 Solvent Isotope Effect on the Lifetime and the Relative Emission Quantum Yield of 4AP	139
3.9 Solvation Times for 3AP and 4AP in 1-Propanol, 1-Butanol and 1-Pentanol .	149
3.10 Rotational Reorientation Times for 4AP in 2-Propanol and 1-Butanol as a Function of Detection Wavelength	155
3.11 Rotational Reorientation Times for 4AP in Alcoholic Solvents, with Macroscopic Viscosities	158
4.1 Wavelengths of Maximum Steady-state Absorption and Emission for Phycobiliprotein Complexes from WT6701 Phycobilisomes.....	175
4.2 Best-fit Emission Decay Parameters for R-Phycoerythrin Complexes $[(\alpha\beta)_{67}]$ Isolated from <i>G. coulteri</i>	190

4.3	Best-fit Emission Risetimes for Isolated Phycobiliproteins and for Rhodamine B Laser Dye Solutions.....	198
-----	--	-----

Chapter 1

Introduction

Emission spectroscopy gives information on the energy of luminescent excited states, and time-resolved emission spectroscopy can yield information on the dynamics of those special excited states. Since there is a novel and intense richness in the chemistry of excited states, it is natural that chemists would try to study excited-state chemistry by using emission spectroscopy. It follows that there would be interest in uncovering the dynamics of the reactions of excited states by time-resolving emission. The studies described here use time-resolved emission spectroscopy to elucidate the nature of the interactions of excited states in two distinctly different physical systems.

In the studies that follow, reactions and interactions that are studied occur on the time scale of 10 ps to 100 ns. The resolution of chemical events on as short a time scale as 10 ps is made possible by the excellent temporal resolution of an ultrafast streak camera system. Data from such a large range of time scales, four orders of magnitude, are easily obtained with the streak camera. The construction, calibration, and implementation of the streak camera system is described in good detail in Chapter 2, and so only general and introductory illustrations of the system will be included here. The function of the streak camera is the temporal resolution of optical signals. The camera has a photocathode, and when optical signals impinge on the photocathode, photoelectrons are created. The photoelectrons are accelerated by a high-voltage grid that lies in close proximity to the photocathode. Triggering the streak camera triggers a high voltage ramp which deflects the photoelectrons. Photoelectrons are differentially deflected depending on their positions relative to the voltage plates when the ramp fires, and temporal information can be obtained from the differential deflection of the photoelectrons. The photoelectrons impinge on a phosphor, and the weak phosphorescence that results is intensified through

five stages of image-enhancers. The final, intensified streak record is imaged onto a linear photodiode array where the intensity is measured. Signals as short as 4 ps are easily resolved with the streak camera system. Each of the camera's records can account for as little as 300 ps (4 ps resolution) or for as much as 100 ns (1.2 ns resolution), depending on the rate of the voltage ramp.

The production of short optical pulses is a second, exceedingly important procedure. The excited states that are to be studied must be produced on a short time scale relative to the dynamics that the excited states will undergo subsequent to excitation, or else those dynamics will be very difficult to follow. The short pulses that are used in streak camera experiments all originate from the cavity of an actively and passively mode-locked, Nd:YAG laser system. Single pulses are selected from the output of the cavity, and amplified. The amplified pulses are used to generate the excitation pulses. The widths of the excitation pulses used in the experiments reported here range from about 10 to 40 ps, full width at half maximum.

The reason to put this streak camera/laser system hardware together is to learn about the energy and dynamics of luminescent excited-states, as much can be learned about excited states by time-resolving emission. Interest in the nature of excited states results from a number of contributions. Excited states can undergo chemical modifications that are not allowed in ground states. For instance, some isomerizations can occur in the first excited state but are strictly not allowed in the ground state. Enrichment in the variety of chemistry exhibited by excited-states also occurs because reactions that are not allowed in the ground state due to the existence of high thermal barriers may have less restrictive barriers in the excited state. The fact that the excited-state molecule is rare and short-lived also makes it an intrinsically interesting commodity. Since the excitation has a finite lifetime all the possible pathways of energy dissipation must compete. The chemistry that is observed is the result of the competition.

The two studies that are described in detail in Chapters 3 and 4 are very different in subject matter but are strongly related nonetheless. In Chapter 3, the study is of solute molecules that are excited to highly dipolar excited states. Subsequent to excitation, the solute molecules interact with the surrounding solvent. In the experiments described in Chapter 4, energy is deposited in distributions of chromophores within light-harvesting complexes, and the migration of the energy is monitored. In both cases, the interest is centered on the unique interactions possible between the excited chromophores and their surroundings.

Time-resolved emission is the tool that is used to study the interaction of excited solute molecules with the surrounding solvent. These studies are possible because the energy level of the excited-solute molecule reflects the interactions of the solute and solvent. If the solvent and solute interact, the interaction can dissipate some of the energy of the excited state, and the emission energy will be lowered. If the rate of interaction is slower than the rate of complete dissipation of excited-state population, then the emission from the excited chromophore will lower in energy as the relaxation occurs. This time-dependent red-shift in the emission maximum is resolved by the streak camera system, and the rate of that red-shift reflects the time scale of the interaction of the solvent and excited solute. Experiments in Chapter 3 exploit the resolution of the streak camera system to measure the real-time interactions of an excited solute molecule with the solvent surrounding it in room temperature solutions. In Chapter 3, the results of the time-resolved measurements indicate that rate of dielectric relaxation of the solvent limits the rate of relaxation of the excited solute and solvent. Predictions of rates of solute-solvent interaction based on this dielectric relaxation model are shown to reproduce experimental results quite well.

In the studies of light-harvesting complexes that are presented in Chapter 4, energy migration is monitored through time-resolved emission. Emission from the lowest en-

ergy, terminal chromophores in a complex occurs after migration of the excitation from the initially excited chromophores to the terminal chromophores. The streak camera system is used to time-resolve just the initial profile of the emission from the terminal chromophores, and thereby determine the rate at which the energy migrated. Through the use of selective comparative experiments, where the distributions of initially excited chromophores are varied by spectrally tuning the excitation source, the rate of migration of energy through several subparticles of the light-harvesting complex has been shown to be extremely fast. A second variety of comparative experiments using intact light-harvesting complexes of wild-type and mutant cyanobacterial strains allows measured energy migration time differences to be correlated with known structural differences. These experiments, and the results from them, are described fully in Chapter 4. The work detailed in Chapter 4 culminates with the introduction of a simple kinetic model which can reproduce experimental results from our studies and those of other groups. The single Appendix to this document contains the mathematical details of that model.

Chapter 2

Picosecond Time-Resolved Emission Studies

A. Introduction

Chemical kinetics is the study of reaction rates. Reaction rates can be measured directly by monitoring the time-dependent concentration(s) of the reacting species or of the resulting products. From such measurements, empirical rate laws and rate constants are determined. Detailed reaction mechanisms can be proposed once the rate law is determined. The preceding formalism can be applied to all reactions, even those taking place on experimentally inconvenient time scales. Reactions taking place in solution, such as those discussed in Chapter 3 between solute molecules and the surrounding solvent, can occur on extremely short time scales. Similarly, energy transfer between chromophores only a few nanometers apart (as in the studies of phycobilisomes and reported in Chapter 4) is very rapid. The experimental methods described below tell how an ultrafast streak camera can be used to monitor the concentrations of reactive species even on very short time scales (<10 ps). A detailed description of the picosecond laser/streak camera system used to obtain the experimental results presented in the thesis is presented below.

B. Streak Camera Fluorimetry

1. Introduction

An ultrafast streak camera can be used to time-resolve any optical signal, including an emission band [1]. Since the intensity of emission is directly proportional to the population of the emitting state, time-resolving the emission yields the excited-state population temporal profile. If both the reactive and reacted molecules are fluorescent, and if the emission from the two can be distinguished spectrally, the entire reaction can

be monitored and the kinetics can be determined in accord with the formalism that introduced this section. The kinetics of the physical systems investigated in this thesis are determined using that formalism.

Interpretation of fluorescence decays with short temporal parameters, for instance, short fluorescence lifetimes, is greatly simplified by the use of short excitation pulses. Statistical limitations do not allow determining parameters of decay shorter than 12-15 percent of the apparent full-width-at-half-maximum (FWHM) of the excitation source [2]. Such short temporal parameters can only be determined under optimal signal-to-noise conditions where the temporal profile of the excitation source is well known. Given these statistical constraints on deconvolving the excitation pulse shape from the fluorescence decay, picosecond laser pulses are clearly required to obtain picosecond resolution.

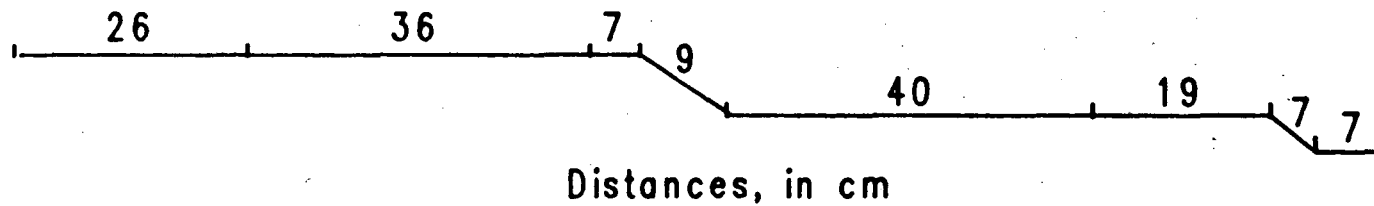
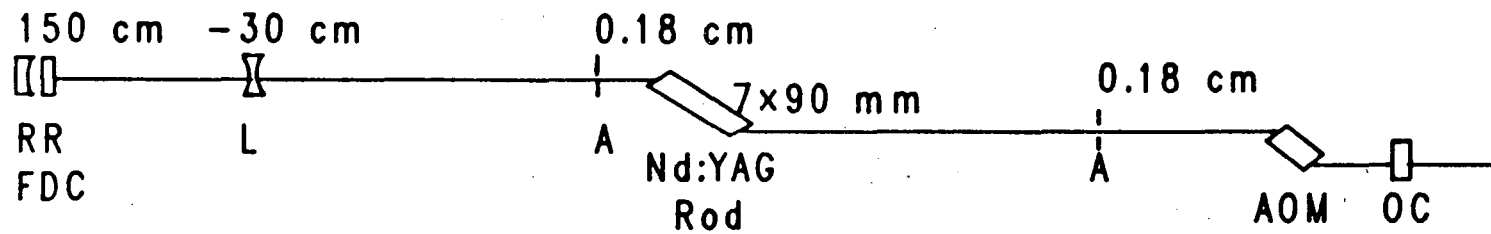
2. Laser system

The source of picosecond pulses in all the experiments described here is an actively and passively mode-locked, Nd:YAG laser (Quantel, YG400AP). A schematic diagram of the laser cavity is shown in Figure 2.1. The laser as available commercially bears only a general resemblance to the laser actually used. Only the design of the laser head and the power supplies remain unchanged. Components changed include: substitution of a flowing dye cell for the stirring dye cell, substitution of higher quality optical components (mirrors, lens, and window) for those originally supplied, introduction of optical mounts of greater structural stability, and substitution of a recirculating water bath with improved temperature control for the recirculator originally supplied. All of these changes served to increase the reliability and stability of the laser output and to simplify alignment procedures.

The laser used in these experiments has been characterized with great care [3], so only typical operating conditions are summarized here. The oscillator is pumped just

Figure 2.1 Diagram of Picosecond Laser Oscillator Cavity

Schematic diagram of actively and passively mode-locked, Nd:YAG laser cavity. The abbreviations are specified in the diagram, as are the distances between optical elements.



RR: Rear Reflector

A: Aperture

FDC: Flowing Dye Cell

AOM: Acousto-optic Modulator

L: Lens

OC: Output Coupler

Figure 2.1

above threshold (1.06 kV; 17 J), resulting in 1064-nm pulse trains with energies of 3-5 mJ that are 10-12 pulses in length. An electrooptic pulse selector (Quantel, PF302) is set to select a single pulse from the center of the train. The single pulse is amplified in a Nd:YAG rod pumped with 51 J, resulting typically in a pulse of 5-20 mJ. Peak powers are in gigawatts, and so intensity-dependent processes like nonlinear frequency summing are efficient. The second, third, and fourth harmonics (532, 355, and 266 nm, respectively) of the 1064-nm Nd:YAG fundamental can each be used as an excitation source for time-resolved emission studies. Pulse widths of the harmonics are typically 20-40 ps, with μJ to mJ energy levels.

A secondary excitation source has been developed in this laboratory that provides a continuously tunable excitation source [4]. A pair of matched potassium dihydrogen phosphate (KDP) crystals pumped by the third harmonic (355 nm) of the Nd:YAG yields tunable pulses in the visible (460 to 630 nm) and near IR (0.8 to 1.6 μm). The pulse width of the visible light is typically 8-15 ps with energies that fluctuate wildly, but average 10 μJ . This tunable source has made possible the phycobilisome experiments described in Chapter 4.

3. Physical Layout of System

The optical configuration of the entire laser and detection system is shown schematically in Figure 2.2. A shutter (A. W. Vincent Associates, Inc., Model SD 122B) controlled by the microcomputer (Digital Equipment Corporation, LSI 11/73) that runs the experiment can intercept pulse trains before single pulse selection. When open, the shutter passes trains from which a single pulse is selected, amplified, and injected into a long (≈ 60 ns) optical delay line. The delay line is needed to insure that the optical event arrives at the streak camera photocathode after the streak is electronically triggered. Although the mirrors of the delay line have high reflectivities (>99.9 percent), the leakage through the

Figure 2.2 Diagram of Ultrafast Streak Camera Time-Resolved Emission Apparatus

Schematic diagram of the ultrafast streak camera time-resolved emission apparatus. The abbreviations used: SHG for second harmonic generating crystal; THG, third harmonic generating crystal; BS, beam splitter; GT, Glan-Taylor prism polarizer; L, lens; F, filter; and Diode Array, intensified photodiode array.

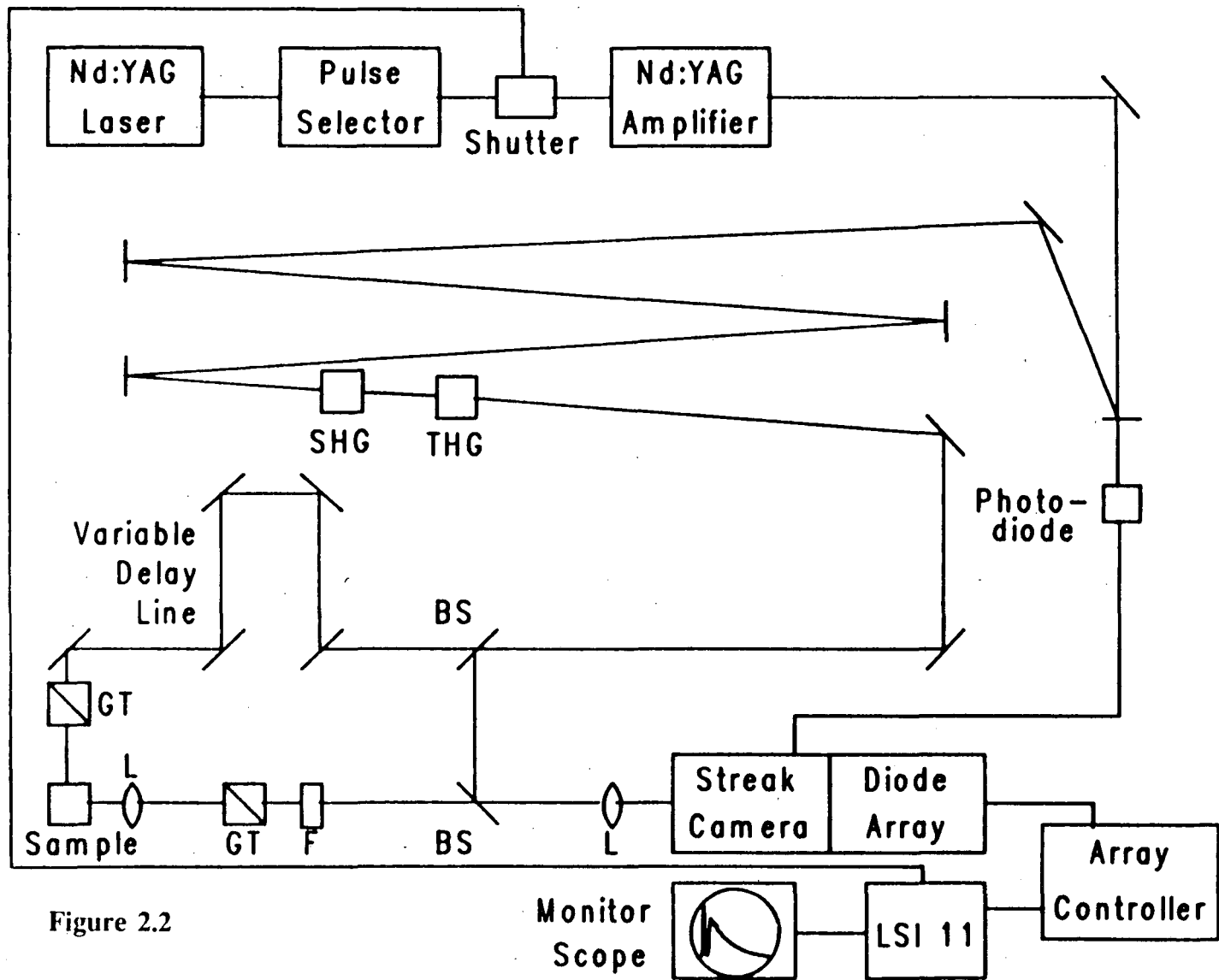


Figure 2.2

mirrors is sufficient to generate substantial signal levels from photodiodes. The leakage through the first mirror in the delay line impinges on a photodiode (Hewlett-Packard, HP 5082-4220) biased at about 90 V and generates the signal used to trigger the streak camera. The trigger is generated early in the optical delay line because there is a considerable electronic delay in turning on the camera (≈ 40 ns on the slowest streak speed). Leakage through a subsequent mirror is used to generate a trigger for the photodiode array readout (Tracor-Northern, TN-1710). Near the end of the delay line, various nonlinear optical crystals are inserted to generate the excitation wavelength desired. The excitation pulse is split into two components. The minor fraction is sent directly into the camera to function as a fiducial, time-marking pulse. The major fraction of the excitation pulse undergoes a further optical delay, and is used to excite the sample. Emission from the sample is collected, polarization-selected using a prism polarizer, and spectrally filtered, typically through 10-nm bandpass filters. Broader bandpass filters and long wavelength pass filters are also frequently used. The resulting signal is optically combined with the fiducial pulse and imaged onto the photocathode of the streak camera (Hadland Photonics, Ltd., Imacon 500). The streak record is intensified using a microchannel plate image intensifier (Hadland Photonics, Ltd., Imacon 20/30). The intensified record of the streak event is imaged onto the intensifier of a photodiode array detector (Tracor-Northern, IDARSS 6300). The digitized output of the 1024-element detector is summed into the buffer of the photodiode array controller before transfer to the LSI 11/73 microcomputer for signal processing.

For the streak camera system, the signal processing organization is of greater importance than the optical configuration. Although virtually any optical signal can be time-resolved, the brightness of a 10-nm slice of an emission band (or even an entire emission band) can be quite limited on a picosecond time scale. Furthermore, substantial signal levels can degrade the temporal resolution of the streak camera [1,5]. Hence,

there is a need for a substantial degree of signal averaging. The overriding concern in the organization of this streak camera system was to enable the accumulation and signal processing of the streak records from individual laser shots at as fast a rate as possible.

As eluded to earlier in this description, an 11/73 microcomputer controls the experiment. The laser oscillator is run at 10 Hz. A mechanical shutter is positioned between the output coupler of the laser and the single pulse selector. The shutter is the on-off switch used by the computer to control the arrival of laser light to the rest of the system. Thereby providing for asynchrony, the shutter serves to prolong the somewhat short life ($\approx 10^7$ shots) of some of the critical electronic components in the pulse selector and streak camera. Computer control is straightforward because the shutter power supply accepts a TTL input such that a five-volt signal opens the shutter, and a zero-volt signal closes it. This TTL input is connected to an output line of a parallel I/O board (ADAC, Inc., ATTL 1664) in the microcomputer. Under program control, switching the appropriate bit in the bus address corresponding to the I/O board opens or closes the shutter.

As a precondition to accumulating data, the photodiode array controller must be put into a cycle of baseline preparation, data acquisition, and data transfer. The Tracor controller contains enough memory to hold eight digitized streak records. One of these memory blocks is reserved to hold the additive inverse of an average dark streak record. Baseline preparation consists of transferring that average dark streak record into each of the seven other memory blocks. Following baseline preparation, triggered acquisition into each of the seven memory blocks is enabled sequentially. After seven streak records have been digitized and stored, the photodiode array controller waits for a signal from the 11/73 microcomputer, and then initiates transfer of the newly acquired streak records to the 11/73 over parallel output lines. After transfer, the cycle repeats, starting with baseline preparation. The photodiode array controller continuously cycles through these operations, functioning as a slave to the 11/73 processor. When accumulating data, the

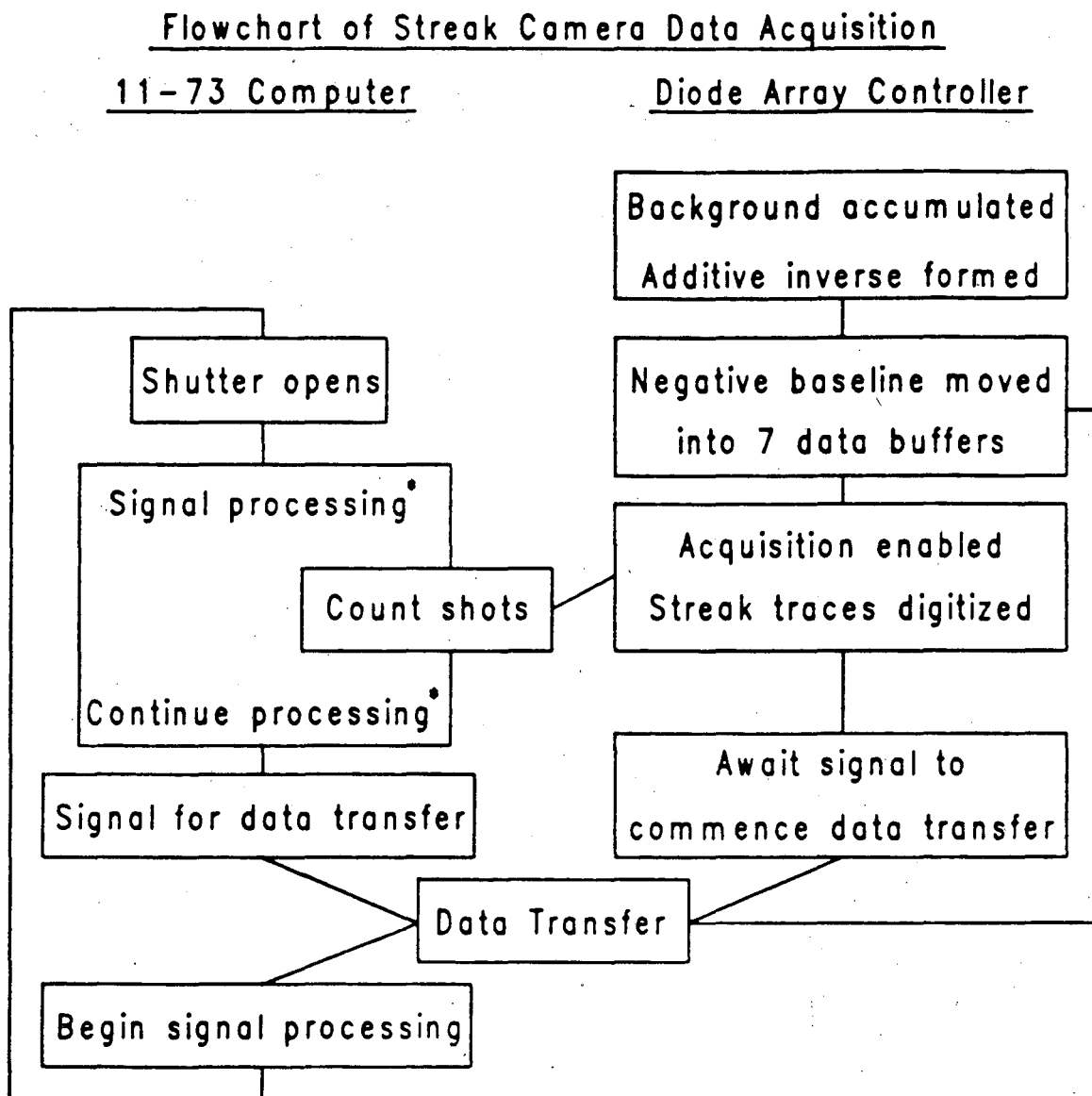
photodiode array controller waits for triggers that only arrive when the 11/73 opens the shutter. The parallel transfer of data only begins when the 11/73 signals that it should occur. The dependence of the photodiode array controller on the operation of the 11/73 system is clearly seen in Figure 2.3, a logical flowchart of the complete data acquisition procedure.

As summarized in Figure 2.3, the program running on the 11/73 orchestrates the data collection procedure. The shutter is opened by the program to begin data accumulation. The photodiode signals fire the streak camera and trigger the photodiode array controller to digitize and store the streak record. Every time the photodiode array controller accepts a trigger, it generates a TTL pulse on the appropriate output pin. The pin is connected to Schmitt input trigger on a real-time clock board (Data Translation, Inc., DT-2769) in the 11/73 backplane. The TTL pulse causes the board to generate a processor interrupt. The interrupt handling routine counts the pulse and resets the clock trigger. After seven pulses have been accumulated, the photodiode array controller is filled, and the shutter is closed. The 11/73 computer signals the photodiode array controller to transfer the contents of its memory by switching a bit on a parallel I/O board (Digital Equipment Corporation, DRV11J) in the 11/73 backplane. The data in the memory buffer of the photodiode array controller are stored as 22-bit integers. However, in a single shot, the signal rarely has any points with greater than 12,000 counts, and cannot have any points with more than 21,000 counts. (The photodiode array analog-to-digital converter has 12-bit (4,096 counts) range. The array is scanned five times, giving total signals that cannot exceed $5 \times 4,096$, or 20,480 counts.) Therefore, only the low order word of the data is transferred to the 11/73 buffer. Immediately following the data transfer, data correction and subsequent signal averaging begins. Simultaneously, the next cycle of data accumulation is started by reopening the shutter. The cycle of data accumulation and processing continues until stopped by the user running the system, or until a predetermined, user-specified number of laser shots

Figure 2.3 Flowchart of Time-Resolved Emission Data Acquisition Process

Logical flowchart detailing ultrafast streak camera time-resolved emission data acquisition process.

Figure 2.3



*Signal processing occurs on second and subsequent cycles

have been accumulated.

4. Data Processing Software

The raw streak records transferred from the photodiode array controller to the 11/73 need a considerable amount of processing before signal averaging can be started. The first checks made on a streak record are of the height, position, and width of the time-marking, fiducial pulse. The signal processing software checks the intensity of the streak record to determine that there are channels with sufficient intensity to indicate that the record did not result from a weak or missed laser shot. If the signal intensity indicates that a pulse is present, the position of the pulse (as a photodiode array channel number) is determined. Shot-to-shot jitter in streak camera triggering, ± 20 ps typically, causes the pulses to be in different positions on the streak camera output phosphor, and hence, on the photodiode array, on different shots. (Streak rates are as fast as 0.3 ps/channel, so ± 20 ps corresponds to a window of almost 140 channels.) The data acquisition program requires that the position of the pulse fall into a user-determined window, usually 100–150 channels wide, for acceptance for subsequent processing. Signals are shifted so that the pulse peaks superimpose. As noted below [6], the width of the user-specified window limits the width of useable data in the final sum. If the fiducial pulse is found in the desired time window, the dataset is corrected (See Section B.5, below) for nonuniformities in streak rate and overall system intensity response. After correction, the position of the fiducial pulse is determined again, since the peak positions are often shifted by the correction procedure. If the fiducial pulse of the corrected dataset is still within the acceptance window, its width is calculated. Since wide pulses limit temporal resolution, the actual width is checked against a user-specified maximum-allowed width. This parameter is usually set so as not to result in a severe constraint in acceptance rates. If the width of the fiducial pulse is acceptable, the data are shifted so that the peak of the fiducial pulse is

in a user-specified channel. Each single shot is summed into two buffers simultaneously. The first buffer contains the running sum of all the datasets accepted. The second buffer is a similar sum, scaled to allow real-time display on a monitor scope using a direct memory access digital-to-analog converter (Data Translation, Inc., DT2771). The display on a monitor scope (Tektronix, Inc., Model 2215 oscilloscope) allows the user to track of the progress of signal averaging.

5. Calibrations and Corrections

The corrections performed on every individual streak record are based on the extensive calibration and characterization that has been performed on the system. The time base is calibrated by injecting pulses into a two-mirror etalon [7] with a variable spacing between the mirrors. For our calibration procedures, the spacing between the mirrors typically varies from 0.8 to 60 cm. The mirror spacing, L , is measured using calipers. The fixed temporal spacing, Δt , of the output pulses from the etalon can then be calculated:

$$\Delta t = \frac{2L}{c}, \quad (2.1)$$

where c is the speed of light. The etalon pulses are time-resolved using the streak camera, allowing the time base of the camera to be calibrated. Figure 2.4 shows the sum of 50 etalon traces, where the individual streak records were aligned and summed, without the customary corrections. The figure clearly shows that the etalon spacings are not uniform across the screen but vary by ± 10 percent. In order to improve the quality of our streak camera data, we have quantified this time-base nonuniformity, and developed routines to correct the streak records for its existence.

In Figure 2.5, data from a series of about 50 etalon traces are presented. This figure shows normalized etalon spacings as a function of photodiode array channel number. Altogether, the spacings between more than 200 etalon pulse pairs are represented in that figure. This figure shows the same nonuniformities responsible for the distortions

Figure 2.4 Etalon Traces, Summed But Uncorrected

The sum of 50 uncorrected time calibration datasets. The peak-to-peak spacings show a systematic variation. Spacings at the center of the photodiode array are smaller than the peak-to-peak spacings at the edges of the array. The values of peak-to-peak spacings are given in the figure.

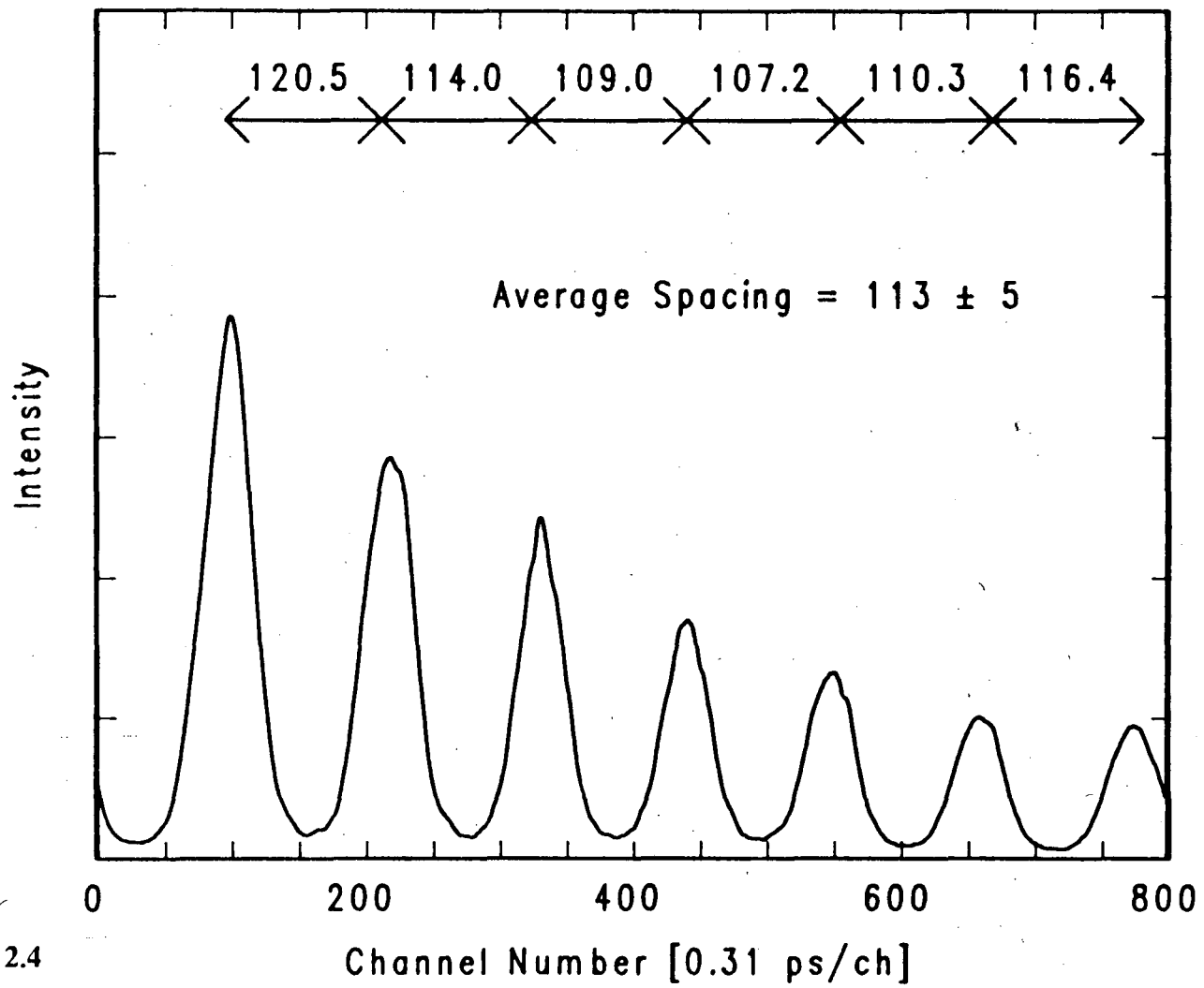
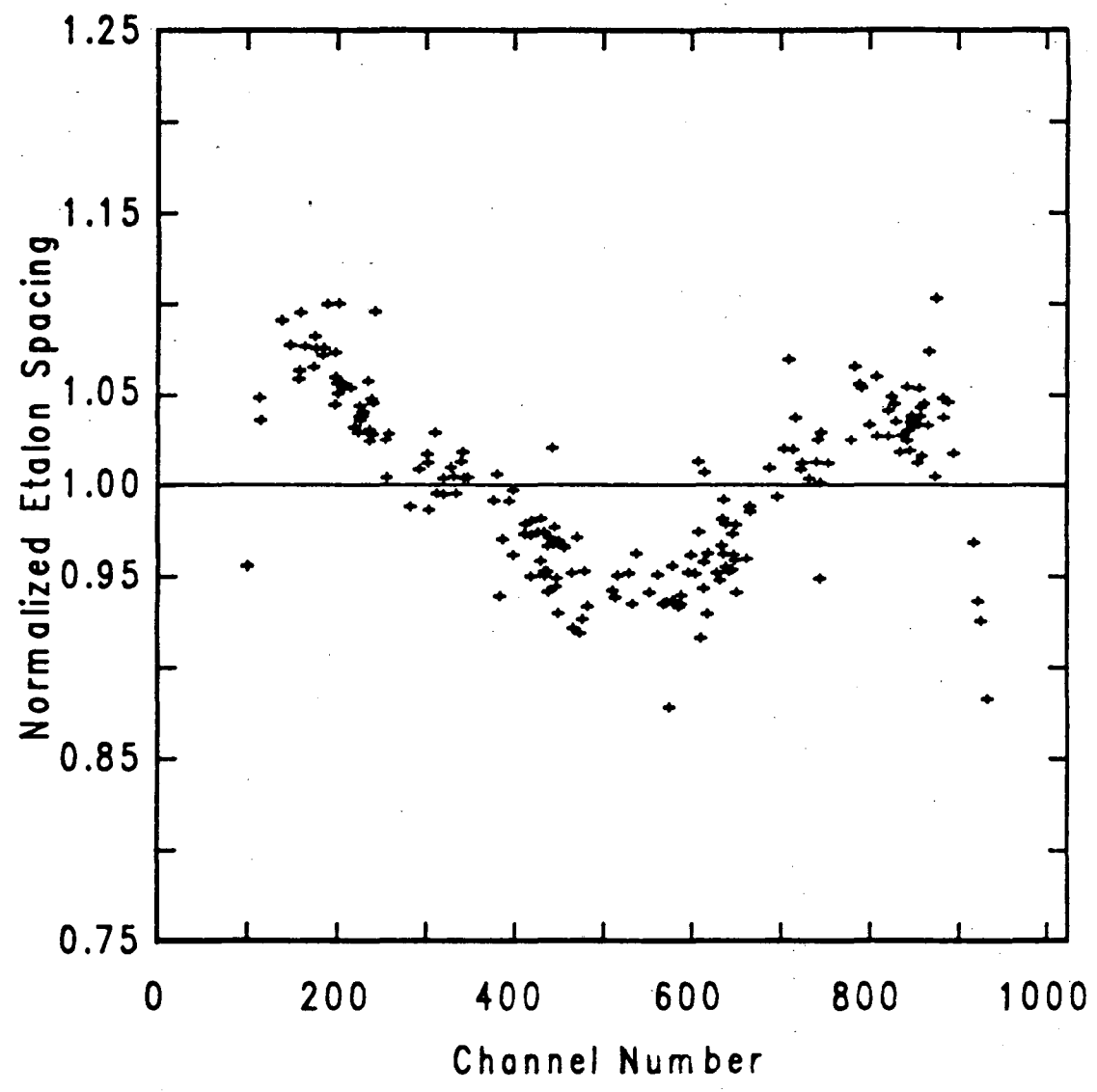


Figure 2.4

Figure 2.5 Normalized Etalon Spacing as a Function of Photodiode Array Channel Number

Data quantifying the non-linear time-base of the streak camera/diode array system. Normalized etalon spacing is plotted as a function of the center channel number. The spacings at both edges of the diode array are systematically larger than the spacings in the center. The sharp drop off at both edges of the array are due to the anomalously small spacings that are measured for pulses that are partially cut off by the edge of the array.

Figure 2.5



in peak-to-peak spacings in Figure 2.4 in more detail. The channels near the edges of the photodiode array show consistently larger than average etalon spacings, indicating that those channels account for less than the average amount of time. Similarly, channels in the center of the array show smaller than average etalon spacings, and consequently account for greater than average amounts of time. The distribution of spacings is symptomatic of a simple geometric distortion, caused when the spherically symmetric streak record is imaged onto the planar image intensifier. The etalon spacing data are used to quantify the actual time base. A correction algorithm has been developed to redistribute signal in the individual streak records from the actual non-linear time base over an artificial, linear time base. The data shown in Figure 2.6 are the sum of the same 50 streak records as used in Figure 2.4, summed after correction of each record. The improvement in spacing uniformity is considerable, 113 ± 5 channels without correction, 114 ± 1 with correction. The time-base calibration has been found to be quite stable, needing updates only when the streak electronics are changed. The second major source of nonuniformity in the streak camera system is due to nonuniform intensity response. To correct for this nonuniform sensitivity, a second calibration procedure is used. Since part of the nonuniformity in the sensitivity is correlated to small changes in the optical alignment of the camera, this second calibration is repeated each day. The standard used is the fluorescence from a molecule that has a lifetime that is long with respect to the time represented in a particular streak record, and that fluoresces with sufficient intensity to provide uniform illumination of the photodiode array on every laser shot. At streak speeds where the streak record is ≈ 1 ns in duration, a strong fluorescer with a fluorescence lifetime of ≈ 10 ns is generally used. Rubrene in cyclohexane is commonly employed. At slower streak speeds, good success has been obtained using aqueous solutions of the transition metal complex, ruthenium(II) tris-(2,2'-bipyridine) dication, $(\text{Ru(II)(bpy)}_3^{2+})$. This complex has a long lifetime (≈ 600 ns), relatively high luminescence quantum yield (≈ 10

percent), and substantial absorption cross section at both 532 and 355 nm. $\text{Ru(II)(bpy)}_3^{2+}$ solutions are effective at all streak speeds except the fastest, where the emission intensity is not quite sufficient to give uniform illumination on each shot. The correction factors necessary to eliminate channel-to-channel sensitivity variations are incorporated into the dataset that corrects the streak speed nonlinearities. Both nonuniformities are thus eliminated simultaneously, with a single computation, eliminating substantial computational overhead.

The effort required to perform the necessary computations is considerable. The correction algorithm takes approximately 0.16 sec per streak record when run on an 11/73 CPU using code generated with the RT-11/Fortran-77 compiler. Because of the computational power of the 11/73 (≈ 80 percent of the speed of a VAX 11/780) these calculations are successfully carried out in real time, and an effective data collection rate as fast as 2.92 Hz can be achieved. The factor that currently limits the data collection rate is the transfer rate of data from the photodiode array controller to the 11/73 memory. The transfer presently takes 0.77 sec to complete transfer of a set of seven records, or 0.11 sec per streak record. A substantial increase in the transfer is probably only possible by increasing the rate of transfer from the LSI 11/2-based photodiode array controller. However, even at an acceptance rate of only 2.92 Hz, accumulation of 1000 shots (typical signal averaging level) takes under six minutes. Production rates of 50-100 such datasets per day are commonly achieved. Even in its present state of development, the system enables substantial quantities of experimental information to be obtained in a relatively short amount of time.

6. Temporal Resolution of the Streak Camera System

One of the important aspects of the streak camera system that has not as yet been discussed is its impressive temporal resolution. The applications of the camera to be

Figure 2.6 Etalon Traces, Summed And Corrected

The sum of 50 etalon traces, corrected individually prior to summing. The datasets summed here are the same datasets that are summed in Figure 2.4. The correction algorithm clearly removes the systematic variation in the etalon spacings.

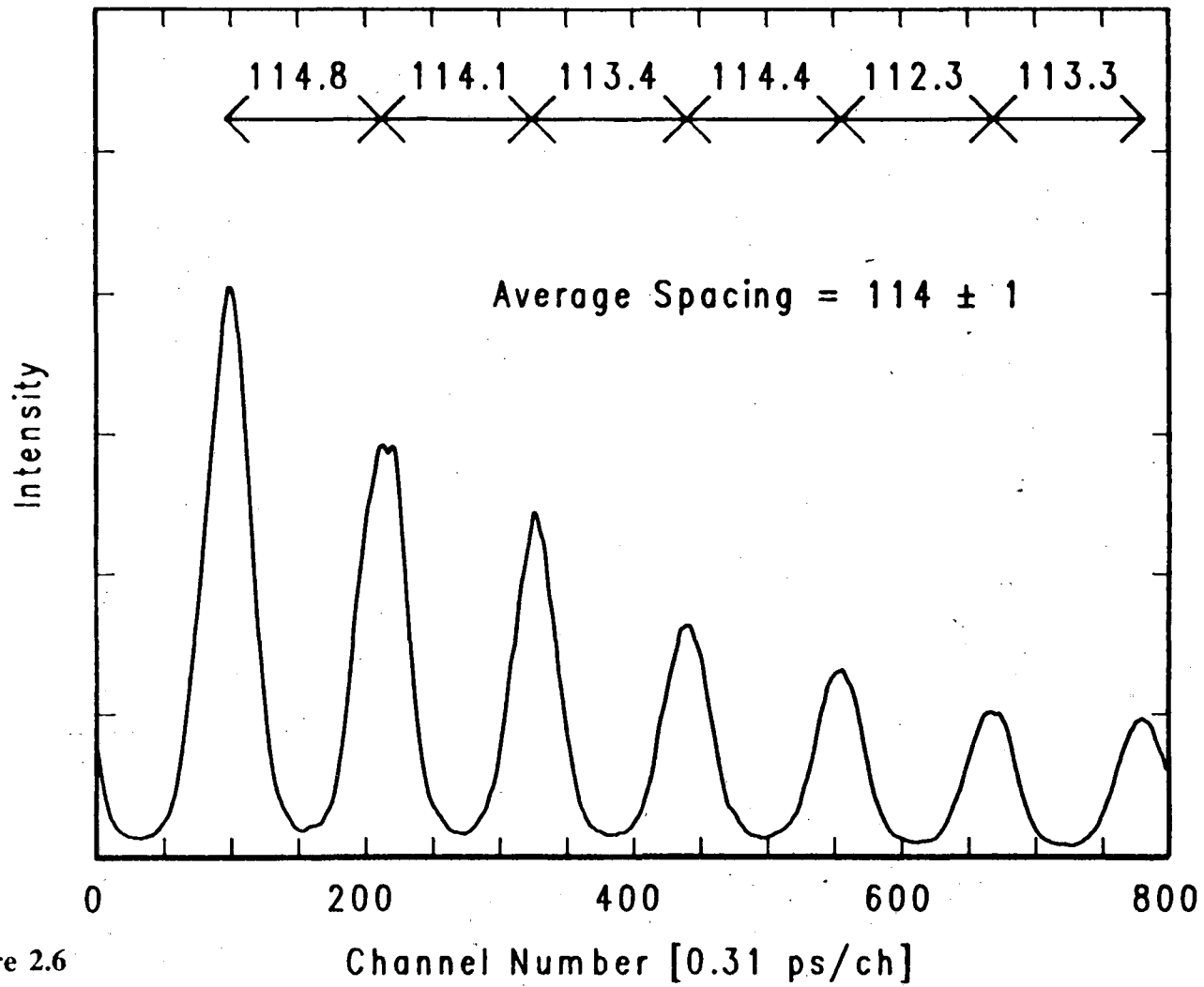


Figure 2.6

discussed in the following chapters require not only fast data acquisition rates, but require that the data obtained have temporal resolution of 10-20 ps. The temporal response of the streak camera system can be judged by the shape of the instrument response function, 10-12 channels for our system. The 12-channel instrument response function indicates that at the fastest streak speed, 0.3 ps/channel, the temporal resolution of the camera is about 4 ps. This resolution must be contrasted with that of single-photon counting instruments, where the instrument response function is ≈ 100 ps in width. In contrast to a single-photon counting apparatus, with the streak camera system, the pulse width (10-40 ps) limits our resolution more than the instrument response function.

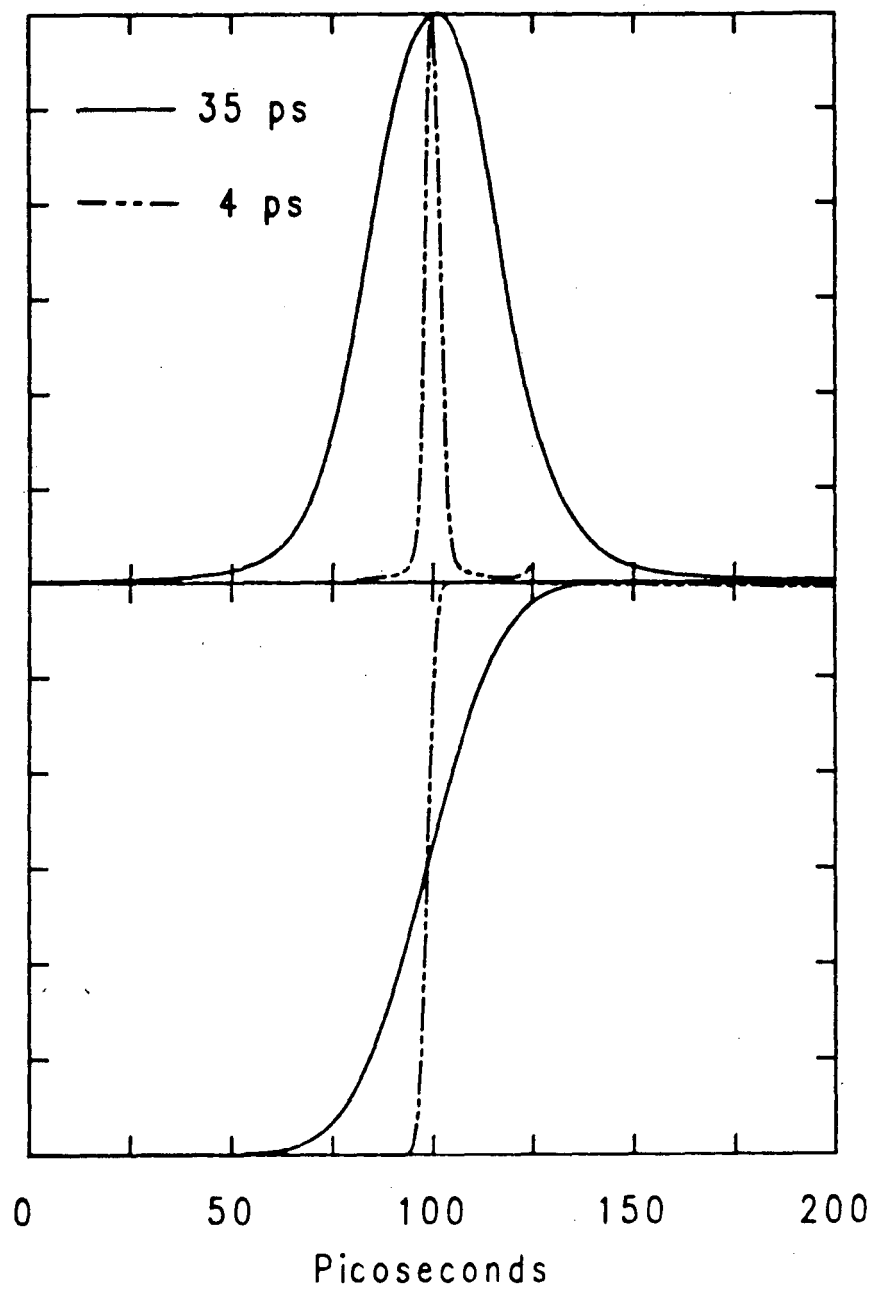
That the pulse-width limits the streak camera system resolution can be appreciated in Figure 2.7, where the relative widths of the instrument-response function and a typical pulse are shown. It is quite clear that the apparent width of the presented 35-ps pulse is not significantly distorted by the width of the response function. One of the common applications of the streak camera system is the investigation of ultrafast rise times. If the emitting state of an excited molecule is directly excited, the rise of emission intensity should be instantaneous. Mathematically, the emission profile should rise as the integral of the excitation pulse shape. In the second panel of Figure 2.7, the integration of the instrument-response function is shown with the integration of the 35-ps pulse. The temporal resolution of the streak camera is clearly not limited by the instrument response function, but by the excitation pulse profile. With our laser system, the shortest excitation pulses that have been observed are on the order of only a few picoseconds [3,4]. With pulses that short, the limitation of the system's resolution would still not be due to the finite instrument-response function.

We have taken data to test the resolution of the streak camera system to fast emission rise times. We have time-resolved emission from α -NPO, a laser dye, in ethanol solution. For bands throughout the emission spectrum of α -NPO, we have found that the onset of

Figure 2.7 Excitation Pulse Width vs. Streak Camera System Instrument Response Function

The top panel of the figure shows the instrument response function (4 ps) along with a typical 35-ps excitation pulse. The lower panel shows the integration of those two pulses. Clearly the ultimate instrumental resolution is not limited by the inherent resolution of the streak camera, but by the actual width of the excitation pulse.

Figure 2.7



emission is extremely prompt, with a rise time of less than or equal to about 8 ps. An instantaneous rise time for emission is the expected result for a molecule of the complexity of α -NPO [8]. In addition, we have studied molecular systems where the emission is expected to have a non-instantaneous rise time. Solutions of 4-(N,N'-dimethylamino)-benzonitrile (DMABN, see Figure 3.2) in polar solvents have been demonstrated to show non-zero rise times [9]. In this system there are two distinct excited states each with a distinct emission spectrum. (The excited-state dynamics of DMABN are discussed in greater detail in Chapter 3.) The excited state with lower energy emission forms from the higher energy excited state, and so one expects to see a correspondence between the growth rate of low energy emission and the decay rate of high energy emission. We have time-resolved 10-nm bands of emission throughout the emission spectrum of excited DMABN in a variety of solvents, and we have seen correspondence between low-energy emission rise times and high-energy emission decay times for DMABN. The relevance of these measurements to determining the temporal resolution of the streak camera is that these time constants can be very short. In ethanol, for example, we see correspondence between the temporal parameters for low and high energy emission. The range of the time constants found is 10–15 ps, indicating that we can measure reliably both short time scale decays and growth terms. The streak camera is extremely sensitive to short time scale temporal parameters.

C. Data Handling

1. Determining Temporal Parameters

The output of the streak camera data acquisition program must be analyzed to yield specific kinetic parameters. One of two different analytical techniques is implemented. If the signal decays appreciably in a trace, we attempt a simple semi-logarithmic analysis, particularly if the decay is long relative to the apparent width of the fiducial pulse. If rise

time information is sought, or if the fiducial pulse has an appreciable width relative to the decay time, then an iterative convolute-and-compare routine is used to recover temporal parameters with the effect of the pulse removed.

The semi-logarithmic analysis is straightforward. The emission from a population of excited molecules frequently shows first-order kinetics, so the excited-state population decays away exponentially in time. Emission intensity is directly proportional to the excited-state population, so the temporal profile of emission often shows a single exponential decay. A semi-logarithmic plot (the natural logarithm of emission intensity as a function of time) will yield a straight line with slope equal to the time constant of the decay. To analyze data by this method, we plot the data semi-logarithmically and determine the linearity of the result. If linear over three or more lifetimes, the slope of the line is our measure of the fluorescence lifetime.

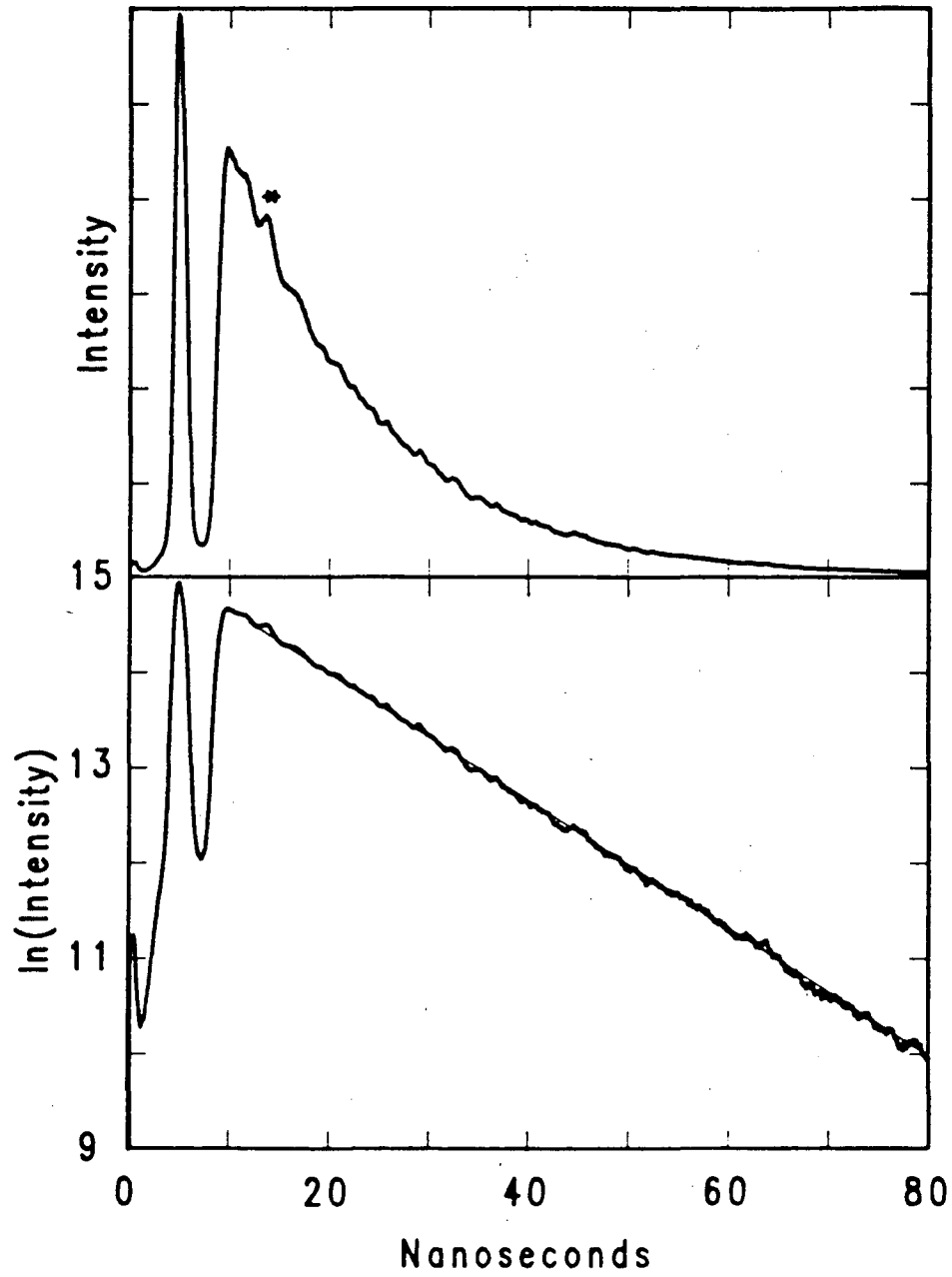
An example of analysis by the semi-logarithmic technique is shown in Figure 2.8. In this figure, the top panel shows ≈ 80 ns of the decay of 3-aminophthalimide in 1-propanol. The decay looks exponential, except for the distortion marked by an asterisk. That distortion is due to leakage of a small fraction of the pulse in the pulse train that follows the main picked pulse. The small distortion is ≈ 10 ns from the main excitation pulse, corresponding to the round trip time expected for the 1.6-m long oscillator cavity. The lower panel shows the semi-logarithmic plot of that data. Except for the distortion due to the second picked pulse, the plot is very linear, as shown by the superimposed straight line. The linearity extends over four lifetimes, and the slope of the line corresponds to a lifetime of 14.9 ± 0.2 ns.

When the semi-logarithmic analysis approach is not effective, for instance because of curvature in the semi-log plot, or because the excitation pulse-width is close to the time constant measured, or because an emission rise time is to be determined, an iterative convolute-and-compare technique is employed. The fiducial pulse is then used analyti-

Figure 2.8 Decay of Emission from 3AP in 1-Propanol

Decay of emission from 3AP in 1-propanol, at 20°C. The time-resolved data are shown in A. The linearity ($r=0.999$) over four lifetimes of the semi-logarithmic plot (B) indicates that the decay is single-exponential. The significance of the asterisk (*) is explained in the text.

Figure 2.8



cally as a record of the temporal profile of the excitation source. Appropriate sums or differences of exponentials are taken, convoluted with the pulse profile, and normalized to the actual signal intensity. The chi-squared, χ^2 , value is then calculated [10]. The parameter space of the constants and pre-exponential factors is iteratively searched using a simplex searching routine². The best-fit parameters are those that minimize χ^2 .

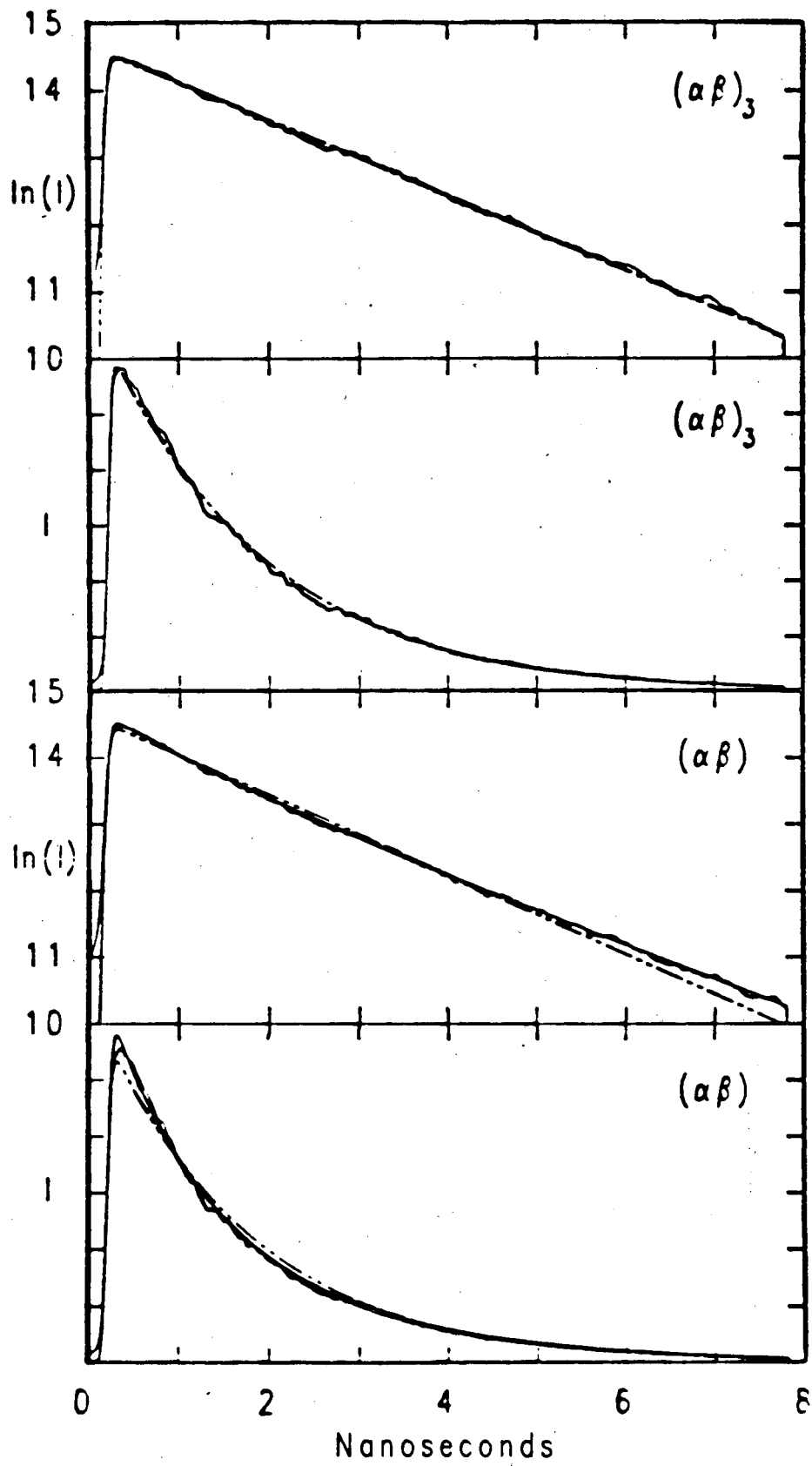
An example of the failure of the semi-logarithmic method is presented in the data of Figure 2.9. Pictured in the figure are datasets that decay significantly within the streak record. The datasets are time-resolved emission from the phycobiliprotein allophycocyanin, detected through a high-pass filter (Corning 2-58), after excitation at 620 nm. The aggregation state of a phycobiliprotein is very sensitive to solution conditions [11]. For the data in the top panels, the aggregation state of the allophycocyanin was trimeric, $(\alpha\beta)_3$. The lower panels are time-resolved emission records from monomeric allophycocyanin, $(\alpha\beta)$. The trimer data, in the top panels, are fit well with just a single exponential decay. The semi-logarithmic plot shows that the single-exponential fit follows the data closely for over four lifetimes. The monomer data however, do not fit well to a single exponential fit. The dashed curve is a single exponential fit to the data. There is clearly curvature in the semi-logarithmic plot of the data. A superior fit is obtained from running the iterative convolution program, to obtain a two-exponential fit to the data. The improvement in the fit is particularly obvious in the semi-logarithmic plot.

The iterative convolution program is also used to determine short time scale temporal parameters, and all rise times. An example of the latter application is given in Figure 2.10, where the rise time of 650-nm emission from a solution of 4-aminophthalimide (4AP) in 1-propanol is plotted. The smooth, solid curve is the computer-generated, best-fit convolution. The rise time that that best fits the experimental curve was 86 ps. The biggest source of error in fitting the early time emission profile is that the exact starting point (the time-zero) of the data is uncertain. This uncertainty is presented graphically

Figure 2.9 Double-Exponential Decay Determination

Emission decay from solutions of allophycocyanin (AP) as a function of time and aggregation state. The top panels are emission detected through a Corning 2-58 high pass filter from trimeric aggregates of AP. The fit (smooth curve) is a single exponential decay, 1.7 ns, that shows excellent agreement with the data over four lifetimes. The lower panel shows emission detected through the same filter, from solutions of monomeric aggregates of AP. The single-exponential fit (dotted curve) is clearly inferior to the double-exponential fit (solid curve). The parameters of that fit are: $\alpha_1=1.0$, $\tau_1=880$ ps and $\alpha_2=1.5$, $\tau_2=1900$ ps.

Figure 2.9



in Figure 2.10, where the two smooth, dashed curves represent the shortest and longest rise times that still give a satisfactory fit. The range in satisfactory fits is 86 ± 10 ps.

2. Generating Emission Spectra At Discrete Times

The final special data-handling technique to be described here is particularly important to the analysis of the solvation work described in Chapter 3, that of spectral reconstructions. After using the streak camera system to resolve temporally 10-nm bands throughout the emission spectrum of the solute/solvent system, the previously discussed semi-logarithmic and iterative convolution fitting routines are used to determine the temporal parameters for each spectral region. The temporal parameters are analytically integrated and then normalized to the intensity found in the corresponding region of the steady-state emission spectrum. The appearance of the spectrum at any instant in time can be calculated because the temporal profiles of all the spectral regions are known, and the analytic integration/normalization procedure insures that the relative intensities found in the steady-state spectrum are reproduced. After calculating the reconstructed spectral profiles at an array of times, the profiles are fit using another simplex-based iterative fitting routine. The spectral profiles are generally fit in energy to Gaussian shapes, where the width, position, and height of the Gaussian are allowed to vary to best-fit the calculated spectra. The course of the temporal variation of the peak of the emission spectrum can therefore be determined.

For this work, the steady-state spectra are measured on a sensitive, computer-controlled steady-state spectrofluorimeter (Spex Industries, Inc., Fluorolog 2). The spectrofluorimeter has provisions for quantum correction of the excitation source using a concentrated Rhodamine B quantum counter. The emission detectors have been calibrated using a standard lamp.

The estimated accuracy of the spectral reconstructions is difficult to determine. How-

Figure 2.10 Initial Profile of Emission from 4AP in 1-Propanol—Rise Time Sensitivity

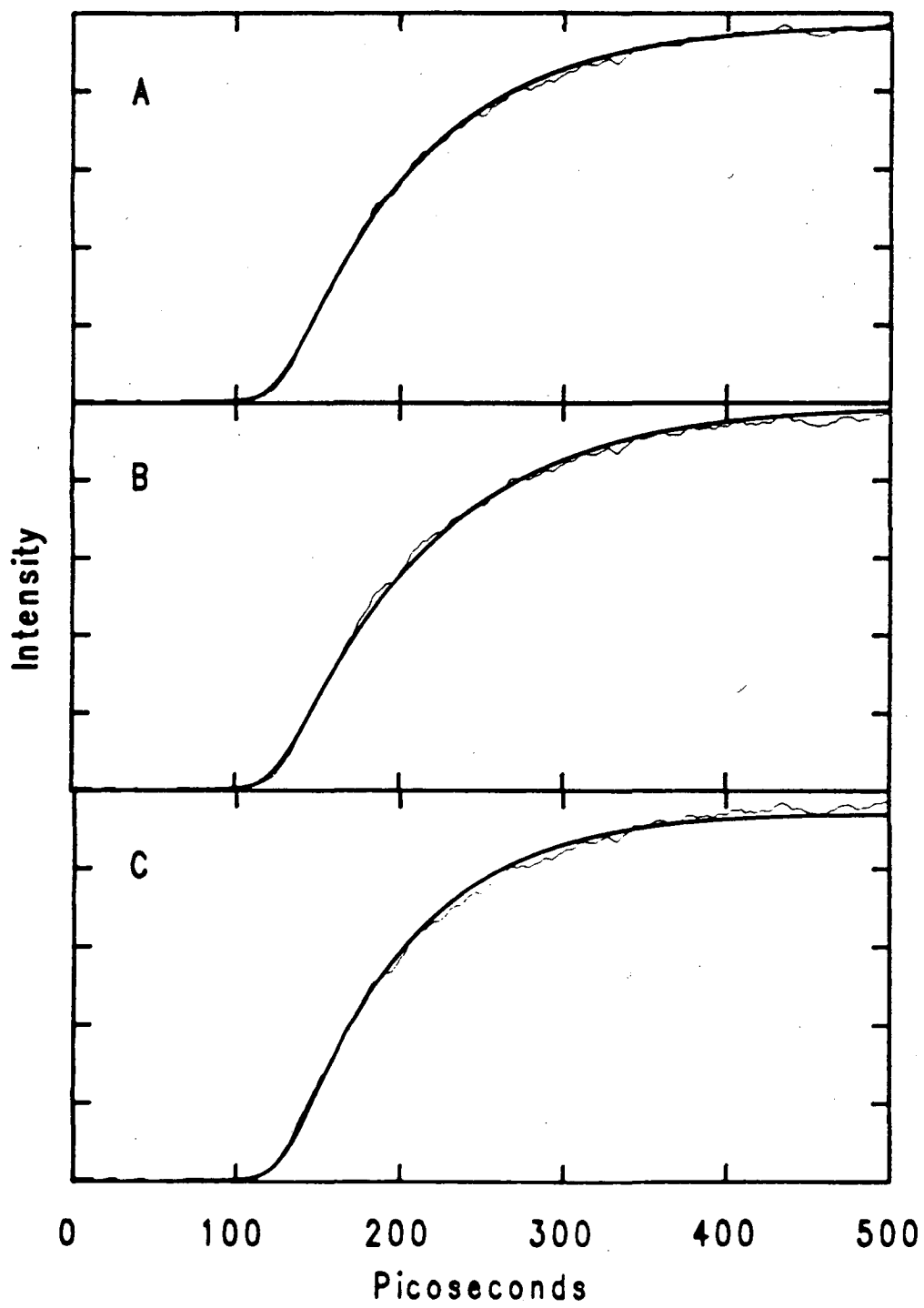
The initial profile of emission of 4AP in 1-propanol is shown in this figure.

A. The fit to the data is the “best-fit” rise time, giving a rise time of 86 ps.

B. This fit is noticeably too long, even after compensating with the time zero. The rise time of this fit is 95 ps.

C. This fit rises too promptly, again in spite of time zero compensation. The rise time of this fit is 75 ps.

Figure 2.10



ever, the spectrum of 4AP in 1-propanol (Chapter 3, Section B) has been completely time-resolved on three separate occasions. In all cases, the temporal parameters have been in close agreement (See Tables 3.1,3.9). From the temporal parameters, the positions of the spectral peak at various times can be calculated. The three independent determinations agree satisfactorily.

One further indication of the quality of the spectral inversion is given in Figure 2.11. The emission spectra as a function of time that are shown in Figures 3.6 and 3.16-3.19 all show very small deviations in emission intensity during the periods of substantial shifting. This intensity-invariance is the result of a very sensitive interplay of the shape of the steady-state spectrum position, and the values of the temporal parameters. In the top panel of Figure 2.11, the time-resolved spectra for 4AP in 1-propanol are given, using the steady-state spectrum of 4AP in 1-propanol to normalize the data. In the center panel of the figure, the time-resolved spectra that result from normalizing the temporal parameters for 4AP in 1-propanol to the steady-state spectrum of 4AP in methanol. The intensities are far more consistent for the 4AP in 1-propanol normalization. The two steady-state spectra are reproduced in the lower panel of the figure, and the sensitivity of the parameters to the position of the normalization spectrum can be appreciated. Although there is no way to predict that the emission spectrum should be of uniform intensity through the spectral shifts, that uniformity is obtained, when the correct normalization spectrum is used.

D. Sample Preparation

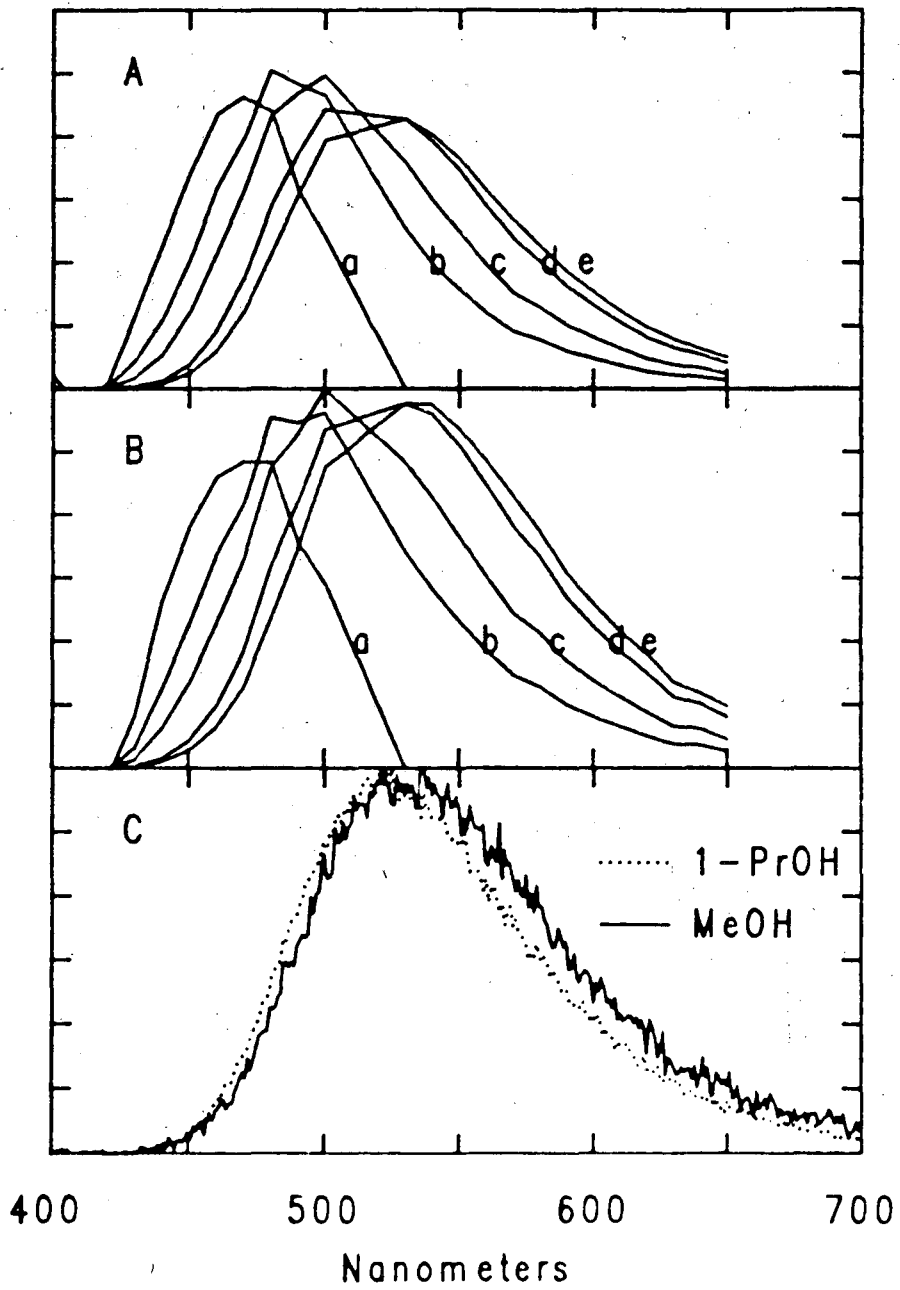
1. Excited-State Solvation Studies

For the studies of 3AP and 4AP time-resolved spectral dynamics, solutions were made up to 10^{-5} to 10^{-4} M in distilled-in-glass grade solvents (Burdick and Jackson). The 4AP was recrystallized from methanol prior to use. Some solutions were degassed by bubbling dry N_2 through them prior to use, but no differences between degassed and

Figure 2.11 Time-Resolved Emission Spectra

This figure gives examples of calculations of time-resolved emission spectra obtained through the inversion process described in Section C.2. The top panel shows the spectra as a function of time for 4AP in 1-propanol, using the correct 4AP in 1-propanol steady-state spectrum for normalization. The center panel shows the spectra calculated for 4AP in 1-propanol using the incorrect 4AP in methanol steady-state spectra spectrum for normalization. The lower panel presents the two steady-state spectra, and indicates the quality of the balance required between spectral parameters and steady-state spectral shape to obtain reliable time-resolved emission spectra.

Figure 2.11



non-degassed solutions were found, so the procedure was dropped. Solutions no more than a few days old were used.

2. Photosynthetic Antenna System Studies

The sample preparations for all of the solutions used in the studies of the photosynthetic antenna systems were produced in the laboratory of Prof. A. N. Glazer, Department of Microbiology, UC Berkeley. Intact phycobilisomes and isolated phycobiliproteins were prepared according to documented procedures. Data were obtained from the samples within a day of preparation for the less stable preparations, and within a few days for all preparations. The work performed by Prof. Glazer and his associates was of the highest possible quality. Their patience with the occasionally glacial progress of the picosecond experiments has been greatly appreciated.

E. References for Chapter 2

1. A. J. Campillo and S. L. Shapiro, *IEEE J. Quant. Electr.* **19** (1983) 585.
2. J. N. Demas, *Excited State Lifetime Measurements* (Academic Press, New York, 1983) 273 pp.
3. H. Nathel, D. M. Guthals, D. W. Anthon, and J. H. Clark, *J. Opt. Soc. Am.* **73**, (1983) 1897; H. Nathel, D. M. Guthals, D. W. Anthon, and J. H. Clark, *Opt. Lett.*, to be submitted.
4. D. M. Guthals, H. Nathel, C. C. Hayden, and J. H. Clark, *J. Opt. Soc. Am.* **73**, (1983) 1896; D. M. Guthals, H. Nathel, C. C. Hayden, and J. H. Clark, *IEEE J. Quant. Elec.*, to be submitted.
5. Hadland Photonics User Manual for the Imacon 500; D. Bradley, S. F. Bryant, J. R. Taylor, and W. Sibbett, *Rev. Sci. Instrum.* **49** (1978) 215.
6. Signals from individual streak records are shifted so that the fiducial pulses are superimposed prior to summing. Therefore, the width of the user-specified window limits the width of useable data in the final sum. As an example, consider the window to be 150 channels wide. For some laser shots, the position of the fiducial pulse might require a shift of 150 channels. In this extreme case, signal from channel 1024 is shifted to channel 874, and there is no information to put into channel 875. The width of the signal-averaged record is therefore limited to 874 channels, or the difference between the 1024-channel width of the photodiode array and the width of the user-specified acceptance window.
7. S. L. Shapiro, A. J. Campillo, V. H. Kollman, and W. B. Goad, *Opt. Commun.* **15** (1975) 308.
8. α -NPO is a laser dye of comparable molecular complexity to Rhodamine B. The photophysics of α -NPO have not been studied with femtosecond resolution, but by analogy with the results for Rhodamine B, it is likely that the rates of excited-state vibrational relaxation are fast, resulting in instantaneous population of the emitting state. The appropriate reference for Rhodamine B is C. V. Shank, E. P. Ippen, and O. Teschke, *Chem. Phys. Lett.* **45** (1977) 291.
9. Z. R. Grabowski, K. Rotkiewicz, A. Siemiarczuk, D. J. Cowley and W. Bauman, *Nouv. J. Chemie* **3** (1974) 443; W. S. Struve, P. M. Rentzepis, and J. Jortner, *J. Chem. Phys.* **59** (1973) 5014; Y. Wang, M. McAuliffe, F. Novak, and K. B. Eisenthal, *ibid.* **77** (1982) 6076; D. Huppert, S. D. Rand, P. M. Rentzepis, P. F. Barbara, W. S. Struve, and Z. R. Grabowski, *ibid.* **75** (1981) 5714; J. Hicks, M. Vandersall, Z. Babarogic, and K. B. Eisenthal, *Chem. Phys. Lett.* **116** (1985) 18.
10. P. R. Bevington, *Data Reduction and Error Analysis for the Physical Sciences* (McGraw-Hill, New York, 1969).
11. A. N. Glazer, in *The Biochemistry of Plants*, M. D. Hatch and M. K. Boardman, eds. (Academic Press, New York, 1982), vol. 8, pp. 51-96; A. N. Glazer, *Biochim. Biophys. Acta* **768** (1984) 29.

Chapter 3

I. Real-Time Measurements of Solvent-Solute Interactions

A. Introduction

Many synthetic chemical reactions are performed in a solvent in the liquid phase. Solvents are generally chosen to enhance the rate of reaction, or the extent of reaction completion, or both. Synthetic chemists choose solvents based principally on experimental experience and intuition, guided by known macroscopic properties [1]. Physical properties of a solvent such as polarity, hydrophobicity or hydrophilicity, viscosity, freezing point, boiling point, and dielectric constant, as well as the practical properties of availability, cost, toxicity, or stability are the variables that a synthetic chemist uses. The guidelines that synthetic chemists formulate based only on macroscopic properties of the solvent have the disadvantage for physical scientists that the microscopic details of the chemical interactions are generally ignored. In order to understand more fully the effect of solvent on condensed phase chemistry, it is important to determine microscopically the nature of solvent-solute interactions.

The problem of extracting microscopic information is difficult, however, because of the nature of the liquid state. Liquids are dense (on the order of 10^{22} molecules/cm³) [2] and disordered. A molecule in solution is constantly being bombarded by the surrounding solvent, experiencing nearest-neighbor collisions on the order of every 0.1 ps [3]. Experiments that probe microscopic solvent environments are difficult to perform, because data on very short time-scales are generally needed. Theoretical calculations of liquid state properties are of little assistance in clarifying details of the microscopic environment, because the calculations are computationally difficult. This computational difficulty is due in part to the large number of particles that must be considered to mimic accurately the real solution, and also because of the short time-scales over which poorly known

interaction potentials must be used [4]. Calculations of liquid state distribution functions including more than just a few picoseconds of time are essentially computationally unapproachable [5].

There is an experimental approach that has been used for years to obtain information on solute-solvent interactions. The approach is spectroscopic, and based on the selective electronic excitation of solute molecules. Generally a single probe chromophore is used to determine the relative rankings of some particular property in a number of solvents. For instance, something as simple as the changes in the absolute positions of absorption bands are indicative of changes in the interactions between the ground-state solute and the solvent. The history of the application of absorption-based investigations to enhance the understanding of solvent-solute interactions is very long. One of the first instances can be traced to Hildebrand's classic work on "regular" solutions where the shape and position of the absorption spectrum of iodine was used to classify solvents systematically [6]. The relative positions of absorption and emission bands in a series of different solvents are evidence of solvent-solute interactions that are different for the ground and electronically excited states. Changes in the magnitude of this energy shift between the positions of absorption and emission bands for a single chromophore in different solvents has also been used to develop a system of solvent classification [7]. The investigations described here elaborate on the use of emission Stokes' shifts to elucidate the details of solute-solvent interactions.

B. Experimental Approach—Dynamic Stokes' Shifts

Stokes' shifts are different for different solvents because the ground and electronically excited states can have significantly different electronic properties [8]. Changes in electronic properties are due simply to differences in electron distributions that exist between the ground and excited states. Physical properties dependent on the electron

distribution are, for instance, Lewis acid-base properties [9] and changes in polarity [10]. It is possible to have a compound that is a weak acid in its ground state and that is highly acidic in its excited state [11]. Conversely, the excited state can have enhanced basicity relative to the ground state [12]. Changes in polarity where the excited state has either greater or lesser polar character than the ground state, or where the direction of the dipole moment changes on excitation are possible [10]. If the solute molecule does undergo changes in electronic properties, the equilibrium solvent configuration around the ground state molecule may be significantly removed from the configuration appropriate for the electronically-excited chromophore. For example, when the excited chromophore has a larger dipole moment than it had in its ground state, significantly greater interactions would be expected to occur between the excited chromophore and a polar solvent than between the solvent and the ground-state chromophore. Our experimental approach takes advantage of electronic excitation to study solute-solvent interactions.

Using visible photons to excite solute molecules can result in the rapid introduction of a changed solute into the solvent. The introduction is rapid since the absorption of a photon of optical frequency takes only 10^{-15} sec. The excitation process is a Franck-Condon transition, where the nuclear coordinates of both the solute and surrounding solvent molecules are unchanged on the time scale of the absorption. Excitation thereby traps the excited chromophore in the solvent configuration appropriate for the ground state. Since the ground state solute-solvent configuration may be significantly removed from the equilibrium configuration of the solvent around the excited solute, relaxation of the solvent around the excited solute can occur. If the lifetime of the excited state is long relative to the rate of the solvent relaxation, one would expect to see emission with a substantial Stokes' shift, because solvent-solute relaxation would lower the energy of the emitting state.

The way our experiments take advantage of the Stokes' shift to study solute-solvent

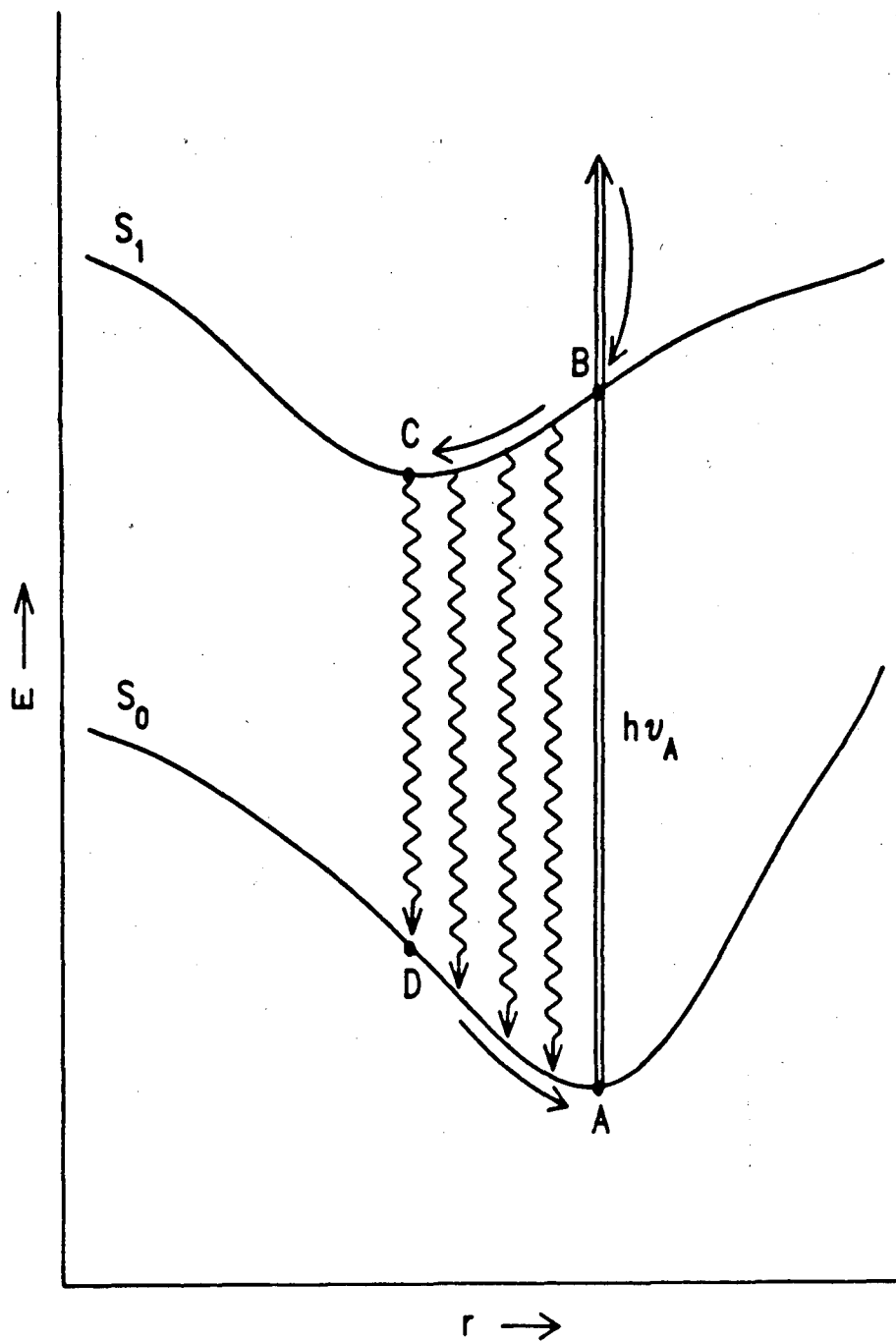
interactions is schematically pictured in Figure 3.1. The figure gives the energy of the ground state, S_0 , and the first excited state, S_1 , as a function of a hypothetical interaction coordinate, the solvation coordinate. The starting point for the experiments is point A, the equilibrium and lowest energy configuration of the solvent around the solute prior to excitation. The absorption of a photon results in a vertical transition to the first excited state, generally with excess vibrational energy. The excess vibrational energy is quickly dissipated (in less than a few tenths of a picosecond [13]), resulting in excited state population at position B, in the ground vibrational level of the excited electronic state. The system evolves, moving toward the equilibrium solute-solvent configuration appropriate for the excited electronic state, point C. Motion from point B to point C results in two contributions to the Stokes' shift. Not only is the energy of the excited-state decreasing with solvent relaxation, but the vertical transition from the excited state to the ground state (at point D) is to a solute-solvent configuration at higher energy than that configuration which is optimum for the ground state. The differences in steady-state Stokes' shifts as a function of solvent are due to differences between the ground and excited electronic states in the relative curvatures and positions of the minima of energy along the solvation coordinate.

Using the absorption of an optical photon to create the excited state potentially allows very short time scale data to be obtained because the excitation process is instantaneous on the time scale of any chemical process like reaction or solvation. In fact, one would expect that after excitation of a group of solute molecules, the emission from the molecules should show a time-dependent red-shift as the population of excited chromophores moved along the reaction coordinate from point B to point C. Emission due to molecules at point B would show a small Stokes' shift due to the vibrational relaxation that has dissipated a small portion of the excitation energy. As the system evolves toward point C, the emission would show a greater and greater Stokes' shift as the energy spacing between

Figure 3.1 Potential Energy Diagram for Solute-Solvent Interaction

The figure shows the potential energy of the ground (S_0) and first (S_1) electronic states as a function of the solvation coordinate. Point A gives the equilibrium solvent-solute configuration. For the excited state, the equilibrium solvation configuration is point C. Initial excitation of ground state solute molecules gives excited state population at point B, the Franck-Condon state. Subsequent to excitation, a competition takes place between relaxation within the excited state (motion from B to C) and relaxation of the excited state (transition from S_1 to S_0). If motion from B to C is slow relative to the lifetime of the excited state, emission will be from the Franck-Condon state. If motion from B to C is fast, emission will be Stokes' shifted. The most interesting case is if the motion from B to C is fast relative to the lifetime of S_1 , but slow relative to instrumental temporal resolution, so that emission will be detected from intermediate solvation configurations. Details of the time scale of motion along the solvation coordinate can be obtained from time-resolved emission.

Figure 3.1



the excited and ground states decreases. The study of dynamic Stokes' shifts enhances the information elucidated by measures of shift magnitudes with kinetic data.

Of course, whether the solvation process is detectable would depend on the rate of relaxation of the excited state relative to the lifetime of the excited state. If the excited-state lifetime is very short relative to the rate of solvent reorganization, the emission would occur with only a small Stokes' shift from an unrelaxed solvent configuration. Unfortunately, the time resolution available is not limited by the time scale of the photon absorption, because single photon excitation is not experimentally feasible. The effective temporal width of the excitation is not as short as 10^{-15} sec, but limited to the temporal width of the experiment's excitation source. If the rate of solvent reorganization is extremely rapid with respect to the temporal width of the excitation source or the time resolution of the detection electronics, the solvation process will not be discernable. Our experimental apparatus is based on excitation using a harmonic of an amplified picosecond pulse from a modelocked Nd:YAG laser, with a width of approximately 40 ps. Emission is spectrally-resolved with 10-nm bandpass filters, and time-resolved with an ultrafast streak camera. With this apparatus, the solvation process can be monitored as it occurs by time-resolving Stokes' shifts of emission.

C. Previous Applications of Time-Resolved Stokes' Shifts

By time-resolving emission, the kinetics of a wide range of chemical reactions have been determined [14]. The basic principle underlying the determinations is described in some detail in the experimental methods section in Chapter 2, but is also summarized here. A molecule that is electronically excited has a number of possible paths available to it. All excited molecules can undergo relaxation. The relaxation can be accomplished with the emission of a photon or radiationlessly. Many excited molecules relax by both pathways. Some electronically excited molecules can also react to form a product that

may or may not retain electronic excitation. All three processes—emission, radiationless decay, and reaction—deplete the population of the excited state. Since the emission of photons is a first-order process, the intensity of emission is directly proportional to the population of the emitting state. If the reacting excited state emits, the apparent time-constant of the emission will be related to the rates of the three processes that deplete population (reaction, radiationless decay, and emission). If the products of the reaction of the excited state retain excitation and have finite emission rates, the rate of formation of those products can be determined by monitoring the growth rate of product emission. It is generally true that product emission is red-shifted from reactant emission, allowing straightforward spectral discrimination between the two states.

One can predict what should be experimentally observed as the excited system reacts. As yet unreacted and unrelaxed initially excited molecules are the source of the high energy emission. The molecules responsible for the high energy emission are directly excited by the laser pulse, and so the temporal profile of the high-energy emission rises promptly. The emission will show fast components of decay because the high energy states are depleted as the reaction proceeds. Unlike the directly excited reactant molecules, the product is not produced directly by the excitation pulse but is populated indirectly by the reaction. The lower energy product emission is not present until the reaction creates product population. Therefore, the temporal profile of the low energy emission will have a growth component corresponding to the rate of the excited-state reaction.

Examples of studies that have exploited time-resolved emission to measure rates of reaction of excited-state molecules are plentiful. For instance, as already mentioned, the changes in electronic properties that can occur between the ground and excited electronic states can cause large changes in the acid-base properties of the molecules. Many aromatic alcohols can have excited states that are radically more acidic than their ground states [9,11,12]. In 1-naphthol, the excited-state pK_a is almost nine orders of magnitude smaller

than the ground state pK_a [15], indicating that the acidity of the excited state is more than nine orders of magnitude greater than the acidity of the ground state. Excitation of a neutral alcohol results in the instantaneous formation of a neutral molecule that is an extremely strong acid. An excited-state proton-transfer reaction can ensue, producing the conjugate base of the alcohol after transfer of the acidic proton to the solvent. Results from our laboratory have shown [11] that if an aqueous solution of 1-naphthol is excited, emission from the conjugate base, naphtholate anion, shows a rise time of 32 ± 5 ps, corresponding to a proton transfer rate of $2.5 \times 10^{11} \text{ sec}^{-1}$. Emission from the neutral 1-naphthol was also observed, and showed a time constant of decay of about 32 ± 5 ps, consistent with its role as the source of naphtholate population. Measurements of other proton transfer rates have been performed in many molecular systems, including 2-naphthol [16], 1-and 2-naphthol derivatives [17], and the hydroxyflavones [18], to cite just a few examples.

There are other classes of reactions that have been studied. After excitation, there may be more than one electronic state that is energetically accessible for the molecule. An example of such a molecular system is 4-(N,N'-dimethylamino)benzonitrile (DMABN). The ground state of DMABN has been shown to be planar, with the carbon and nitrogen atoms of the dimethylamino group in the same plane as the benzene ring [19] (see Figure 3.2A). There are two electronically excited states, a planar state and a "twisted intramolecular charge-transfer" (TICT) state (Figure 3.2B). The planar excited state is the state in which Franck-Condon transitions from the ground state terminate. The TICT state is strongly dipolar in nature [20] and is stabilized in polar solvents relative to the planar excited state. The TICT state, like the conjugate base in the previous example, is not directly formed by the excitation process, but only forms after the excited-state reaction, which is in this case a geometric rearrangement. In polar solvents, the low energy emission is from the TICT state and its temporal profile shows a measureable rise

Figure 3.2 The Structure of 4-(N,N'-Dimethylamino)benzonitrile (DMABN)

The structure of ground state DMABN is planar (3.2A). In non-polar solvents, this is also the geometry of the lowest energy excited state. In polar solvents, the lowest energy geometry is the "twisted internal charge-transfer" (TICT) state (3.2B).

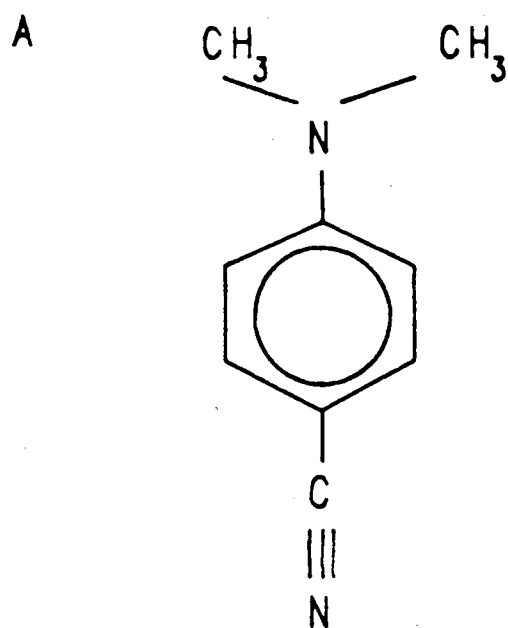
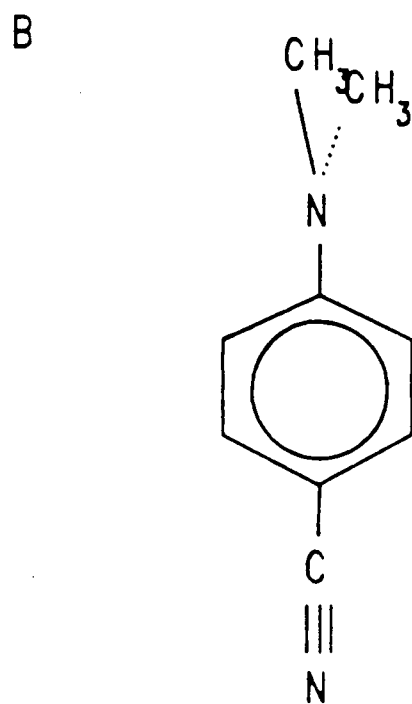


Figure 3.2



time, with the growth rate of the emission related to the rate constant of the excited-state rearrangement. The high energy emission from the Franck-Condon state shows a fast decay with a time constant approximately equal to the high energy decay time [21,22].

For each of these two examples, there were two distinct excited states available to the molecular systems. The two excited states that play a part in excited-state proton-transfer are simply the excited neutral and the excited deprotonated conjugate base. For DMABN and similar molecular systems the Franck-Condon and TICT states are distinct. For both types of reaction, the solvent is intimately involved in the process: for the excited-state proton-transfer reactions, the solvent acts as the base; for DMABN, the solvent changes the relative energies of the two electronic states. Solvent properties have been shown to influence strongly the reaction rates determined [22,23] for both reactions. However, the substantial changes in molecular structure that occur in the excited states of the solute molecules complicate the complete determination of the role of the solvent. A simpler situation, which might allow the determination of the role of the solvent alone, would be one where there was only a single excited electronic state with which the solvent interacted. A candidate for such a system is found in 4-aminophthalimide (4AP, structure given in Figure 3.3) [24], a molecule with a highly polar excited state [25,26]. Previous studies of excited-state reactions have shown that 4AP shows time-dependent Stokes' shifts [26].

In the previous studies of 4AP [27], Ware measured distinct red-shifts as a function of time in cold (temperatures below 200 K) solutions of 4AP in 1-propanol. The data were rationalized by proposing that the excited 4AP molecules form an exciplex with solvent molecules. The emission shows a time-dependent red-shift because as the exciplex forms the excited-state of 4AP lowers in energy. The temporal resolution of the system used to study the spectral dynamics was on the order of several nanoseconds, and so the fastest shifts that could be resolved reliably were on a time scale longer than 10 ns.

Figure 3.3 The Structure of the Aminophthalimides

The molecules referred to in this work as 4-aminophthalimide (4AP) and 3-aminophthalimide (3AP) are pictured here. Standard nomenclature given in references 24 and 63.

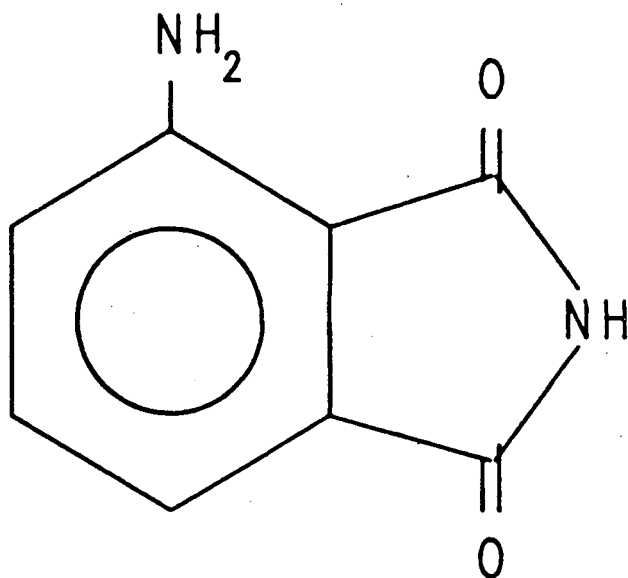
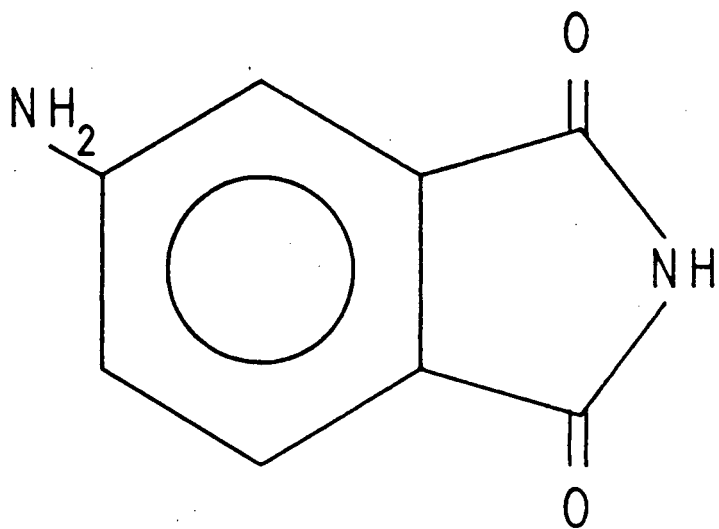


Figure 3.3

3-Aminophthalimide



4-Aminophthalimide

Solutions of 4AP in 1-propanol gave spectral shifts on a slow enough time-scale to be measured, provided that the temperature of the solutions was less than -50°C . For no solutions warmer than -50°C were time-dependent spectral shifts were observed. We have used the ultrafast streak camera system that is described in Chapter 2 of this thesis to elaborate upon Ware's work by increasing the time resolution by three orders of magnitude. With resolution on the order of picoseconds, spectral dynamics in room temperature solutions of 4AP in 1-propanol are observable [27]. The remainder of the third chapter of this thesis will describe in detail the data obtained for room-temperature and near room-temperature solutions of 4AP in a wide variety of solvents. These data are direct, real-time measurements of solute-solvent interactions in room temperature solutions, and represent the first time such clear determinations have been made.

Ware and his coworkers gathered time-dependent spectral shifts of emission as evidence of solvation of excited-state 4AP. Their experimental apparatus was a single-photon counting instrument that was designed to run as a time-resolved fluorescence spectrometer [26,28]. A nanosecond flashlamp with a temporal width of about five nanoseconds was used as the excitation source. The signal from a photomultiplier was gated with approximately 0.5 ns resolution. Either signals at fixed wavelength and varied time could be detected (simple emission decay curves), or signals could be spectrally resolved at a fixed delay relative to the excitation pulse. In the case of spectral resolution at fixed delay, the finite width of the excitation pulse and finite resolution of the electronic gating circuit limited Ware's smallest observation times to about 12 ns. At times shorter than 12 ns, distortions in the emission profiles were observed and attributed to the width of the lamp pulse. With short time scale observation limited to 12 ns, Ware observed no detectable shift in the emission of 4AP in 26°C 1-propanol between the spectrum detected at 12 ns and that detected at times greater than three emission lifetimes (≈ 40 ns).

The presentation of our re-investigation of Ware's work best begins with a long time

scale look at phenomena similar to that measured by Ware. The first 80 ns of emission detected at 480 and 650 nm from a solution of 4AP in 20°C 1-propanol using our streak camera system is shown in Figure 3.4. On a time scale of 80 ns, (with resolution of about 2 ns as indicated by the detected width of the 40 ps excitation pulse), the decay curves at 480 and 650 nm are essentially identical, with an emission lifetime of 10.5 ± 0.5 ns for both curves. On a long time scale, the emission spectrum of room temperature 4AP in 1-propanol decays away without any spectral dynamics. These data are completely consistent with the long time scale determinations made by Ware and his coworkers.

When the time-resolution of the streak camera system is about 10 ps instead of 2 ns, the temporal profiles of emission detected at 650 and 480 nm from 4AP in solutions of 1-propanol room temperature solutions are dramatically different. (See Figure 3.5.) The higher energy emission, 480 nm, shows a component of decay that is fast relative to the 10.5 ns fluorescence lifetime of the excited state. Consistent with the solvation picture presented in Figure 3.1, the low energy emission, 650 nm, grows in on a time scale that is long relative to the width of the excitation profile. The fast decay of the high energy emission and the growth of the low energy emission means that the emission spectrum shifts red as a function of time. Clearly with increased time resolution, the emission of 4AP in 1-propanol, even at room temperature, shows relaxation that is analogous with that which Ware's time resolution allowed him to detect only in much colder solutions.

D. Results from a Picosecond Fluorimeter

With the streak camera system in its present configuration, detection of the emission spectrum at a fixed time relative to the excitation pulse is not possible, so the experiment that is the picosecond extension of one of Ware's nanosecond experiments is not possible. However, we have developed a method that allows us to use the streak camera as a picosecond fluorimeter, as described in Section C of Chapter 2. We use the streak

Figure 3.4 Emission from 4AP in 1-Propanol—Fluorescence Lifetime at 650 and 480 nm

80 ns of emission from 4AP detected at 650 nm (dotted line) and 480 nm (solid line). Sharp feature at left is the image of the 45-ps excitation pulse, and is an indication of the temporal resolution of the detection system during these two scans. (The width of the excitation source appears to be just over one nanosecond in duration, although its actual temporal width is far smaller. The discrepancy is due to the finite focus of the streak camera system when to streak rate is slow enough to measure a long fluorescence lifetime. At the streak rate shown in this figure, the camera cannot distinguish between the temporal widths of any pulse of 1 ns or less.) Both profiles decay away with a single exponential lifetime of 10.5 ± 0.5 ns.

Figure 3.4

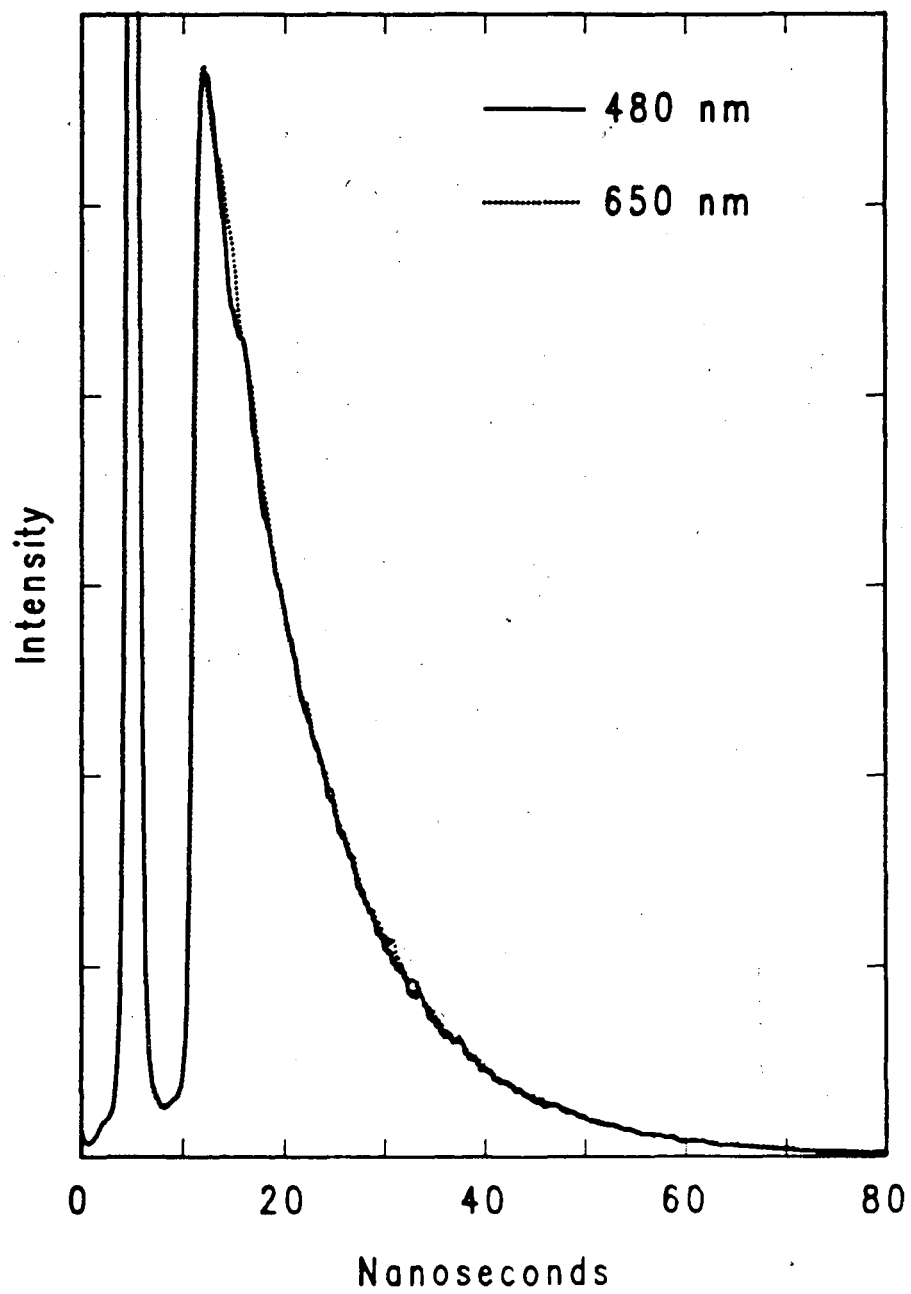
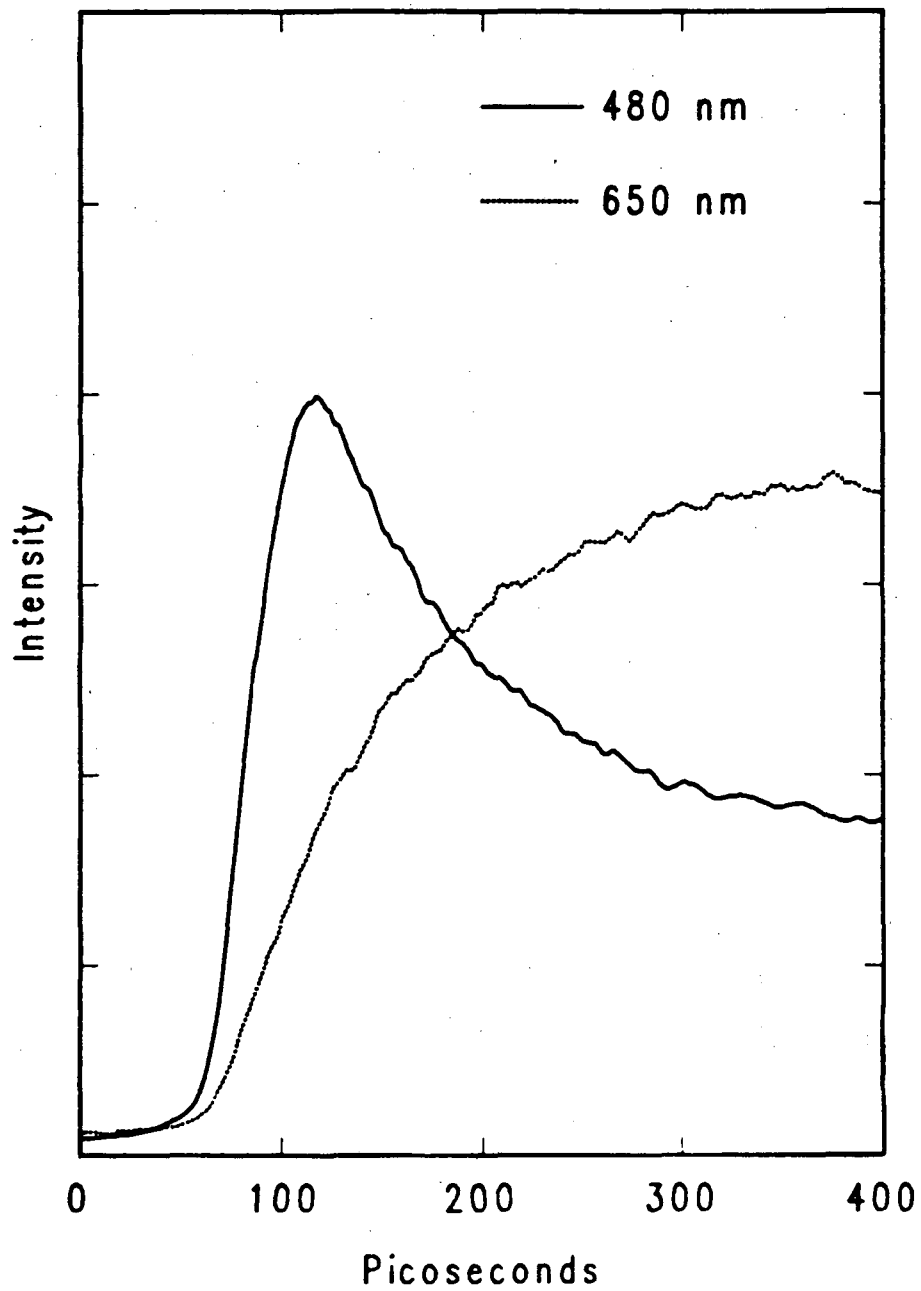


Figure 3.5 Emission from 4AP in 1-Propanol—Initial Temporal Profiles at 650 and 480 nm

The first 300 ps of emission from 4AP detected at 650 nm (dotted line) and 480 nm (solid line). The 480-nm profile has a component of decay that is much faster than the 10.5-ns emission lifetime; the profile detected at 650 nm does not exhibit prompt emission but has a finite growth rate.

Figure 3.5



camera to time-resolve narrow bands of emission throughout the emission spectrum of the molecular system under study. We then have temporal information with picosecond resolution over the entire range of spectral points of the emission spectrum. The inversion of that data to spectral information at discrete temporal points with retention of picosecond resolution is straightforward. The detailed description is in Chapter 2, Section C.

1. 4AP in 1-Propanol

The streak camera data taken throughout the emission spectrum of 1-propanol solutions of 4AP are shown in Figure 3.6A–C. The smooth curves superimposed on the data are the computer-generated best-fits to the data. The parameters of the fits are given in Table 3.1. Consistently throughout the high energy, or blue edge, of the emission, the temporal profiles show fast components of decay. All of the lower energy, or redder, emission profiles show delayed growth. Just a short consideration of the data brings about the realization that the emission band is shifting the maximum of intensity to the red. Blue emission that is initially intense decays away on a time scale that is fast with respect to the fluorescence lifetime. The red edge of the spectrum has no intensity early in time, but increases in intensity, again on a time scale fast relative to excited-state decay.

The data are, however, subtly different than data for some of the excited-state systems described earlier in this chapter. For example, in the case of 1-naphthol, the decay of emission profiles detected on the blue edge of the emission band show a time constant consistent with the rise times of the red edge of the emission band [11]. Time-resolved data for excited-state DMABN show similar behavior, with red edge rise times agreeing within experimental uncertainties with blue edge decay times [20–22,27,29]. The agreement of the time constants for the profiles of both the blue and red edge of the emission band in these two systems is consistent with the idea that the red state is formed from the blue-emitting state. In contrast to these two-state systems, the temporal parameters given

Figure 3.6 Time-Resolved Emission Spectrum for 4AP in 1-Propanol—Initial Profiles

Data and computer-generated fits (smooth curves) for emission profiles detected at 10-nm intervals. Figure 3.6A shows emission bands from 410 to 500 nm; Figure 3.6B shows bands from 510 to 600 nm; and Figure 3.6C shows bands from 610 to 700 nm. Detected band is selected using 10-nm bandpass interference filters. All of the high energy emission (410 through 490 nm) show components of decay that are fast on the time scale of 300 ps. Similarly, the lowest energy profiles (600 through 700 nm bands) clearly show initial growth rates that are not prompt. Temporal parameters from these fits are given in Table 3.1.

Figure 3.6A

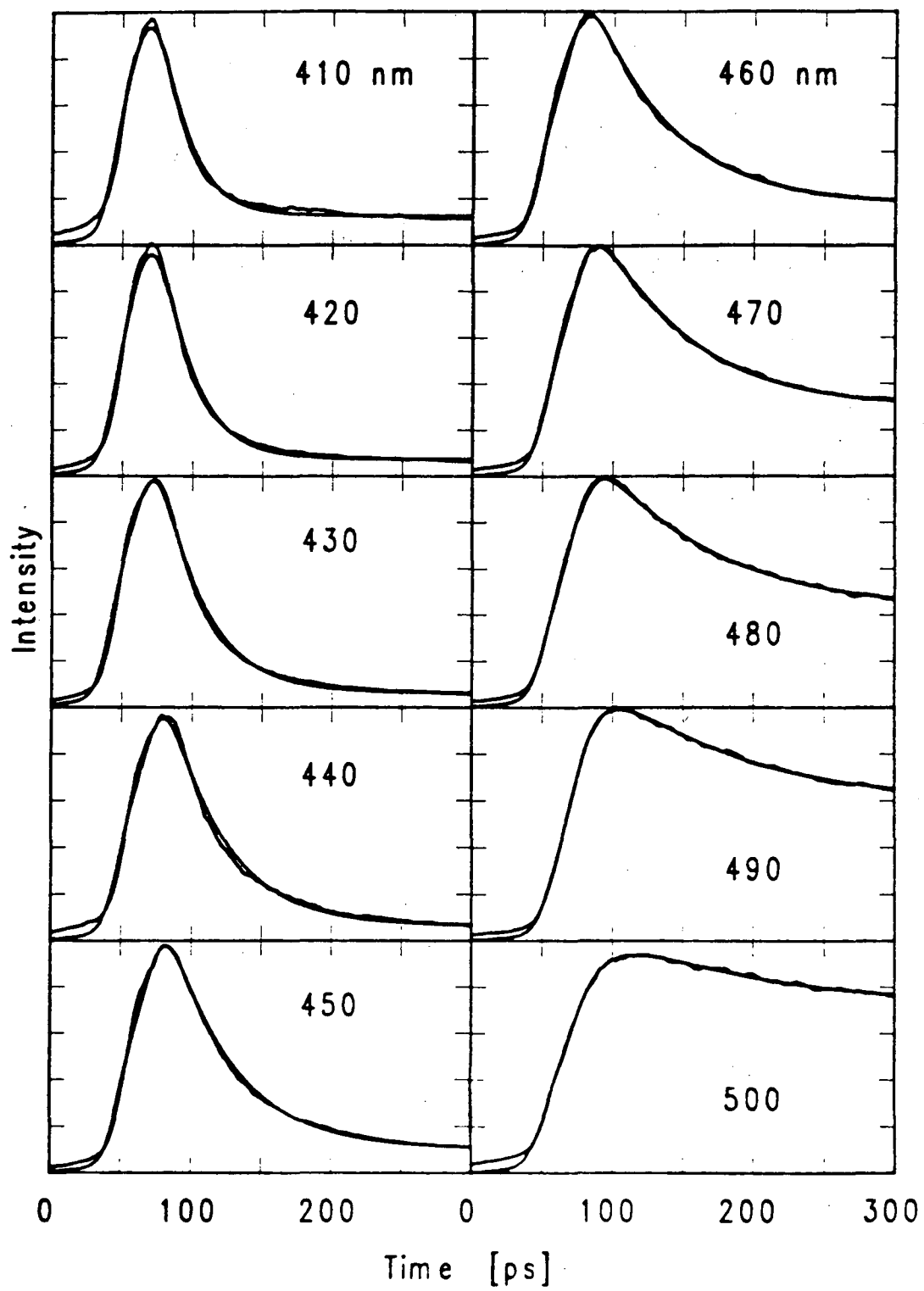


Figure 3.6B

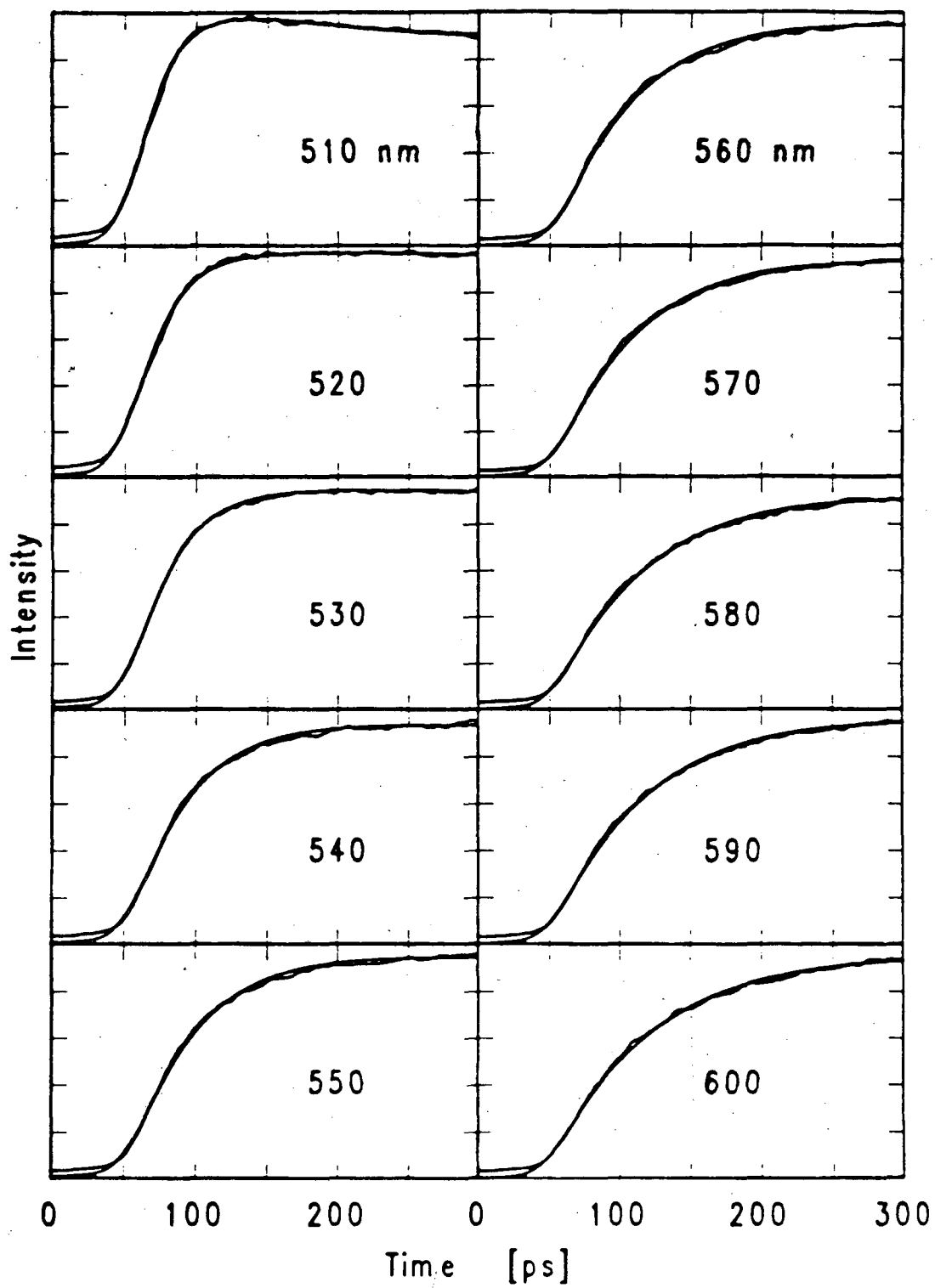


Figure 3.6C

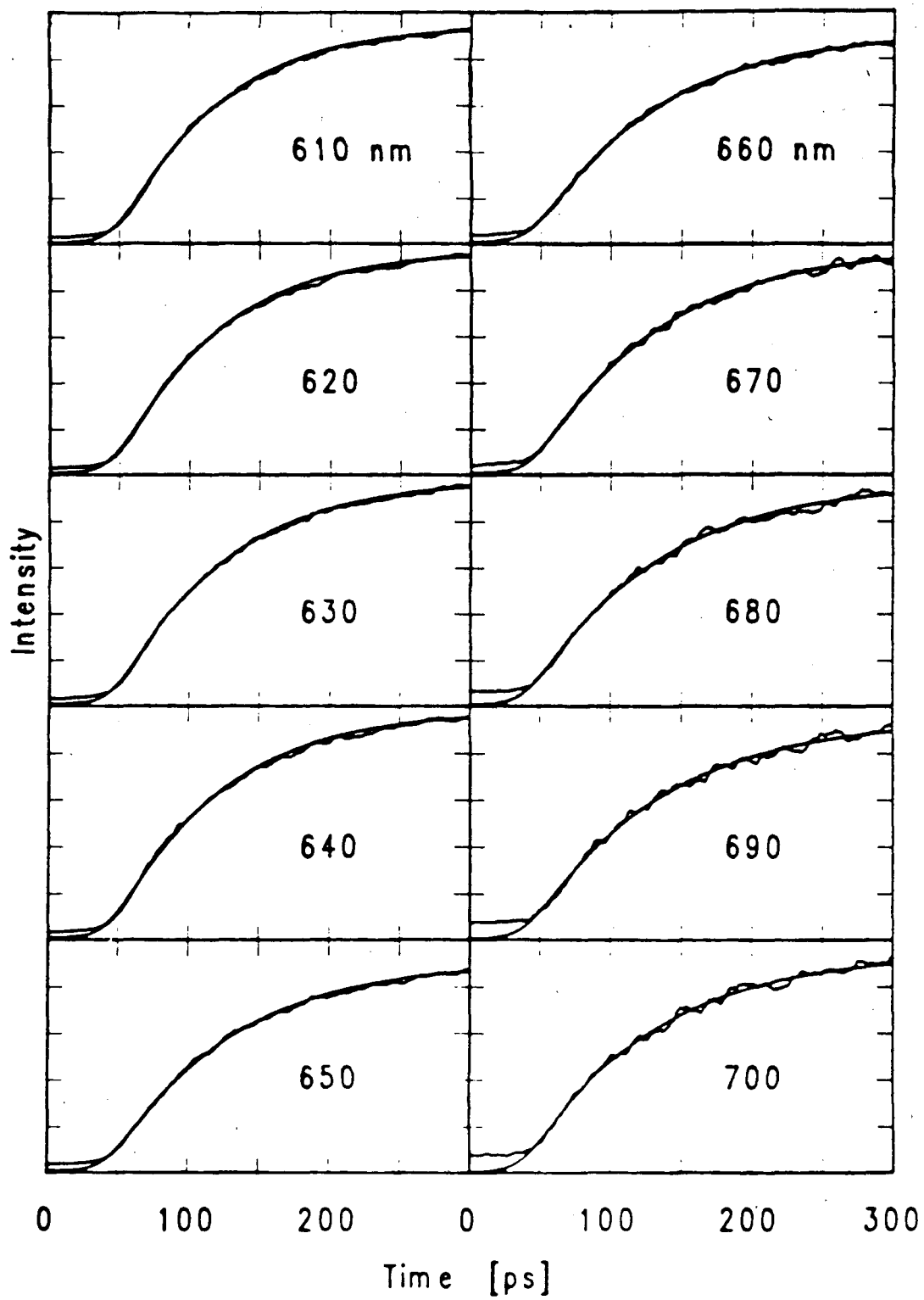


Table 3.1

Parameters of fits to 4AP in 1-propanol spectrally- and temporally-resolved data. The time constants in picoseconds, τ_i , and their relative amplitudes, α_i , are given. The wavelength refers to the wavelength of maximum transmission of the interference filter used during the accumulation of each profile.

Wavelength	τ_1, α_1	τ_2, α_2
400	18., 59.5	10600., 1.
410	22., 38.2	10600., 1.
420	26., 67.5	10600., 1.
430	33., 56.5	10600., 1.
440	43., 48.3	10600., 1.
450	51., 63.8	10600., 1.
460	63., 8.0	10600., 1.
470	78., 4.1	10600., 1.
480	87., 2.3	10600., 1.
490	11., -1.	10600., 1.
500	21., -1.	10600., 1.
510	19., -1.	10600., 1.
520	30., -1.	10600., 1.
530	40., -1.	10600., 1.
540	48., -1.	10600., 1.
550	53., -1.	10600., 1.
560	61., -1.	10600., 1.
570	75., -1.	10600., 1.
580	73., -1.	10600., 1.
590	78., -1.	10600., 1.
600	78., -1.	10600., 1.
610	78., -1.	10600., 1.
620	84., -1.	10600., 1.
630	89., -1.	10600., 1.
640	81., -1.	10600., 1.
650	86., -1.	10600., 1.
660	87., -1.	10600., 1.
670	83., -1.	10600., 1.
680	90., -1.	10600., 1.
690	101., -1.	10600., 1.
700	122., -1.	10600., 1.

The uncertainties in the short time scale measurements are ± 10 percent.

in Table 3.1 for emission from solutions of 4AP in 1-propanol shows a more complicated spectral dependence, without simple correspondence of red and blue edge parameters.

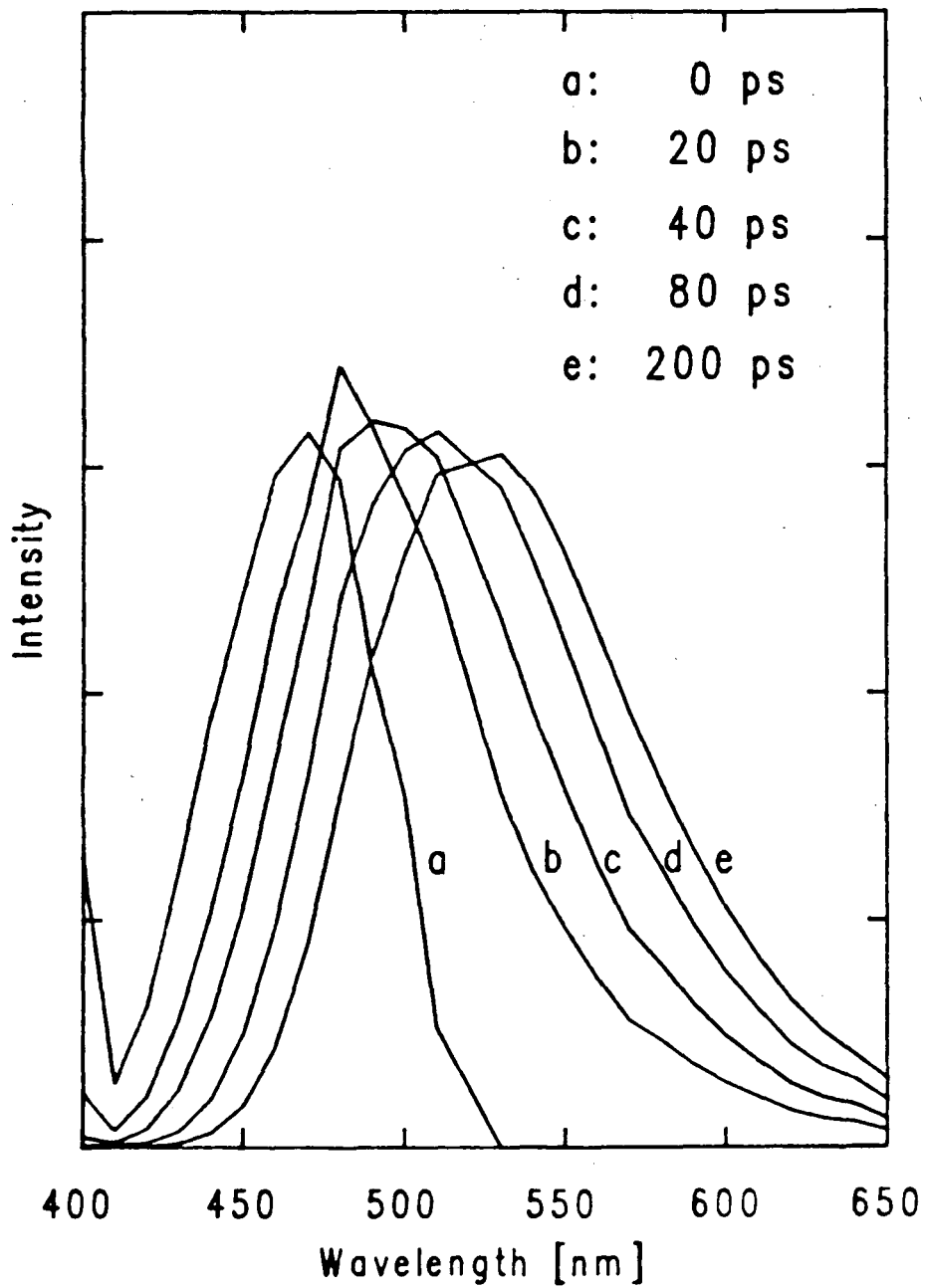
Inspection of the data presented in Table 3.1 shows that there are combinations of red and blue profiles that have parameters that taken alone might lead to the conclusion that blue- and red-emitting states are kinetically related. For instance, the fall time determined for the emission detected at 480 nm, 77 ps, is in agreement with the rise time measured at 630 nm and the decay time measured for 460 nm, 54 ps, agrees with the rise time detected at 570 nm. However, the parameters for the 630 and 480 nm data are not consistent with the parameters for the 460 and 570 nm data. The rise times that best fit the data at increasing wavelengths on the red edge are longer and longer as the detection wavelength increases. Similarly, the emission bands that show a blue edge decay have fall times that are longer for the longer emission wavelengths. In the case of the two-state systems (for instance, see reference 11), a single fast temporal parameter can be used to fit all the spectral data. Only the amplitudes of the pre-exponential factors for the short and long time scale components need to be changed, and statistically satisfactory fits can be obtained for all spectral regions of the data. The situation is apparently more complex for the emission spectrum of 4AP in 1-propanol than for 1-naphthol in that the blue emission is not simply related to the red emission spectrum. A single temporal profile cannot be found that will give satisfactory fits for all spectral regions of the data. It is therefore inconsistent with the 4AP data to assume that there are only two states in the excited-state of 4AP. An initially formed unsolvated state is not just simply becoming a solvated state; instead the excited-state process resulting in the detected temporal profiles of emission is of a more continuous nature.

When the temporal data of discrete emission bands is inverted to calculate the effective emission band at discrete times, the spectra shown in Figure 3.7 are obtained. These spectra are the output of our "picosecond fluorimeter". It is clear that the emis-

Figure 3.7 Emission Spectra for 4AP in 1-Propanol at Selected Times

The emission profile at any instant in time can be calculated after the spectrum has been completely time-resolved. The spectra shown here clearly shift to longer wavelength as a function of time.

Figure 3.7



sion spectra shift smoothly to lower energy as a function of time. The emission from a two-state system, like 1-naphthol [11], plotted following the same procedure, shows a clear isosbestic point. The isosbestic point in the emission spectra at discrete times is a point at which the emission intensity does not change on a time scale that the emission band changes dramatically. The existence of the isosbestic point in two-state systems is due to the fact that above some wavelength it is surely true that the temporal profiles of emission will all show a rise time. Similarly, it is also true that below some wavelength, all the profiles of emission will have a component that decays rapidly. In between these two points, the emission will have fast components of decay that will at least partially balance the components of emission that grow in gradually. The isosbestic point, which is in that intermediate region, signifies the point at which the intensity of the fast-decaying components exactly fills in for the emission from the relaxed state that is growing in. Because the fast-decaying signal and the signal that grows in gradually have the same time constant, the signals balance mathematically, resulting in an isosbestic point. For 4AP, there is no point at which the emission from an unrelaxed state balances the emission from the relaxed state, and so there is no isosbestic point.

More analysis can be performed on the spectra at discrete time that are calculated. At any time, the wavelength of maximum emission can be determined. (The procedure used to determine the emission maximum is to calculate the spectrum as a function of energy, and then fit the band with a Gaussian profile.) The position of the Gaussian that fits the calculated data best is used as the wavelength of maximum emission. After fitting data like that from Figure 3.7 (using points from 0 to 5 ns), the position of the emission maximum as a function of time is obtained. The data are shown in Figure 3.8. The way that the emission maximum relaxes as a function of time looks exponential. Indeed, Figure 3.9 shows the appropriate semi-logarithmic plot, that of the peak position as a function of time relative to the peak position at long times. The plot shows a strong linear

Figure 3.8 Emission Maximum as a Function of Time for 4AP in 1-Propanol

Data like that in Figure 3.7 are fit to determine the wavelength of peak emission intensity as a function of time. The spectra are fit in wavenumber space to a Gaussian peak shape. The peak position in kKaisers (kK) is plotted here as a function of time. The smooth relaxation of the emission spectrum of 4AP is clear. In addition, as the emission spectrum shifts to lower energy, the spectrum broadens.

Figure 3.8

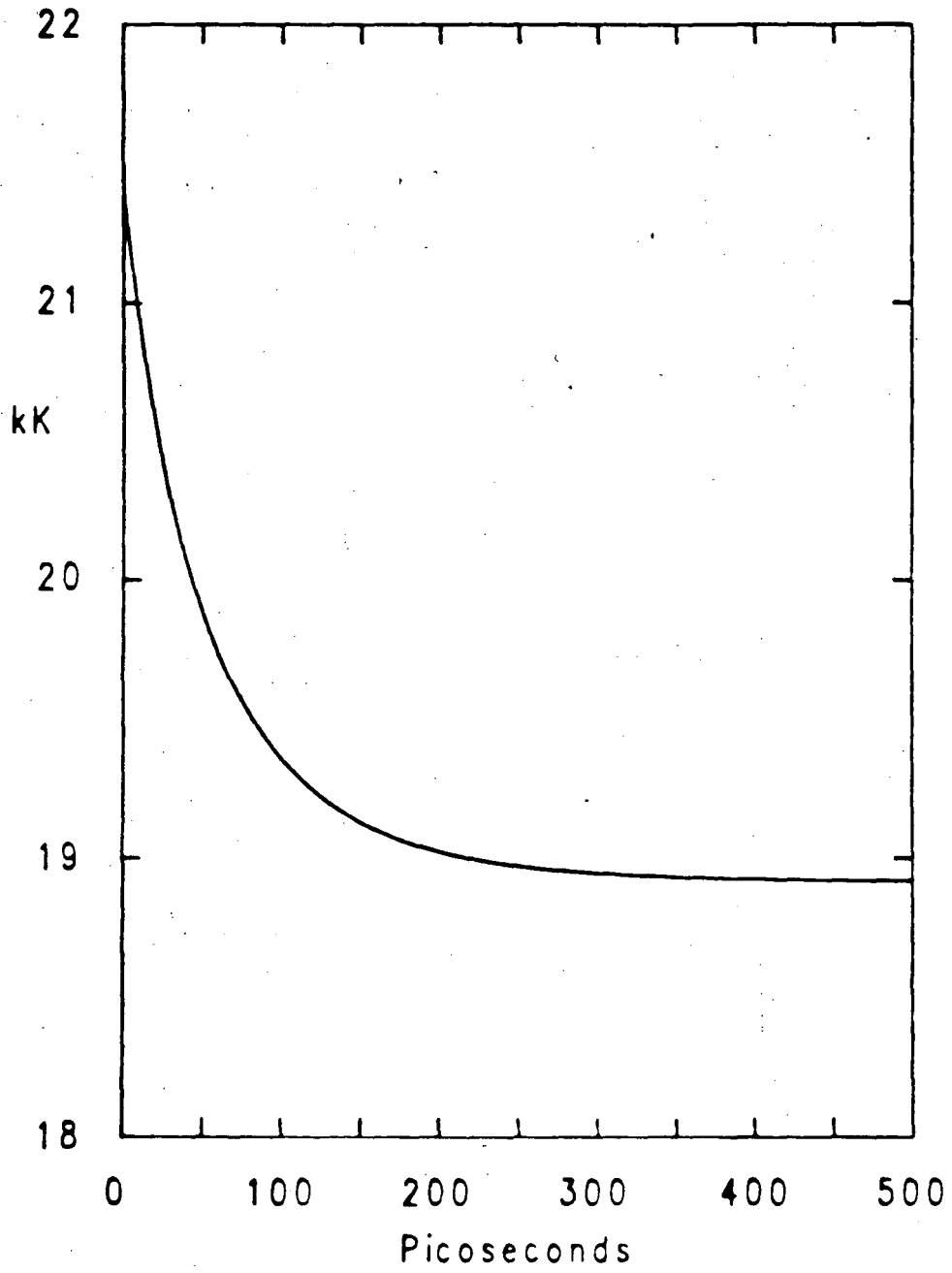
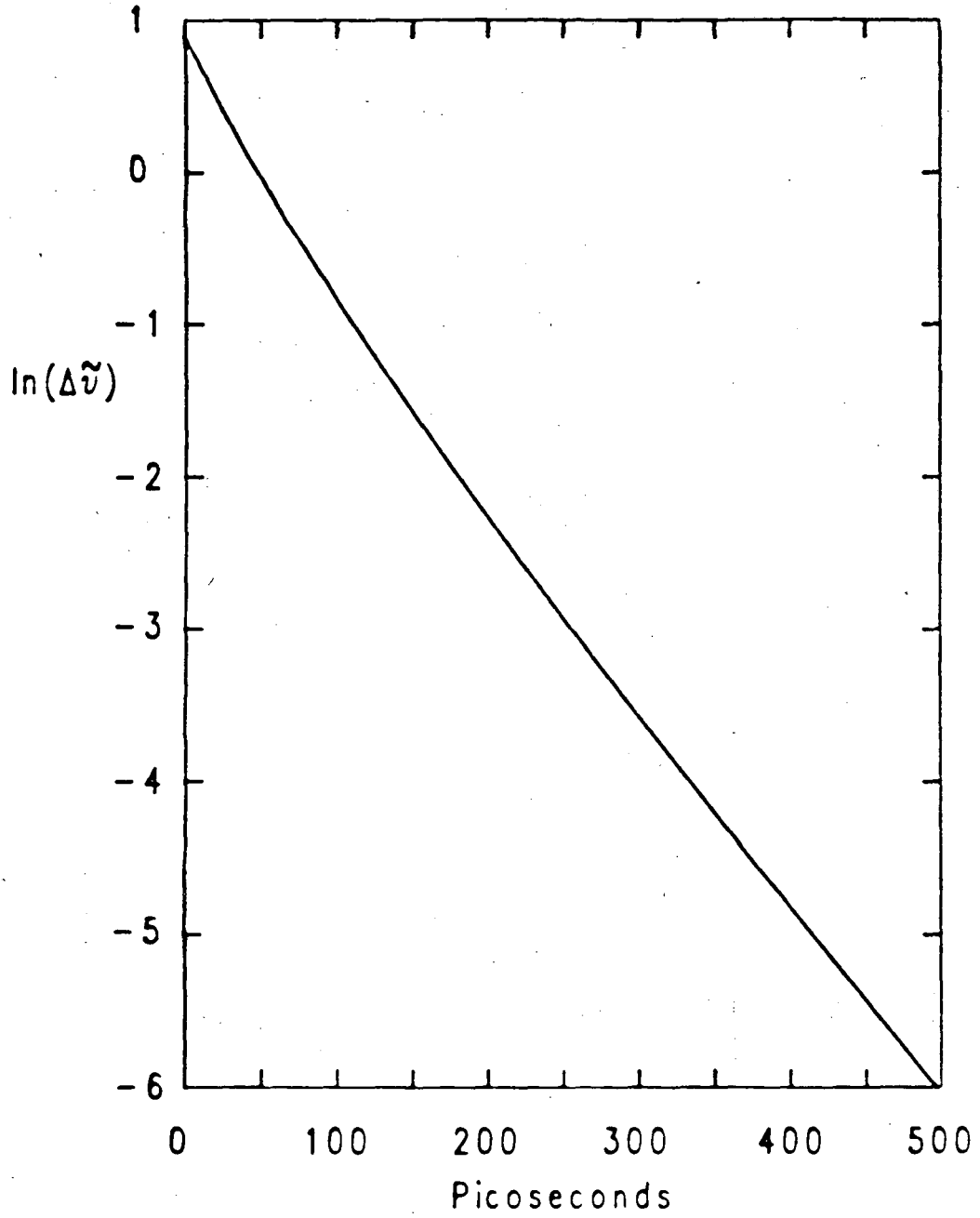


Figure 3.9 Semi-logarithmic Plot of Emission Maximum as a Function of Time for 4AP in 1-Propanol

As can be seen in Figure 3.8, the wavelength of peak emission shows an apparent exponential relaxation to the long wavelength emission maximum. Plotted here is $\ln(\Delta\tilde{\nu}(t))$, where $\tilde{\nu}(t)$ is the peak position in kKaisers at time t and $\Delta\tilde{\nu}(t) = \tilde{\nu}(t) - \tilde{\nu}(t = \infty)$. $\tilde{\nu}(t = \infty)$ is the fully relaxed position of the emission band. Because the rate of relaxation is so fast (≈ 70 ps), the fully relaxed emission profile is virtually equal to the position at 2 ns. The function plotted here is therefore $\ln(\Delta\tilde{\nu}(t))$, where $\Delta\tilde{\nu}(t) = \tilde{\nu}(t) - \tilde{\nu}(t = 2 \text{ ns})$.

Figure 3.9



correlation ($r=-0.998$), with a decay time of 69 ± 10 ps. (The initial portion of the semi-logarithmic plot has a faster time constant of decay, but that fast decay is not reproducible, and is not included in the determination of the decay time.) The relaxation of the emission spectrum as a function of time is easily resolvable with our picosecond fluorimeter for 4AP in 1-propanol. By a systematic study of spectral relaxation, one should be able to determine the solvent parameters that lead to resolvable spectral dynamics.

2. 4AP in Toluene

In toluene, the emission spectrum of 4AP is Stokes'-shifted to a smaller extent than in the more polar 1-propanol. The emission and absorption spectra of 4AP in toluene are given in Figure 3.10, and the spectra for 4AP in 1-propanol are reproduced for comparison. Toluene is a slightly polar, aromatic hydrocarbon solvent. The interaction expected between the slightly polar toluene and the excited-state of 4AP would be smaller than the interaction of the same excited electronic state and 1-propanol. The steady-state data are easily reconciled with the known macroscopic properties (like the polarity) of the solvents. The time-resolved measurements of the initial edge of the emission of 4AP in toluene is given in Figure 3.11. The emission rises promptly and then decays with a long lifetime (15.2 ± 0.5 ns). There are no spectral dynamics observed for the emission from toluene solutions of 4AP. The time-resolved data are also easily understood and consistent with intuitive expectations.

3. 4AP in Acetonitrile

After finding interesting dynamics for the spectral relaxation of 4AP in 1-propanol and not finding any interesting behavior for toluene, we sought other solvent systems that would show resolvable spectral relaxation. The logical solvent with which to begin is a solvent for which emission from 4AP shows a substantial Stokes' shift. Such a solvent is acetonitrile. Figure 3.12 shows the positions of the absorption and emission spectra

Figure 3.10 Steady-state Emission and Absorption Spectra of 4AP in 1-Propanol and Toluene

The steady-state emission and absorption spectra of 4AP in both 1-propanol and toluene show the large difference in Stokes' shift as a function of solvent polarity. The solvent polarity affects not only the position of the emission maximum, but also the absorption peak. The absorption peak of 4AP in toluene is slightly blue-shifted from its position for 4AP in 1-propanol, and the change in the position of the emission spectra is even larger. The Stokes' shift in toluene is only 5400 cm^{-1} , compared with the shift of 7700 cm^{-1} for 1-propanol.

Figure 3.10

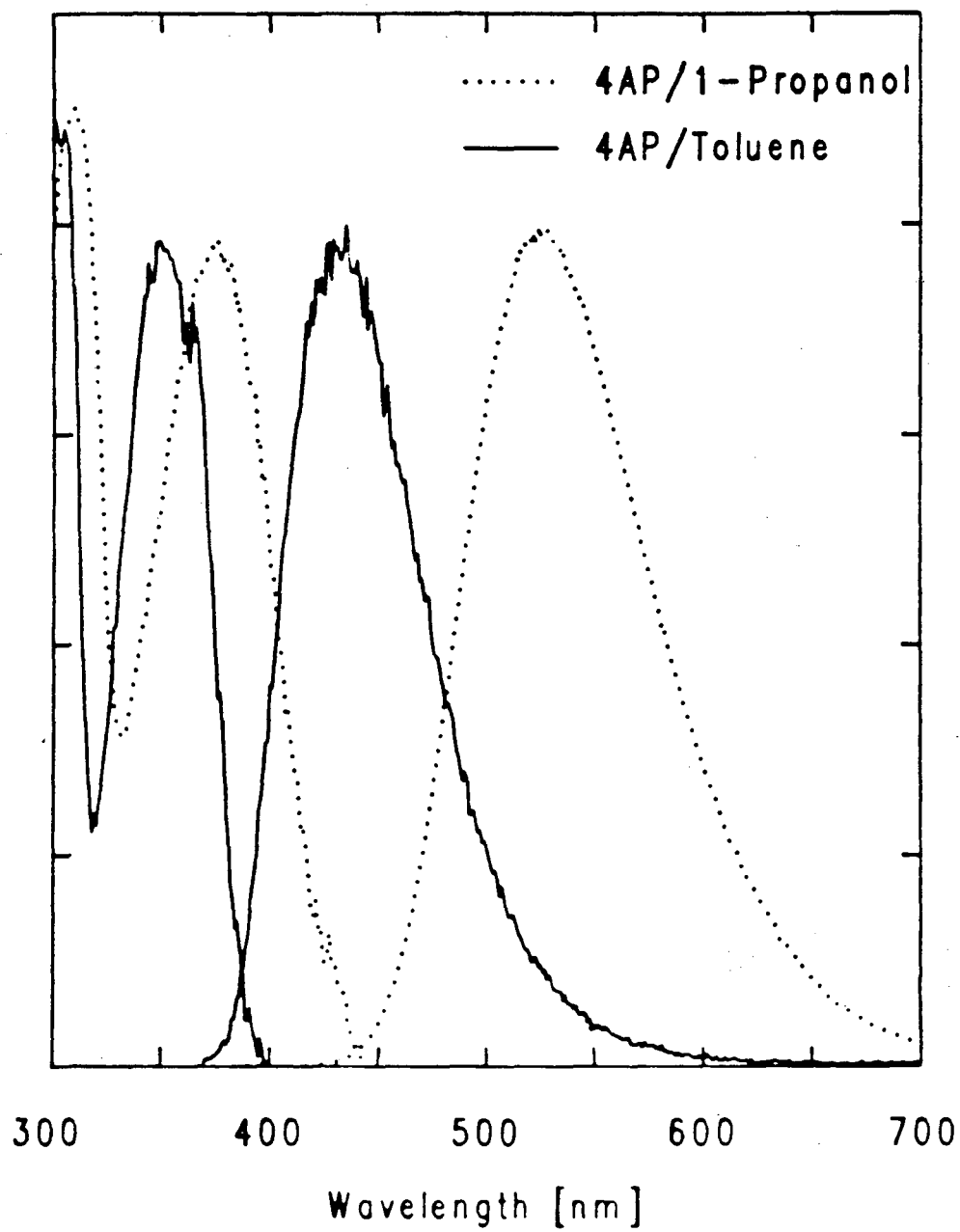
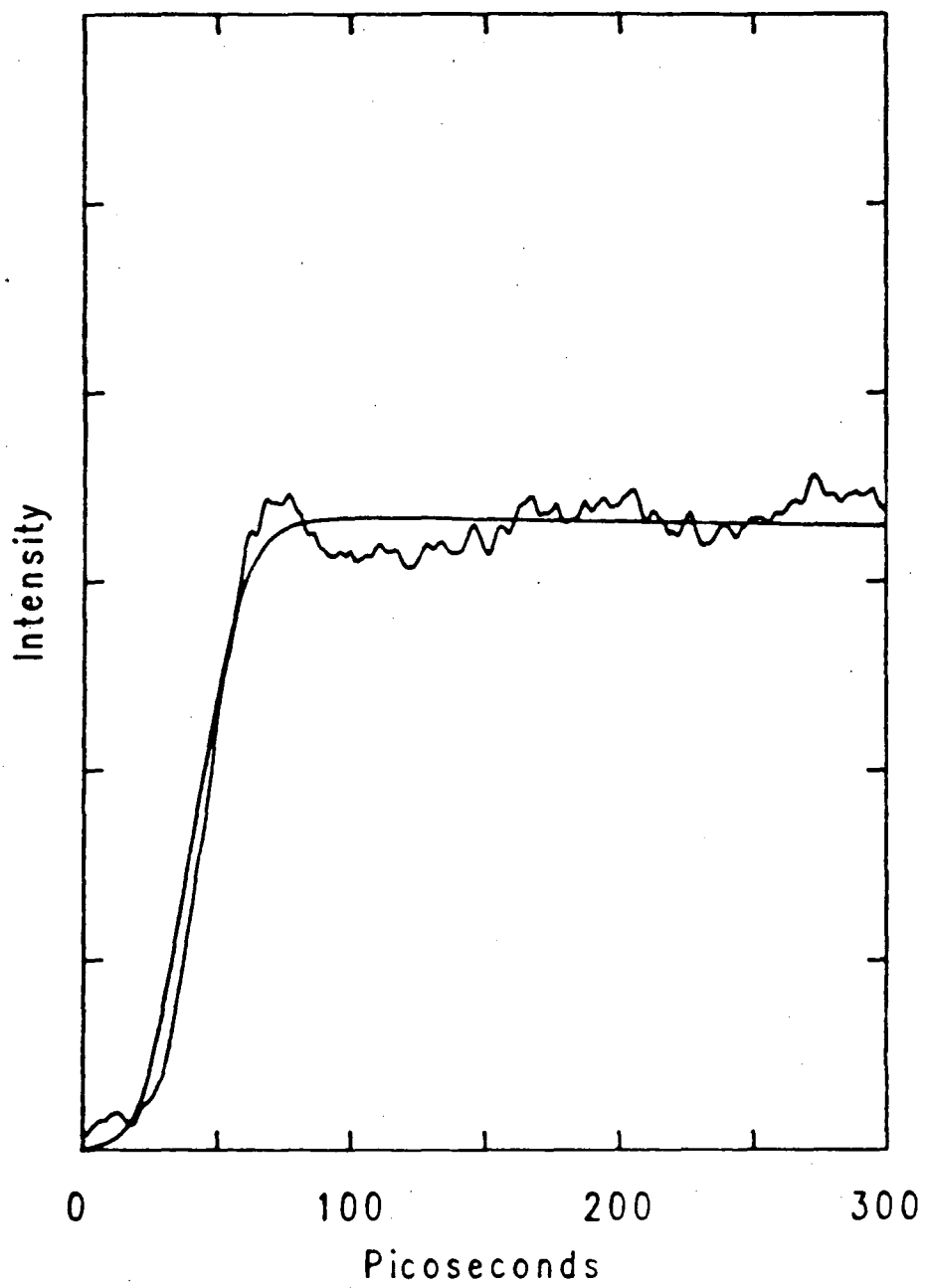


Figure 3.11 Time-Resolved Emission of 4AP in Toluene—Initial Temporal Profile

The profile of emission from 4AP in toluene detected at 450 nm is shown in this figure. The rise time is unresolvably fast, indicating that the emission is prompt on the time scale of 20 ps. There are no resolvable spectral dynamics for any emission band of 4AP in toluene.

Figure 3.11



of 4AP in both 1-propanol and acetonitrile. The Stokes' shift of emission of 4AP in 1-propanol is very large, $7700 \pm 100 \text{ cm}^{-1}$ [30]. In acetonitrile, the magnitude of the Stokes' shift is slightly smaller, $6900 \pm 100 \text{ cm}^{-1}$, but still large. The substantial Stokes' shifts for these two solvents are indicative of the substantial interaction that can occur between polar solvents and the dipolar excited state of 4AP [25].

Short time scale time-resolved emission from 4AP in acetonitrile is shown in Figure 3.13. In dramatic contrast to the temporal profile of emission from the red edge of the emission band of 4AP in 1-propanol (Figure 3.5), the red-edge emission of 4AP in acetonitrile has a prompt rise. The longest time constant that can fit the rising edge of the emission is 15 ps, instantaneous relative to the profiles detected with 1-propanol as the solvent. The fall time of the red edge of the decay is $15.0 \pm 0.4 \text{ ns}$. Blue-edge emission from 4AP does not show the fast components of decay that were so evident for 4AP in 1-propanol. The blue edge of the emission band rises promptly and decays away with a 15-ns lifetime. The emission band for 4AP in acetonitrile therefore shows no interesting dynamics. All regions of the emission band merely rise promptly and decay away uniformly. While this result is the same as that which might have been predicted for toluene, it is a surprising result for acetonitrile, because the steady-state data indicate a rather intense interaction between acetonitrile and the excited-state of 4AP.

However, the resolution of the streak camera system does not preclude the possibility of fast relaxation occurring. The width of the 355-nm excitation pulse, $40 \pm 10 \text{ ps}$, limits resolution of the rising edge of the emission band to about 15 ps. (Emission rise times of about one-third the pulse width or less are indistinguishable with the present apparatus. This limits the resolution of the streak camera system to about 15 ps for the excitation conditions in this series of experiments.) If the relaxation process took 15 ps or less, the effect the relaxation process would have on the red edge of the emission band would be unresolvable. On the basis of just the red edge rise time, the relaxation, if it occurs,

Figure 3.12 Steady-state Emission and Absorption Spectra of 4AP in Acetonitrile and 1-Propanol

The steady-state emission and absorption spectra of 4AP in both 1-propanol and acetonitrile show that the molecule exhibits strong Stokes' shifts in both solvents. In the alcohol, the Stokes' shift is 7700 cm^{-1} , while in the nitrile solvent the shift is not quite as large, 6900 cm^{-1} .

Figure 3.12

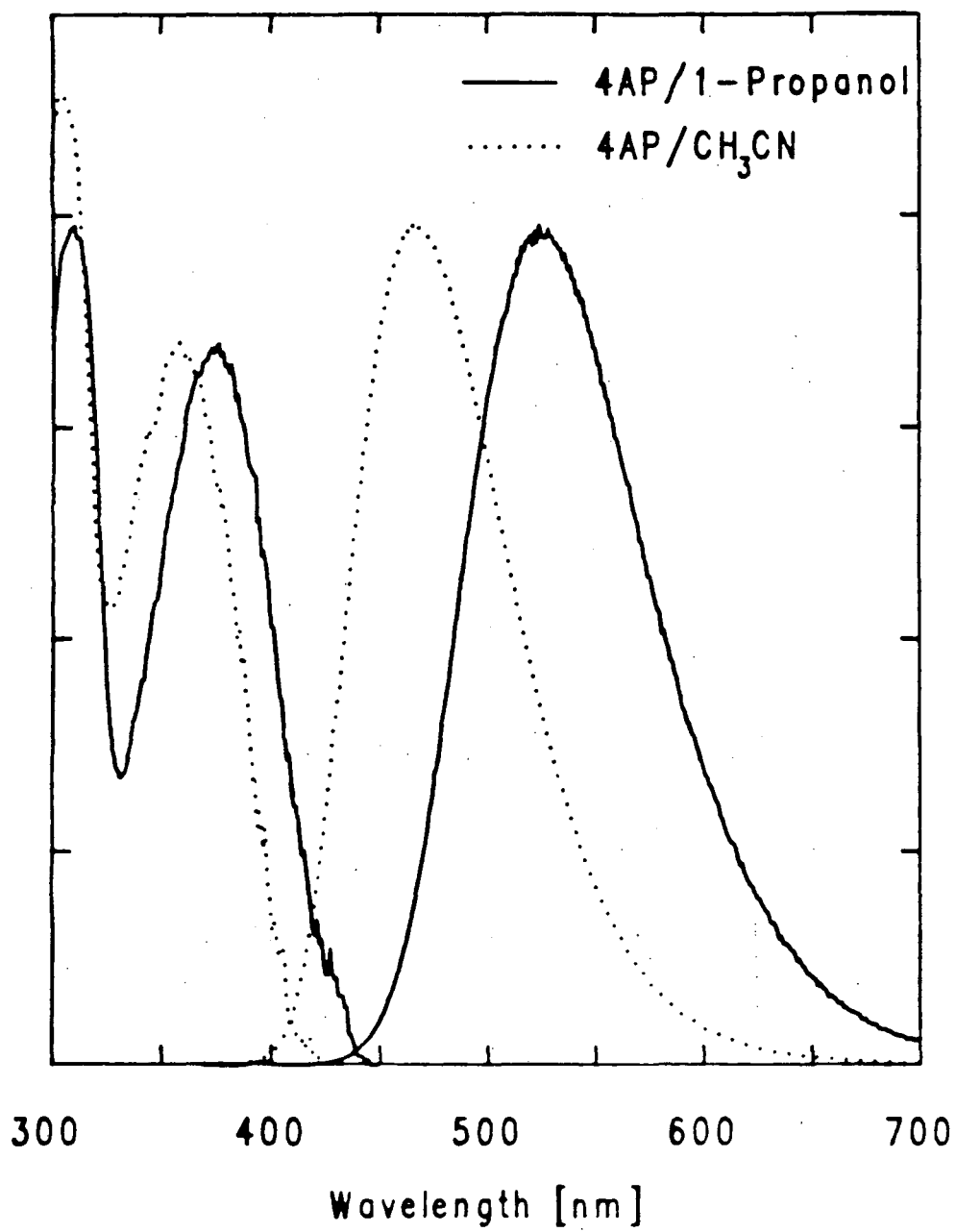
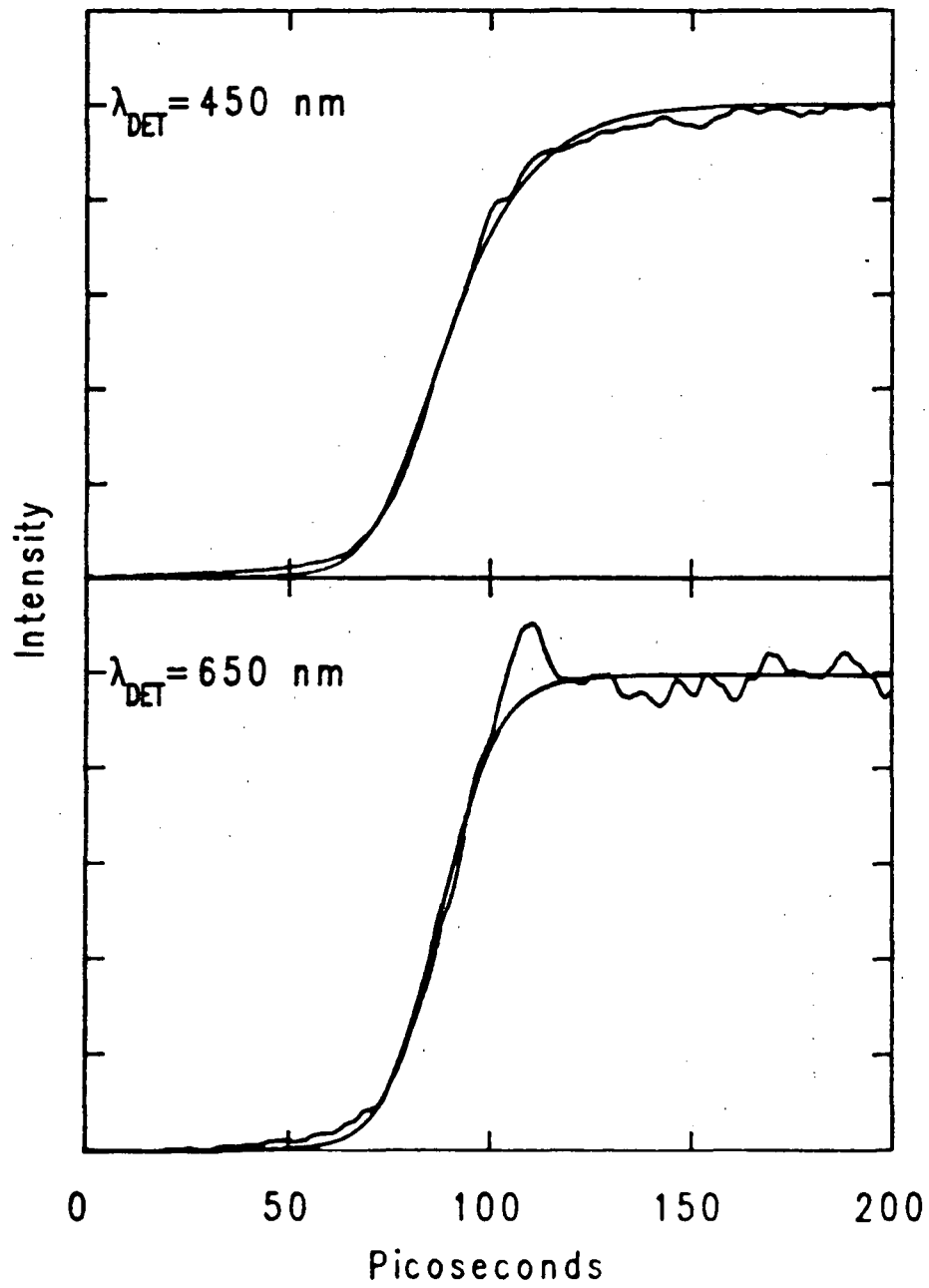


Figure 3.13 Time-Resolved Emission of 4AP in Acetonitrile—Initial Temporal Profiles.

Emission profiles of 4AP in acetonitrile show that the growth rate of emission is extremely rapid (<20 ps time constant of growth) in all spectral regions. There are no fast components of decay observed from solutions of 4AP in acetonitrile that can be cleanly assigned as originating from 4AP.

Figure 3.13



occurs on a time scale of less than 15 ps. (It is also possible that some relaxation on a similarly fast time scale is occurring in toluene solutions of 4AP.)

The blue edge of the emission is generally more sensitive to fast decay dynamics than the red edge [31], as can be demonstrated with the following calculations. The mathematical representation of a two component exponential decay is:

$$I(t) = Ae^{(-t/\tau_a)} + Be^{(-t/\tau_b)} \quad (3.1)$$

where the two time constants τ_a and τ_b refer to the short and long time constants of decay, respectively. What is actually detected by the camera is the convolution of this decay function with the detected excitation pulse profile:

$$S(t) = (P(t) * I(t)), \quad (3.2)$$

where $P(t)$ is the pulse profile. This convolution can be rewritten:

$$S(t) = (P(t) * Ae^{(-t/\tau_a)}) + (P(t) * Be^{(-t/\tau_b)}) \quad (3.3)$$

If τ_a is very short relative to the width of the pulse, the result of the convolution will be just to produce an image of $P(t)$. The magnitude of that image relative to the size of the second term of the sum will be proportional to the size of τ_a . The second term of the convolution, that containing the long lived decay component, has a profile that increases initially like the integral of the excitation pulse, and then decays away on a long time scale. The sum of the two components is then a pulse shape that is superimposed on the integral of the pulse shape, considering only the early edge of the emission profile. The superposition of the two signals would be easy to distinguish from only the integral of the pulse shape (See Figure 2.7). The streak camera system is particularly well suited to detecting selectively the early edge of the emission profile, and so particularly sensitive to determining whether there is a fast component of emission decay. Processes occurring on as fast a time scale as 1 ps would leave an easily detected signature [31]. Clearly

there is no fast component superimposed on the initial edge of the temporal profile of 4AP in acetonitrile, even on the blue edge of the emission pictured in Figure 3.11.

However, there is a complicating problem. The highest energy luminescence from the sample cannot be cleanly detected. The signal from the fluorescing sample is contaminated with Raman scattering of the excitation beam by the solvent. Raman scattering is an instantaneous process, and so the temporal profile of the Raman signal follows the excitation pulse profile. It is difficult to distinguish fast emission from Raman, unless the Raman cross section is so small as to make Raman scattering an unimportant contribution to the total signal. Raman signal is detectable in pure acetonitrile, meaning that the bluest emission bands for 4AP in acetonitrile do show an image of the excitation pulse superimposed on the initial edge of the emission signal. This fast signal is attributed to Raman scattering from the solvent. The presence of the pulse image may be masking any fast processes that could be occurring for 4AP in acetonitrile and mean that only the red edge of the emission band can be used to determine the upper limit on how long the relaxation process takes. As previously discussed, the prompt rising edge of the red bands of emission of 4AP in acetonitrile means that the slowest possible time constant of relaxation consistent with the experimental data is 15 ps, still markedly different than the dynamics observed for 4AP in 1-propanol. The spectral dynamics in acetonitrile are instantaneous relative to the streak camera system's resolution of 15 ps.

The profile of 4AP in acetonitrile is the same as for 4AP in toluene. It is clearly not intuitively plain that toluene and acetonitrile solutions of 4AP would show similar spectral dynamics on the basis of the steady-state spectra. Solvents with dramatically different extents of interaction with the chromophore surprisingly show similar dynamics. When two solvents both interact strongly with the solute (based again on steady-state spectroscopic determinations) these results for acetonitrile and 1-propanol indicate that the solvent able to form hydrogen bonds is more interesting dynamically than a similarly

polar solvent that lacks hydrogen-bond donating ability.

4. 4AP in an Assortment of Other Solvents

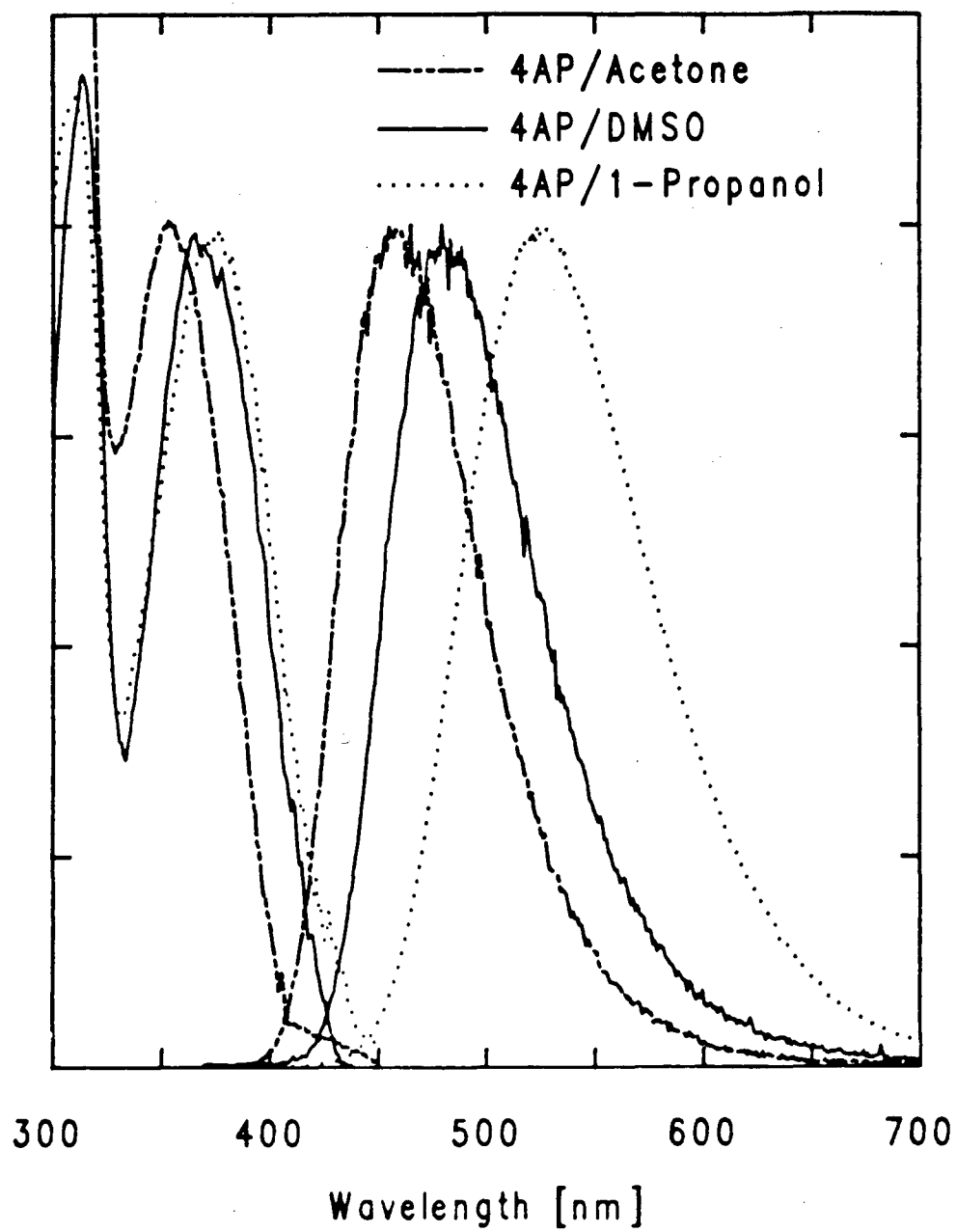
A possible explanation of why spectral relaxation is resolvable in 1-propanol but not resolvable in acetonitrile is that the viscosity of acetonitrile (0.35 cP, [32]) is so much smaller than the viscosity of 1-propanol (2.26 cP). A solvent that shares some characteristics with 1-propanol and acetonitrile is dimethylsulfoxide (DMSO). In this oxygen-containing solvent, 4AP shows emission with a substantial Stokes' shift (the shift is comparable to acetonitrile, $6900 \pm 100 \text{ cm}^{-1}$). The steady-state absorption and emission spectra are plotted in Figure 3.14 for reference. The substantial electron density on the oxygen atoms of DMSO makes it a particularly strong hydrogen bond acceptor [33]. Conveniently, 4AP is easily soluble in DMSO. The polarity of DMSO is intermediate relative to 1-propanol and acetonitrile, with $\epsilon(\text{DMSO})=47$, $\epsilon(\text{acetonitrile})=88$, and $\epsilon(1\text{-propanol})=21$ [34]. The viscosity of DMSO, 2.2 cP [35], is considerably greater than that of acetonitrile, and comparable to that of 1-propanol. When the emission from 4AP in DMSO is time-resolved, there are no fast time scale components of decay or indications of delayed growth that are observed. The emission of 4AP in DMSO rises promptly in all spectral regions and decays away uniformly. Because neither acetonitrile nor DMSO show any evidence of spectral relaxation, polarity alone does not seem to be sufficient to cause time-dependent emission shifts. The viscosity of DMSO and 1-propanol are comparable, and only the hydrogen-bond-donating solvent shows spectral shifts as a function of time that are resolvable. This evidence pinpoints the ability of a solvent to form hydrogen bonds as a key property leading to resolvable spectral dynamics.

Some of the other solvents that have been tested include acetone, cyclohexane, tetrahydrofuran, and dioxane. When the emission from 4AP in any these solvents is time-resolved, no spectral dynamics are observed. Some of these solvents show sub-

Figure 3.14 Steady-state Spectra of 4AP in DMSO, 4AP in Acetone, and 4AP in 1-Propanol

Emission and absorption spectra for 4AP in DMSO, acetone, and 1-propanol are shown together to allow simple comparison.

Figure 3.14



stantial interaction on the basis of the positions of the steady-state spectra [36]. The time-resolved data indicate that all the interactions result in fast relaxation, if there is any relaxation process at all. It is quite clear that the class of molecules that do not show any resolvable relaxation is a much larger class than the class of solvents, which includes 1-propanol, that shows resolvable relaxation.

When other simple alcohols are studied, the time-resolved emission profiles do show evidence of resolvable relaxation. A solvent which displays detectable spectral shifts is ethanol. The best-fit parameters for emission profiles of 4AP in ethanol are given in Table 3.2, with the parameters for some other simple alcohols. For ethanol, the time scale of the relaxation is far faster than that exhibited by 4AP with 1-propanol as the solvent. (See Table 3.1). With 1-butanol or 1-pentanol as solvent, the best-fit parameters are considerably slower than with 1-propanol as solvent. The two structural isomers, 2-propanol and 1-propanol, have parameters that are similar in value. All alcohols studied so far show relaxation that is quite easily resolvable. In general, for all solvents studied, the only solvents in which 4AP has interesting spectral dynamics are hydrogen-bond donating solvents. There is clearly an important role for the formation of hydrogen bonds in the solvation process. The data that has been only briefly described for 4AP in ethanol and the other alcohols can be analyzed in greater detail by calculating the spectra at discrete times in the fashion that was done from the parameters for the data for 4AP in 1-propanol. This analysis will be contained in the next section.

The fact that hydrogen-bond donation is such an important solvent parameter gives some information on what the nature of the relaxation process might be. In a similar molecular system with aromatic carbonyl groups, coumarin, the excited-state was shown to have increased basicity relative to its ground state [37]. In the excited-state, the oxygen atoms have greater electron density, making them stronger hydrogen bond acceptors, in a Lewis acid-base sense [38]. Similarly, an increase in electron density has been calculated

Table 3.2

Parameters of fits to 4AP in four alcohol solvents, spectrally- and temporally-resolved. The time constants are given in picoseconds, τ_i , with their relative amplitudes, α_i .

Wavelength (nm)	Ethanol τ_i, α_i	2-Propanol τ_i, α_i	1-Butanol τ_i, α_i	1-Pentanol τ_i, α_i
400	12.,43.1 9850.,1.	12.,990. 12500.,1.		37.,24.5 12000.,1.
410	15.,29.2 9850.,1.	14.,97.1 12500.,1.	28.,178. 11000.,1.	42.,26.3 12000.,1.
420	18.,44.9 9850.,1.	22.,74.3 12500.,1.	34.,145. 11000.,1.	51.,39.0 12000.,1.
430	22.,41.1 9850.,1.	30.,82.7 12500.,1.	43.,126. 11000.,1.	68.,39.4 12000.,1.
440	26.,27.2 9850.,1.	39.,37.0 12500.,1.	55.,63.7 11000.,1.	85.,28.6 12000.,1.
450	32.,13.3 9850.,1.	56.,14.5 12500.,1.	68.,19.7 11000.,1.	111.,15.2 12000.,1.
460	36., 6.7 9850.,1.	64., 6.6 12500.,1.	87., 8.2 11000.,1.	142., 7.1 12000.,1.
470	46., 3.0 9850.,1.	84., 3.1 12500.,1.	124.,4.0 11000.,1.	181., 3.4 12000.,1.
480	46., 1.8 9850.,1.	115.,1.7 12500.,1.	188.,2.5 11000.,1.	224., 1.9 12000.,1.
490	66., 0.7 9850.,1.	118.,0.8 12500.,1.	165.,1.0 11000.,1.	235., 0.9 12000.,1.
500	10.,-1. 9850.,1.	116.,0.6 12500.,1.	292.,0.5 11000.,1.	319., 0.4 12000.,1.
510	12.,-1. 9850.,1.	16.,-1. 12500.,1.	28.,-1. 11000.,1.	42.,-1. 12000.,1.
520	19.,-1. 9850.,1.	23.,-1. 12500.,1.	35.,-1. 11000.,1.	45.,-1. 12000.,1.
530	45.,-1. 9850.,1.	38.,-1. 12500.,1.	50.,-1. 11000.,1.	65.,-1. 12000.,1.
540	37.,-1. 9850.,1.	46.,-1. 12500.,1.	60.,-1. 11000.,1.	83.,-1. 12000.,1.
550	39.,-1. 9850.,1.	52.,-1. 12500.,1.	70.,-1. 11000.,1.	93.,-1. 12000.,1.

Table 3.2, cont.

Wavelength (nm)	Ethanol τ_i, α_i	2-Propanol τ_i, α_i	1-Butanol τ_i, α_i	1-Pentanol τ_i, α_i
560	47.,-1. 9850.,1.	58.,-1. 12500.,1.	83.,-1. 11000.,1.	114.,-1. 12000.,1.
570	51.,-1. 9850.,1.	61.,-1. 12500.,1.	99.,-1. 11000.,1.	123.,-1. 12000.,1.
580	54.,-1. 9850.,1.	69.,-1. 12500.,1.	94.,-1. 11000.,1.	134.,-1. 12000.,1.
590	56.,-1. 9850.,1.	70.,-1. 12500.,1.	104.,-1. 11000.,1.	143.,-1. 12000.,1.
600	57.,-1. 9850.,1.	73.,-1. 12500.,1.	110.,-1. 11000.,1.	143.,-1. 12000.,1.
610	57.,-1. 9850.,1.	75.,-1. 12500.,1.	117.,-1. 11000.,1.	152.,-1. 12000.,1.
620	57.,-1. 9850.,1.	80.,-1. 12500.,1.	116.,-1. 11000.,1.	159.,-1. 12000.,1.
630	59.,-1. 9850.,1.	83.,-1. 12500.,1.	126.,-1. 11000.,1.	160.,-1. 12000.,1.
640	58.,-1. 9850.,1.	78.,-1. 12500.,1.	110.,-1. 11000.,1.	157.,-1. 12000.,1.
650	60.,-1. 9850.,1.	81.,-1. 12500.,1.	135.,-1. 11000.,1.	168.,-1. 12000.,1.
660	62.,-1. 9850.,1.	95.,-1. 12500.,1.	105.,-1. 11000.,1.	174.,-1. 12000.,1.
670	66.,-1. 9850.,1.	90.,-1. 12500.,1.	112.,-1. 11000.,1.	177.,-1. 12000.,1.
680	63.,-1. 9850.,1.	86.,-1. 12500.,1.	126.,-1. 11000.,1.	181.,-1. 12000.,1.
690	64.,-1. 9850.,1.	87.,-1. 12500.,1.	107.,-1. 11000.,1.	182.,-1. 12000.,1.
700	63.,-1. 9850.,1.	84.,-1. 12500.,1.	105.,-1. 11000.,1.	185.,-1. 12000.,1.

to occur on the carbonyls of 4AP between its ground and first electronically excited state [39]. The change in dipole moment that exists between the ground and first electronically excited states [25] is a reflection of the shifting of electron density from the nitrogen atom of the amino-group to the oxygen atoms of the carbonyls. The shift in electron density results in a higher dipole moment in the excited-state than in the ground state. (See Figure 3.15.) The increased basicity of the carbonyls must be the driving force behind the strong interactions of the excited-state of 4AP and hydrogen-bond donating solvents.

E. Relaxation of 4AP in a Series of Linear Alcohols

The parameters from the time-resolved analysis of 4AP in ethanol, 2-propanol, 1-butanol and 1-pentanol can be inverted to give spectra at discrete times. The results of those calculations are shown in Figures 3.16–19. In all these plots, the spectra smoothly progress toward lower energy as a function of time. The only change that occurs from alcohol to alcohol is that the time scale of the relaxation is longer for alcohols with longer alkane chains. The analysis procedure continues with the fitting of the spectral bands as a function of time. The peak positions plotted as a function of time are plotted in Figure 3.20. The rate of spectral shift of 4AP in ethanol is extremely rapid as the spectrum reaches its terminal position within about 100 ps; the spectral shift that occurs in 1-pentanol takes many times longer. When the semi-logarithmic relaxation is plotted (Figure 3.21), the change in the time constant of the decay for the various alcohols is seen clearly. The slopes of the plots of the semi-logarithmic plots of peak position as a function of time give the time constant of the relaxation. The time constant of the relaxation will be referred to here as the solvation time, τ_S . The solvation times for 4AP in each of the alcohols discussed so far are given in Table 3.3. The solvation times for 4AP range from about 50 ps for ethanol to almost 200 ps for 1-pentanol.

The time scale of the solvation process is reminiscent of other phenomena that have

Figure 3.15 Diagram of Charge-Transfer Character of 4AP Excited State

Electronic excitation of 4AP results in transfer of charge density from the nitrogen of the amino group to the oxygen atoms of the carbonyl groups. This gives charge-transfer character to the excited state and results in strong interaction of the excited-state of 4AP and polar solvents. Greater electron density on the oxygen atoms of the carbonyl groups in the excited state than in the ground state makes the oxygen atoms better bases in the excited state than in the ground state.

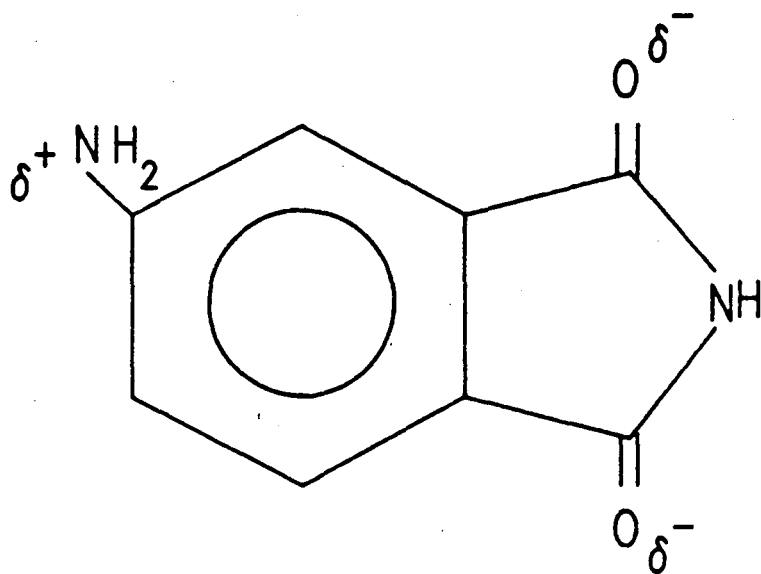


Figure 3.15

Figure 3.16 Emission Spectra for 4AP in Ethanol at Selected Times

Figure 3.16

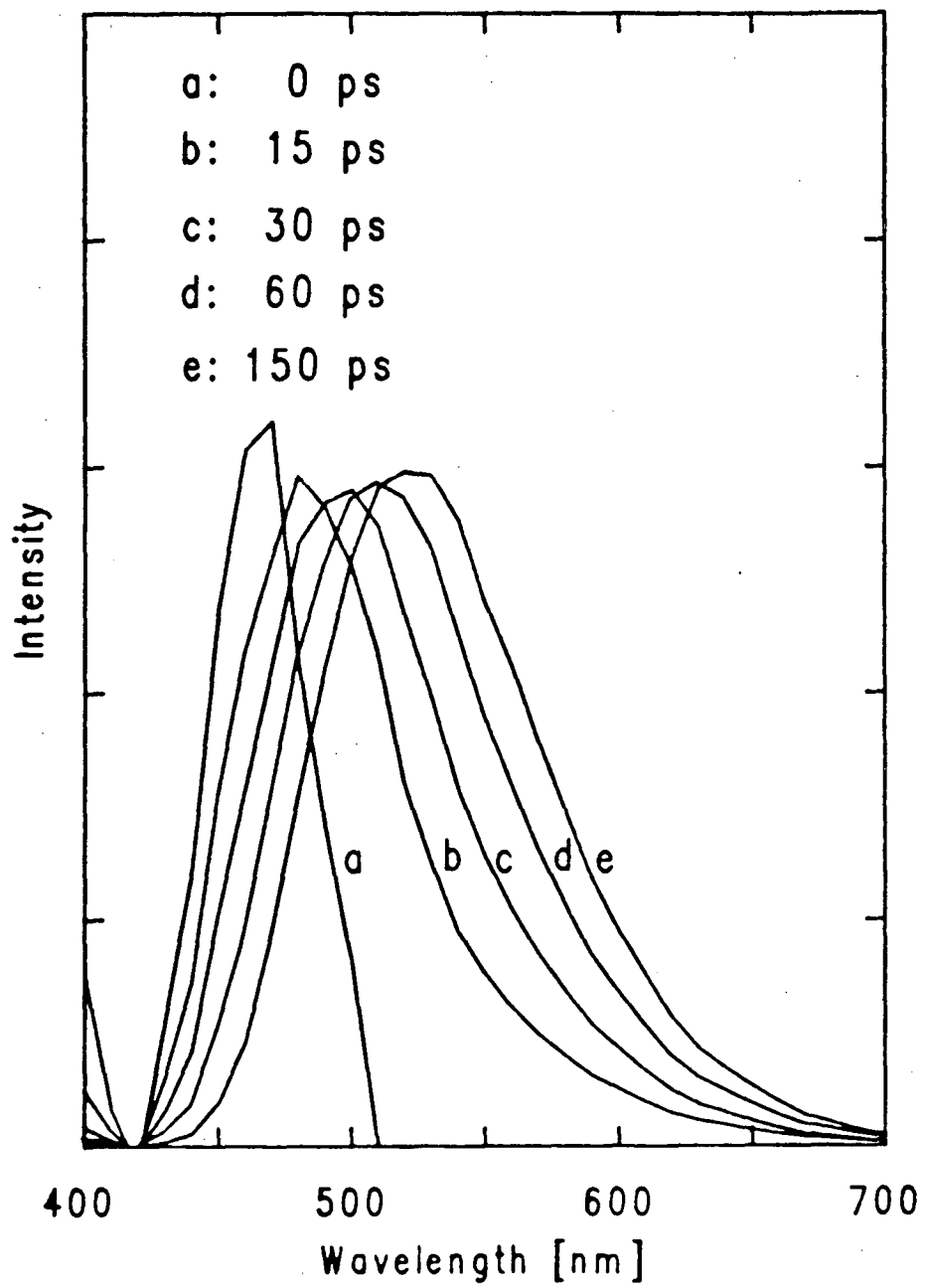


Figure 3.17 Emission Spectra for 4AP in 2-Propanol at Selected Times

Figure 3.17

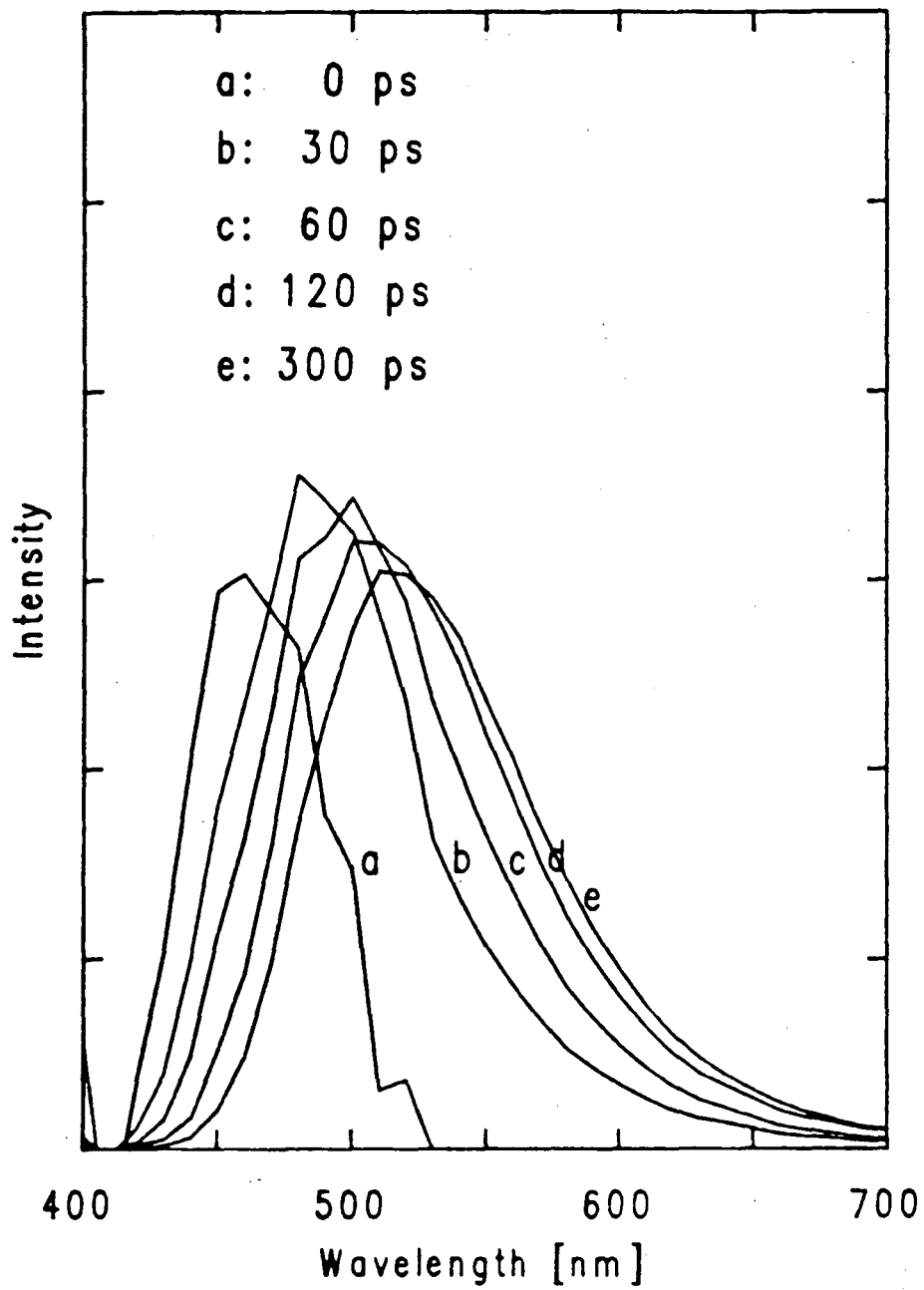


Figure 3.18 Emission Spectra for 4AP in 1-Butanol at Selected Times

Figure 3.18

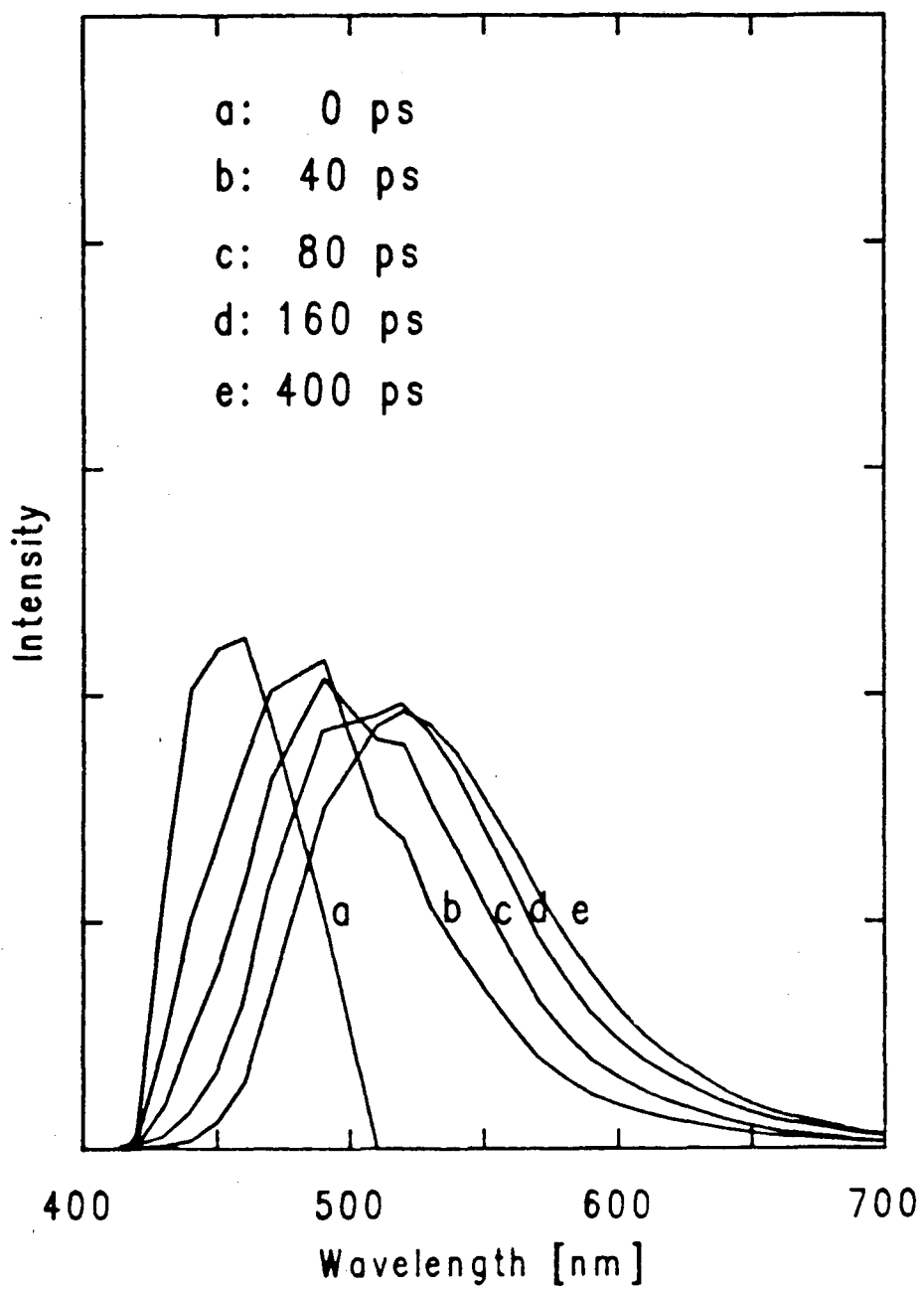


Figure 3.19 Emission Spectra for 4AP in 1-Pentanol at Selected Times

Figure 3.19

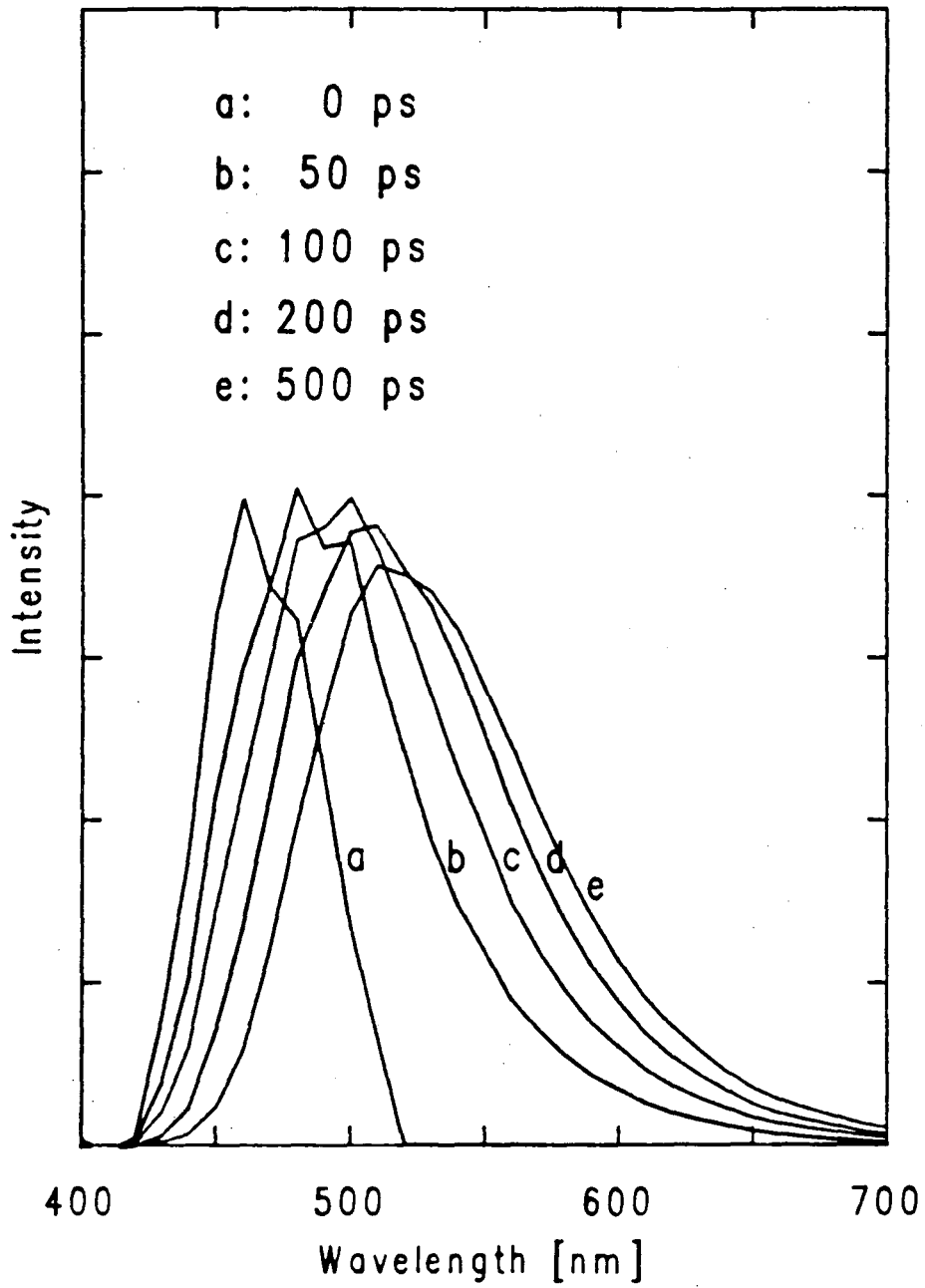


Figure 3.20 Peak Positions as a Function of Time for 4AP in a Number of Simple Alcohols

Data like that in Figures 3.16–19 are used to determine the position of peak emission intensity of 4AP as a function of time in each of the alcohols. The length of the relaxation grows as the length of the alcohol hydrocarbon chain increases.

Figure 3.20

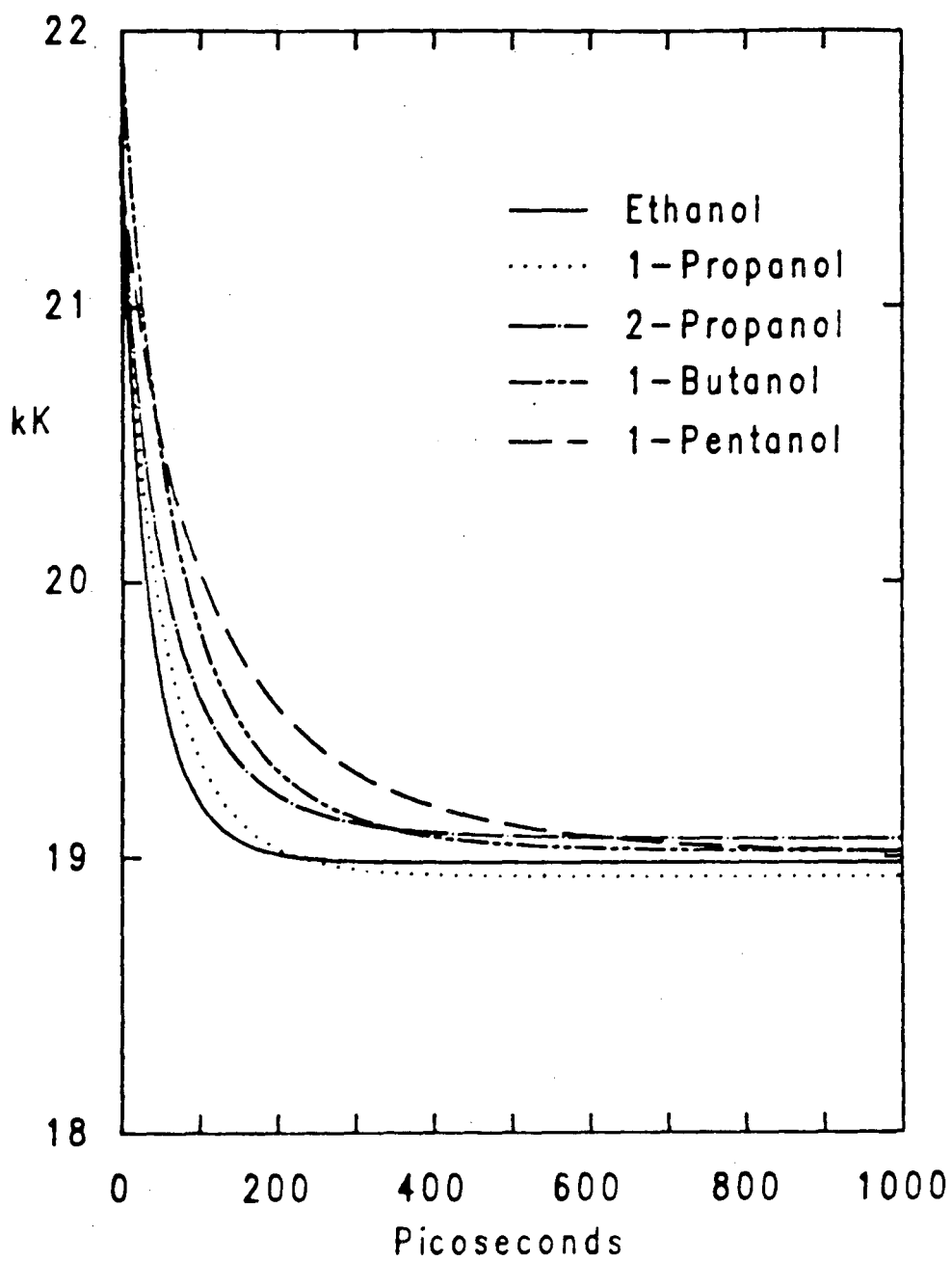


Figure 3.21 Semi-logarithmic Plot of the Peak Positions as a Function of Time for 4AP in a Number of Simple Alcohols

Data in this figure calculated from the data shown in Figure 3.20. The plot is of $\ln(\Delta\tilde{\nu}/\Delta\tilde{\nu}_0)$, where $\nu(t)$ is the peak position in kKaisers as a function of time, $\Delta\tilde{\nu}(t) = \tilde{\nu}(t) - \tilde{\nu}(t = \infty)$, and $\Delta\tilde{\nu}_0 = \Delta\tilde{\nu}(t = 0)$. The value $\tilde{\nu}(t = \infty)$ is approximated by the peak position at between 2 and 5 ns, depending on the alcohol and explained in the caption for Figure 3.9. Curve A is for 4AP in ethanol; curve B, 1-propanol; curve C, 2-propanol; curve D, 1-butanol; curve E, 1-pentanol.

Figure 3.21

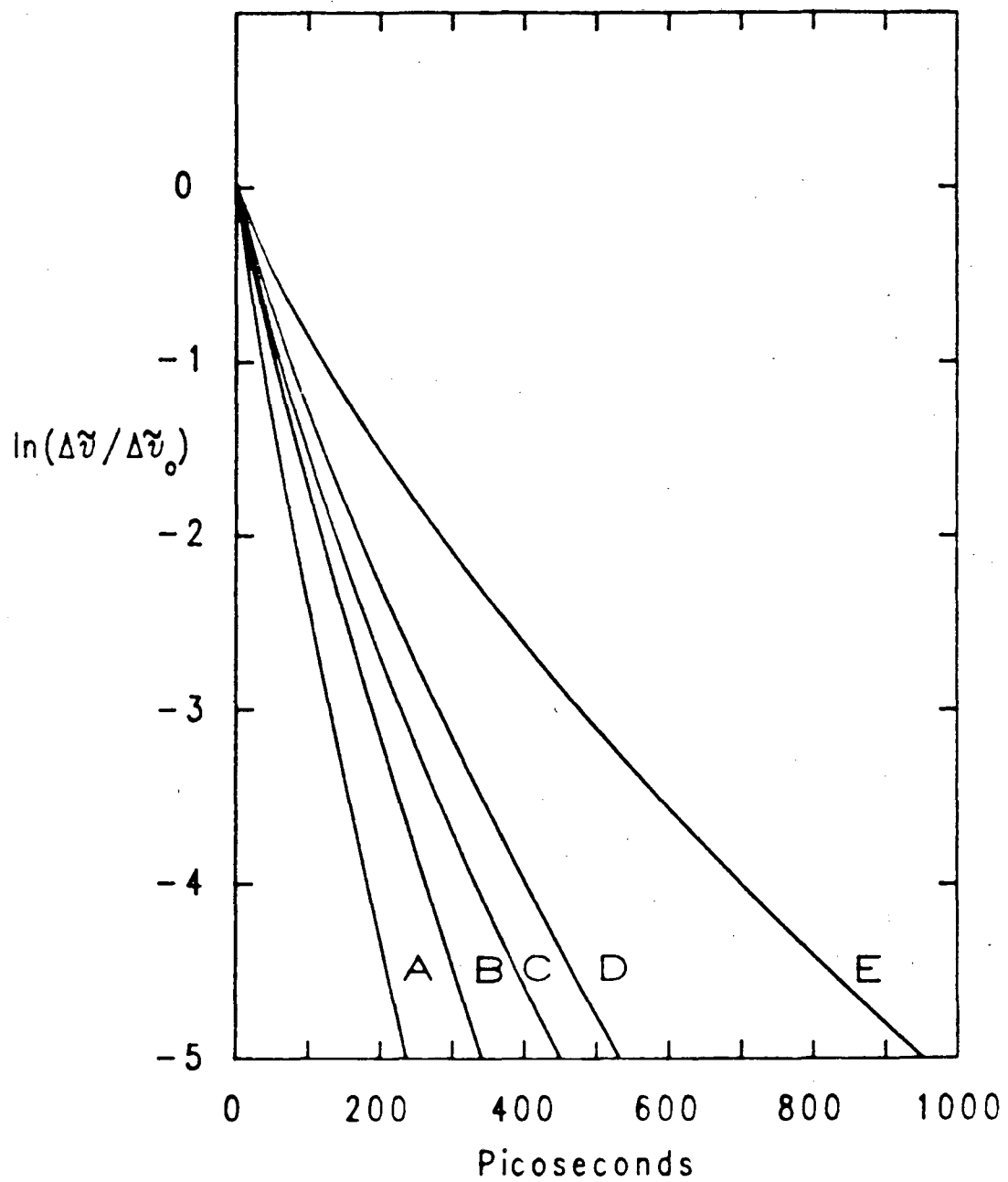


Table 3.3

Solvation times for 4AP in ethanol, and the other alcohols, as calculated from the slopes of the semi-logarithmic plots of peak position as a function of time.

Solvent	Solvation Time τ_S , in ps
Ethanol	48 ± 8
1-Propanol	69 ± 10
2-Propanol	89 ± 15
1-Butanol	111 ± 25
1-Pentanol	191 ± 50

been studied in alcohols. Time constants for the solvation of electrons in alcohols have been measured in pulse radiolysis experiments [40]. These time constants are remarkably similar to the relaxation times exhibited by 4AP emission. Kosower [41] has tabulated the rate of many intramolecular electron transfer reactions, and the time constants in corresponding solvents are again similar. (These are reactions that occur for DMABN and similar molecules, where electronic excitation is to a Franck-Condon state that undergoes subsequent conversion to a charge-transfer state.) A strong correlation between these two relaxation phenomena and the dielectric relaxation times for the alcohols in a field of constant charge has been found [40,41]. In fact, the constant-charge dielectric relaxation times [42] are very close in magnitude to the solvation times determined for 4AP in the alcohols. These values (and the values of related molecular properties [43]) are tabulated with the solvation times in Table 3.4. The strong correlation between the time constants of dielectric relaxation in a field of constant charge and the solvation times is evident.

1. Solvation and Dielectric Relaxation of the Solvent

The question arises: Why should there be a correlation between the dielectric relaxation rate and the rate of solvation? All three of the phenomena just discussed:

- 1) electron solvation,
- 2) formation of a charge-transfer state, and
- 3) solvent relaxation around a newly changed dipole moment,

would be expected to probe the dielectric properties of a solvent. They all involve the introduction or change of charge. The dielectric relaxation rate quantifies the fastest rate at which the solvent can respond to a change in potential or an introduction of charge. Very early on in the study of dielectric phenomena, Debye realized that the interactions between solvent molecules in a polar liquid would cause the reorientation of the dipole moments of the solvent to lag behind the changes in direction of an applied field [44,45].

Table 3.4

Solvation times of 4AP in a series of solvents and the dielectric data for the same solvents at 20°C.

Solvent	Ref.	ϵ_S	$\epsilon_{\infty 1}$	τ_1 in ps	τ'_1 in ps	Solvation Time τ_S , in ps
Ethanol	A	25.2	4.9 ± 0.4	200 ± 15	39 ± 6	48 ± 8
1-Propanol	B	21.1	4.0 ± 0.4	430	81 ± 8	69 ± 10
	C	20.5		382 ± 10	75 ± 10	
	D	20.9		410 ± 30	78 ± 15	
2-Propanol	E*	19.9	3.5 ± 0.6	460 ± 46	81 ± 21	89 ± 15
	F			588	103 ± 18	
1-Butanol	B	17.7	3.6 ± 0.4	668	136 ± 14	111 ± 25
	C	17.9		631 ± 15	127 ± 16	
	G	17.1		569	120 ± 13	
1-Pentanol	B	15.2	3.3 ± 0.4	927	201 ± 20	191 ± 50

τ_1 is the time constant of the principal region of dielectric dispersion for the alcohols. When corrected by the ratio of $\epsilon_{\infty 1}/\epsilon_S$, the resulting time constant is τ'_1 , the longitudinal dielectric relaxation time. The principal source of error in the dielectric relaxation time measurements is in the determination of the dielectric constant $\epsilon_{\infty 1}$.

* Interpolated from data at other temperatures.

References:

- A) M. W. Sagal, *J. Chem. Phys.* **36** (1962) 2437.
- B) S. K. Garg and C. P. Smyth, *J. Phys. Chem.* **69** (1965) 1294.
- C) R. Chahine and T. K. Bose, *J. Chem. Phys.* **65** (1976) 2211.
- D) T. Koshii, H. Takahashi, and K. Higasi, *Bull. Chem. Soc. Japan* **48** (1975) 993.
- E) D. Bertolini, M. Cassettari, and G. Salvetti, *J. Chem. Phys.* **78** (1983) 365.
- F) H. A. Rizk and I. M. Elanwar, *Z. für Phys. Chemie, N. F.* **62** (1968) 225.
- G) H. A. Rizk and N. Youssef, *Z. für Phys. Chemie, N. F.* **58** (1968) 100.

The time constant of the lag in reorientation is characteristic of any given material, and corresponds to the time required for molecular rearrangements to occur. The strong association between individual molecules in alcohols (attributed to hydrogen bonding) causes the rates of dielectric relaxation for the alcohols to be particularly slow.

The phenomenon of dielectric relaxation is measured by determining the dielectric constant of a material when a time-varying applied potential is varied over a range of frequencies. When a static electric field is applied polar solvent molecules will rearrange (eventually) into the lowest energy configuration. It may take the solvent molecules some characteristic amount of time to rearrange into that low energy configuration. The process of rearrangement is referred to as dielectric relaxation, and the characteristic time constant is the measure of the dielectric relaxation rate. If an applied voltage is varied at some high frequency, for instance, by the application of an optical electromagnetic wave, the solvent molecules will not be able to keep up with the field, and the solution will be transparent to the radiation. When the frequency of an applied field is such that the field oscillates on a time scale near but less than the time scale of dielectric relaxation, the dipoles in the solvent just begin to reorient. The result will be a response of the sample, with a phase difference between the incident radiation and the response of the sample. The sample will absorb radiation, with the absorbed energy being dissipated in thermal motion of the solvent molecules. When the frequency of the applied wave is slower than the time constant of reorientation, the molecules in the sample will be able to keep up with the varying field, and there will be no lag.

2. Dielectric Relaxation Under the Conditions of Constant Charge

The time constant which correlates so well with the solvation time measured for 4AP is the time constant of dielectric relaxation under the condition of constant charge. The following derivation, which follows that of Mozumder closely [42], shows why that

particular time constant is the appropriate one, and also how it is related to the ordinary dielectric relaxation rates. The Debye equations that agree with the experimentally observed dispersion phenomena [44,45] were derived to give the electric displacement (proportional to the polarization) as a function of the applied, time-varying electric field:

$$D(t) = \epsilon_{\infty} E(t) + \int_{-\infty}^t E(u) \alpha(t-u) du \quad (3.4)$$

where $D(t)$ is the electric displacement, $E(t)$ is the time-varying electric field, ϵ_{∞} is the high frequency dielectric constant, and α is the function describing the decay of polarization. Debye assumed the form of the polarization decay was exponential [44], in accord with many other natural processes:

$$\alpha(t) = \alpha_0 e^{(-t/\tau_1)} \quad (3.5)$$

where τ_1 is the relaxation time, and α_0 is a constant. The combination of equations (3.4) and (3.5) leads to the following derivative equation:

$$t \left(\frac{d}{dt} \right) (D - \epsilon_{\infty} E) + (D - \epsilon_{\infty} E) = \tau_1 \alpha_0 E \quad (3.6)$$

The constant α_0 is determined by considering what occurs when a static, not a time-varying, field is applied. In that case, the derivative with time is constant (eventually all transients will decay away). By the definition of the static dielectric constant, ϵ_S ,

$$D = \epsilon_S E \quad (3.7)$$

when a static field is applied. Using the conditions of a static applied field, the definition of α_0 can be obtained from (3.6):

$$\alpha_0 = \frac{(\epsilon_S - \epsilon_{\infty})}{\tau_1} \quad (3.8)$$

Rewriting (3.6) with this definition of α_0 yields

$$t \left(\frac{d}{dt} \right) (D - \epsilon_{\infty} E) + (D - \epsilon_{\infty} E) = (\epsilon_S - \epsilon_{\infty}) E \quad (3.9)$$

When an ion or electron is introduced suddenly into a solution, or when a dipole is suddenly introduced, it is not the applied field that is held constant, but the charge that remains constant. To determine what occurs when an ion or dipole is introduced suddenly, equation (3.9) should be solved using boundary conditions appropriate for constant charge. Under the conditions of constant charge,

$$\frac{dD}{dt} = 0, \quad (3.10)$$

and the following equation can be obtained:

$$\frac{dE}{dt} = \frac{1}{\tau_1 \epsilon_\infty} (D - \epsilon_S E). \quad (3.11)$$

A time-dependent dielectric constant, $\epsilon(t)$, can be defined:

$$E(t) = D[\epsilon(t)] \quad (3.12)$$

so that when $\frac{dD}{dt} = 0$,

$$\frac{dE}{dt} = D \left(\frac{d}{dt} \right) [\epsilon(t)]^{-1} \quad (3.13)$$

Substitution into equation 11, yields

$$\frac{d}{dt} [\epsilon(t)]^{-1} = (\tau_1 \epsilon_\infty)^{-1} [1 - \epsilon_S (\epsilon(t))^{-1}] \quad (3.14)$$

Integration and using the initial condition that $\epsilon \rightarrow \epsilon_\infty$ as $t \rightarrow 0$ gives

$$[\epsilon(t)]^{-1} = \epsilon_S^{-1} + (\epsilon_\infty^{-1} - \epsilon_S^{-1}) e^{(-t/\tau')} \quad (3.15)$$

where

$$\tau' = \frac{\epsilon_\infty}{\epsilon_S} \tau_1. \quad (3.16)$$

In general $\epsilon_S \gg \epsilon_\infty$. Equation (3.16) therefore implies that the rate of relaxation is considerably faster under the condition of constant charge than under the condition of constant applied field. The appropriate constants, τ_1 , ϵ_S , and ϵ_∞ for the alcohols are included in Table 3.4 with the solvation times and the constants τ' .

One note of importance for the alcohols is that the alcohols exhibit more than one region of dispersion [43]. The time constants listed in Table 3.4 are for the principal region of dielectric dispersion, which in the alcohols is the lowest frequency dispersion. The existence of more than one rearrangement process, which is the physical interpretation of more than one region of dispersion, means that the constants ϵ_S and ϵ_∞ that are appropriate to use to modify τ_1 are not the static and optical frequency dielectric constants, but are the dielectric constants that are static and of high frequency on the time scale of the dispersion. For the first region of dispersion, these constants are referred to by Garg and Smyth as ϵ_{01} and $\epsilon_{\infty 1}$. For the lowest frequency dispersion, ϵ_{01} is the usual ϵ_S . The values for $\epsilon_{\infty 1}$ differ by as much as a factor of two from the optical frequency dielectric constants. The work by Kosower discussed earlier [41] used the optical dielectric constant in place of the correct $\epsilon_{\infty 1}$ value, meaning that the time constants he calculated for the dielectric relaxation times for the alcohols were too small by as much as a factor of two. The present work uses the correct high frequency constant [46].

3. Molecular Mechanisms for Dielectric Relaxation of Alcohols

The physical rearrangement process that is associated with the principal dispersion region has been the topic of much discussion [43,47,48]. In general, there is a consensus that the dispersion must be related to the peculiarly large amount of association that exists for the alcohols because of the hydrogen bonding network. Garg and Smyth [43] and others [47] assert that the alcohols exist in a dynamic "microcrystalline structure" because of the formation of bridging hydrogen bonds. The structure is dynamic because thermal fluctuations cause hydrogen bonds to be broken and reformed continuously. The principal dispersion region is associated with the reorientation of the dipole that occurs by the process of breaking a hydrogen bond, rotation of the alcohol molecule, and reformation of the hydrogen bond with a new neighbor. The slowness of the rearrangement process

is attributed to the rate-limiting step of hydrogen-bond rupture. According to Dannhauser and, independently, Böttcher [48], the hydrogen bonds between molecules result in the formation of ordered polar multimers with long persistence times. The longest dielectric relaxation time is associated with the reorientation of the largest such multimers, and the shorter times to dimers or monomers. The presence of strong hydrogen bonds is essential to both interpretations; Garg and Smyth use the activation of strongly bound structures to limit the rate of reorientation, and Dannhauser assumes that the hydrogen bonds are even stronger, owing to the apparent persistence of the multimer structure on the time scale of the dispersion frequency.

Regardless of the proposed mechanism for the rearrangement process, the important consideration is that the hydrogen-bonding network of the alcohols causes the response of an alcohol solution to a change in charge distribution to be slow. The strong degree of association of the alcohols is responsible for the anomalously slow response of the alcohols relative to other solvents. However, the interpretation of the molecular rearrangement presented by Garg and Smyth, and others [43,47], as being responsible for the principal region of dielectric dispersion is particularly appealing because it invokes hydrogen bond rupture as the reason the process is so slow. The excited-state of 4AP has greater electron density on the carbonyls than its ground state precursor. The increased basicity of the carbonyl groups can be seen as a driving force for enhancement of the extent of hydrogen bonding between solvent molecules and excited 4AP molecules, relative to the extent of hydrogen bonding with ground state 4AP. The rate of hydrogen bond formation is limited by the rate of bond fission, according to Garg and Smyth. If the process of solvation of 4AP is indeed related to the formation of hydrogen bonds between the solvent and the excited 4AP molecule, then the time constant of solvation should also be limited by the rate of hydrogen bond fission. With either the molecular picture due to Garg and Smyth or the one of Böttcher and Dannhauser, the effect is the

same: the rate of relaxation of the solvent around the excited-state is equal to the rate of solvent dielectric relaxation, and that rate is particularly slow for the alcohols because of the extensive hydrogen bonding network.

F. Using Dielectric Relaxation As a Predictive Model of Excited-State Solvation Dynamics

The measurements of the solvation time of 4AP in the alcohols show a strong correspondence to the time constants of dielectric relaxation. The time constant of dielectric relaxation is known for a large number of solvents and under a large number of experimental conditions. To determine if the dielectric relaxation rate really predicts the rate of solvation, the emission spectrum of 4AP can be time-resolved in solvents under experimental conditions where the dielectric relaxation times are known. The solvation time can be determined from the details of the time-resolved emission spectrum, and the quality of the correlation between the solvation time and the time constant of dielectric relaxation determined.

1. 4AP in non-Alcoholic Solutions

Before showing the results of different experiments, it is important to demonstrate that the results already presented for the solvation of 4AP in a variety of solvents are consistent with the dielectric relaxation model. Dielectric dispersion is measured for more substances than just simple alcohols [49]. However, for most substances at room temperature, the rates of dielectric relaxation are much faster than the rate of relaxation of the alcohols because such solutions lack the hydrogen-bonded superstructure which impedes relaxation for the alcohols. For instance, the time constant of dielectric relaxation in room temperature acetonitrile is 5 ps [50]. Once the correction for constant charge is made, the time constant of solvation that the dielectric relaxation model would predict is far less than 1 ps. Given that the resolution of the streak camera system is about 20 ps,

the dielectric relaxation model would predict that the solvation of 4AP in acetonitrile could not be discerned. When the time-resolved emission of 4AP in acetonitrile was time-resolved, it was indeed determined that the dynamics of the Stokes' shift were too fast to detect. Actually, the prediction of the dielectric relaxation model for all of the non-alcoholic solvents discussed in Section D is that the relaxation would be too fast to detect with the limited temporal resolution of the streak camera system. The dielectric relaxation times for DMSO, acetone, and the other solvents are given in Table 3.5, along with their static and optical dielectric constants.

The smallest of the alcohols, methanol, has anomalously slow dielectric relaxation for a molecule of its size. However, the relaxation in methanol would be predicted by the dielectric relaxation model to be faster than can be resolved with the streak camera. (See Table 3.5.) This is in accord with experimental observations [51].

Besides the alcohols, there are other hydrogen-bonding solvents that have anomalously slow dielectric relaxation rates. The dielectric relaxation rates of the N-methyl-amides without the correction for constant charge are slow enough that the relaxation could be detectable on the streak camera, as the time constant for N-methyl-formamide at 25°C is 200 ps (extrapolated from data contained in reference 52). However, the static dielectric constant for N-methyl-formamide is enormous, 182. Once the dielectric relaxation time is corrected for the constant charge environment, the time constant of the relaxation is less than 10 ps. The prediction of the dielectric relaxation model would therefore be that the solvation of 4AP would be too fast to be observed with the streak camera system. This prediction is indeed consistent with recent observations [53].

2. Solvation and Temperature Variations

When the temperature of a substance is changed, the dielectric relaxation rate changes. Investigations of dielectric relaxation have exploited this variation to measure the activa-

Table 3.5

Dielectric relaxation times for a series of solvents, at 20°C, except where noted.

Solvent	Dielectric Relaxation Times, ps	Corrected Dielectric Relaxation Times, ps	Ref.
Acetonitrile	6	<1	A
DMSO	20	2.5	B
N,N-Dimethylformamide	10	1	C*
Formamide	42	3	D
N-methylformamide (11°C)	250	13	C
Methanol	56	7	E
	47	6	B
	56	7	D

* Interpolated from data at other temperatures.

References:

- A) M. Evans, *J. Mol. Liq.* **25** (1983) 149.
 B) H. Behret, F. Schmithals, and J. Barthel, *Z. für Phys. Chemie, N. F.* **96** (1975) 73.
 C) S. J. Bass, W. I. Nathan, R. M. Meighan, and R. H. Cole, *J. Phys. Chem.* **68** (1964) 509.
 D) B. P. Jordan, R. J. Sheppard and S. Szwarnowski, *J. Phys. D.* **11** (1978) 695.
 E) D. Bertolini, M. Cassettari and G. Salvetti, *J. Chem. Phys.* **78** (1983) 365.

tion energies associated with the dielectric relaxation processes, and so many accounts of the variation of dielectric relaxation with temperature are available in the literature [43,54]. To test if the rate of solvation of excited-state 4AP tracked changes in the dielectric relaxation rate with changes in temperature, the emission from temperature-controlled solutions of 4AP in 1-propanol was time-resolved. As expected, even the steady-state emission bands show slight shifts with changes in temperature. Figure 3.22 shows the magnitude of the shifts (about 5 nm for each 20°C change in temperature). The effect on the temporal profiles of emission is much more dramatic, and is shown in Figures 3.23 and 3.24. For the red edge of the emission (Figure 3.25), the colder solutions clearly show slower rates of growth. Similarly, the blue edge of the emission band shows slower rates of decay in the colder solutions (Figure 3.26). The complete list of temporal parameters for the entire spectrum at all three temperatures is given in Table 3.6. The spectra of 4AP in 1-propanol at all three temperatures can be calculated at an array of times (as was done already at T=20°C) and the positions of the emission band determined as a function of time. The semi-logarithmic plots based on that analysis are given in Figure 3.27. The time constants of those plots, along with the dielectric relaxation times at the appropriate temperatures are given in Table 3.7. The agreement is quite satisfactory.

3. Isotope Effects on the Photophysics of 4AP

As presented in Section E.3, the anomalously slow dielectric relaxation of the alcohols is attributed to the extent of the hydrogen bonding network that impedes rapid reorientation. Thermal fluctuations disrupt the superstructure that the alcohols form. The substitution of specifically deuterated alcohols (R-OD, alcohol-d) should mean that the thermal fluctuations in the superstructure are lessened, because the heavier deuterons have lower zero point energies than the corresponding protons. The dielectric relaxation

Figure 3.22 Steady-state Emission From 4AP in 1-Propanol at T=0, 20, and 40°C

Emission from 4AP in 1-propanol shifts slightly but significantly on changes in temperature.

Figure 3.22

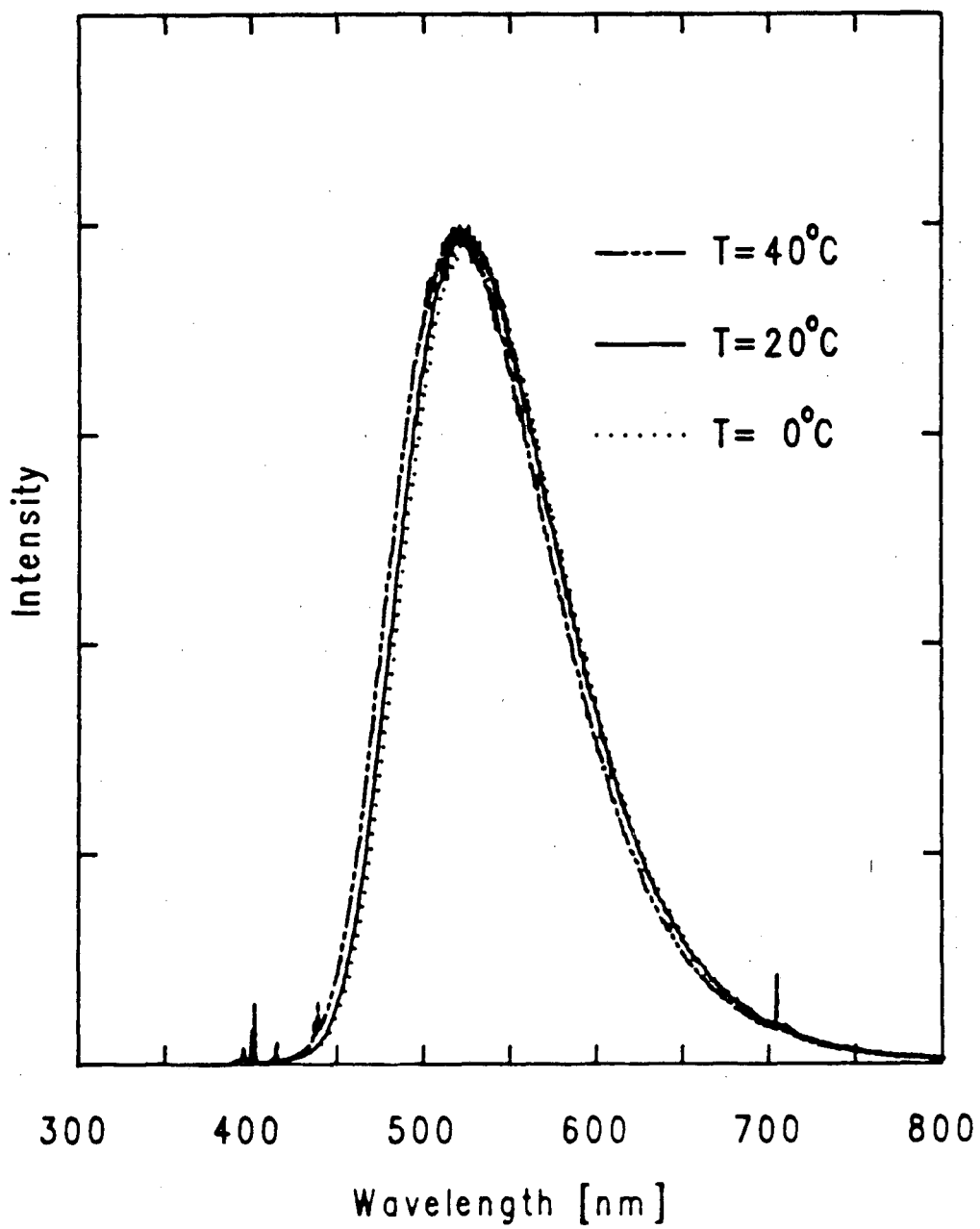


Figure 3.23 Time-Resolved Emission from 4AP in 1-Propanol at T=0, 20, and 40°C Detected at 650 nm.

The initial profiles of this low energy emission from 4AP detected at 650 nm are shown. The emission in colder solutions clearly shows slower growth rates than corresponding emission from warmer solutions. The smooth curves superimposed on the data are computer-generated fits. The time constants of the fits are: at 0°C, $\tau=170$ ps; 20°C, 87 ps; 40°C, 51 ps.

Figure 3.23

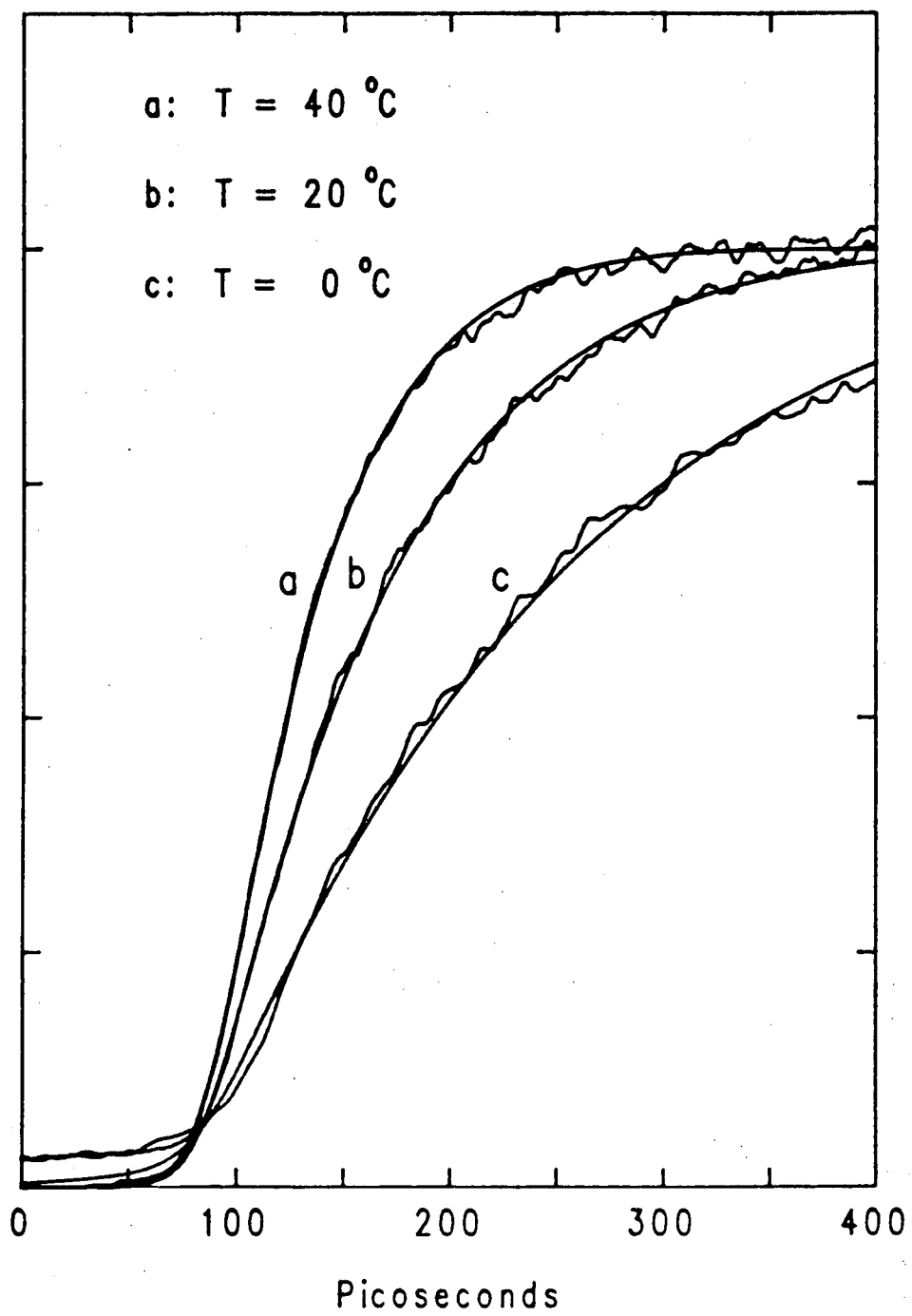


Figure 3.24 Time-Resolved Emission from 4AP in 1-Propanol at T=0, 20, and 40°C Detected at 450 nm.

The initial profiles of this high energy emission from 4AP detected at 450 nm are shown. The emission in colder solutions shows components of fast decay that are slower than in warmer solutions. Computer-generated fits (smooth curves) are superimposed on the data. From the fits, the time constants for the fast components of decay, τ , and their amplitudes, α , are: at 0°C, $\alpha=14.9$, $\tau=79$ ps; at 20°C, 16.5, 43 ps; at 40°C, 9.5, 30.15 ps.

Figure 3.24

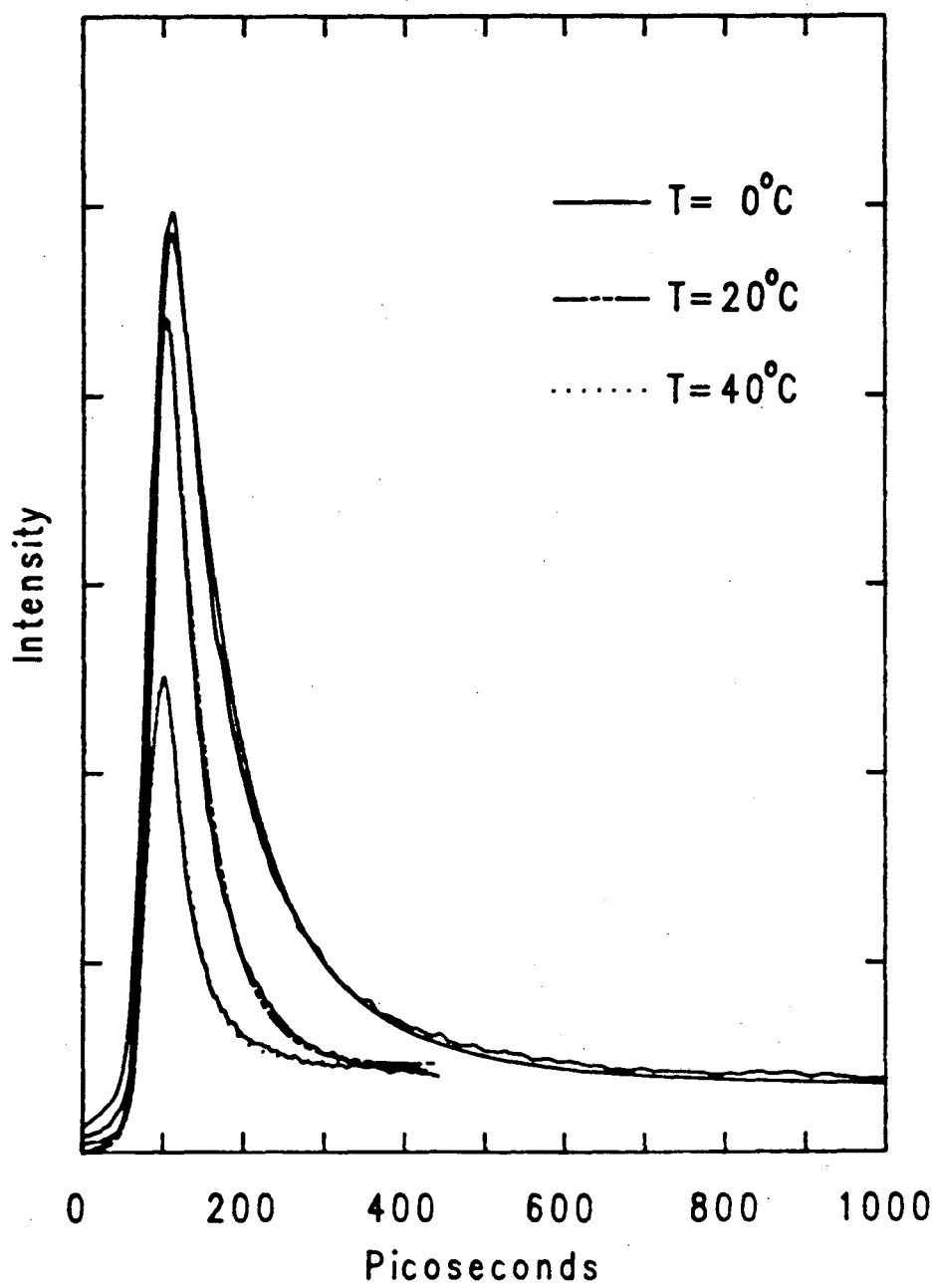


Figure 3.25 Semi-logarithmic Plot of Peak Positions as a Function of Time for 4AP in 1-Propanol at T=0, 20, and 40°C

Figure 3.25

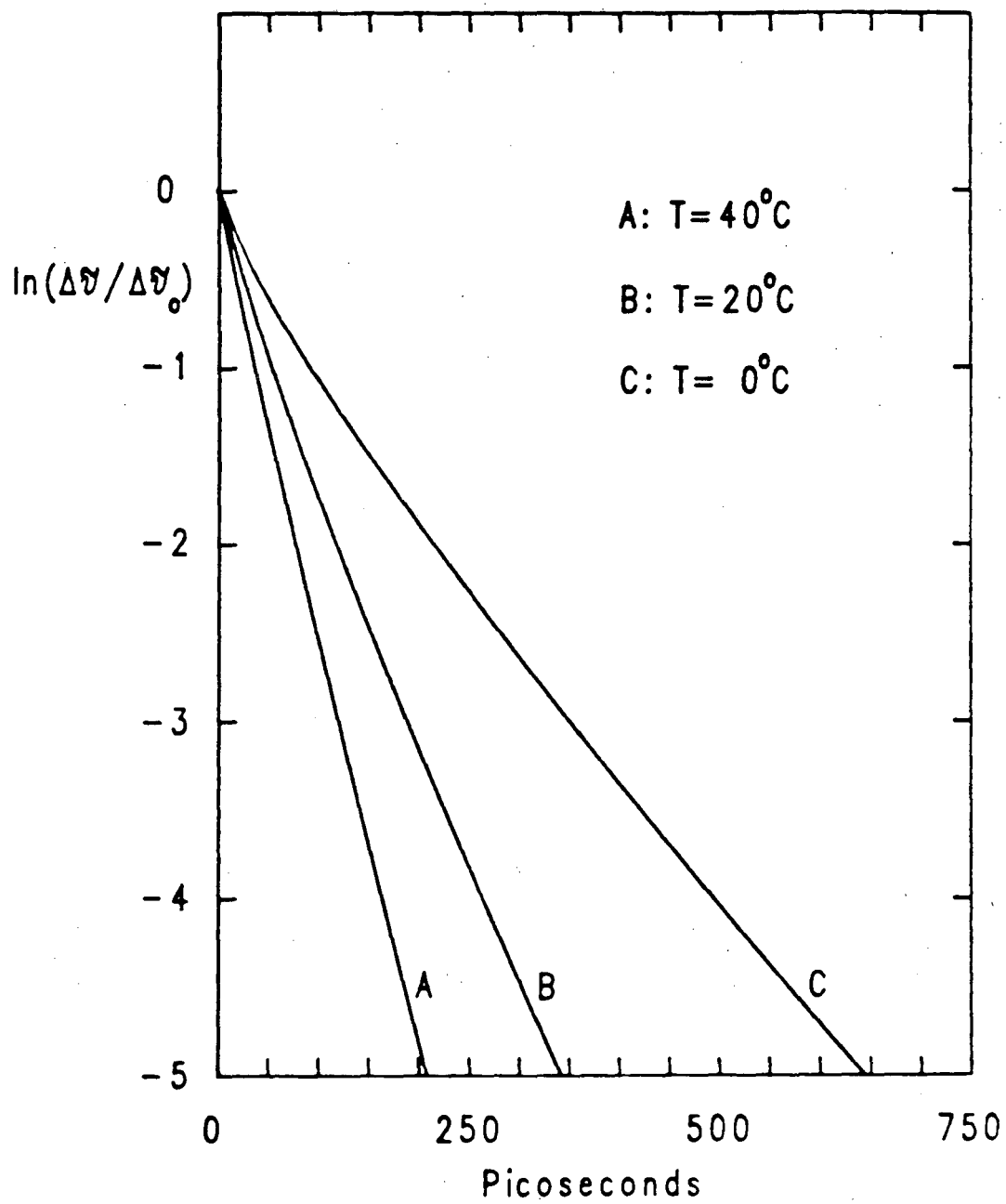


Table 3.6

Parameters of fits to 4AP in 1-Propanol, at three different temperatures (0, 20, and 40°C), spectrally- and temporally-resolved. The time constants are given in picoseconds, τ_i , with their relative amplitudes, α_i .

Wavelength (nm)	T=0°C τ_i, α_i	T=20°C τ_i, α_i	T=40°C τ_i, α_i
400	63., 2.0 11500., 1.	21., 20.0 10600., 1.	14., 12.4 11100., 1.
410	38., 8.8 11500., 1.	18., 18.9 10600., 1.	15., 12.5 11100., 1.
420	37., 8.5 11500., 1.	21., 32.9 10600., 1.	16., 18.4 11100., 1.
430	40., 15.6 11500., 1.	29., 34.0 10600., 1.	21., 18.6 11100., 1.
440	62., 22.7 11500., 1.	38., 26.9 10600., 1.	25., 15.2 11100., 1.
450	79., 14.9 11500., 1.	43., 16.5 10600., 1.	30., 9.5 11100., 1.
460	98., 8.0 11500., 1.	54., 8.0 10600., 1.	37., 5.2 11100., 1.
470	128., 4.9 11500., 1.	61., 4.1 10600., 1.	43., 2.9 11100., 1.
480	140., 2.2 11500., 1.	77., 2.1 10600., 1.	50., 1.6 11100., 1.
490	182., 1.0 11500., 1.	85., 1.2 10600., 1.	52., 1.0 11100., 1.
500	175., 0.5 11500., 1.	98., 0.6 10600., 1.	43., 0.8 11100., 1.
510	30., -1. 11500., 1.	19., -1. 10600., 1.	14., -1. 11100., 1.
520	32., -1. 11500., 1.	20., -1. 10600., 1.	11., -1. 11100., 1.
530	42., -1. 11500., 1.	27., -1. 10600., 1.	18., -1. 11100., 1.
540	66., -1. 11500., 1.	38., -1. 10600., 1.	25., -1. 11100., 1.
550	87., -1. 11500., 1.	42., -1. 10600., 1.	28., -1. 11100., 1.

Table 3.6, cont.

Wavelength (nm)	T=0°C τ_i, α_i	T=20°C τ_i, α_i	T=40°C τ_i, α_i
560	100.,-1. 11500.,1.	52.,-1. 10600.,1.	34.,-1. 11100.,1.
570	110.,-1. 11500.,1.	55.,-1. 10600.,1.	37.,-1. 11100.,1.
580	122.,-1. 11500.,1.	63.,-1. 10600.,1.	37.,-1. 11100.,1.
590	135.,-1. 11500.,1.	64.,-1. 10600.,1.	41.,-1. 11100.,1.
600	135.,-1. 11500.,1.	71.,-1. 10600.,1.	42.,-1. 11100.,1.
610	138.,-1. 11500.,1.	73.,-1. 10600.,1.	43.,-1. 11100.,1.
620	153.,-1. 11500.,1.	73.,-1. 10600.,1.	44.,-1. 11100.,1.
630	154.,-1. 11500.,1.	78.,-1. 10600.,1.	48.,-1. 11100.,1.
640	157.,-1. 11500.,1.	77.,-1. 10600.,1.	47.,-1. 11100.,1.
650	170.,-1. 11500.,1.	87.,-1. 10600.,1.	51.,-1. 11100.,1.
660	167.,-1. 11500.,1.	88.,-1. 10600.,1.	52.,-1. 11100.,1.
670	173.,-1. 11500.,1.	91.,-1. 10600.,1.	53.,-1. 11100.,1.
680	191.,-1. 11500.,1.	91.,-1. 10600.,1.	50.,-1. 11100.,1.
690	192.,-1. 11500.,1.	94.,-1. 10600.,1.	51.,-1. 11100.,1.
700	173.,-1. 11500.,1.	90.,-1. 10600.,1.	49.,-1. 11100.,1.

Comparison with the 1-propanol parameters in Table 1 gives an indication of the reproducibility of the parameters; the values here and those in Table 1 are from two completely independent spectral runs.

Table 3.7

Solvation times of 4AP in 1-propanol, at three different temperatures, with the constant-charge dielectric relaxation times.

Temperature in °C	Solvation Time τ_S , in ps	Dielectric Relaxation Time, Corrected τ_S , in ps	Ref.
0	129 ± 20	134 ± 13	A
20	69 ± 10	82 ± 8 78 ± 14	B C
40	42 ± 5	60 ± 12 44 ± 6	B C

The principal source of error in the dielectric relaxation time measurements is in the determination of the dielectric constant $\epsilon_{\infty 1}$.

References:

- A) R. Chahine and T. K. Bose, *J. Chem. Phys.* **65** (1976) 2211.
 B) S. K. Garg and C. P. Smyth, *J. Phys. Chem.* **69** (1965) 1294.
 C) T. Koshii, H. Takahashi, and K. Higasi, *Bull. Chem. Soc. Japan* **48** (1975) 993.

rates for three simple alcohols have been determined [55–57]. For deuterated methanol (methanol-d) [55], the time constant of the relaxation is about 35 percent greater than for ordinary methanol. For 1-propanol [56], the increase in the relaxation time upon deuteration is about 20 percent. The longer the alcohol chain the less sensitive the time constant is to deuteration, because the change in the dielectric relaxation rate for 1-octanol upon deuteration is only 10 percent [57]. Noticeable effects were found only in the time constants of dielectric relaxation; for instance, the changes in dielectric constant were very small ($\ll 1$ percent changes).

When the emission from 4AP is time-resolved in deuterated solvents, the most obvious change in the emission profiles are on a long time scale. There is a stark difference between the emission decay time of 4AP in deuterated methanol (methanol-d), and the corresponding decay in ordinary methanol. As shown in Figure 3.26, the decay is longer in the deuterated solvent than in its undeuterated counterpart. The difference in lifetimes is considerable, 6.8 ± 0.3 ns for methanol, and 16.9 ± 0.5 ns for methanol-d. The steady-state absorption and emission spectra for both isotopes can be superimposed, although the emission intensity is noticeably enhanced in the deuterated solvent [58]. The data for the relative emission quantum yield and lifetime of 4AP in methanol and methanol-d, and in two other pairs of alcohols are given in Table 3.8. The relative quantum yields of emission are consistent with the lifetimes measured for all three pairs, indicating that the change on deuteration is in the non-radiative decay rate. For all three alcohols, the non-radiative decay rates are slower in the deuterated solvent. Changes in non-radiative rates with deuteration of the solvent have been reported for other molecular systems that have excited states with charge transfer character [59,60]. The effect of deuteration on the non-radiative rates certainly indicates solvent participation in the relaxation process, and has been explained in terms of the theory of radiationless transitions [60,61]. For an electronic transition with a large energy gap, the Franck-Condon factors will be domi-

nated by the high frequency vibrational modes. When the solvent forms hydrogen bonds with a highly polar excited state that are stronger than the hydrogen bonds that form between the solvent and the ground state, internal conversion from the excited state to the ground state results in considerable vibrational excitation of the high-frequency modes involved in the hydrogen bonding. For example, if the following hydrogen bond forms in the excited state (as would be the case for 4AP),



internal conversion of the excited molecule with the carbonyl moiety will leave the alcohol with considerable O-H vibrational excitation. In the formalism of the theory of radiationless transitions, the O-H vibrational modes should be considered as acceptor modes in the transition between the excited and ground states. Because the vibrational frequency of the alcohol is lowered upon deuteration, the Franck-Condon factor for the internal conversion transition is decreased in the deuterated solvent. By the theory of radiationless transitions, then, the rate of internal conversion will be slower in the deuterated alcohol than in the undeuterated, or ordinary, alcohol. The theory of radiationless transitions is completely consistent with the experimental results, that the quantum yield of emission is greater and the lifetime of emission is longer in an alcohol-d than in an ordinary alcohol. In light of the theory of radiationless transitions, the magnitude of the isotope effect on the lifetime can in fact be considered a signature of the importance of high frequency modes in the excited-state solvation process. Clearly the isotopic identity of the proton involved in the excited-state interaction is extremely important when 4AP is the solute, giving rise to a change in lifetime by almost a factor of three. The excited-state of 4AP clearly has a strong interaction with the hydroxy group of the alcoholic solvent.

If the dielectric relaxation model for excited-state solvation is accurate, when the emission from 4AP in a deuterated alcohol is time-resolved with higher time resolution, changes in the emission profiles more subtle than the change in lifetime should be

Figure 3.26 Emission from 4AP in Methanol and Methanol-d—Fluorescence Lifetimes

Long time scale emission decays of 4AP in both methanol and deuterated methanol are shown. The isotope effect on the lifetime is obviously quite large. The lifetime in ordinary methanol is 6.8 ± 0.3 ns, while the smaller non-radiative rate in deuterated methanol leads to a lifetime of 16.9 ± 0.5 ns.

Figure 3.26

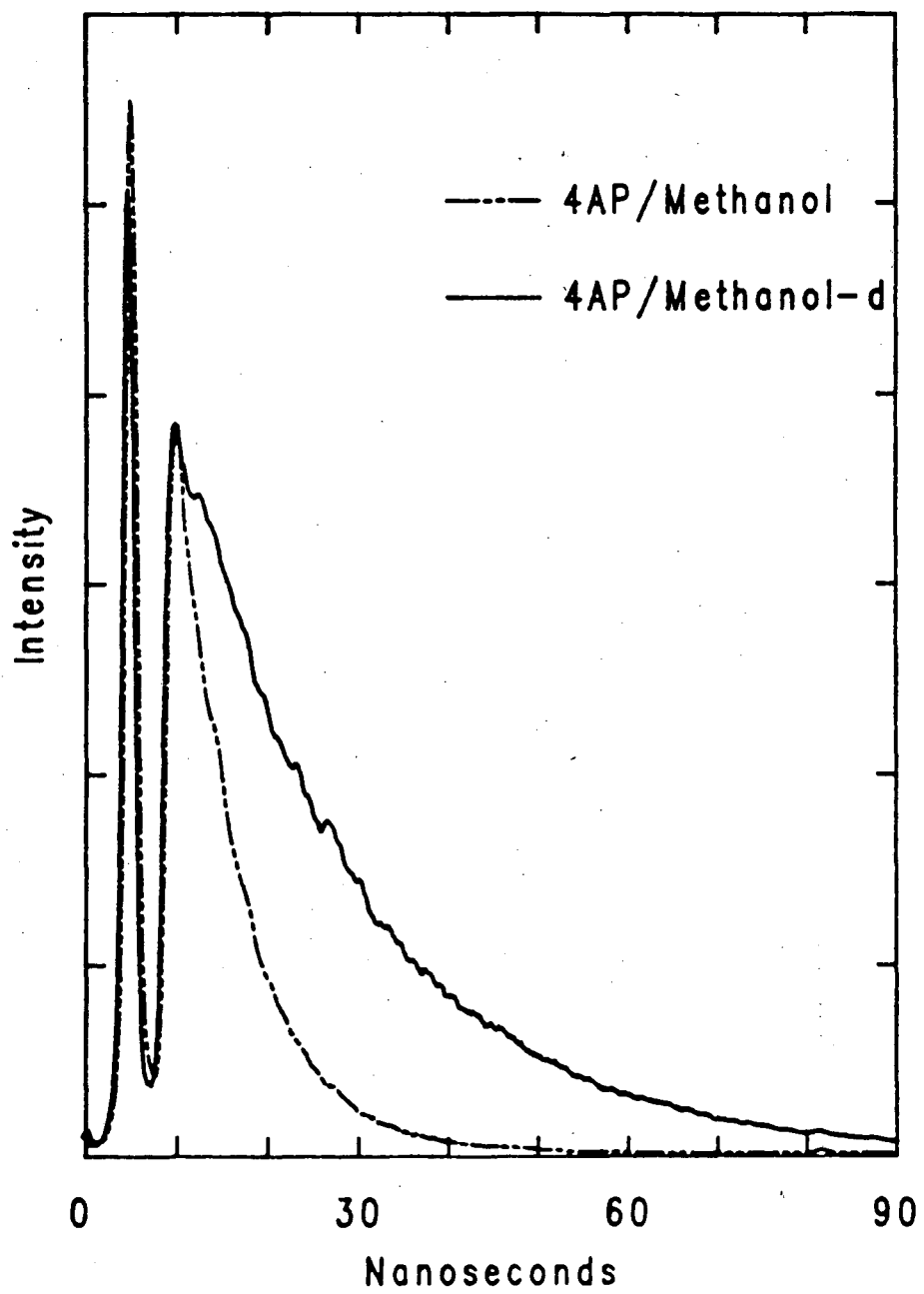


Table 3.8

Solvent isotope effect on the lifetime and (relative) emission quantum yield of 4AP.

Solvent	τ_{fl} (ns)	$\tau_{fl}(D)/\tau_{fl}(H)$	$\Phi(D)/\Phi(H)$
Methanol-d	16.9 ± 0.5	2.49 ± 0.18	2.6
Methanol	6.8 ± 0.3		
Ethanol-d	19.4 ± 0.5	1.88 ± 0.18	1.7
Ethanol	10.3 ± 0.7		
2-Propanol-d	20.9 ± 0.4	1.72 ± 0.15	1.6
2-Propanol	12.1 ± 0.8		

Relative emission quantum yields, $\Phi(D)/\Phi(H)$, determined for the relative intensities of emission from solutions of the same optical density at the excitation wavelength 355 nm. The emission intensities were recorded on a computer-controlled spectrofluorimeter (Spex Fluorolog, Spex Industries, Inc.).

discernable. These subtle changes in emission profiles would be due to changes in the solvation times that are predicted to occur on the basis of the changes in the dielectric relaxation times for the isotopically substituted alcohols. The temporal profiles of the red edge of the emission band of 4AP in 2-propanol and 2-propanol-d are compared in Figure 3.27. The emission shows a rise time in the deuterated solvent that is about 20 percent longer than the rise time in the ordinary alcohol. The change in the time constant of dielectric relaxation for 1-propanol has been reported at about 20 ± 10 percent [56]. Because 1- and 2-propanol have the same length hydrocarbon chain, it is likely that the isotopic substitution in 2-propanol has an effect of about the same magnitude [55]. Therefore, the dielectric relaxation model would predict an increase in solvation time of about 20 percent when changing from 2-propanol to 2-propanol-d. The time-resolved data for 2-propanol and 2-propanol-d are completely consistent with the predictions of the dielectric relaxation model.

The accurate prediction of the dielectric relaxation model for the isotope effect on the solvation time serves to eliminate simultaneously another possible model. The solvation times that have been determined correlate quite well with the viscosities of the alcohols in which they have been determined. However, the effect of isotopic substitution results in only a very small increase in the viscosity [62]. Even for methanol, where the effect is the largest, the viscosity of methanol-d is greater than the viscosity of methanol by only 3 percent. The data for the other alcohols give changes in the viscosity on deuteration of a similar magnitude [62]. The large increase in the solvation time on deuteration is inconsistent with the small increase in the viscosity, but quite accurately predicted by the increase in the dielectric relaxation time.

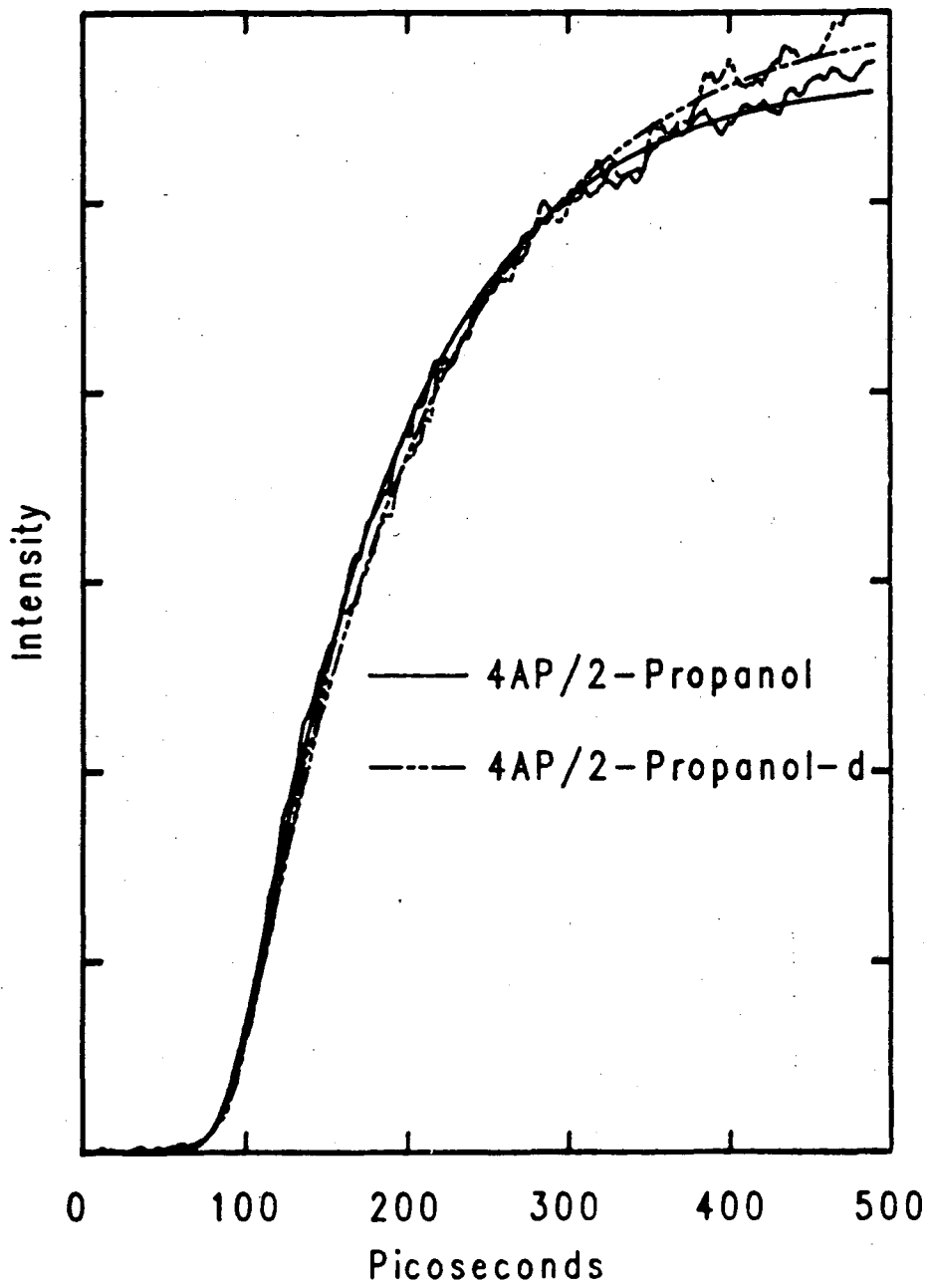
4. Solvation of a Different Solute in Linear Alcohols

The data and arguments presented so far all point to the solvation of 4AP as being a

Figure 3.27 Emission from 4AP in 2-Propanol and 2-Propanol-d—Initial Profiles of Low Energy Emission

Emission from 4AP detected at 650 nm in both ordinary and deuterated 2-propanol are shown. The effect of isotopic substitution is obvious. The emission in 2-propanol shows a slower growth rate than the emission from 4AP in ordinary 2-propanol. The rise times for these datasets are: 2-propanol-d, 127 ps; 2-propanol, 107 ps.

Figure 3.27



solvent-dependent phenomenon. If the solvation times really are solvent-dependent, then the solvation times should be invariant for changes in solute. There would naturally be limitations to this expected invariance because the solute would have to resemble 4AP in some important ways. For instance, the new solute would also have to be of the “giant-dipole” class, and most likely would have to have aromatic carbonyl groups so that the physics of interaction of the solvent with the excited solute would be similar. In addition, the molecule cannot undergo photochemical changes like 1-naphthol or DMABN. Such a molecule exists; the structural isomer of 4AP, 3-aminophthalimide (3AP) [63], is very similar to 4AP. The structure is included in Figure 3.3 with the structure for 4AP to allow straightforward comparison.

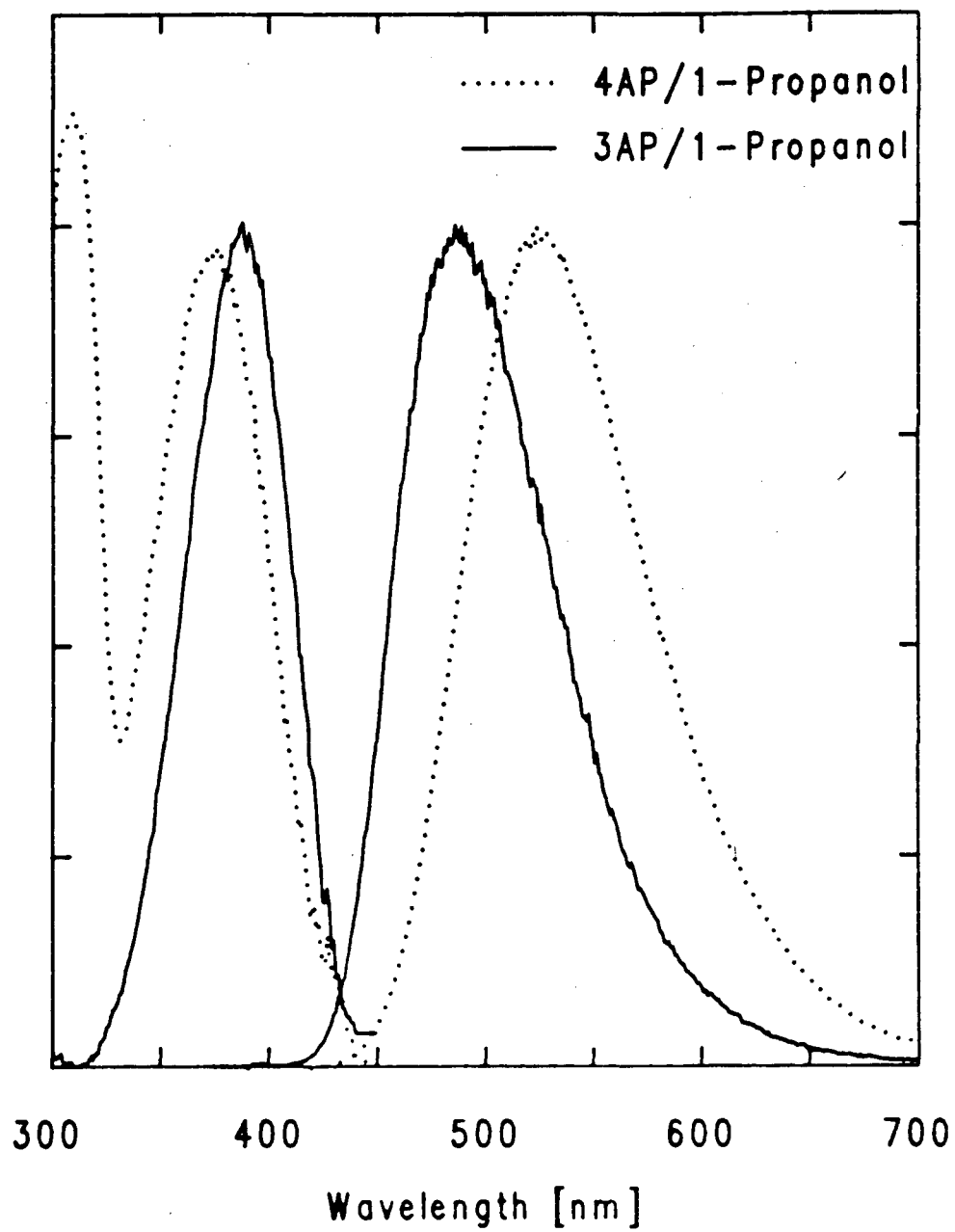
As with 4AP, the emission from 3AP is considerably Stokes'-shifted in polar solvents. However, for the same solvent, the magnitude of the Stokes' shift of 3AP is smaller than the shift exhibited by 4AP. In Figure 3.28, the emission and absorption spectra of 3AP in 1-propanol are presented with the spectra of 4AP in 1-propanol. Not only is the emission of 3AP in 1-propanol of higher energy than the emission from 4AP, the absorption of 3AP peaks at a lower energy. The Stokes' shift for 4AP in 1-propanol is $7700 \pm 100 \text{ cm}^{-1}$, while the shift for 3AP in the same solvent is only $5500 \pm 100 \text{ cm}^{-1}$. The difference between the two molecules can be justified by comparing the structures. The NH_2 -group on 3AP can interact with one of the carbonyls, shielding it from interaction with the solvent. The amino group on 4AP can have no such shielding interaction, and therefore more interaction with the solvent.

The Stokes' shift of 3AP in 1-propanol can indeed be time-resolved, even though the magnitude of the shift is so much smaller. Figure 3.29 shows the initial profile of emission from 3AP in 1-propanol detected at 650 nm. The data for 4AP at 650 nm are shown in the figure for comparison. The emission rise time is somewhat faster for the 3AP solution than for the 4AP solution, 70 ps for 3AP and 87 ps for 4AP. The

Figure 3.28 Steady-state Emission and Absorption Spectra for 3AP in 1-Propanol and 4AP in 1-Propanol

Emission and absorption spectra for solutions of 3AP in 1-propanol and 4AP in 1-propanol show that the magnitude of the Stokes' shift is considerably smaller for the case of 3AP. Not only is the absorption spectrum of 3AP in 1-propanol red-shifted relative to that of 4AP, but the emission spectrum of 3AP is also blue-shifted relative to that of 4AP.

Figure 3.28



solvation is clearly occurring faster with 3AP as the solute than with 4AP, although the time scales of the solvation are similar. After a complete spectral analysis, the solvation times of 3AP can be determined. Solvation times are listed with the temporal parameters in Table 3.9. The solvation of 3AP is on a faster time scale than for 4AP, although still within the uncertainty associated with the dielectric relaxation times for the alcohols. It is clearly the case that dielectric relaxation is important in determining the dynamics of solvation for both of the aminophthalimides. The differences that are detected between the dynamics of the relaxation of 4AP and 3AP are small enough that the importance of dielectric relaxation to the mechanism of excited-state solvation cannot be questioned.

However, the argument that was presented for 4AP indicated that the quality of the correlation between the dielectric relaxation times and the solvation times was because the two processes had the same solvent-dependent rate-limiting step. Even though the solvation times for both solutes agree with the measured dielectric relaxation times within the uncertainty of that measurement, in addition, the solvation times should agree with one another if the dynamics are really controlled by only a solvent-dependent property. That is, whatever the difference between the measurement of the solvation time of 4AP and the relaxation time for that solvent, that difference should remain constant for 3AP. The difference in solvation times for 3AP and 4AP indicates that something about the process must be solute dependent.

Evidence from a smaller isotope effect in 3AP than for 4AP indicates that the physics of the interaction of an alcohol with electronically excited 3AP molecule differ from those of the interaction of an alcohol with excited 4AP. While the quantum yield of 4AP in methanol-d increased by almost a factor of three relative to the quantum yield in ordinary methanol, the effect is considerably smaller for 3AP. The relative quantum yield for 3AP in deuterated methanol was only 33 percent enhanced relative to the yield for 3AP in methanol. The small change in the non-radiative rates for 3AP on deuteration indicates

Figure 3.29 Time-Resolved Emission from 3AP and 4AP in 1-Propanol—Initial Profiles

The first 300 ps of emission detected at 650 nm for both 4AP in 1-propanol and 3AP in 1-propanol are shown. Both emission spectra show slow growth rates. The smooth curves are computer-generated fits to the data. The rise times from the computer fits are: 3AP, 57ps; 4AP, 87 ps.

Figure 3.29

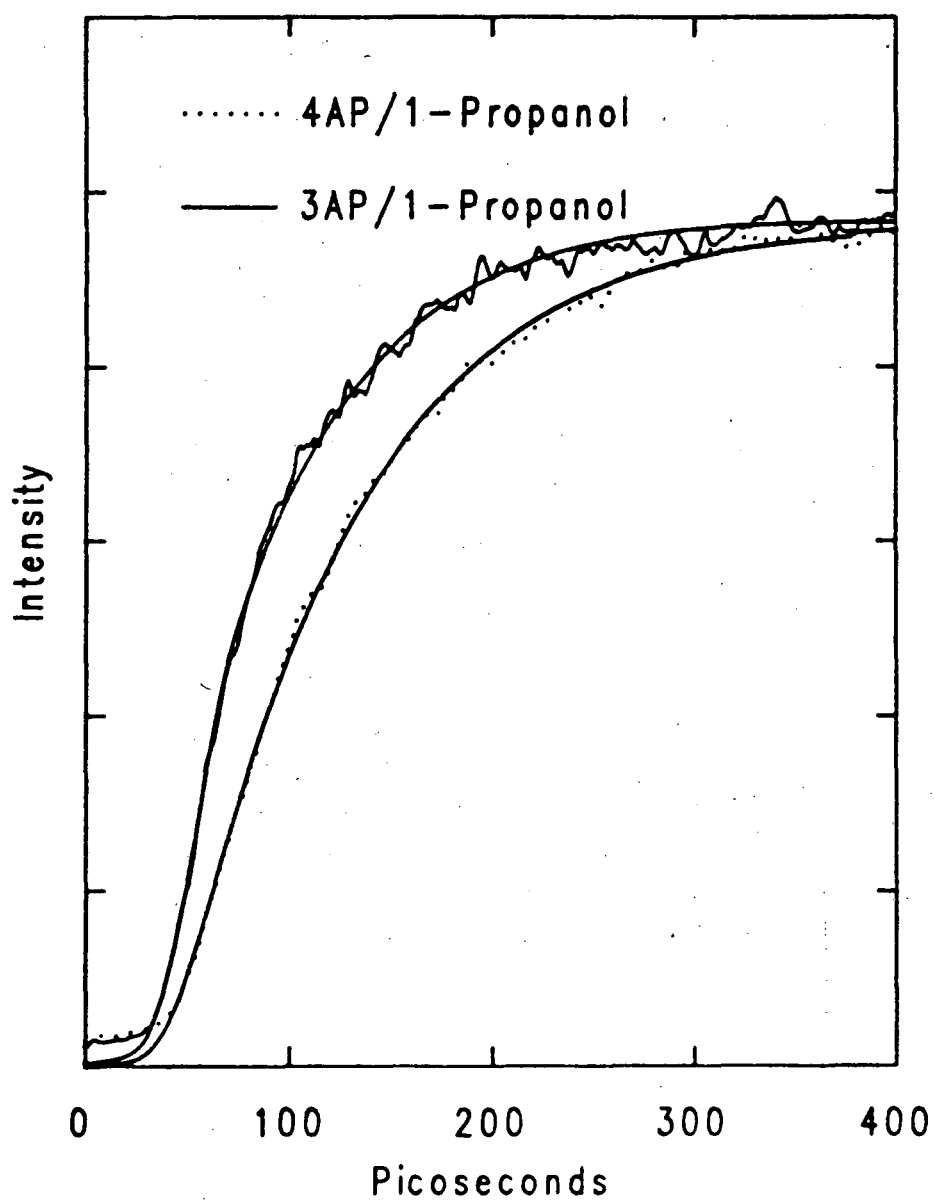


Table 3.9

Solvation times for 3AP and 4AP in 1-propanol, 1-butanol, and 1-pentanol as calculated from the slopes of the semi-logarithmic plots of peak position as a function of time.

Solvent	4AP τ_s , in ps	3AP τ_s , in ps
1-Propanol	69 ± 10	55 ± 10
1-Butanol	111 ± 25	106 ± 20
1-Pentanol	191 ± 50	162 ± 25

that the extent of hydrogen bond formation is not changed as significantly between the ground and excited state of 3AP as it was for 4AP. The differences in the details of the solvation process are reflected in the differences measured for the dynamics.

G. Studies of the Rotational Diffusion of 4AP

A second type of time-resolved emission measurement can add some detail to the results presented so far. The diffusional motion of a solute molecule can generally be monitored in a straightforward way by performing time-resolved polarization measurements. From the measurements of solvation dynamics, the reddest emission is from the most solvated solute molecules, while the bluest emission is from the Franck-Condon excited-state. Taking polarization measurements at an array of detection wavelengths will allow any differences in diffusion rates with degree of solvation to be determined.

Only the most basic reasons that time-resolved polarization measurements give information on solute motion are described here because other works contain far more explicit information [65,66]. The laser pulse used to excite the sample is linearly polarized. A solute molecule with its absorption dipole moment parallel to the polarization of the laser pulse is preferentially excited, resulting in an anisotropic distribution of excited molecules. The emission dipole within each excited molecule is geometrically related to the absorption dipole, so that the distribution of emission dipoles reflects the anisotropic distribution of initially excited molecules. The resulting emission generally has polarization anisotropy. As the excited molecules undergo random orientational diffusion, the anisotropy decreases and therefore the emission polarization decreases. The rate of decay of the degree of polarization anisotropy as a function of time is directly related to the rate of rotational diffusion.

The excitation beam is vertically polarized relative to the plane defined by the excitation and detection axes. (See Figure 2.2.) The temporal profile of emission that is

polarized parallel to the excitation beam, $I_{\parallel}(t)$, is measured in one streak camera experiment. In an independent experiment, the emission polarized perpendicularly (in the plane of the excitation and detection axes) is time-resolved, yielding $I_{\perp}(t)$. The two datasets are scaled so that the intensities match at long times, in a process that is referred to as tail-matching [66]. The temporal profile of the anisotropy is calculated from the scaled datasets by the following formula:

$$r(t) = \frac{I_{\parallel}(t) - I_{\perp}(t)}{I_{\parallel}(t) + 2I_{\perp}(t)} \quad (3.17)$$

In practice, the decay of $r(t)$ is exponential, and the time constant of the decay related to the rate of orientational diffusion. The analysis of time-resolved anisotropy consists of determining the slope of the semi-logarithmic plot of the anisotropy as a function of time.

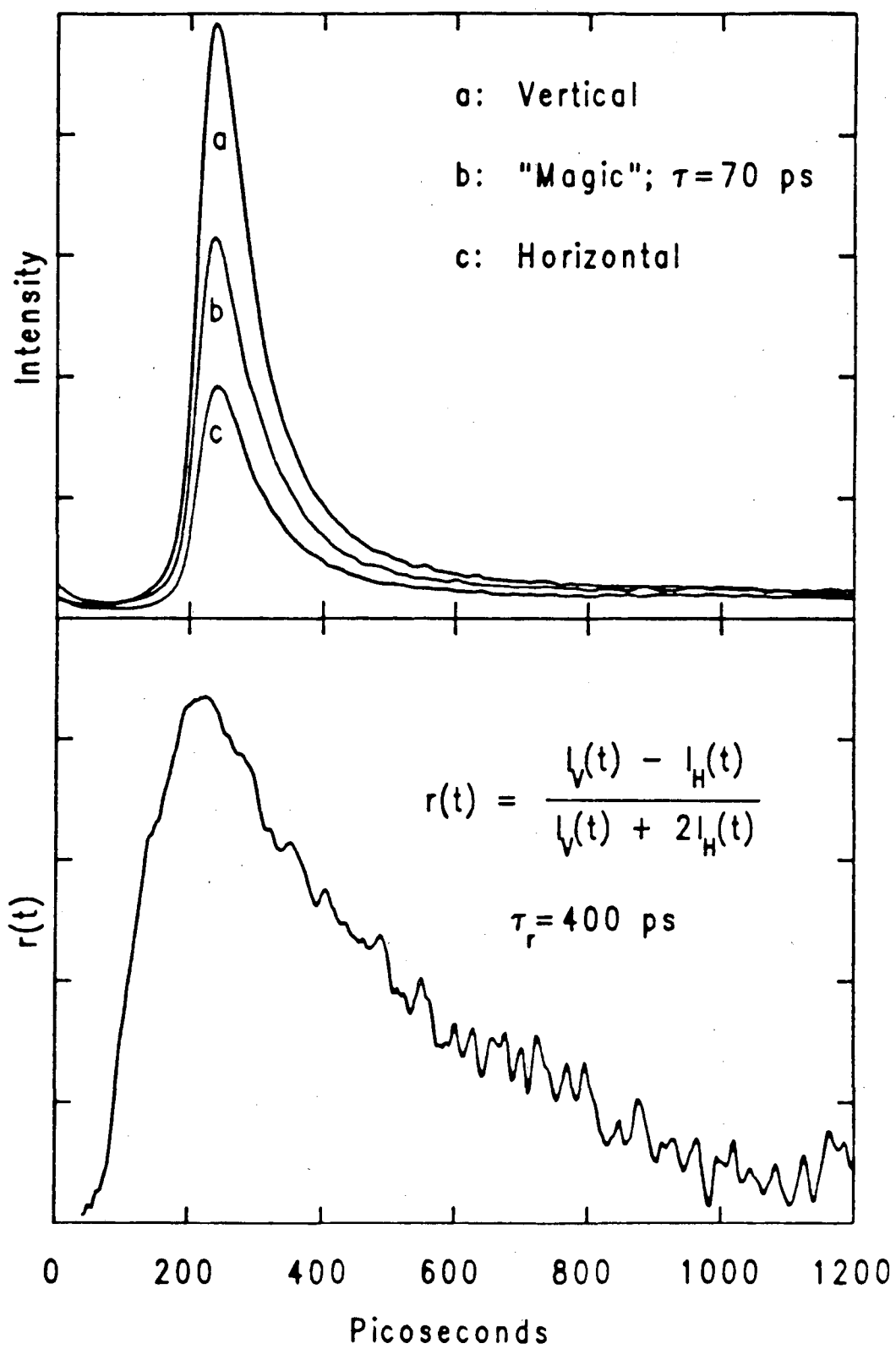
The type of data obtained for 4AP is presented in Figure 3.30 for 4AP in 1-butanol detected at 450 nm. In the top panel of that figure, the tail-matched streak camera data for both the vertical and horizontal polarizations are presented. The third dataset, labelled “magic” is emission polarized at 54.7° from the vertical. 54.7° from the vertical is magical because detection at that angle balances the contribution of parallel and perpendicular polarizations so as to be insensitive to dipole reorientation. The lower panel of Figure 3.30 shows the anisotropy function calculated according to equation (3.17). The time constant of the decay of the anisotropy is 400 ps. The fast component of decay of the magic dataset (in the top panel) is due to the loss of high energy emission because of solvation, and has a time constant of 70 ps. The solvation is clearly extremely rapid on the time scale of solute reorientation.

When the decay of polarization anisotropy is measured at individual wavelengths spanning the emission band of 4AP, there is no detectable wavelength dependence (Table 3.10). Red emission from solvated excited solute molecules depolarizes at the same rate as blue emission from incompletely solvated excited solute molecules. This wave-

Figure 3.30 Time-Resolved Fluorescence Polarization Anisotropy for 4AP in 1-Butanol

Time-resolved emission from 4AP in 1-butanol detected at 450 nm is shown. The detection is through prism polarizers that select emission polarized parallel (vertically) to the excitation beam or perpendicular (horizontal) to the excitation beam. Also shown is emission polarized at 54.7° from the vertical (magic angle). The three profiles in the upper portion of the figure were tail-matched between 1.2 and 1.5 ns (see text). The difference between the emission vertically and horizontally polarized decreases on a time scale much longer than the decay evident in the magic angle profile. The lower panel of the figure is a plot of that difference, the anisotropy, $r(t)$. The time scale of the decay of the anisotropy is 400 ps, while the magic angle profile has a fast time scale decay of 70 ps.

Figure 3.30



length independence means that the orientational diffusion rate is independent of the extent of solvation. The orientational diffusion constant is proportional to the volume of the particle that is diffusing, according to the Debye-Stokes-Einstein (DSE) hydrodynamic theory [44]. The invariance of the rotational diffusion time indicates that the volume of the solute is not a function of the extent of solvation.

Not only does the reorientation time depend on the volume of the diffusing particle, the reorientation time of a compound is proportional to the macroscopic viscosity of the solution, according to DSE theory. In a series of linear alcohols, simple chromophores have been shown to follow the predictions of this hydrodynamic theory [67]. Data for 4AP reorientation times for the series of linear alcohols are plotted in Figure 3.31, and the agreement with the DSE prediction is quite good. The data from that figure, with the data for the rotational diffusion times in deuterated solvents, are given in Table 3.11. Particularly interesting is the agreement of the time constants for the deuterated solvents, which differ very little from their undeuterated counterparts. Unlike the solvation process, the reorientation is strongly correlated with the macroscopic viscosity, and so independent of isotopy.

H. Conclusions

The development of a streak camera system with optimized data collection rates has made possible new studies of excited-state solvation dynamics. The streak camera system has enough sensitivity and runs at a high enough repetition rate to allow narrow bands of emission to be time-resolved with 20 ps resolution. Without undue operator fatigue, bands throughout the emission spectrum of a solute can be time-resolved, and so the temporal profile of the entire luminescence determined. Such measurements allow the recovery of the emission profile at discrete times, and therefore allow the temporal resolution of emission Stokes' shifts.

Table 3.10

Rotational reorientation times for 4AP in 2-propanol and 1-butanol as a function of detection wavelength. Time constants are given in picoseconds.

Wavelength (nm)	τ_r , in ps	
	2-Propanol	1-Butanol
400	320	
410	310	
420	338	410
430	343	423
440	335	404
450	344	427
460	324	438
470	300	400
480	330	424
490		420
500	307	411
520		421
530		410
550	312	420
600	339	405
650	316	390
700	341	400
Average τ_r :	326 ± 15	414 ± 13

Figure 3.31 Rotational Reorientation Times for 4AP in a Series of Linear Alcohols as a Function of Viscosity

Figure 3.31

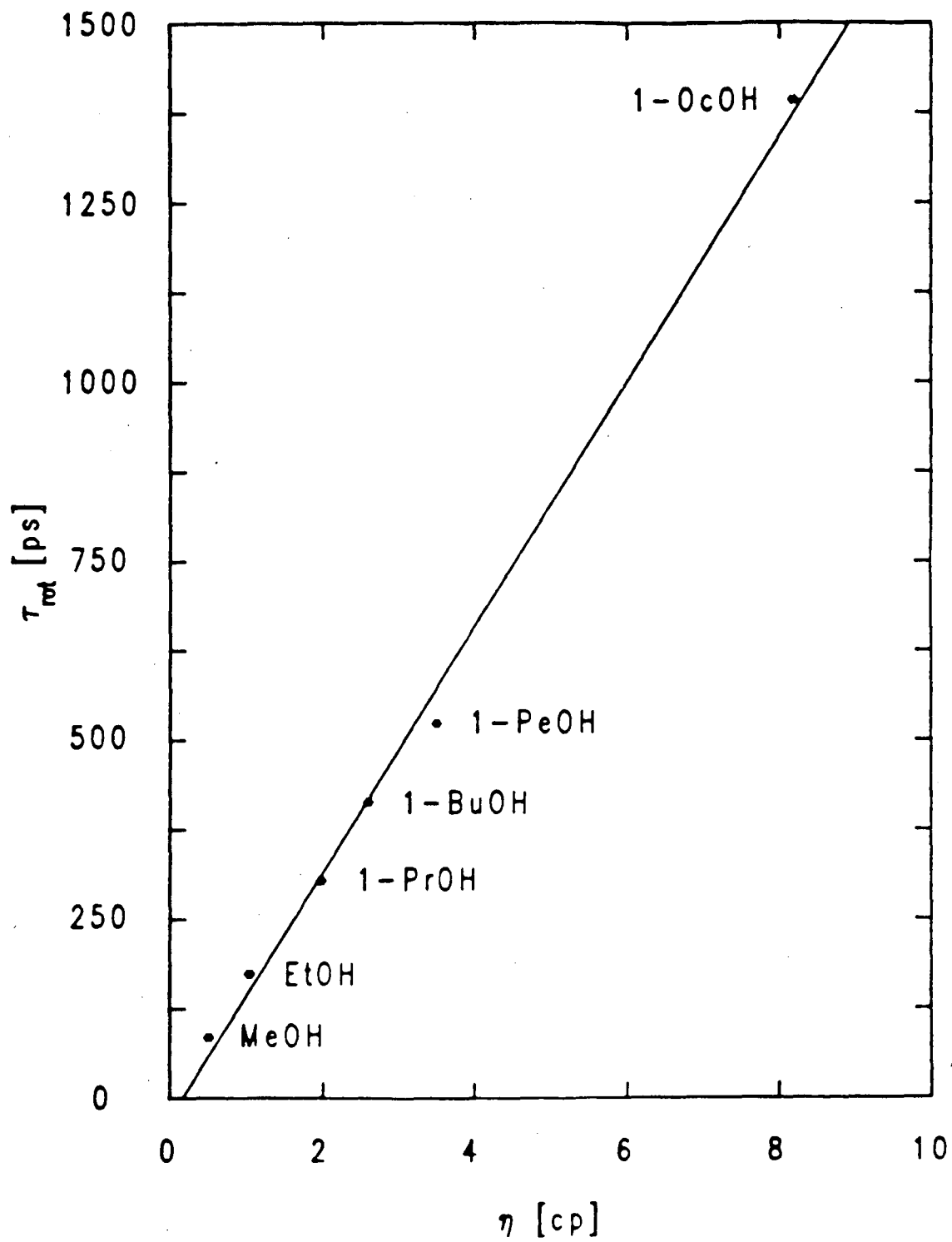


Table 3.11

Rotational reorientation times for 4AP in alcohols, listed with the macroscopic viscosities. All measurements were taken at $20 \pm 3^\circ\text{C}$.

Solvent	Rotational Reorientation Time τ_r , in ps	Viscosity η , in cP
Methanol	81 ± 6	0.53
Methanol-d	83 ± 8	0.54
Ethanol	160 ± 12	1.06
Ethanol-d	162 ± 16	1.09
1-Propanol	301 ± 31	2.00
2-Propanol	326 ± 15	2.26
2-Propanol-d	347 ± 25	2.32
1-Butanol	414 ± 13	2.62
1-Pentanol	520 ± 10	3.53
1-Octanol	1390 ± 90	8.2

Resolving temporal profiles of narrow bands of emission from 4AP with 20 ps resolution has allowed the Stokes' shift of that chromophore to be time-resolved, even in room temperature solvents. The details of the excited-state solvation dynamics of 4AP have been elucidated through systematic study of such time-resolved shifts. The dynamics of the Stokes' shift are such that the position of the emission maximum moves toward a final position in an approximately exponential fashion. The time constant of the relaxation is what we determine for solvents under a variety of experimental conditions, and what we call the solvation time. Our systematic study of the solvation time shows that it is well correlated with the dielectric relaxation time of the solvent, not only for the alcohols, but for many solvents of widely varying properties. The correlation survives tests of isotopic substitution and temperature variation. The solvation of the structural isomer of 4AP, 3AP, has a time constant that is close to the time constant of the relaxation of 4AP. The solvation time of 3AP agrees with the dielectric relaxation rate within the error associated with the dielectric measurement. Our conclusion based on these studies is that the rate of solvation is limited by the same molecular process that limits the rate of dielectric relaxation.

I. Future Directions

The experiments that are described here give a unified view that the molecular mechanisms that control the rate of solvation are intimately connected to the molecular mechanisms that control the solvent's dielectric relaxation rate. Picosecond time-resolved emission measurements allow the determination of the dynamics of Stokes' shifts. Further experiments that exploit this measurement technique will undoubtedly enhance the present understanding of the details of short time scale solvent-solute interactions.

There are a number of possible lines of investigation that are worth pursuing. Experiments aimed at determining which solute properties contribute to the generation of

time-dependent Stokes' shifts might give more detailed information about the molecular motions of the solvent responsible for the spectral dynamics. An interesting test of the importance of dielectric relaxation prediction would be to measure the spectral relaxation times in mixed solvent environments. The dielectric relaxation time of alcohols has been shown to be faster in alcoholic solvents that have a small quantity (<0.1 M) of a hydrocarbon solvent added in [68]. This experiment will serve to distinguish the contribution of dielectric relaxation and the contribution of diffusion. Experiments of these types are presently underway in our laboratory [69].

J. References for Chapter 3

1. C. Reichardt, *Solvent Effects in Organic Chemistry*, (Verlag-Chemie, Weinheim, West Germany, 1979).
2. G. W. Castellan, *Physical Chemistry*, 2nd ed. (Addison-Wesley, Reading, Massachusetts, 1971), p. 87.
3. S. F. Fischer and A. Laubereau, *Chem. Phys. Lett.* **35** (1975) 6.
4. W. G. Hoover, *Ann. Rev. Phys. Chem.* **34** (1983) 103–27.
5. J. P. Boon and S. Yip, *Molecular Hydrodynamics* (McGraw-Hill, Inc., New York, 1980), Chapter 1.
6. J. H. Hildebrand, J. M. Prausnitz, and R. L. Scott, *Regular and Related Solutions* (Van Nostrand Reinhold Co., New York, 1970), Chapter 1.
7. K. Dimroth and C. Reichardt, *Liebigs. Ann. Chem.* **727** (1969) 93.
8. Th. Förster, *Z. Elektrochem.* **45** (1939) 548; E. Lippert, *Z. Naturforsch.* **10a** (1955) 541; N. Mataga, Y. Kaifu, and M. Koizumi, *Bull. Chem. Soc. Japan* **28** (1955) 690.
9. A. Weller, *Z. Elektrochem.* **56** (1952) 662; Th. Förster, *Z. Elektrochem.* **54** (1950) 531; Th. Förster, *Naturwissenschaften* **36** (1949) 186.
10. R. S. Mulliken, *J. Am. Chem. Soc.* **72** (1950) 600; *ibid.* **74** (1952) 811.
11. S. P. Webb, S. W. Yeh, L. A. Philips, M. A. Tolbert, and J. H. Clark, in *Ultrafast Phenomena IV*, D. H. Auston and K. B. Eisenthal, eds., (Springer-Verlag, New York, 1984) 371; S. P. Webb, S. W. Yeh, L. A. Philips, M. A. Tolbert, and J. H. Clark, *J. Am. Chem. Soc.* **106** (1984) 7286; S. P. Webb, S. W. Yeh, L. A. Philips, L. M. Tolbert, and J. H. Clark, *J. Phys. Chem.*, in preparation.
12. J. F. Ireland and P. A. H. Wyatt, *Adv. Phys. Org. Chem.* **12** (1976) 131; A. J. Campillo, J. H. Clark, S. L. Shapiro, K. R. Winn, and P. K. Woodbridge, *Chem. Phys. Lett.* **67** (1979) 218.
13. C. V. Shank, E. P. Ippen, and O. Teschke, *Chem. Phys. Lett.* **45** (1977) 291.
14. A. J. Campillo and S. L. Shapiro, *IEEE J. Quant. Electr.* **19** (1983) 585.
15. The change in pK_a upon electronic excitation for 1-naphthol has been determined from the picosecond measurements of excited-state proton-transfer described in [11]; see also S. P. Webb, Ph.D. Thesis, University of California, Berkeley, 1985; Lawrence Berkeley Laboratory Report 19510.
16. W. R. Laws and L. Brand, *J. Phys. Chem.* **83** (1979) 795; C. M. Harris and B. K. Selinger, *J. Phys. Chem.* **84** (1980) 891.
17. S. L. Shapiro, K. R. Winn, and J. H. Clark, in *Picosecond Phenomena II* R. M. Hochstrasser, W. Kaiser, and C. V. Shank, eds. (Springer-Verlag, Berlin, Germany, 1980) p. 227.

18. G. J. Woolfe and P. J. Thistlethwaite, *J. Am. Chem. Soc.* **103** (1981) 6916; P. K. Sengupta and M. Kasha, *Chem. Phys. Lett.* **68** (1979) 382; A. J. G. Strandjord and P. F. Barbara, *J. Phys. Chem.* **89**, (1985) 2355; A. J. G. Strandjord, D. E. Smith, and P. F. Barbara, *ibid.* **89** (1985) 2362.
19. Z. R. Grabowski, K. Rotkiewicz, A. Siemiarczuk, D. J. Cowley and W. Bauman, *Nouv. J. Chemie* **3** (1974) 443.
20. W. S. Struve, P. M. Rentzepis, and J. Jortner, *J. Chem. Phys.* **59** (1973) 5014.
21. Y. Wang, M. McAuliffe, F. Novak, and K. B. Eisenthal, *J. Phys. Chem.* **85** (1981) 3736; Y. Wang and K. B. Eisenthal, *J. Chem. Phys.* **77** (1982) 6076; D. Huppert, S. D. Rand, P. M. Rentzepis, P. F. Barbara, W. S. Struve, and Z. R. Grabowski, *J. Phys. Chem.* **75** (1981) 5714.
22. J. Hicks, M. Vandersall, Z. Babarogic, and K. B. Eisenthal, *Chem. Phys. Lett.* **116** (1985) 18.
23. Discussed in S. P. Webb, Ph.D. thesis, University of California, Berkeley, 1985; Lawrence Berkeley Laboratory Report 19510.
24. 4-Aminophthalimide is the trivial name for the compound. Official nomenclature is: 5-amino-1H-isoindole-1,3(2H)-dione.
25. A. N. Perov, *Opt. Spectrosc.* **38** (1975) 597.
26. W. R. Ware, P. Chow, and S. K. Lee, *Chem. Phys. Lett.* **2** (1968) 356; W. R. Ware, S. K. Lee, G. J. Brant and P. Chow, *J. Chem. Phys.* **54** (1971) 4729.
27. S. W. Yeh, L. A. Philips, S. P. Webb, L. F. Buhse, and J. H. Clark, in *Ultrafast Phenomena IV*, D. H. Auston and K. B. Eisenthal, eds. (Springer-Verlag, New York, 1984) 359.
28. W. R. Ware, in *Creation and Detection of the Excited State*, A. Lamola, ed. (Marcel-Dekker, New York, 1971) 213; R. G. Bennett, *Rev. Sci. Instrum.* **31**, (1960) 1275.
29. We have time-resolved bands throughout the emission spectrum of DMABN in a number of solvents, repeating with greater thoroughness the results reported in references 20–22, and 27. There is good agreement between the fall times measured for the blue edge of the decay and the rise times determined for the red edge of the emission profile. While there are some unsolved questions about emission profiles in the intermediate spectral region (between the red and blue edges), the rate of growth of low energy signal is the same as the rate of decay of the high energy signal.
30. The Stokes' shift is measured from peak of the lowest energy absorption feature to the peak of the emission spectrum.
31. Calculations related to the sensitivity of the streak camera system to short time scale decay components are given in L. A. Philips, W. T. Brown, S. P. Webb, S. W. Yeh, and J. H. Clark, in *Ultrafast Phenomena IV*, D. H. Auston and K. B. Eisenthal, eds. (Springer-Verlag, New York, 1984) 477; see also L. A. Philips, Ph.D. Thesis, University of California, Berkeley, 1985; Lawrence Berkeley Laboratory, Report LBL-19511.

32. All viscosities reported in this thesis were measured on a temperature-controlled viscometer, (Wells-Brookfield Cone/Plate Digital Viscometer) unless otherwise specified.
33. G. C. Pimentel and A. L. McClellan, *The Hydrogen Bond* (W. H. Freeman and Company, San Francisco, 1960), pp. 194–197.
34. *CRC Handbook of Chemistry and Physics*, 62nd Edition, Robert C. Weast, ed. (CRC Press, Boca Raton, Florida, 1981), p. E-61.
35. International Critical Tables, for dielectric constants.
36. Wavelengths of absorption and emission maxima for 4AP in assorted solvents:

Solvent	λ_{max}^A nm	λ_{max}^F nm	Stokes' Shift cm^{-1}
CCl_4	344	411	2400
Toluene	350	431	5400
Dioxane	354	445	5800
DMSO	373	481	6000
Acetone	358	457	6100
Acetonitrile	360	475	6700
2-Propanol	375	519	7400
1-Butanol	372	521	7700
1-Propanol	370	524	7700
Methanol	370	532	8200

37. S. L. Shapiro and K. R. Winn, *Chem. Phys. Lett.* **71** (1980) 440; A. J. Campillo, J. H. Clark, S. L. Shapiro, K. R. Winn and P. K. Woodbridge, *Chem. Phys. Lett.* **67** (1979) 218.
38. T. H. Lowry and K. S. Richardson, *Mechanism and Theory in Organic Chemistry* (Harper and Row, New York, 1976).
39. L. F. Buhse, unpublished result obtained by using the MNDO calculation program; M. J. S. Dewar and W. Thiel, *J. Am. Chem. Soc.* **99** (1977) 4899; Program from Quantum Chemistry Program Exchange, Indiana University, QCPE No. 455.
40. W. J. Chase and J. W. Hunt, *J. Phys. Chem.* **79** (1975) 2835.
41. E. M. Kosower, *J. Am. Chem. Soc.* **107** (1985) 1114; E. M. Kosower, and D. Huppert, *Chem. Phys. Lett.* **96** (1983) 433; D. Huppert, H. Kanety, and E. M. Kosower, *Discuss. Faraday Soc.* **74** (1982) 161.
42. A. Mozumder, *J. Chem. Phys.* **50** (1969) 3153; R. Schiller, *J. Chem. Phys.* **43** (1965) 2760; *ibid.* **47** (1967) 2278; J. Hubbard and L. Onsager, *J. Chem. Phys.* **67** (1977) 4850; J. Hubbard, *J. Chem. Phys.* **68** (1978) 1649.
43. S. K. Garg and C. P. Smyth, *J. Phys. Chem.* **69** (1965) 1294.

44. P. Debye, *Polar Molecules* (Dover, New York, 1928); K. S. Cole and R. H. Cole, *J. Chem. Phys.* **9** (1941) 341.
45. H. Fröhlich, *Theory of Dielectrics* (Oxford University Press, Oxford, England, 1958), 2nd ed.
46. An enlightening conversation about this point with K. B. Eisenthal during his sabbatical at UC Berkeley is gratefully acknowledged.
47. C. Brot and M. Magat, *J. Chem. Phys.* **39** (1963) 841; G. E. McDuffie and T. A. Litovitz, *J. Chem. Phys.* **39** (1963) 729.
48. W. Dannhauser, *J. Chem. Phys.* **48** (1968) 1918; P. Bordewijk, F. Gransch, and C. J. F. Böttcher, *J. Phys. Chem.* **73** (1969) 3255.
49. C. P. Smyth, *Dielectric Behavior and Structure* (McGraw-Hill Book Co., New York, 1955) Chapter IV.
50. M. Evans, *J. Mol. Liq.* **25** (1983) 149.
51. The emission of 4AP in methanol gave barely detectable dynamic shifts. The longest time constant of red-edge emission growth was ≈ 25 ps, too fast to measure reliably.
52. S. J. Bass, W. I. Nathan, R. M. Meighan, and R. H. Cole, *J. Phys. Chem.* **68** (1964) 509.
53. L. F. Buhse, unpublished result.
54. For instance, R. Chihane and T. K. Bose, *J. Chem. Phys.* **65** (1976) 2211; T. Koshii, H. Takahashi, and K. Higasi, *Bull. Chem. Soc. Japan* **48** (1975) 993.
55. D. W. Davidson, *Can. J. Chem.* **35** (1957) 458.
56. D. W. Davidson and J. Wheeler, *J. Chem. Phys.* **36** (1959) 1357.
57. The change in the dielectric relaxation time for deuterated 1-octanol relative to the ordinary alcohol is referred to in [54] as being from the following report: M. Corval and L. Reinisch, *Compt. rend.* **234** (1952) 724; and also as being a private communication from M. Magat.
58. This measurement is discussed in the literature: Th. Förster and K. Rokos, *Z. für Phys. Chemie N. F.* **63** (1969) 208.
59. Examples are found in the following articles: K. G. Spears and K. M. Steinmetz, *J. Phys. Chem.* **89** (1985) 3623; M. J. Mirbach, M. F. Mirbach, W. R. Cherry, N. J. Turro, and P. Engel, *Chem. Phys. Lett.* **53** (1978) 266; E. Gudgin, R. Lopez-Delgado, and W. R. Ware, *J. Phys. Chem.* **87** (1983) 1559.
60. Y. Wang, *J. Phys. Chem.* **89** (1985) 3799.
61. S. Okajima and E. C. Lim, *Chem. Phys. Lett.* **70** (1980) 283; K. F. Freed, in *Topics in Applied Physics*, vol. **15**, F. K. Fong, ed., (Springer-Verlag, West Berlin, 1970) 23.

62. I. B. Rabinovich, *The Influence of Isotopy on the Physicochemical Properties of Liquids* (Consultants Bureau, New York, 1970).
63. 3-Aminophthalimide is the trivial name for the compound. Official nomenclature is: 4-amino-1H-isoindole-1,3(2H)-dione.
64. T. Okamura, M. Sumitani, and K. Yoshihara, *Chem. Phys. Lett.* **94** (1983) 339.
65. T. Tao, *Biopolymers* **8** (1969) 609.
66. G. R. Fleming, J. M. Morris, and G. W. Robinson, *Chem. Phys.* **17** (1976) 91.
67. T. J. Chuang and K. B. Eisenthal, *Chem. Phys. Lett.* **11** (1971) 368; D. H. Waldeck and G. R. Fleming, *J. Phys. Chem.* **85** (1981) 2614; L. A. Philips, S. P. Webb, S. W. Yeh, and J. H. Clark, *J. Phys. Chem.* **89** (1985) 17.
68. C. Campbell, J. Crossley, and L. Glasser, *Adv. in Mol. Relax. Proc.* **9** (1976) 63; T. Koshii, E. Arie, M. Nakamura, H. Takahashi, and K. Higasi, *Bull. Chem. Soc. Japan* **47** (1974) 618; R. Minami, K. Itoh, H. Sato, H. Takahashi, and K. Higasi, *Bull. Chem. Soc. Japan* **54** (1981) 1320; J. Crossley and S. C. Srivastava, *Adv. in Mol. Relax. Proc.* **8** (1976) 111.
69. L. F. Buhse, Ph.D. thesis, University of California, Berkeley, 1986.

Chapter 4

II. Kinetics of Energy Flow in a Photosynthetic Antenna System

A. Introduction

Optical spectroscopic investigations have been used to study a vast array of biologically important systems [1], including the dynamics of hemoglobin oxygenation and deoxygenation [2], the structure [3] and the mobility [4] of proteins, and the flexibility and structure of DNA [5]. Two biological processes particularly amenable to optical spectroscopic study are those that naturally include visible photons—vision [6] and photosynthesis [7]. The latter, the process whereby plants, algae and photosynthetic bacteria convert light energy into chemical energy, is related to the work discussed here. Described in the pages that follow are the time-resolved experiments that have been recently performed [8,9] to study the dynamics of energy transfer within a subsystem of a natural photosynthetic apparatus.

B. Photosynthetic Antenna Systems

Plants, algae, and some bacteria use photosynthesis to supply themselves with chemical energy. The conversion of light energy to chemical energy occurs in reaction centers, which consist in part of particular membrane-bound chlorophyll (or bacteriochlorophyll) molecules. Complexes associated with the reaction center cause electronic excitation of the (bacterio)chlorophyll to induce a charge separation. The resulting electrochemical potential drives the synthetic portions of the photosynthetic operation. Although much is known about the details of these processes, this general description is sufficient for the present discussion. Of concern here will only be details of the pathway of energy flow before it arrives at the reaction center.

The photosynthetic reaction centers of all plants and algae are surrounded by chromophores called antenna pigments [10–15]. These antenna chromophores absorb light

energy and transfer it efficiently to the reaction center. Such antenna systems are postulated to have evolved for reasons of economy. The organism with antenna chromophores needs to produce fewer copies of the specialized complexes of the reaction center because more efficient use of each reaction center is made. The chromophores surrounding the reaction center increase the absorption cross section of the reaction center in linear proportion to their number. Therefore, the effective rate of light absorption by the reaction center is increased, and the rate of the light-driven reactions of photosynthesis increases. Reaction centers with antennae are in effect illuminated more brightly at the same incident intensity than are isolated reaction centers. A general feature of antenna systems is that almost every photon absorbed in the antenna results in excitation within the reaction center [13]. This near unit quantum efficiency and the resulting potential practical applicability of synthetic homologs in solar energy conversion schemes [16] has made antenna systems the subject of much study.

The antenna chromophores of most plants and algae are located within the photosynthetic membrane with the reaction center [17]. In such organisms, intact antennae cannot be easily isolated from the photosynthetic membranes, and so information on their molecular structure is limited [11]. In turn, the structural basis for their highly efficient energy transfer cannot be determined. Fortunately, not all antenna systems are membrane-bound. In red algae and cyanobacteria, light is harvested by phycobilisomes, peripheral membrane complexes that can be isolated from the photosynthetic membranes without loss of structural or functional properties. Many structural studies have been performed on phycobilisomes [12], and the structural basis for the energy transfer function of phycobilisomes is well understood. The studies of energy transfer dynamics presented here were performed on phycobilisomes and make use of the wealth of structural data available for these antenna structures.

C. Phycobilisomes and Phycobiliproteins

1. Morphology

Phycobilisomes from different organisms differ structurally, although there are unifying characteristics. The molecular weights of these antenna complexes range from 7×10^6 to 15×10^6 Daltons. All phycobilisomes are composed of phycobiliproteins, a family of intensely colored polypeptides that carry covalently bound open-chain tetrapyrrole prosthetic groups as chromophores. Phycobilisomes contain between 300 and 800 tetrapyrrole chromophores, and absorb light over much of the visible spectrum. All phycobilisomes have two structural domains, a core that is the site of attachment of the phycobilisome to the photosynthetic membrane, and rods that are attached to and emanate radially from the core.

The structures of the phycobilisomes from the cyanobacterium *Synechocystis* 6701 (WT6701) [18] and from the mutant strains CM25 [19] and UV16 [20] are shown diagrammatically in Figure 4.1. The core substructures are identical for all three particles. The structures of the WT6701 and CM25 phycobilisomes differ only in that the C-phycoerythrin (C-PE) complexes that form the periphery of the rod substructures in WT6701 are missing in the mutant.

Close examination of the rods of WT6701 (Figure 4.1A, [21]) shows that the rods are cylindrical structures composed of double disks. Each double disk is a single phycobiliprotein complex that contains six copies each of two phycobiliprotein subunits and a single polypeptide named for its linker function. The "linker" function is two-fold. First, these polypeptides function to stabilize the individual phycobiliprotein complexes in hexameric double disks, or in trimeric single disks. The second function of a linker polypeptide is in the specification of the assembly of the phycobiliprotein complexes into phycobilisomes. In addition, the linker polypeptides of certain phycobiliprotein com-

Figure 4.1 Schematic Diagram of Phycobilisome Structure

Schematic diagram of the structure of the wild-type phycobilisome from *Synechocystis* 6701 (A), and of the phycobilisomes from the mutant strains CM25 (B) and UV16 (C). The number and type of bilin chromophores in each domain of the structure is given in parentheses, using the abbreviations PEB, phycoerythrobilin, and PCB, phycocyanobilin. The constituent protein subunits of the domains are listed using the following abbreviations: α^{PE} and β^{PE} , α and β subunits of phycoerythrin complexes; α^{PC} and β^{PC} , α and β subunits of phycocyanin complexes; AP, allophycocyanin; α^{APB} , α subunit of APB; L denotes a linker polypeptide, the subscript its location (R, rod; RC, rod-core junction; C, core; CM, core-membrane junction), the superscript its molecular weight in kDaltons. Figure 1D is a detailed diagram of the core substructure, identical for all three particles.

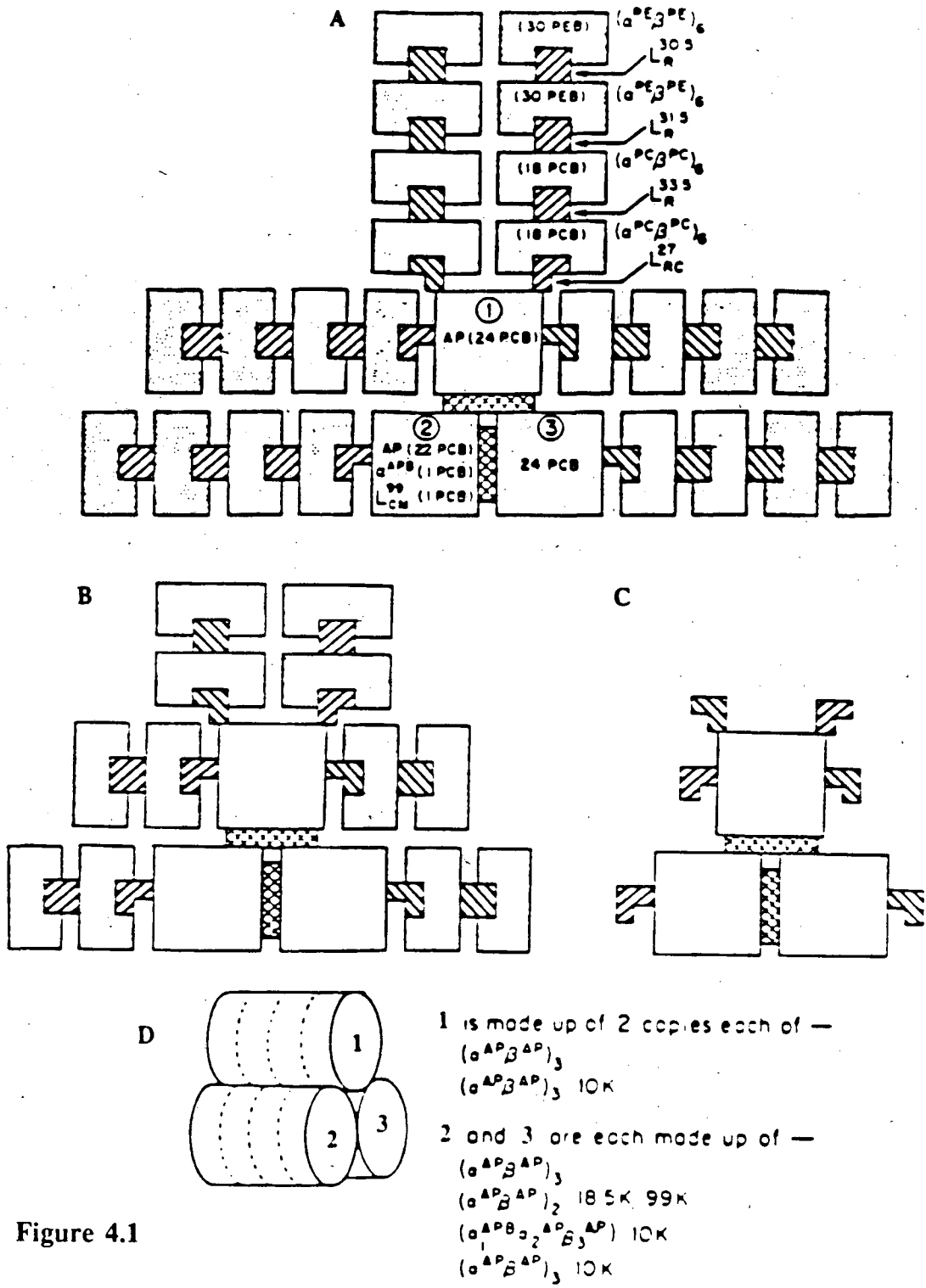


Figure 4.1

plexes contribute to light harvesting because they carry chromophores. Recent crystallographic work on a phycocyanin complex [22] has led to a suggestion of another role of the linker polypeptide. The proximity of the linker polypeptide to the positions of some phycobiliprotein chromophores could cause substantial perturbation to the electronic energy levels of the chromophores [23,24]. The energy level perturbations are postulated to enhance the behavior of those certain chromophores as energy traps [22]. The rods of WT6701 are made up of two types of phycobiliprotein complexes, C-phycoerythrin (C-PE, an average of 1.6 disks per rod) and C-phycocyanin (C-PC, two disks per rod).

The cores of all phycobilisomes, including the three studied here, are composed of allophycocyanin complexes. The WT6701 family of phycobilisomes has cores which contain two copies each of two types of polypeptides carrying chromophores that function as terminal energy acceptors in the phycobilisome. As detailed in Figure 4.1D, these are the allophycocyanin B (APB) complex, and the complex containing the 99 kDalton linker polypeptide, L_{CM}^{99} [18,19].

2. Spectroscopy

The phycobiliprotein complexes that are the building blocks of phycobilisomes are in themselves complicated structures. The hexameric double disks from the rods of some marine algae can contain as many as 34 bilin chromophores [14]. Some phycobiliproteins contain sets of chromophores with distinct absorption and emission characteristics. For instance, the phycobiliprotein R-phycoerythrin (R-PE) from the marine algae *Gastrocionium coulteri* contains 34 bilins of two types, phycourobilin and phycoerythrobilin. The absorption spectrum (Figure 4.2) shows three features—the bluest (496 nm) corresponding to the phycourobilin chromophores, and the two redder features to phycoerythrobilins in two different protein environments. Steady-state polarization data have been interpreted to show that only the reddest of the absorption features corresponds to

chromophores that emit directly [25]. These reddest-absorbing chromophores are called fluorescing, or f-type, chromophores. The chromophores that account for the higher energy absorption features do not directly fluoresce, but do act to sensitize fluorescence, and are therefore called sensitizing, or s-type, chromophores. Emission comes from the f-type chromophores regardless of excitation wavelength. When the excitation is originally localized in a s-type chromophore, energy transfer is believed to precede fluorescence.

The organization of the phycobiliprotein complexes in the phycobilisome is energetically specific [12]. Each of the phycobiliproteins that constitute the 6701 family of phycobilisomes has been analyzed spectrally [18]. The steady-state emission and absorption characteristics are given in Table 4.1. The C-PE complexes located at the periphery of the rods have their greatest absorption cross section at wavelengths shorter than any other complex of the phycobilisome. The C-PC complexes that compose the inner portions of the rods have their greatest absorption at wavelengths just longer than C-PE. There is substantial overlap of the emission spectrum of C-PE and the absorption spectrum of C-PC. The principal component of the core, allophycocyanin (AP) has its absorption maximum at longer wavelengths than C-PC, and there is again substantial overlap between the emission spectrum of C-PC and the absorption spectrum of AP. The terminal emitters have the longest wavelength absorption maximum of any of the chromophores in the phycobilisome. The flow of energy in a phycobilisome is in the direction of the energy gradient; that is, energy flows from the periphery of the rods toward the core and then to the terminal chromophores within the core. The spatial distribution of the components of the phycobilisome causes the structure to act like a funnel. Energy collected throughout the entire spatial volume of the phycobilisome is ultimately localized (following energy transfer) on the terminal emitters. The energy is not only funneled spatially but also homogenized spectrally. Due to the combination of the various chromophores' absorption characteristics, the phycobilisome has finite ab-

Figure 4.2 Absorption Spectrum of an Isolated R-Phycoerythrin Complex

The absorption spectrum of R-phycoerythrin phycobiliprotein complexes isolated from phycobilisomes of *Gastroclonium coulteri*. The phycobiliprotein complexes are isolated as hexameric double disks, $(\alpha\beta)_6\gamma$. The preparation was in 0.05 M Na-phosphate buffer (pH=7.0, $A_{565 \text{ nm}}=13.7/\text{cm}$). Each α subunit contains 2 PEB (phycoerythrobilin) chromophores, each β subunit contains 2 PEB and 1 PUB (phycourobilin) chromophores, and the linker polypeptide, γ , contains 1 PEB and 3 PUB chromophores. The absorption peak at 490 nm is due to the PUB chromophores; the low energy peaks at 535 and 565 nm are both due to PEB chromophores. The features at 496 and 535 nm correspond to high-energy sensitizing (s-type) chromophores; the peak at 565 is due to the fluorescing (f-type) chromophores [23].

Figure 4.2

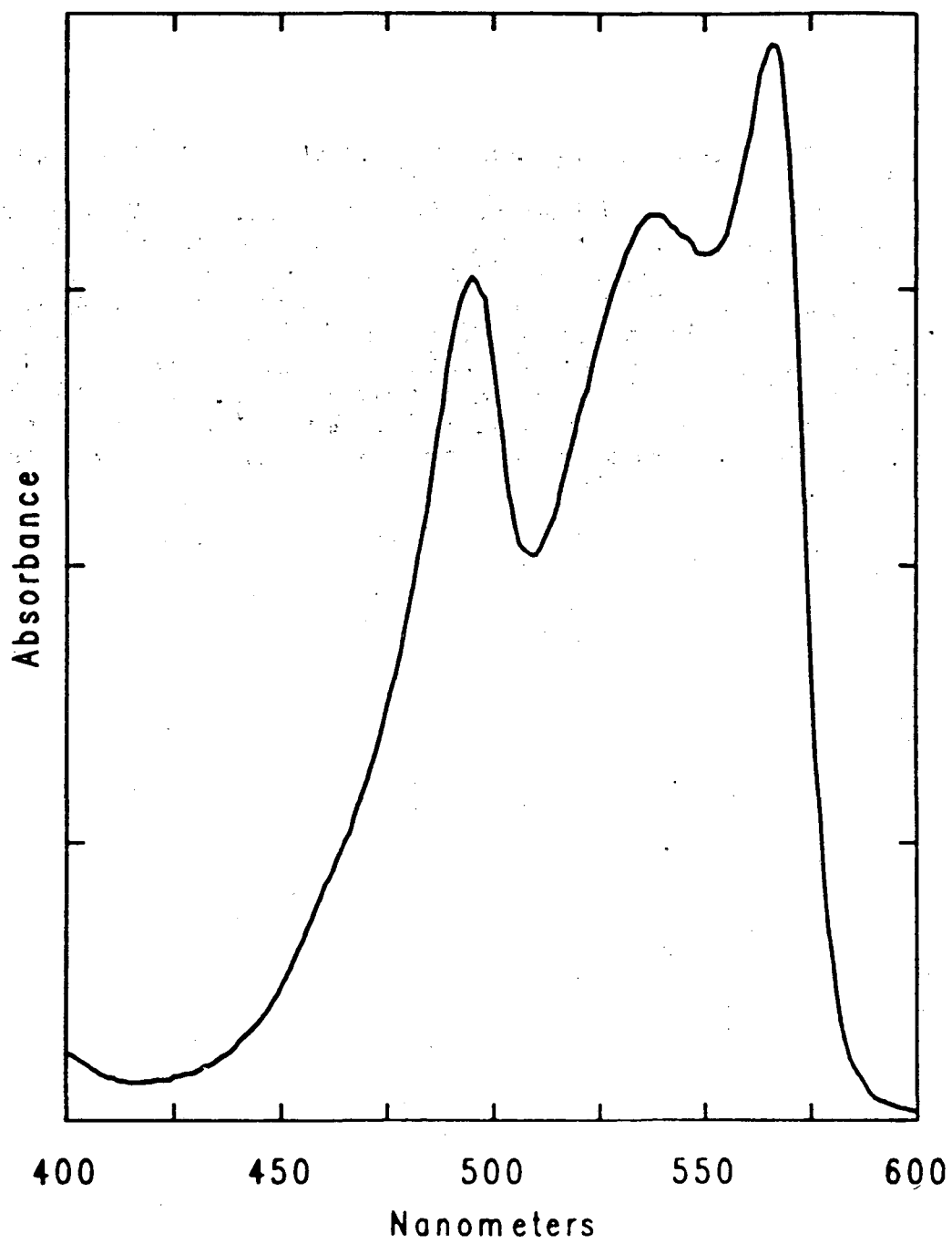


Table 4.1

Wavelengths of maximum steady-state absorption and emission for phycobiliprotein complexes isolated from wild-type *Synechocystis* 6701 phycobilisomes. Complexes named as in Figure 4.1.

Complex	Absorption Maximum (nm)	Emission Maximum (nm)
C-PE(30.5K)	565	576
C-PE(31.5K)	565	576
C-PC(33.5K)	620	642
C-PC(27K)	630	649
AP, AP(10K)	650	660
APB, AP(99K)	670	680

sorption cross section throughout the visible spectrum. The energy absorbed by any of the chromophores is emitted by the terminal chromophores, meaning that the effective emission spectrum of all absorbed light is the spectrum of the terminal emitters, peaked at 680 nm. Although this means that there has been a loss of a fraction of the energy of absorbed photons that had shorter wavelengths than 680 nm, light at 680 nm is what is required at the reaction center.

The similarity of the steady-state emission spectra of all three of the phycobilisomes studied here (Figure 4.3B) is completely consistent with the idea that the overwhelming contribution to the emission spectrum at wavelengths longer than 660 nm is from identical chromophores in each phycobilisome. The absorption spectrum of each phycobilisome is however dramatically different (Figure 4.3A). The absorption shoulder present in CM25 but absent in UV16 is due to the phycocyanin complexes that CM25 has and UV16 lacks. Similarly the absorption peak in WT6701 at 570 nm is due to phycoerythrin complexes missing from the phycobilisomes of both mutant strains. That the absorption spectra show such marked differences and that the emission spectra are virtually identical is evidence of the level of efficiency with which energy is transferred from the higher energy chromophores to the core. Measured by emission quantum yields, the quantum efficiency of energy transfer within isolated phycobilisomes has been determined to be greater than 90 percent [8,26].

D. Experimental Approach

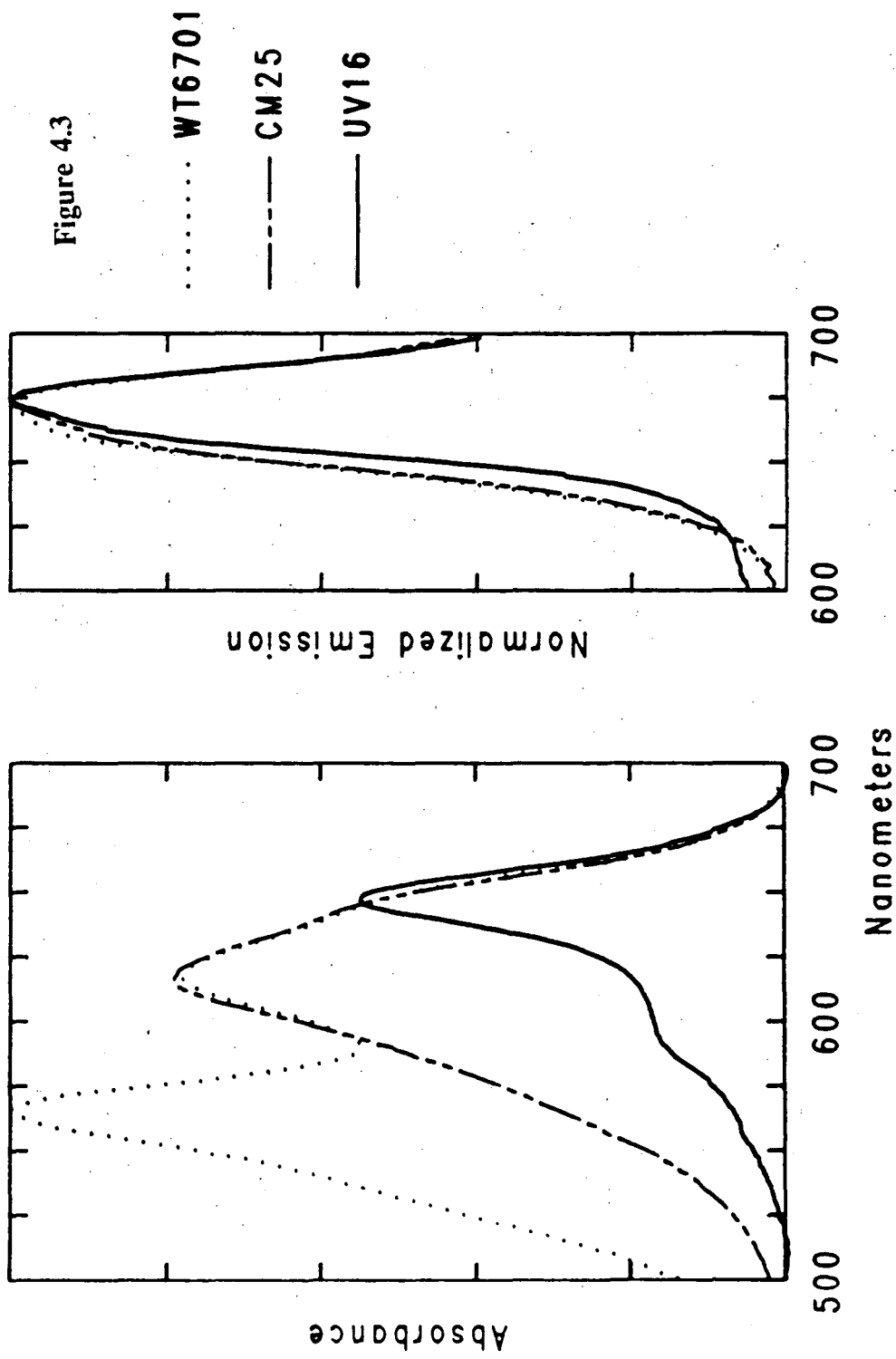
Because the quantum yield of energy transfer within phycobilisomes is high, the energy transfer steps must occur quickly relative to both the radiative and the dissipative non-radiative pathways that are open to the excited states involved. A simple calculation can be performed to estimate the expected rate of energy transfer based on quantum yield data. One can propose the following sequence of five energy transfer steps for energy

Figure 4.3 Steady-state Spectra of the *Synechocystis* 6701 Family of Phycobilisomes

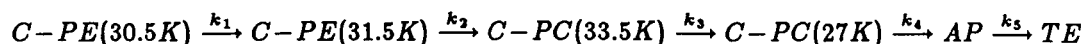
A. Steady-state absorption spectra of *Synechocystis* 6701 wild-type and mutant phycobilisomes. The absorption feature at 570 nm in the WT6701 phycobilisome is due to C-PE complexes missing in the mutants' incomplete phycobilisomes. The CM25 spectrum peaks at 620 nm because of the presence of 12 C-PC double disks in the phycobilisome. The absorption spectrum of UV16 is very close to the absorption of pure AP complexes.

B. Steady-state emission spectra of *Synechocystis* 6701 wild-type and mutant phycobilisomes. The emission spectra of all three particles are similar because all emission redder than 660 nm is from identical terminal chromophores.

The WT6701 phycobilisome preparation was in 0.75 M NaK-phosphate buffer solution (pH 8, $A_{532 \text{ nm}} = 5.1/\text{cm}$). CM25 phycobilisomes were also in 0.75 M NaK-phosphate buffer (pH 8, $A_{630 \text{ nm}} = 6.0/\text{cm}$). The UV16 preparation was in 0.65 M NaK-phosphate buffer (pH 7, $A_{650 \text{ nm}} = 0.5/\text{cm}$).

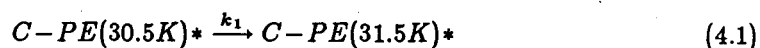


originally localized in the peripheral C-PE complex in WT6701 to get to the terminal chromophores (TE):

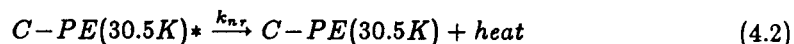


For simplicity, all transfer steps will be assumed to be equally efficient. To get 90 percent overall transfer efficiency, each of the five transfer steps must be at least 98 percent efficient. The pathway of energy transfer in each of the above steps must compete with the radiative and other non-radiative pathways that can dissipate energy. For the first PE complex, C-PE(30.5K), the possible pathways are:

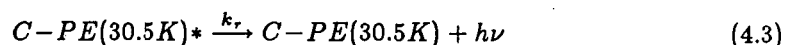
1) Energy transfer



2) Non-radiative energy loss, or quenching



3) Radiative loss



where asterisks indicate electronically excited complexes. The fluorescence lifetimes (τ_{fl}) of the isolated phycobiliprotein complexes, generally about 2 ns, are indicative of the sum of the rates of radiative (k_r) and non-radiative decay (k_{nr}) in the absence of energy transfer:

$$\tau_{fl} = \frac{1}{k_r + k_{nr}} \quad (4.4)$$

The quantum yield of energy transfer, ϕ , is the ratio of the rate of energy transfer relative to the sum of the rates of all competing processes:

$$\phi = \frac{k_1}{k_1 + k_{nr} + k_r} \quad (4.5)$$

Define

$$k_1 = (\tau_1)^{-1}. \quad (4.6)$$

Therefore,

$$\phi = \frac{(\tau_1)^{-1}}{(\tau_1)^{-1} + (k_r + k_{nr})}. \quad (4.7)$$

Substituting (4.4) into (4.7) gives

$$\phi = \frac{(\tau_1)^{-1}}{(\tau_1)^{-1} + (\tau_{fl})^{-1}} \quad (4.8)$$

A little algebra yields

$$\phi = \frac{\tau_{fl}}{\tau_{fl} + \tau_1} \quad (4.9)$$

For each transfer step to be 98 percent efficient (ϕ) relative to the 2 ns fluorescence decay (τ_{fl}) the transfer (τ_1) must occur within roughly 40 ps. This estimate is conservative because the efficiency of energy transfer within phycobilisomes may (and does [8]) exceed 90 percent. Even by this conservative estimate, picosecond time resolution will be needed to measure the energy transfer dynamics within phycobilisomes.

Picosecond time-resolved measurements of the temporal profiles of emission can be used to study the dynamics of energy transfer within phycobilisomes and isolated phycobiliproteins. Almost all the emission from phycobilisomes is from the terminal chromophores. If an excitation pulse is absorbed into a distribution of chromophores not including the terminal chromophores, energy transfer will precede terminal chromophore emission. The energy transfer will result in a time-dependent increase in population of excited terminal emitters. The intensity of the terminal chromophore emission will be directly proportional to its excited-state population. By time-resolving the rising edge of the emission from the terminal chromophores, information on energy transfer rates can be obtained. Experiments measuring terminal chromophore emission profiles can also be performed on phycobiliproteins. In phycobiliproteins, the f-type chromophores are the terminal emitters. Selective excitation of s-type chromophores would result in s to f

transfer prior to emission, and the emission profile would depend on the s to f transfer rate.

Time-resolved emission from phycobilisome chromophores other than the terminal chromophores can also yield information on the energy transfer dynamics of phycobilisomes. If the emission profile of a single chromophore bed is independently monitored, the rate of energy flow into and out of that bed can be determined. If spectral isolation of individual chromophore types can be achieved, the interpretation of the temporal profiles is unambiguous. The only spectrally isolated chromophores within a phycobilisome are the highest energy ones. For example, the emission from WT6701 phycobilisomes at 570 nm is due only to emission from C-PE. When the 570-nm emission from WT6701 is time-resolved, the rate of energy flow from the C-PE chromophores to the C-PC chromophores can be determined. In phycobiliprotein samples, decay constants of emission of high energy s-type chromophores would give information of the rate of s to f energy transfer.

E. Power Considerations

Picosecond experiments on a phycobilisome or phycobiliprotein sample must be performed with extreme caution because excitation with a picosecond laser pulse often involves very high light intensities. The power densities typically obtained from any one of the harmonics of an amplified picosecond Nd:YAG laser can easily exceed 10^{16} photons/cm² per pulse [27]. This energy (≈ 1 mJ/pulse) arrives in approximately 30 ps, corresponding to 3×10^7 watts. The laser beam is typically focussed in our experiments to 0.1 cm², making the energy density 3×10^8 watts/cm². Phycobilisomes gather light *in vivo* under the relatively low illumination levels of solar irradiation. Solar energy illuminates a naturally occurring phycobilisome with 0.1 watts/cm² [28]. Irradiation with a typical picosecond light pulse therefore illuminates the phycobilisome 10^9 times more brightly

than solar irradiation. These power considerations serve to warn a careful experimentalist. Signals detected must be checked carefully for anomalous intensity dependencies.

In a previous study of input power density on the emission profiles of isolated phycobiliproteins by Wong and coworkers [29], a strong dependence was observed. Fast components of decay became apparent at the highest input intensities. The power range covered in that study was only from 10^{13} to 5×10^{14} photons/cm², and evidence supporting a low intensity plateau region at 10^{13} photons/cm² for emission from a PE sample was sketchy at best. In order to be certain that appropriate input power densities exist, we have re-investigated the power dependence of emission profiles from isolated phycobiliproteins.

Data showing the strong power dependence we observe are presented in Figure 4.4. The time-resolved emission depicted emanates from a sample of R-PE isolated from *G. coulteri* [30]. Emission resulting when the sample was irradiated with the unattenuated 532-nm beam shows a large amplitude, short time-scale decay, typical of singlet-singlet annihilation caused by multiple excitations within a single chromophore domain [29,31–36]. As the power is attenuated by successive powers of three, the amplitude of the fast decay decreases, and the apparent rapidity of the fast decay increases. The power density of the unattenuated beam is 10^{16} photons/cm² per pulse. By the time the beam is attenuated to 10^{13} photons/cm², annihilation is no longer apparent, entirely consistent with the sketchy data presented by Wong [29]. The longer time-scale data shown in Figure 4.5 would be more sensitive to changes in shape of the decay. It is quite clear that after-attenuation by a factor of 10^3 , further attenuation has no effect on the decay shape. The plateau in this case lasts over four orders of magnitude of input power—from 10^{13} photons/cm² to 10^{10} photons/cm². (For our typical experimental setup, 10^{10} photons/cm² corresponds to an incident pulse energy of about 1 nJ. This power level is more typical of that employed in single-photon counting experiments than of that associated with streak

Figure 4.4 Emission profiles of R-Phycocerythrin Isolated from *Gastroclonium coulteri* as a Function of Excitation Intensity

The aggregation state of the phycobiliprotein was $(\alpha\beta)_6\gamma$. The preparation was in 0.05 M Na-phosphate buffer (pH=7.0, $A_{565\text{ nm}}=13.7/\text{cm}$). The excitation wavelength was 532 nm. The detection band was selected using a RG610 (Schott) high pass filter. Intensities of each curve listed in the figure are given relative to the unattenuated beam, which has an intensity of 10^{16} photons/cm² per pulse.

Figure 4.4

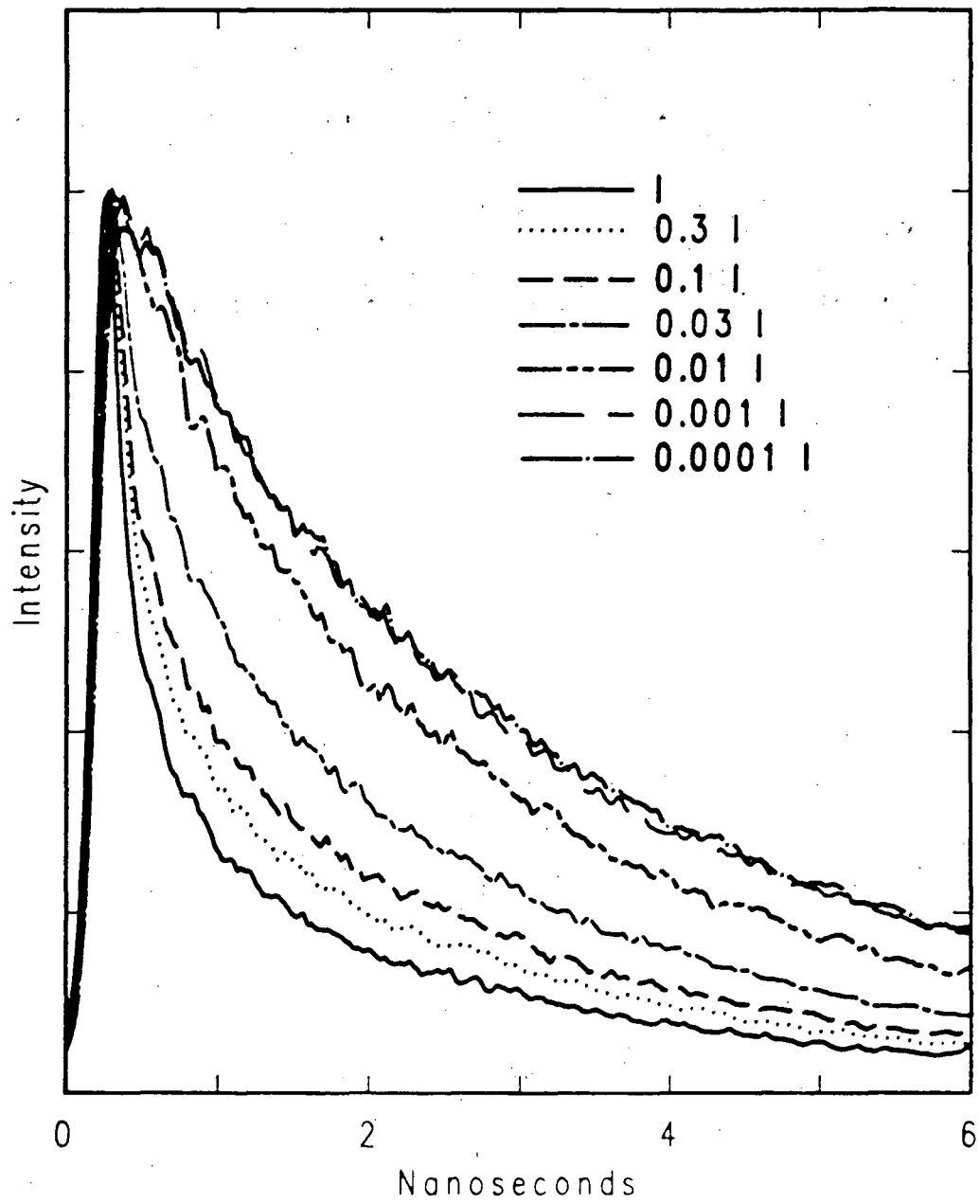
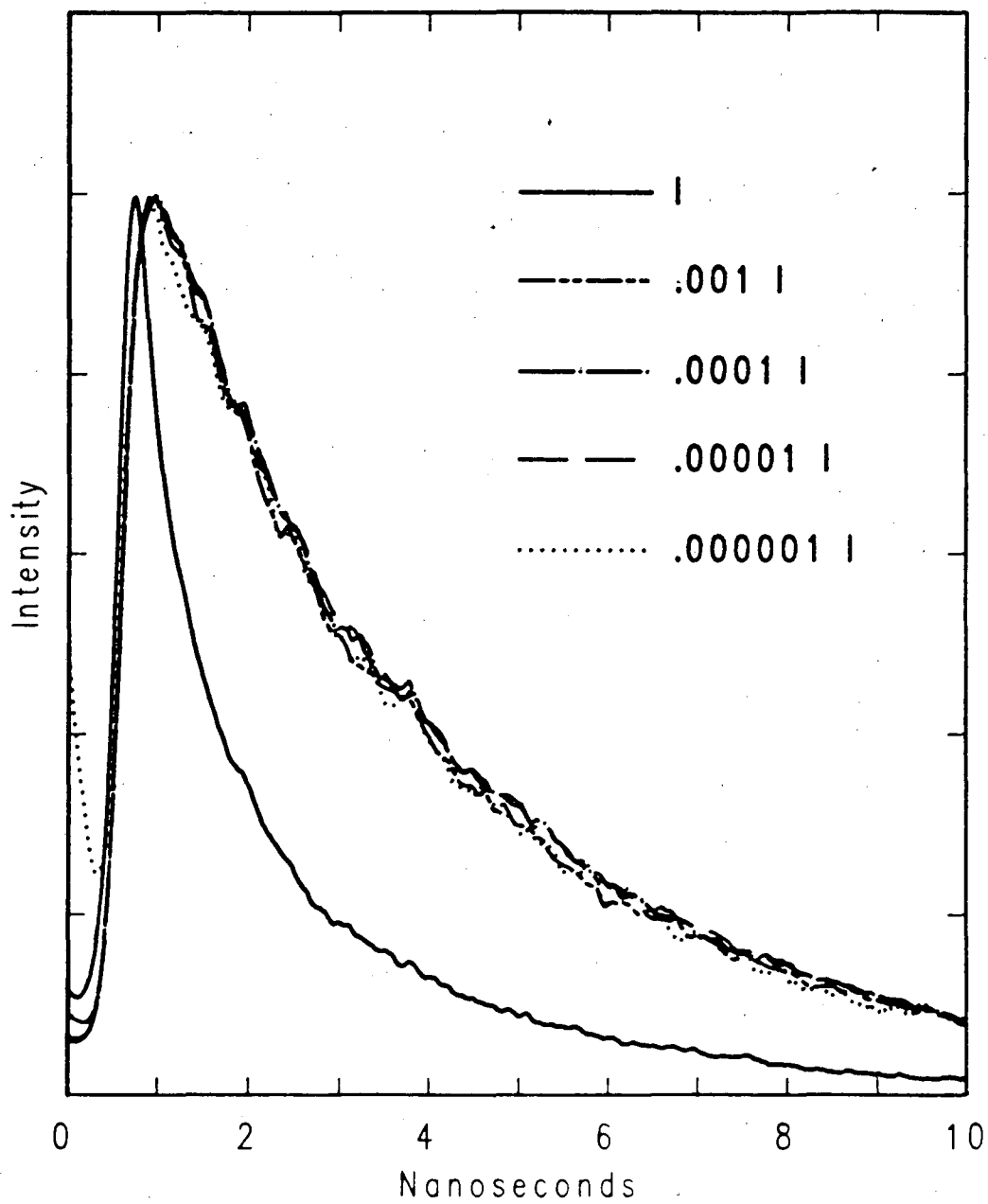


Figure 4.5 Phycobiliprotein Emission Profiles as a Function of Excitation Intensity

Emission profiles of R-phycoerythrin ($\alpha\beta$)₆ γ isolated from *Gastroclonium coulteri* as a function of excitation intensity. The preparation was in 0.05 M Na-phosphate buffer (pH=7.0, $A_{565\text{ nm}}=13.7/\text{cm}$). The excitation wavelength is 532 nm; the detection band is selected with a RG610 (Schott) high-pass filter. The unattenuated beam photon flux is 10^{16} photons/cm² per pulse. Beyond attenuation of 10^3 , emission profiles are independent of input intensity.

Figure 4.5



camera work [37]. It is the sensitivity of the streak camera system that enables us to exercise such low excitation levels.) Except for the power study just discussed, the power densities used during the acquisition of all data used to understand energy transfer in phycobilisomes and phycobiliproteins were lower than 10^{14} photons/cm². In addition, all experimental results taken on phycobilisomes and phycobiliproteins presented in the pages that follow were taken using at least two power densities to be sure the data were free from anomalies due to intensity effects.

The intensity threshold for the appearance of a fast-decaying component was examined in some detail not only in the aforementioned phycobiliprotein study [29], but also in studies [31,33] on components of other photosynthetic antenna systems. These studies have shown that many antenna components show a significant decrease in their emission quantum yield as a function of input intensity. The quantum yield is determined by numerically integrating the exponential fits obtained for a given temporal profile. The integral of the data taken at low input intensities is used as a standard so that relative emission quantum yields as a function of input intensity can be determined. The data presented in Figure 4.6 show the first 500 picoseconds of emission at six different power levels. Fits to these data, and to data at other power levels (not included in the figure for clarity), have been obtained. The parameters that best fit the experimental data as a function of input power are tabulated (Table 4.2). Using the low intensity data as a standard of emission yield, the quantum yields of emission as a function of input intensity can be calculated. The quantum yields that result are included in Table 4.2, and plotted as a function of the logarithm of input intensity in Figure 4.7.

The top ordinate of the plot is the number of absorptions, or hits, per particle, or domain. The calculation of the number of hits, x , per domain is straightforward:

$$x = \sigma\Phi \quad (4.10)$$

where σ = absorption cross section and Φ = photon flux. For R-PE at 532 nm, σ =

Figure 4.6 Initial Profiles of Emission from R-Phycoerythrin as a Function of Input Intensity

Time-resolved emission from R-phycoerythrin [$(\alpha\beta)_6\gamma$] isolated from *Gastroclonium coulteri*. The preparation was in 0.05 M Na-phosphate buffer (pH=7.0, $A_{565\text{ nm}}=13.7/\text{cm}$). Emission detected through an RG-610 high-pass filter after excitation with 532-nm beam. Input intensities as labelled in the figure with the unattenuated input (I) having an intensity 10^{16} photons/cm². Excitations below 10^{13} photons/cm² result in identical profiles.

Figure 4.6

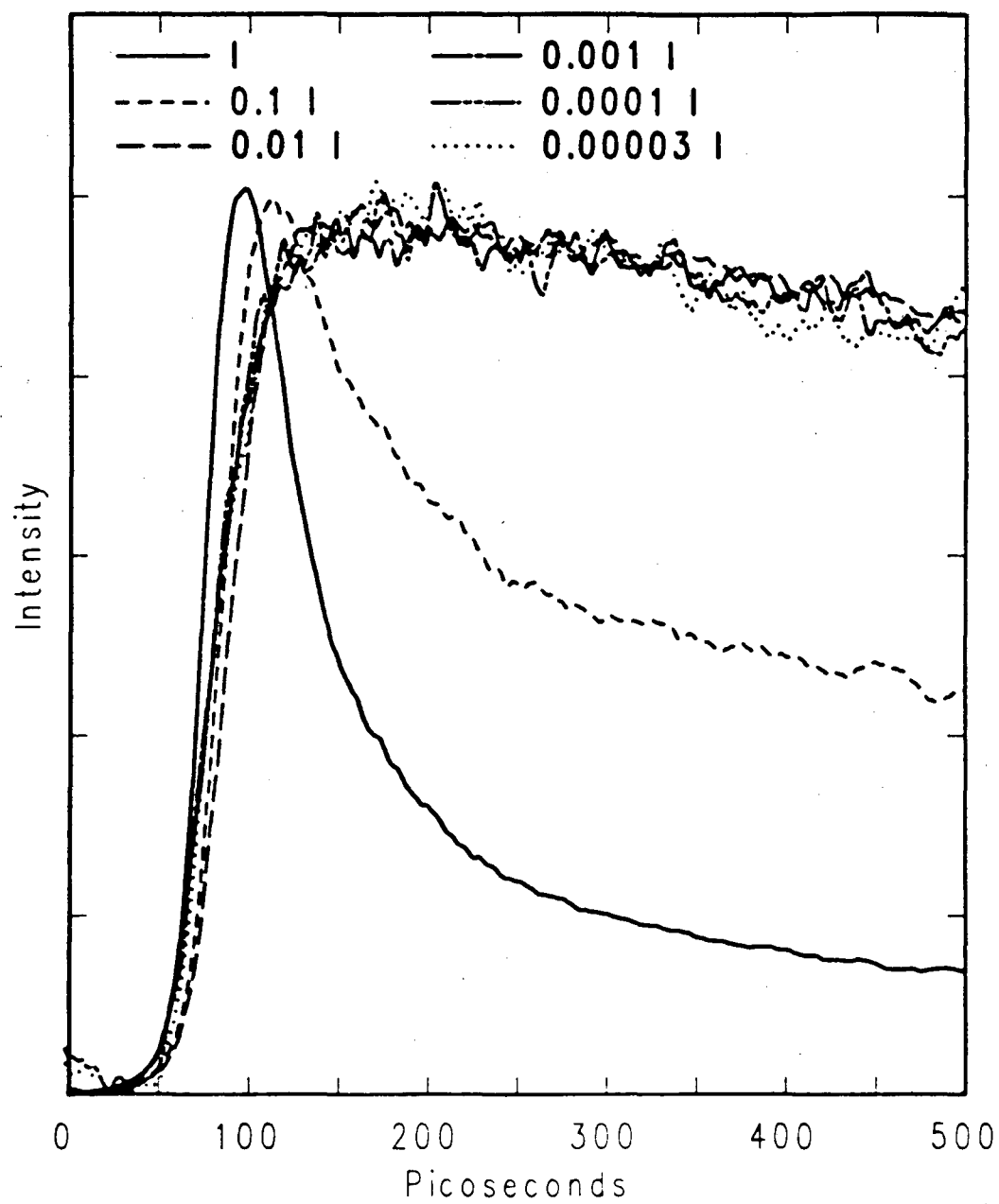


Table 4.2

Best-fit emission decay parameters for R-phycoerythrin complexes isolated from *G. coulteri* as a function of input intensity. Quantum yield determined by numerical integration of decay parameters relative to decay of low intensity signals as described in text. Components with time constants shorter than 100 ps are from fits to data like that shown in Figure 4.6; components with time constants longer than 1 ns are from fits to longer time scale data, like that shown in Figures 4.4 and 4.5.

Intensity (Photons/cm ²)	τ_{1,α_1}	τ_{2,α_2}	τ_{3,α_3}	Quantum Yield	Hits per Domain
All times are in ps; amplitudes are relative.					
10 ¹⁰	*	—	3150.,1.	0.92	0.00002
3×10 ¹⁰	16.,-1.	—	3480.,1.	1.01	0.00006
10 ¹¹	17.,-1.	—	3580.,1.	1.04	0.0002
3×10 ¹¹	12.,-1.	—	3510.,1.	1.02	0.0006
10 ¹²	11.,-1.	—	3450.,1.	1.01	0.002
3×10 ¹²	13.,-1.	—	3450.,1.	1.01	0.006
10 ¹³	14.,-1	—	3370.,1.	0.98	0.02
3×10 ¹³	9.,-1.	—	3220.,1.	0.94	0.06
10 ¹⁴	6.,-1.	—	3030.,1.	0.88	0.2
3×10 ¹⁴	95.,0.40	—	2800.,1.	0.59	0.6
10 ¹⁵	63.,1.62	—	2750.,1.	0.32	2.
3×10 ¹⁵	18.,3.69	91.,1.92	2720.,1.	0.13	6.
10 ¹⁶	11.,13.2	76.,4.09	2750.,1.	0.05	20.

$$\tau_{ave} = 3430 \pm 140 \text{ ps}$$

The average lifetime, τ_{ave} , was calculated only from data taken using excitation power densities in the range of 10¹⁰ to 10¹³ photons/cm².

* Fast time scale data too weak to detect reliably.

Figure 4.7 Relative Quantum Yields of Emission as a Function of Excitation Intensity for R-Phycoerythrin

Relative quantum yields (RQY) for R-phycoerythrin data as a function of incident intensity. Relative quantum yields calculated as described in text. Smooth curve calculated according to the theory of Mauzerall, detailed in text. The horizontal displacement between the experimental data and the calculated curve is most likely due to an underestimate of the photon flux.

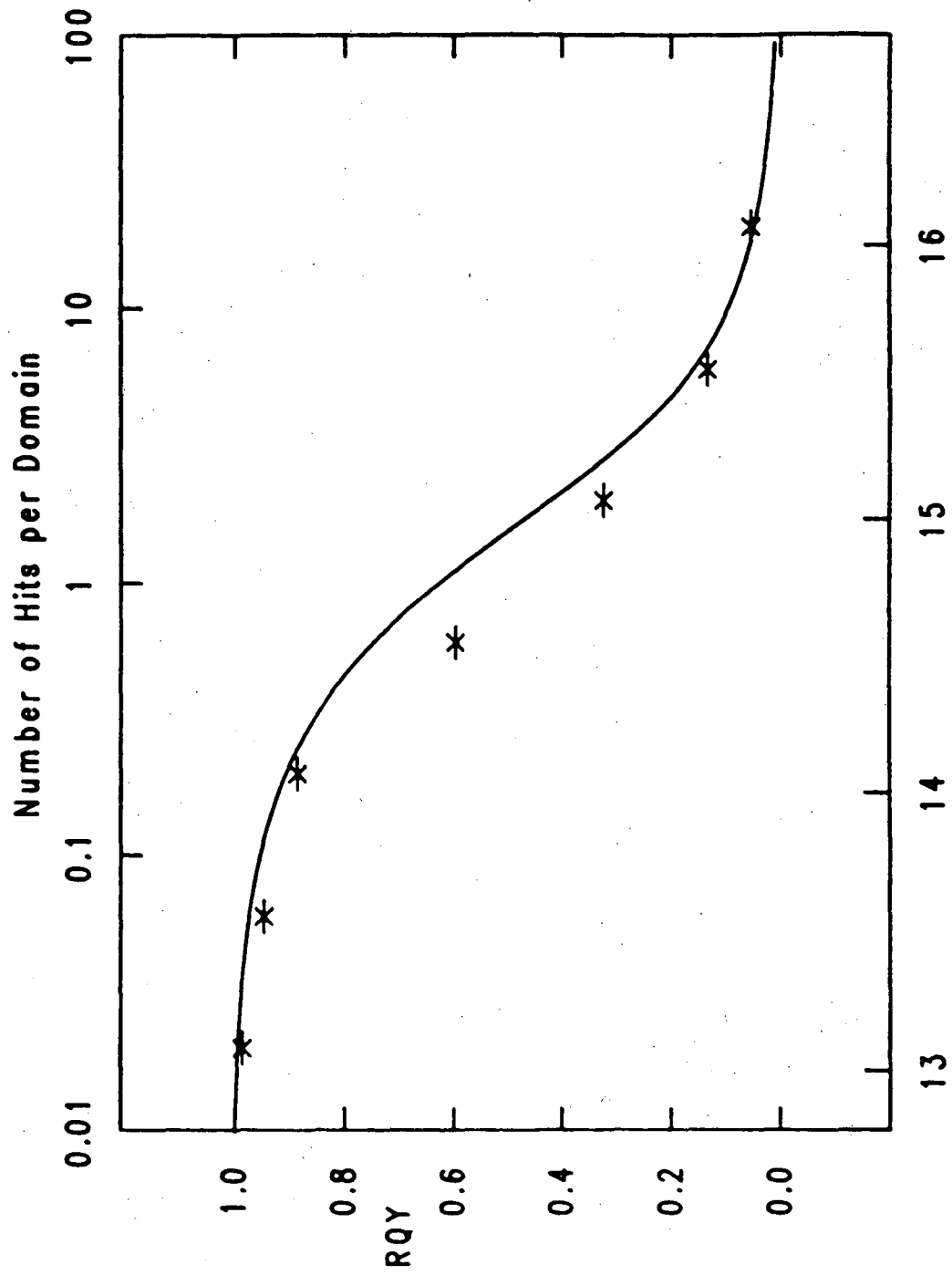


Figure 4.7

13

14

15

16

2×10^{-15} cm² per particle, so that at the highest intensities used, 10^{16} photons/cm², there are an average of 20 hits per particle. The number of hits is linear function of intensity, as is shown in the upper ordinate of Figure 4.7.

Plotted with the experimental data is a smooth curve generated from a theory of Mauzerall [32,36]. Mauzerall's theory of exciton annihilation predicts the quantum yield, ϕ , relative to the quantum yield at low excitation intensities, ϕ_0 , as a function of the number of excitations in each domain:

$$\phi = \phi_0 \left(\frac{1 - e^{-x}}{x} \right) \quad (4.11)$$

The function plotted is the relative quantum yield (RQY), ϕ/ϕ_0 , as a function of x , defined in equation (4.10). The ordinate of the continuous curve is the number of excitations or hits per domain, and is on the top axis of the graph. There is clear agreement between the shape of the plot from Mauzerall and the general shape of the experimental points. (There is an apparent horizontal displacement between the experimental data and the predicted curve, which is very likely an error in the estimation of the input power level. Probably due to non-uniformity in the intensity profile of the Gaussian TEM₀₀ excitation beam [38], the input intensity has been under-estimated by about a factor of two.) The general agreement between the calculation from Mauzerall and the experimental data is consistent with previously reported investigations of phycobiliproteins [29].

F. Emission Rise Times of Phycobiliproteins

A phycobiliprotein complex is the smallest subunit of a phycobilisome that retains in isolation the spectral and structural properties attributed to it in the intact phycobilisome [14]. As discussed in detail above, the chromophores in a phycobiliprotein complex can be divided into two classes, s- and f-type. If only s-type chromophores are excited, emission from f-type chromophores occurs only after energy transfer. The rise time of emission from the sample measures the s to f transfer time. The time constant of that

intracomplex transfer is important to determine, because the intracomplex transfer is the first energy transfer event that occurs in intact phycobilisomes.

The low excitation-intensity profiles shown in Figure 4.6 for the complex R-PE isolated from phycobilisomes of *G. coulteri* show the rise time of emission after excitation with 532-nm pulses. The best-fit parameters are given in Table 4.2. As the input power is decreased to levels corresponding to the plateau region in the lifetime data (Section E), the fast-decaying component disappears. Throughout the plateau regime, the rise time of the emission band is uniform and prompt (≤ 15 ps), over a wide range of excitation powers. There is no evidence of anomalous power dependencies on the signal from R-PE in the power regime of 10^{13} to 3×10^{10} photons/cm². Absorption by R-PE of 532-nm photons results in excitation of a combination of both s-type and f-type chromophores. The rise time presented above for the emission might be partly due to the transfer of the excitation from s to f chromophores. The measured rise time of the excitation transfer is less than 15 ps, which is as fast as can be resolved with a pulse width (FWHM) approaching 40 ps. The time constant of s to f transfer consistent with the emission data is clearly quite short, but information on the s to f transfer is not simply obtained from that single data point. With a tunable excitation source, the dependence of the emission rise time on the initial excitation ratio of s and f chromophores could be determined.

The excitation source used in the above series of experiments was the second harmonic of the Nd:YAG fundamental frequency. Using an optical parametric source (OPS), tunable picosecond pulses throughout the visible spectrum can be obtained [39]. The proportion of s- to f-type chromophores initially excited can be varied by varying the excitation wavelength. The pulses from the OPS are significantly shorter temporally than the second harmonic of the Nd:YAG laser. Use of the OPS as the excitation source has the additional advantage of increasing time resolution. The series of emission rise times shown in Figure 4.8 was obtained with excitation at a series of excitation wavelengths

as indicated in the absorption spectrum of R-PE included at the top of the figure. The striking similarity of all four of the time-resolved curves demonstrates that emission is as prompt when s-type chromophores sensitize the emission as when f-type chromophores are directly excited. The rise time data are summarized in Table 4.3. The last curve in the series is not R-PE emission but emission from the laser dye Rhodamine B (Rho B, Exciton Chemical Company). The Rho B curve would be expected to show an instantaneous rise time, because the fluorescent state is populated within 0.2 ps after electronic excitation [40]. The finite rise time determined for Rho B, 6 ps, is indicative of the finite temporal resolution of the streak camera system with the given 15-ps excitation pulse width. The R-PE curves are indistinguishable from any curve for Rho B, and so the emission from the phycobiliprotein solution is as prompt as emission from a laser dye. The s to f transfer must take less than 8 ps, determined from the time constant of the rise of emission excited by the OPS. (The decrease in excitation pulse width from 40 ps for the second harmonic to 20 ± 5 ps for the OPS accounts for the decrease in the upper limit of the transfer time-constant from 15 to 8 ps, still instrument-limited). Exciting the phycobiliprotein, a complex containing 34 bilin chromophores, results in emission as prompt as that from a single chromophore.

R-PE represents the high extreme of bilin content amongst phycobiliprotein complexes. A complex from the low extreme of chromophore content is AP, the principal constituent of the cores of all phycobilisomes. AP, like R-PE, can be isolated from intact phycobilisomes with high retention of the spectral characteristics attributed to it in the intact phycobilisome [41]. Allophycocyanin is isolated in trimers $(\alpha\beta)_3$, and each trimer contains only six phycocyanobilins. Three of the chromophores are believed to be identical sensitizers, while the other three are identical fluorescers. Emission data for AP complexes isolated from *Anabaena variabilis* along with the absorption spectrum are shown in Figure 4.9. Emission from a solution of Rho B is included again for compar-

Figure 4.8 R-Phycoerythrin Rise Times as a Function of Excitation Wavelength

Curves a–d show the first 90 ps of emission from R-PE from *G. coulteri* with best-fit convolution. The solution conditions were: 0.05 M Na-phosphate buffer, pH = 7.0, $A_{565 \text{ nm}} = 13.7 / \text{cm}$). Emission resulted from samples excited at the wavelengths indicated in the absorption spectrum included at the top of the figure. The curve in the last panel is emission from Rho B excited at 470 nm, detected at 600 nm. Rise time parameters for the computer-generated fits: curve a, $\tau_r = 6.6$ ps; curve b, 2.2 ps; curve c, 6.5 ps; curve d, 4.6 ps; and Rho B, 7.0 ps.

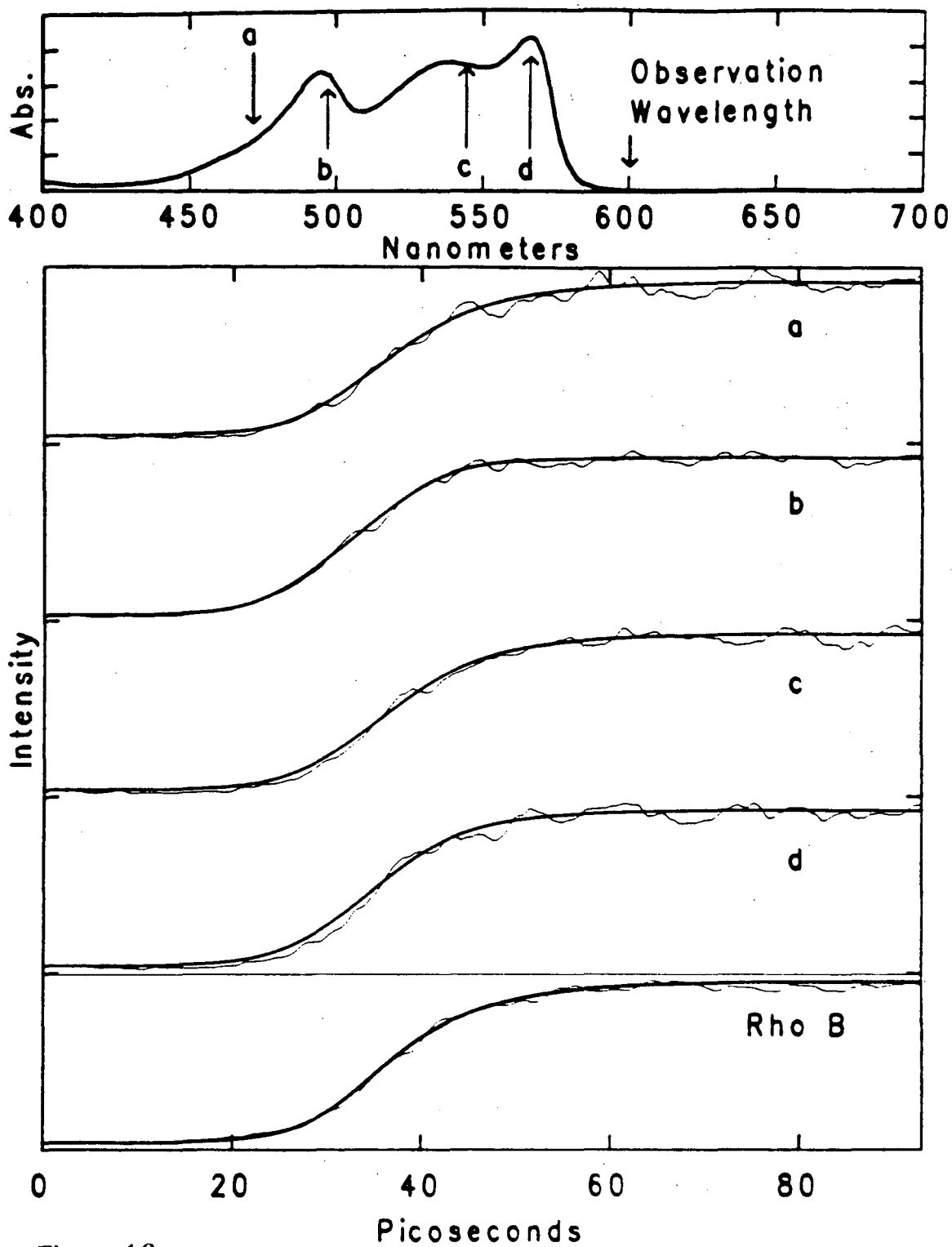


Figure 4.8

Table 4.3

Best-fit emission rise times for isolated phycobiliproteins and for Rhodamine B laser dye solutions. All measurements taken under the same experimental conditions using the OPS as the excitation source.

Excitation Wavelength (nm)	Detection Wavelength (nm)	Best-Fit Rise Time (ps)
R-Phycoerythrin:		
470	600	6.6
496	600	2.2
540	600	6.5
565	600	4.6
Allophycocyanin:		
532	670	0.2
575	670	6.9
619	670	5.5
Rhodamine B:		
470	600	7.0
470	600	0.8
532	600	7.0
532	600	8.7
532	600	7.7

ison. Results for AP emission are tabulated with those for R-PE emission in Table 4.3. The emission from AP is as prompt as emission for Rho B regardless of excitation wavelength. In both the high and low extremes of bilin content, the movement of electronic energy within phycobiliprotein complexes is unresolvably fast. Short time scale emission profiles from phycobiliprotein complexes are indistinguishable from those obtained from a solution of a single chromophore.

Phycobiliprotein complexes are small objects. For example, R-PE is a disk-shaped complex, 120 Å in diameter and 60 Å high. Isolation of a single chromophore in such a small volume (6.8×10^{22} liter) results in an effective chromophore concentration of about 2.4×10^{-3} M. Since R-PE contains 34 bilins, the resulting chromophore concentration within R-PE is about 0.1 M. At concentrations that high, chromophores in random orientations have been shown to have radically different fluorescent behavior. For instance, rhodamine 6G is generally a fluorescent molecule, but solutions with concentrations of even just 0.01 M fluoresce with a very small quantum yield [42] because of excitation trapping and quenching by dimers. In the R-PE complex, the chromophores are at most 30 Å apart, assuming the chromophores are distributed to maximize inter-chromophore separation. The actual spacings could therefore be much smaller. Chromophores within 10 Å of one another can form an exciton [43]. The formation of an exciton profoundly affects the energies of the electronic levels, and is reflected in shifts and splittings in the absorption and emission spectra. It is possible, particularly in light of the high chromophore content of the phycobiliproteins, that excitons form.

Evidence for exciton formation is found by comparison of native and denatured phycobiliproteins [14]. Spectral changes can also be due to substantial changes in chromophore environment or chromophore conformation upon folding of the proteins [23,24]. The contributions of the two effects to the observed spectral shifts can not be distinguished easily. However, the distinction has important ramifications on understanding

Figure 4.9 Allophycocyanin Rise Times as a Function of Excitation Wavelength

Curves a–c show the first 90 ps of emission from AP complexes isolated from *Anabaena variabilis* with best-fit computer-generated convolution. The preparation was in 0.05 M Na-phosphate buffer (pH=7.0, $A_{532 \text{ nm}}=2.7/\text{cm}$). Emission resulted for samples excited at the wavelengths as indicated in the absorption spectrum included at the top of the figure. The last panel is emission from Rho B excited at 470 nm, detected at 600 nm. Rise time parameters for the computer-generated fits: curve a, $\tau_r = 0.2$ ps; curve b, 6.9 ps; curve c, 5.5 ps; Rho B, 7.0 ps.

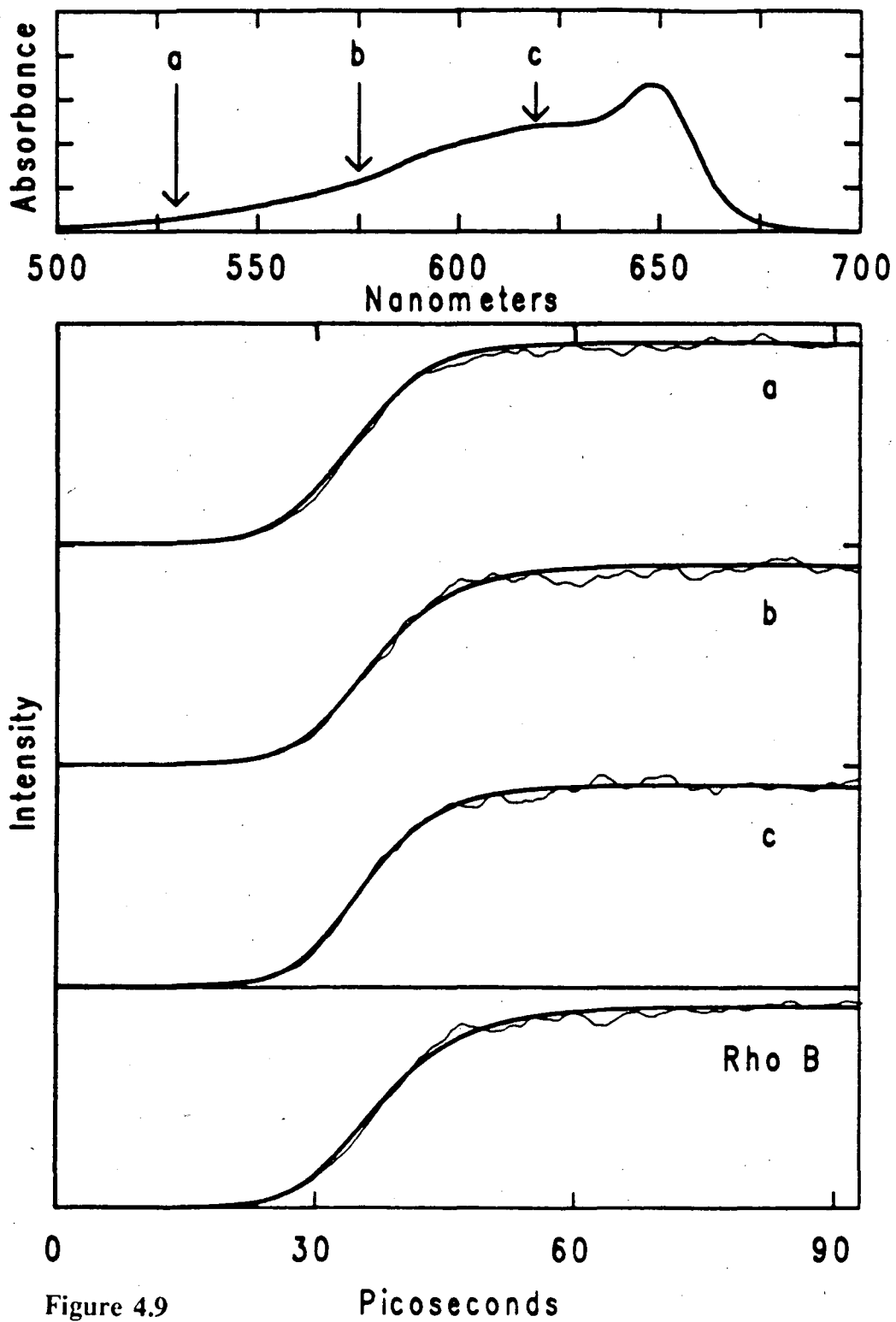


Figure 4.9

Picoseconds

the nature of excitation transport within the complexes. If excitons form, then distinguishing between s-type and f-type chromophores may not be appropriate. It may be that considerable amounts of the absorption, even at the blue edge of the absorption spectrum, is into the high energy band of a fluorescing exciton. Exciton formation is therefore not excluded by the time-resolved results, as blue-edge excitation could be direct excitation of the fluorescing chromophores, which would result in the prompt emission profiles that are observed. The data that originally brought about the distinction between s and f chromophores were steady-state emission polarization spectra. In those measurements, different absorption wavelengths gave different levels of emission polarization, with red excitation giving strong retention of polarization and blue excitation giving lower levels of polarization retention. Instead of having single chromophores acting independently and giving this behavior, it is possible that there are excitons formed that result in the same polarization behavior.

One way of distinguishing between exciton formation and s to f transfer would be if emission from other than the f-type chromophores could be detected. Emission at higher energies would be compelling evidence for the s to f transfer model of energy transfer within phycobiliproteins. One would expect that the s-type chromophores, once excited, could fluoresce with a finite quantum yield. Time-resolving the high energy emission would measure the rate of depletion of the s-type chromophore beds. If there is high energy emission, there is no way to justify it within the framework of exciton formation, except as emission from a highly excited vibrational state, which is improbable [40,44]. Experiments to detect the high energy emission were performed on R-PE. Only at high input intensities was emission at short wavelengths (550 nm) detectable. At input levels in the plateau region where the long wavelength emission was detectable, no short wavelength emission could be detected. The negative result, if definite, would call into question the s to f transfer model. When the excitation is localized on the s-type

chromophores, it should be subject to degradation by radiative as well as non-radiative pathways. However, it is possible that emission is present but below experimental detection levels. S-type chromophores could have diminished radiative rates relative to the f-type chromophores, making the high energy emission difficult to detect.

One further experiment that sheds light on the intradisk transfer question is on the quantum yield of emission as a function of excitation wavelength for the AP complex from *Anacystis nidulans*. Emission was spectrally resolved on a computer-controlled spectrofluorimeter (Spex Industries, Fluorolog 2). The quantum yield was measured relative to absorption as a function of wavelength. The relative quantum yield as a function of wavelength is presented in Figure 4.10B. The data in the figure are the result of a few determinations at each wavelength on at least two different AP samples. Within the experimental scatter which results principally from uncertainties of the absorption spectrum for the weakly absorbing samples (≤ 0.1 A/cm), the quantum yield is independent of excitation wavelength. As the wavelength is scanned from higher to lower energy, the proportion of excitation into s and f chromophores changes. One would expect that if the s to f transfer model were applicable to the phycobiliprotein samples, the emission quantum yield would be higher when the f-chromophores are directly excited than when the s-chromophores sensitize their excitation. The reason for this expectation is that when the excitation is localized on the s-chromophores, dissipative pathways are accessible to the excitation that are not accessible to the directly excited f-type chromophores. However, this evidence is still not conclusive; the kinetic data show that s to f transfer, if it occurs, is fast. The dissipative pathways would have to be extremely fast to compete effectively with a transfer time of less than 8 ps.

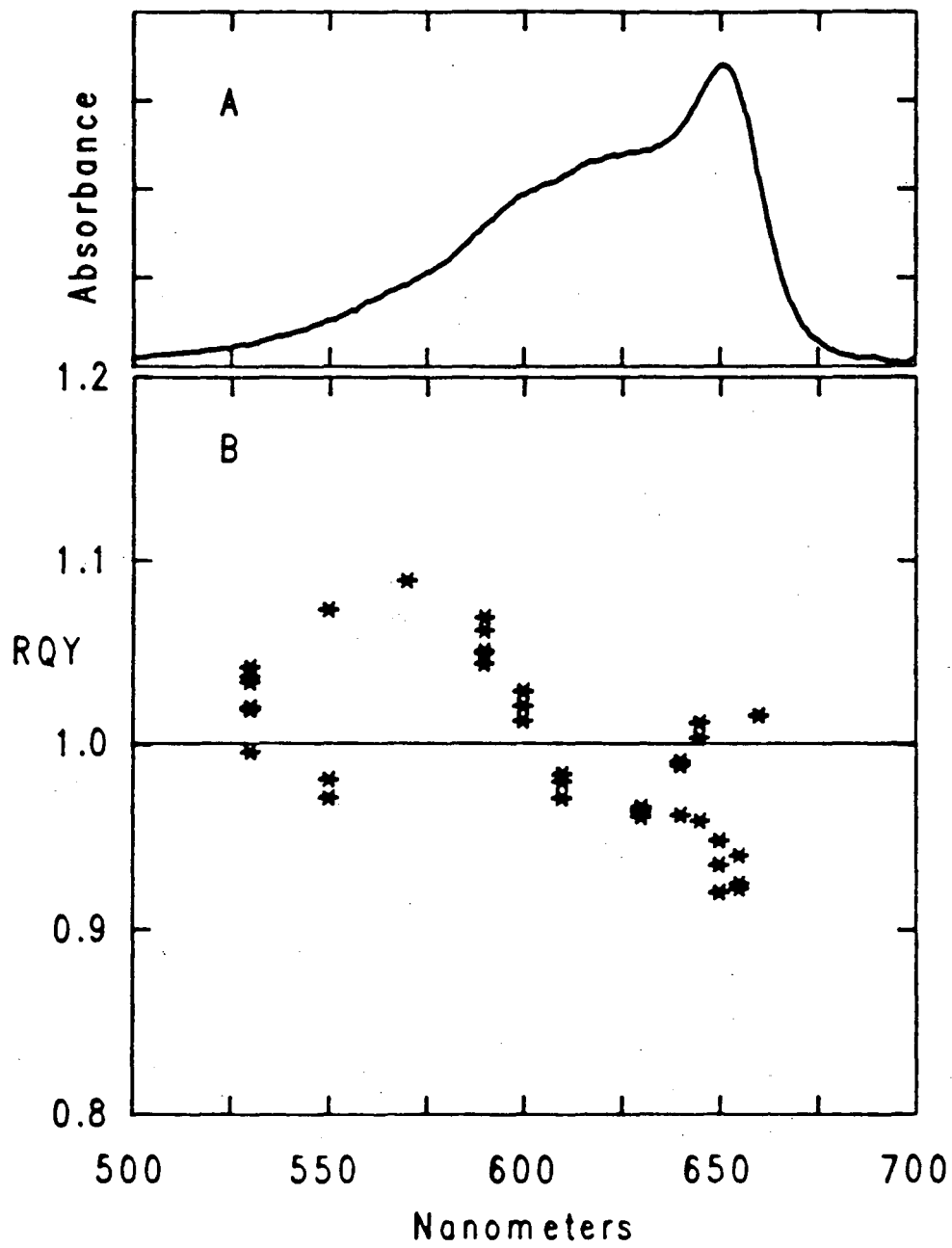
Although the question of the nature of the excitation transfer within isolated phycobiliprotein complexes is unresolved, the fact that energy is emitted so promptly from these complicated structures has important implications on the interpretation of data for intact

Figure 4.10 Relative Quantum Yield as a Function of Excitation Wavelength for Allophycocyanin Complexes

A. Absorption spectrum of *Anacystis nidulans* AP. The preparation was in 0.75 M Na-phosphate buffer (pH=7.0, $A_{650\text{ nm}}=0.08/\text{cm}$).

B. Relative quantum yield of emission as a function of excitation wavelength. Scatter evident in plot is indicative of experimental uncertainty in determining the relative absorption cross sections for the weakly absorbing ($<0.1\text{ A/cm}$) samples.

Figure 4.10



phycobilisomes. Excitation of phycobiliproteins results in prompt emission, $\tau_r \leq 8$ ps. Therefore, the longest time that energy can be said to be localized on non-emitting chromophores within phycobiliproteins is 8 ps, a time that is over-estimated by finite experimental resolution. The phycobiliprotein complexes show by their short time scale profiles of emission that they are extremely efficient at energy communication, because the rate of intracomplex energy transfer is unresolvably fast.

G. Time-Resolved Emission of Intact Phycobilisomes

Studies of emission from intact phycobilisomes can be used to gain insight into the dynamics of energy transfer within the macromolecular assemblages. The experiments described in this section yield information on energy transfer within both of the distinct structural domains of phycobilisomes—the rods and the cores. While all of the phycobilisome particles studied here are from the cyanobacteria *Synechocystis* 6701 and two mutant strains of 6701, comparisons with literature values for phycobilisomes of various morphologies and various biliprotein content show the results obtained here to be quite general.

Some dramatic evidence of the efficiency of energy transfer within phycobilisomes is shown in Figure 4.11, where time-resolved emission from intact and dissociated phycobilisomes is compared. The emission in Figure 4.11 is from two samples of the phycobilisomes of the cyanobacteria *Synechocystis* 6701 (WT6701). One of the phycobilisome samples was dissociated by the dilution of the phycobilisomes into a low salt buffer. Both samples were excited with 532-nm photons, resulting in selective excitation of phycoerythrin chromophores. Emission from the dissociated sample detected at 570 nm shows a fluorescence trace with a long lifetime. This emission is entirely due to the directly excited phycoerythrin complexes. The profile measured under the identical experimental conditions for the intact phycobilisomes contrasts notably, showing a sharp

decay to a zero background. This signal is also due entirely to emission from phycoerythrobilin chromophores that have been directly excited. The fast decay is evidence of an efficient non-radiative de-excitation pathway available to phycoerythrin in the intact phycobilisomes not possible in the dissociated chromophores. That fast non-radiative decay is due to the highly efficient energy transfer to lower energy phycocyanin chromophores that occurs in intact phycobilisomes.

When the decay at 570 nm is detected with faster time resolution (125 ps full scale instead of 8 ns), the fast decay time can be accurately determined. In Figure 4.12, emission from intact WT6701 phycobilisomes is shown. The smooth curve is the computer-generated fit to the data, and shows that the decay time of the 570-nm emission is 28 ± 4 ps. The emission at 570 nm is due only to decay of excited phycoerythrobilin because all other chromophores emit considerably to the red of 570 nm. This emission is therefore spectrally isolated, and indicative of the population as a function of time within only the phycoerythrobilin chromophore bed. Thus, the C-PE pigment bed of WT6701 phycobilisomes transfers excitation to the phycocyanin complexes of the phycobilisome with a transfer time of 28 ± 4 ps.

The emission decay time determined for C-PE in WT6701 phycobilisomes is consistent with measurements reported in the literature for other PE containing phycobilisomes. For instance, the phycobilisomes from the red algae *Nostoc* sp. have been studied by Wong and coworkers [45]. The rods from the *Nostoc* phycobilisomes are morphologically very similar to the rods of WT6701. The decay time measured for B-phycoerythrin (B-PE) emission from intact phycobilisomes was 34 ± 13 ps. Data from yet another laboratory on phycobilisomes from *Rhodella violacea* [46], also similar morphologically to WT6701 gave a decay time of 34 ps for emission from B-PE.

Emission detected at 680 nm is from the terminal emitters of the phycobilisome [21]. The rise time determined for that emission is associated with the transit time of the ex-

Figure 4.11 Time-Resolved Emission from Intact and Dissociated WT6701 Phycobilisomes

8 ns of emission detected at 570 nm from samples of *Synechocystis* 6701 wild-type phycobilisomes. Excitation wavelength was 532 nm for both datasets. The sharp features at ≈ 800 ps are the fiduciary pulses for the datasets, and indicate the time resolution of the camera (≈ 100 ps) under the experimental conditions of these two datasets. The intact phycobilisomes (solid curve) were isolated in 0.75 M NaK-phosphate buffer (pH=8.0, $A_{532 \text{ nm}}=5.1/\text{cm}$). The phycobilisomes were dissociated (dotted curve) by dialysis to equilibrium against 0.02 M NaK-phosphate buffer (pH=8.0, $A_{532 \text{ nm}}=2.0/\text{cm}$).

Figure 4.11

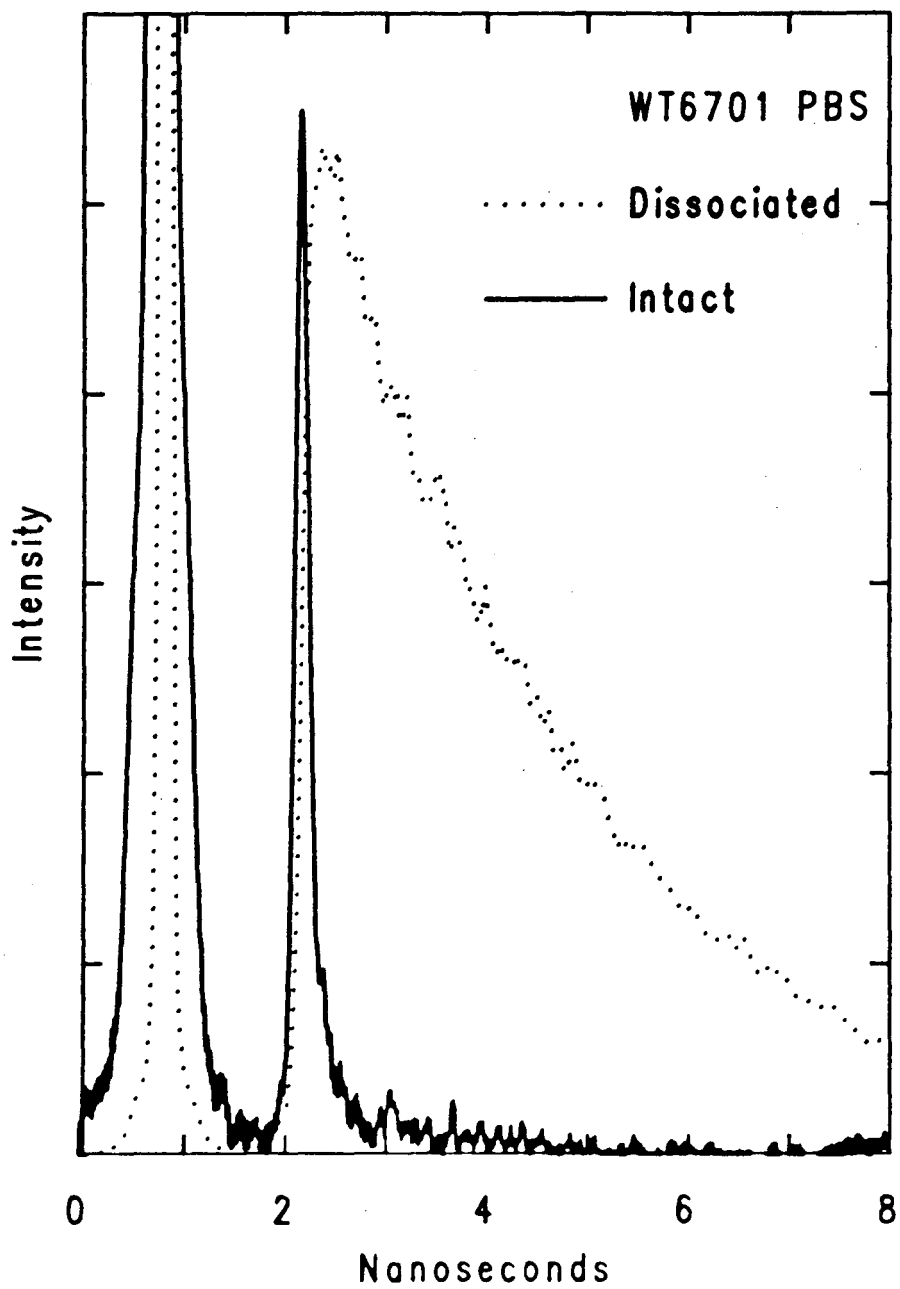
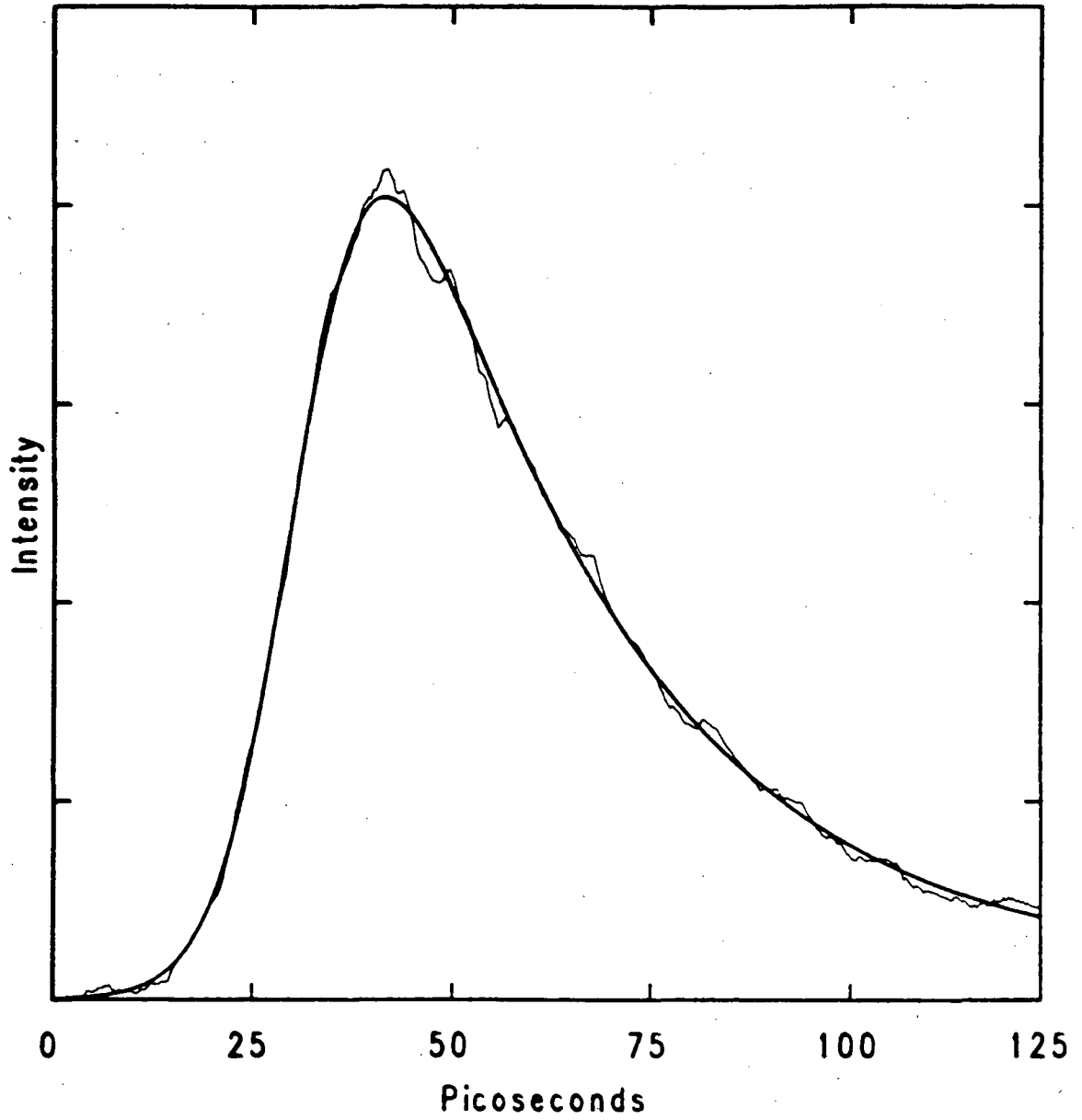


Figure 4.12 Short Time Scale Emission from Intact WT6701 Phycobilisomes.

Emission from WT6701 phycobilisomes detected at 570 nm with excitation at 532 nm. Smooth curve is computer-generated fit with fast decay component of 27 ps. The intact phycobilisomes (solid curve) were isolated in 0.75 M NaK-phosphate buffer (pH=8.0, $A_{532 \text{ nm}}=5.1/\text{cm}$).

Figure 4.12



citation through the phycobilisomes from that subset of chromophores that was initially excited. To aid in the interpretation of the terminal chromophore time-resolved emission data, we used phycobilisomes from mutant strains. These mutant strains produce phycobilisomes with well-documented structural deficiencies. The phycobilisomes from the *Synechocystis* mutant strain CM25 lack the phycoerythrin complexes that make up the periphery of the rods of the WT6701 phycobilisomes, but are otherwise identical to the WT6701 antennae. (See Figure 4.1). Excitation of a sample of WT6701 phycobilisomes at 570 nm will result in excitation that is primarily localized in the phycoerythrin subcomplexes. (75 percent of the excitation will be localized in the phycoerythrin complexes; 22 percent in the phycocyanin complexes; and 3 percent in the allophycocyanin core complexes. See Figure 4.13 for a schematic representation of the initial distribution of chromophore excitation.) Excitation of a CM25 phycobilisome sample with 570-nm light will result in excitation of the phycocyanin complexes preferentially (84 percent of the excitation will be localized in the phycocyanin complexes, and 16 percent in the allophycocyanin core complexes; see Figure 4.13). Because the CM25 particle is effectively a sub-particle of the WT6701 phycobilisome, the difference between the rise times detected for the two samples will be due to the structural differences between the two particles. The difference in rise times between WT6701 particles and CM25 particles will measure the time it takes energy to travel from the C-PE complexes to the C-PC complexes.

The time-resolved terminal chromophore emission of both WT6701 and CM25 phycobilisomes after excitation with 570-nm light is shown in Figure 4.14A, with the computer-generated fits. The rise time of the WT6701 phycobilisome emission, 56 ± 8 ps, is slower than the rise time of the CM25 phycobilisome, 25 ± 4 ps, by 30 ± 5 ps. This time difference is due to the energy transfer steps needed to get energy originally localized in the C-PE complexes to the C-PC complexes. For WT6701, there are an average of 1.6

Figure 4.13 Excitation Distributions for WT6701 and CM25 Phycobilisomes with Excitation at 570 nm

Distribution is calculated taking into account the structural inhomogeneity of rod length in the wild-type phycobilisome.

Initial Excitation Distributions

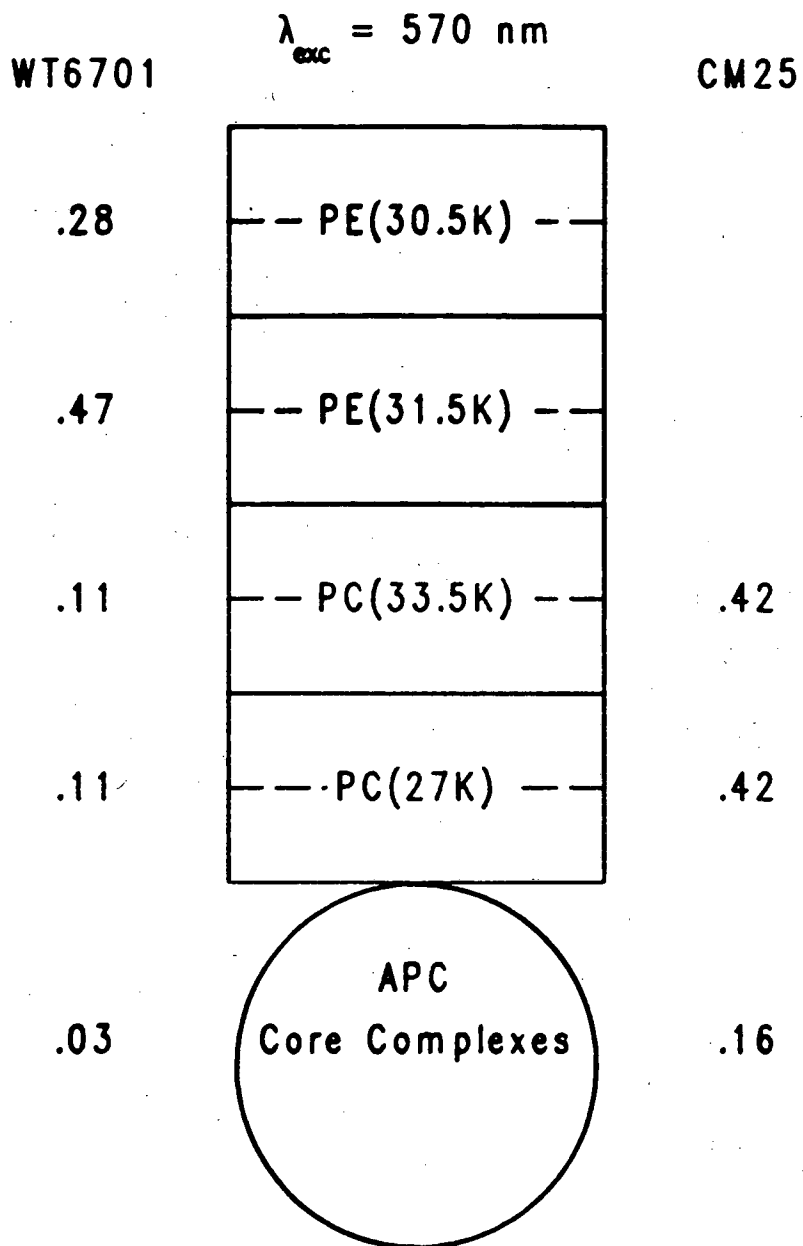


Figure 4.13

C-PE disks per rod, and traversing the 1.6 disks takes approximately 30 ps.

If the identical distribution of excited chromophores could be excited in both the WT6701 and CM25 phycobilisomes, the legitimacy of the comparison between the two particles could be assayed. Fortunately, the chromophores that make up the phycobilisomes of CM25 are a well-known subset of those that make up the WT6701 phycobilisomes. The highest energy-absorbing chromophores from WT6701, those of C-PE, are missing from the CM25 phycobilisomes. Excitation wavelengths too long to result in C-PE excitation (>600 nm) give excitation distributions for the two phycobilisomes that are identical. The initial excitation distributions for excitation of CM25 and WT6701 with 620-nm light are given schematically in Figure 4.15, with two-thirds of the excitation localized in phycocyanin complexes, and the last third of the excitation localized in allophycocyanin core complexes. When emission from the terminal chromophores is detected after 620-nm excitation, the time-resolved data are identical as plotted in Figure 4.14B. Both emission profiles show a 25-ps rise time. The relevancy and accuracy of the comparative study is confirmed.

In the previously mentioned study of *Rhodella* phycobilisomes [46], the rise time of terminal chromophore emission was measured. The *Rhodella* phycobilisome rods are the same length as those of the WT6701 phycobilisomes, but are composed of different biliproteins (three B-PE complexes and a single phycocyanin complex.) After excitation with 571-nm pulses, 672-nm emission showed a rise time of 55 ps. The results for WT6701 phycobilisomes gave a risetime of 56 ± 8 ps, strongly suggesting that the rod's length is of more importance than the rod's biliprotein composition.

The existence of another *Synechocystis* mutant that produces phycobilisomes that are devoid of rods, strain UV16 (Figure 4.1C, [9,20]), allows the dynamics of energy transfer within the core of the phycobilisome to be unravelled. When the UV16 phycobilisomes are excited with 620-nm light, the excitation is principally (95 percent) localized on

Figure 4.14 Time-Resolved Emission for WT6701 and CM25 Phycobilisomes

Time-resolved emission from WT6701 (heavy traces) and CM25 (light traces) phycobilisomes. Excitation wavelengths were 570 nm (A) and 620 nm (B). The smooth curves are computer-generated fits to the data with rise times of 47 ps [WT6701, (A)], 21 ps [CM25, (B)], and 25 ps (B). The phycobilisomes were isolated in 0.75 M NaK-phosphate buffer at pH 8.0. For CM25, $A_{620 \text{ nm}}=7/\text{cm}$, and for WT6701, $A_{620 \text{ nm}}=6/\text{cm}$.

Figure 4.14

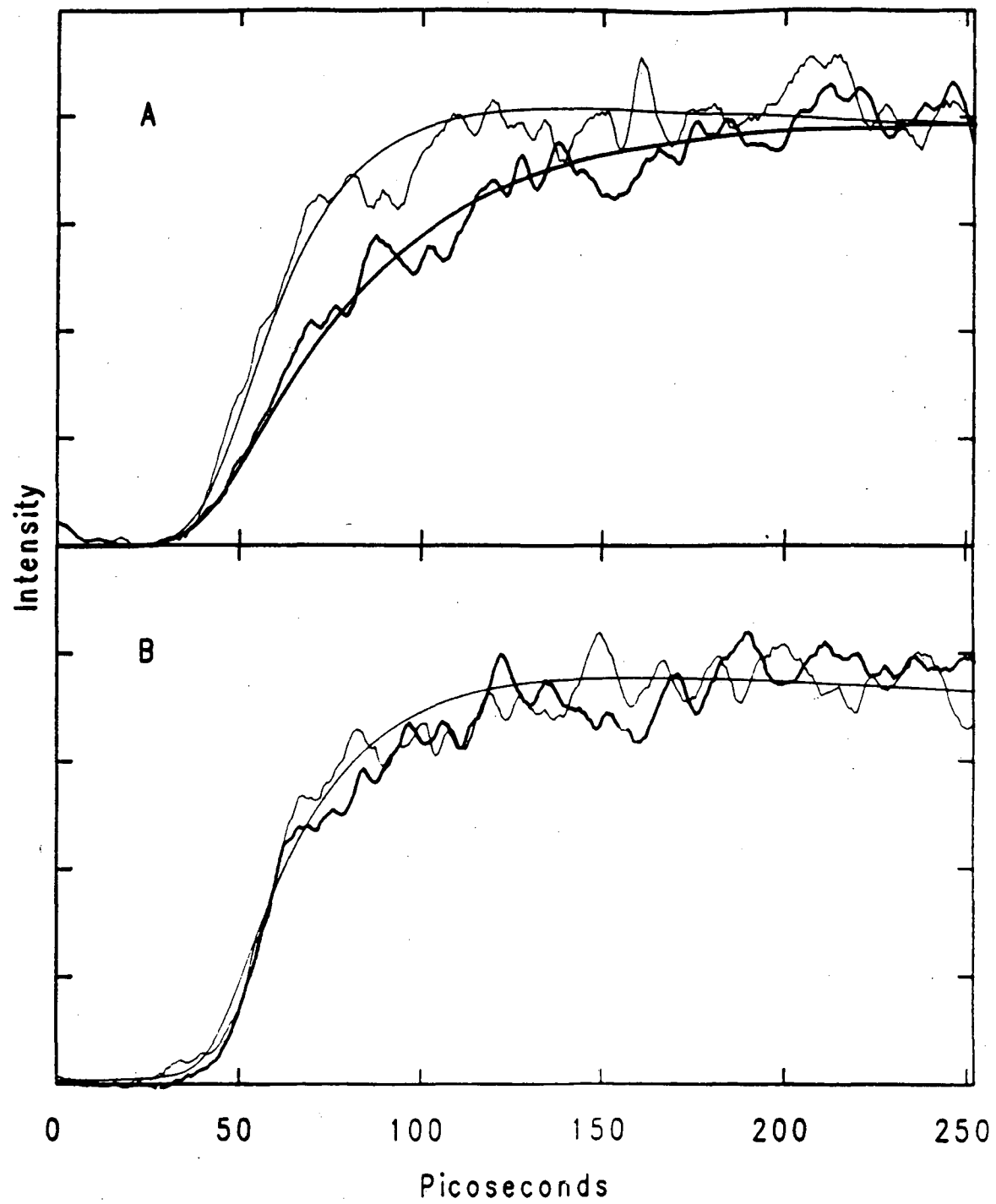


Figure 4.15 Excitation Distributions for WT6701 and CM25 Phycobilisomes with Excitation at 620 nm

Distributions are identical for the two particles because the high-energy absorbing C-PE complexes of the WT6701 particles are spectrally bypassed with 620-nm excitation.

Initial Excitation Distributions

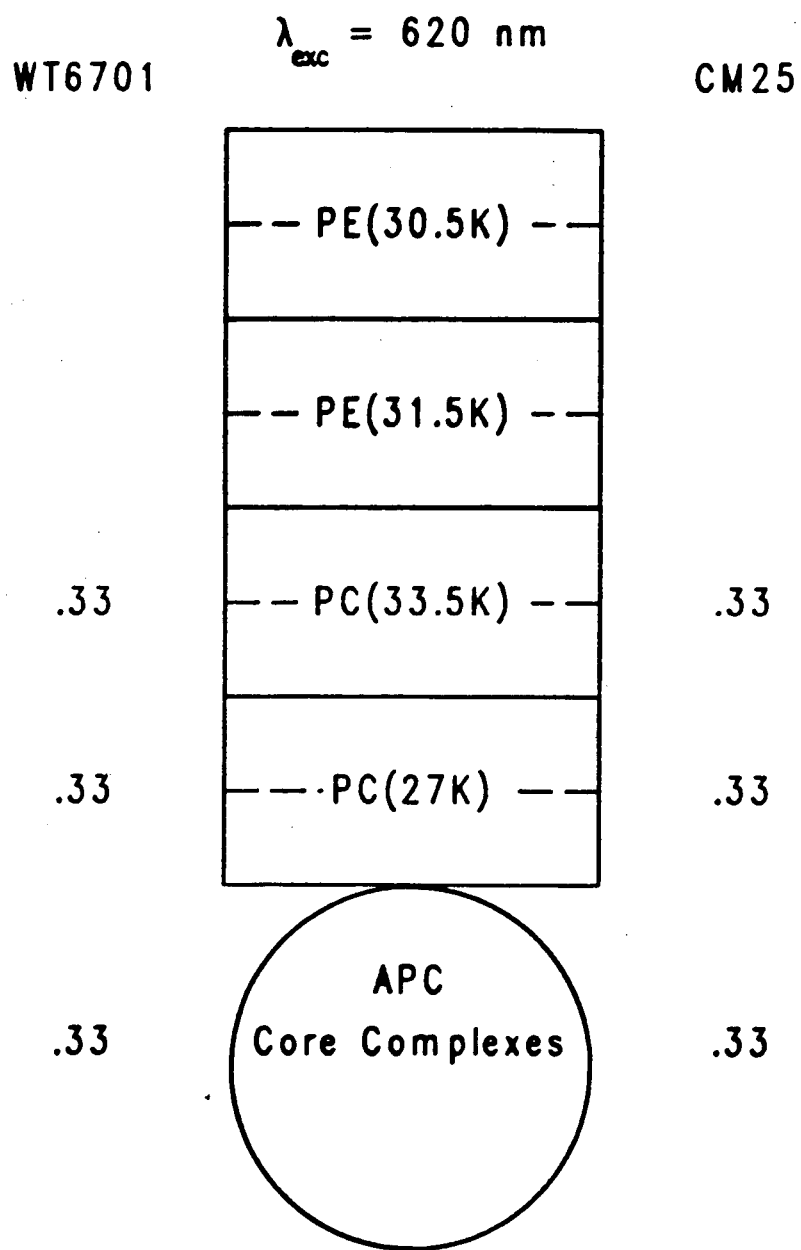


Figure 4.15

the AP chromophores. The remaining 5 percent of absorption of 620-nm photons is due to the terminal chromophores. The terminal chromophores are two allophycocyanin B complexes (APB) and two high molecular weight complexes, L_{CM}^{99} . Emission from the phycobilisome is from the terminal chromophores which are principally excited by energy transfer from the AP chromophores. Time-resolved emission from the terminal chromophores is shown in Figure 4.16A. The rise time of the UV16 emission is very prompt. The profile of emission from CM25 phycobilisomes excited at 620 nm is included in Figure 4.16A for comparison. Excitation of CM25 phycobilisomes results in excitation predominantly localized in the rods (Figure 4.15). The difference between the rise time of the UV16 emission and the rise time of CM25 excited at 620 nm is quite dramatic. Emission from a solution of the laser dye Nile blue A (Eastman Kodak Chemicals) is shown in Figure 4.16B for comparison. Emission from a Nile blue solution should show no detectable rise time [47]. The curve that fits the laser dye data gives a 6-ps rise time and therefore demonstrates the finite time resolution of the streak camera system under the excitation conditions used. The rise time determined for the UV16 emission was indistinguishable from that for the Nile blue solution, and therefore the rise time of the UV16 emission is at most 6 ps, instrument-limited. Emission from the core of the phycobilisome is as prompt as emission from a single chromophore, even though the core is a complex containing 72 chromophores.

H. Kinetic Modelling of the Phycobilisome

1. General Background

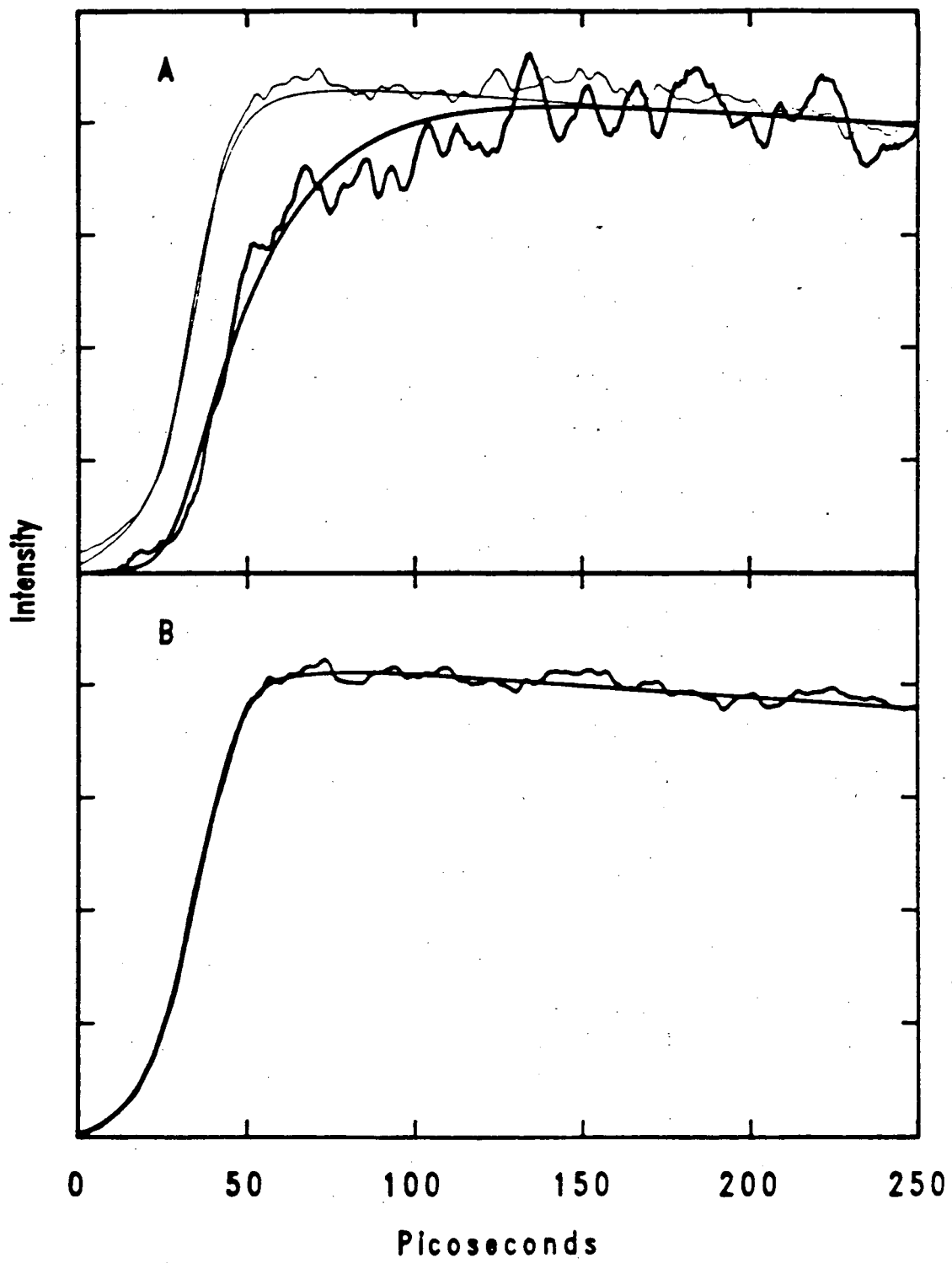
The experiments on intact phycobilisomes have yielded information on energy migration in both of the structural domains of phycobilisomes. The experiment measuring the C-PE decay time in isolated WT6701 phycobilisomes and the experiment comparing rise times for WT6701 and CM25 terminal chromophore emission both timed energy trans-

Figure 4.16 Time-Resolved Emission from CM25 and UV16 Phycobilisomes and from Nile Blue A Laser Dye

A. Thin trace shows emission profile detected from UV16 terminal chromophores after excitation with 620-nm pulses. The CM25 phycobilisomes were in 0.75 M NaK-phosphate buffer, pH=8.0, $A_{620\text{ nm}}=8.0/\text{cm}$. The UV16 preparation was in 0.65 M NaK-phosphate buffer, pH=7.0, $A_{650\text{ nm}}=0.5/\text{cm}$. Thick trace is terminal chromophore emission from CM25 phycobilisomes, also after 620-nm excitation. Smooth curves are computer-generated fits. The UV16 data have a rise time of 6.6 ps; the CM25 data have a best-fit rise time of 25 ps.

B. Emission from Nile Blue A laser dye excited with 620-nm pulses, with best-fit convolution. Rise time of fit is 6 ps.

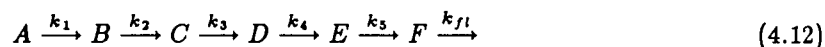
Figure 4.16



fer occurring in the rods of the phycobilisome. Emission from UV16 phycobilisomes measured the intracore energy migration rate. From the experiment on isolated phycobiliprotein complexes, the time it takes energy to migrate within a complex is known to be small. Putting these data together with a small number of simple assumptions, a model for energy transfer dynamics in phycobilisomes can be generated. In this section the model will be defined and discussed.

The first and most basic fact to be assimilated into an energy transfer model is that energy transfer within individual phycobiliprotein complexes takes a very short amount of time. Energy transfer within isolated phycoerythrin complexes takes at most 8 ps. Since intradisk transfer takes less than 8 ps, and since the phycobilisome data show that it takes about 30 ps for excitation to migrate through 1.6 C-PE disks, the intradisk transfer time is inconsequentially small relative to the interdisk transfer time. Energy transfer within the phycobiliprotein subunits will be assumed to occur on so fast a time scale as to be kinetically insignificant. This assumption, justified by the kinetic data obtained, is equivalent to stating that disk-to-disk transfer, not intradisk transfer, limits the flow of energy within phycobilisomes. This assumption serves to simplify the modelling because it limits the number of kinetically important transfer steps to just disk-to-disk transfers.

When only disk-to-disk and disk-to-core transfers are important to energy transfer, the following set of kinetic equations is sufficient to model energy transfer in a phycobilisome the size of WT6701:



where k_1 through k_5 are energy transfer rate constants, and A through E correspond to the sequence of phycobiliprotein components C-PE(30.5K), C-PE(31.5K), C-PC(33.5K), C-PC(27K), AP complexes, respectively; see Figure 4.1. State F corresponds to the terminal chromophores, APB and L_{CM}^{99} . The last rate constant, k_{fl} , is the rate of decay of the terminal chromophore as measured by the fluorescence lifetime. This energy

transfer mechanism results in six coupled first-order linear differential equations. The equations are straightforward to solve, and so the temporal profile of the population of any of the chromophores of the phycobilisome determined. The solutions to the equations are presented in the Appendix. Using the solutions, the population of any of the chromophores as a function of time can be calculated after specifying the rate constants and initial populations (see Appendix). Of particular interest to the discussion at hand is the fact that the profile of chromophore F population corresponds to what is measured when the terminal chromophore is experimentally detected. The sum of the population of chromophores A and B (the C-PE chromophores) corresponds to detection of 570-nm emission from WT6701 samples. The experimentally measured emission profiles can be used with the model to determine limits on the energy transfer rate constants, k_i , that are consistent with experiment.

It is important to note that we are aware that the fitting procedure we have used, particularly when studying the terminal chromophore rise times, has resulted in a gross over-simplification of the actual dynamics. We have fit all the data assuming the functional form of the data was the sum of two exponential terms, one rising and one falling term, and have given both terms equal amplitudes. Such data treatment is only appropriate for extremely simple experimental systems. In previous studies on multichromophoric systems like phycobilisomes and phycobiliproteins [48,49] or chloroplasts [50], and even studies on single-chromophore systems with multiple ground-state conformations [23,24,51], emission profiles have been analyzed as the sum of as many as four exponentials. Evidence is growing [50,51] that although such treatments give satisfactory statistical results, the fits still grossly over-simplify the actual dynamics. The model presented here predicts that the terminal chromophore signal would be the sum of six exponential terms. Experimental limitations of finite signal-to-noise ratios make the determination of six unique exponential terms impossible. However, the simplification we

have used does not bias our results. Artificial datasets are calculated using the model, and then fit with two exponential terms in a way equivalent to the fitting of the actual data. Some combinations of rate constants yield calculated datasets that give fits consistent with the actual data fits. Such successful combinations of rate constants are considered to be relevant to the actual energy transfer dynamics in phycobilisomes.

One would not expect that the number of successful combinations of rate constants to be finite, but there are interesting and reasonable simplifying assumptions about accessible values that can be made. For instance, one can assume that energy transfer rates would be approximately the same between any pair of disks. Supporting arguments for the rationality of this assumption include the fact that the distance between disks is a constant throughout the phycobilisome. Energy transfer rates depend on chromophore spacings, and there is no reason to expect the inter-disk chromophore distances to be a dramatic function of disk type. Furthermore, the existence of a single inter-disk transfer that was significantly slower than any other would introduce a bottle-neck in the energy flow, which would not be beneficial to the bacteria or algae. Although one may argue that energy transfer between like chromophore disks (i.e., PE-to-PE or PC-to-PC transfer) would be faster because excitation migration would be near-resonant, the idea that all the rates are approximately equivalent is clearly an interesting case to analyze.

2. Phycobilisome Rods

Data on WT6701 and CM25 phycobilisomes gave information on energy transfer within the rods of the phycobilisomes. Of the two types of measurements made on WT6701 phycobilisomes, data which concerns only a single chromophore bed are the easiest with which to begin. The experimentally measured fall times of 570-nm emission from intact WT6701 phycobilisomes indicated the rate of population decay from C-PE chromophores only. Experimentally, the 570-nm emission shows a fast component of

decay with a 28 ± 5 ps lifetime. For the kinetic model, states A and B are the two C-PE chromophores, and so the sum of the profiles of states A and B is the mathematical equation that corresponds to the C-PE population as detected experimentally.

$$C-PE(t) = A(t) + B(t) \quad (4.13)$$

From the Appendix,

$$A(t) = A_0 e^{-k_1 t} \quad (4.14)$$

$$B(t) = \left(\frac{k_1}{k_2 - k_1} \right) A_0 e^{-k_1 t} + \left[B_0 - \left(\frac{k_1}{k_2 - k_1} \right) A_0 \right] e^{-k_2 t} \quad (4.15)$$

The initial populations, A_0 and B_0 are a function of excitation wavelength. Because WT6701 has an average of 1.6 PE disks per rod, there is a higher probability of excitation of state B than of state A, by a factor of 1/0.6. Therefore, B_0 equals $1.7 A_0$, yielding

$$C-PE(t) = \left(\frac{k_2}{k_2 - k_1} \right) A_0 e^{-k_1 t} + \left(\frac{1.7k_2 - 2.7k_1}{k_2 - k_1} \right) A_0 e^{-k_2 t} \quad (4.16)$$

The calculated transfer times k_1^{-1} and k_2^{-1} (assuming that k_1^{-1} and k_2^{-1} are equal) which give calculated profiles consistent with the experimentally determined 28 ± 5 ps fall time are 24 ± 5 ps.

The profile of terminal chromophore population is given in the model by $F(t)$. There are four experimentally determined emission rise times that the model calculations should be able to reproduce. Terminal chromophore emission profiles were measured for each of two phycobilisomes (CM25 and WT6701) after excitation with both 570- and 620-nm pulses, resulting in four rise times. Since the two datasets taken with 620-nm excitation resulted in the same distribution of initially excited chromophores, the kinetic model would give equivalent predictions. That only three of the datasets are distinct, according to the model, is consistent with experiment. Since the initial excitation distribution determines exactly the form of $F(t)$ (see Appendix), and excitation with 620-nm pulses results in the same initial excitation distribution for both phycobilisomes, the model

predicts that $F(t)$ is the same for both phycobilisomes. As is shown in Figure 4.14B, the experimentally measured profiles for both phycobilisomes after excitation with 620-nm pulses are the same.

To reproduce the experimentally determined phycobilisome emission data for excitation with 570-nm pulses, the initial excitation distributions as given in Figure 4.13 are used. The range of values for k_3^{-1} and k_4^{-1} that reproduces the experimental emission rise time for CM25 is 24 ± 5 ps. When k_3^{-1} and k_4^{-1} are held to values near 24 ps, the WT6701 emission rise time data for excitation at 570 nm can be reproduced if k_1^{-1} and k_2^{-1} are also about 24 ps. All of the experimental emission profiles (both rise and fall times) can be reproduced successfully with rate constants for the transfer of energy between disks of the rods in the range of 24 ± 5 ps. The underlying assumption of the kinetic model is that disk-to-disk transfer is the rate-limiting step for energy flow within phycobilisomes. Using the model, the experiment data can be synthesized using energy transfer rate constants in the range 24 ± 5 ps.

3. Phycobilisome Core

The emission from the UV16 phycobilisomes gave the result that the 72 chromophores of the core are not distinguishable on the basis of time-resolved emission with 6 ps resolution from the decay of a simple well-behaved single chromophore. This result means that the energy transfer steps that occur within the core must be extremely fast. Details of core structure must be incorporated into the model of phycobilisome energy transfer. The 6701 family of phycobilisomes have three cylinders in the core (as shown in Figure 4.1D), and only the two basal cylinders (B) contain the terminal chromophores. There are therefore two possible pathways for energy transfer within the phycobilisome core. When the excitation is initially localized in an upper cylinder complex (U), two

intracore transfers are necessary to deliver the excitation to the terminal chromophores:



However, when the excitation is initially localized in one of the basal cylinders, only one transfer step is needed:



The differential equations that result are presented and solved in the Appendix. As in the previous section, the terminal chromophore population can be calculated as a function of time. For this modified case, the terminal chromophore population arises from both of the above parallel energy transfer pathways. From the Appendix, equation (A.17) gives the terminal chromophore temporal profile:

$$TE(t) = U'_0 e^{-k_{5a}t} + B'_0 e^{-k_{5b}t} + (-B'_0 - U'_0) e^{-k_{fl}t} \quad (4.19)$$

where

$$U'_0 = \left(\frac{k_{5b}}{k_{fl} - k_{5a}} \right) \left(\frac{k_{5a}}{k_{5b} - k_{5a}} \right) U_0$$

and

$$B'_0 = \left(\frac{k_{5b}}{k_{fl} - k_{5b}} \right) \left[B_0 - \left(\frac{k_{5a}}{k_{5b} - k_{5a}} \right) U_0 \right]$$

as a function of the rate constants k_{5a} , k_{5b} , and k_{fl} , and the initial populations of the upper and basal cylinders, U_0 and B_0 . U_0 and B_0 can be calculated from known chromophore counts and absorption cross sections. There are a multitude of rate constants k_{5a} and k_{5b} that would give terminal chromophore rise times of 6 ps or less. Three illustrative cases are described here. If k_{5a} and k_{5b} are equal, then both must be less than or equal to $(5 \text{ ps})^{-1}$. If k_{5a} is much faster than k_{5b} , the slowest possible value of k_{5b}^{-1} consistent with the experimental results is 6 ps. Similarly, if k_{5b} is much faster than k_{5a} , the slowest experimentally consistent value of k_{5a}^{-1} is 11 ps. (The difference in limiting values is due to the fact that initially $B_0 = 2U_0$, so that two-thirds of the energy travels according to (4.18) and only one-third according to (4.17).)

The model that has been able to reproduce the experimental data is extremely simple, in that energy flow in phycobilisomes can be successfully represented as sequential transfer through just six chromophoric units. Each antenna actually contains over 600 chromophores. The phycobilisome has been said to be a macromolecular assemblage optimized for energy collection [14]. The simplification of energy flow within this 600+ chromophore-laden complex to transfers between only six kinetically significant chromophore beds is evidence of spectral and structural optimizations. The work presented here indicates that the transfer rates, approximately 24 ps for transfer between disks, are fast enough to allow less than 2 percent loss per transfer [8].

I. Kinetic Modelling of Other Phycobilisomes

The characteristics of phycobilisomes that promoted our study of phycobilisomes—the ease of clean isolation, the enormous quantity of structural and functional data available, the library of well-characterized mutants, and the potential practical applications for solar energy conversion schemes—have also prompted others to work in this field. The experimental results obtained by others using time-resolved emission investigations like ours, as well as absorption recovery techniques, generally are in agreement with the results presented here, although the interpretations of the results are quite different. Using the kinetic model described here our results can be seen to be consistent with those of other workers, even though some results seem at first disparate. The examples that follow show that, whereas our data show no evidence of the slow transfer times reported by others, making their conclusions for the dynamics of energy transfer in phycobilisomes and phycobiliproteins inconsistent with our data, their data exhibit consistencies with our predictions. The agreement between experimental results spans experiments performed on phycobilisomes of varying organismal origin and morphology.

As already cited in Section G, results that have been reported for phycobilisomes

from both *Nostoc* [45] and *Rhodella violacea* [46] are in agreement with the results we have obtained for *Synechocystis* phycobilisomes. The results for both *Rhodella* and *Nostoc* phycobilisomes are also completely consistent with the kinetic model we have proposed. The fall times of emission from the phycoerythrin complexes of all three phycobilisomes were the same, given experimental uncertainties. The rise time of terminal chromophore emission, reported only for the *Rhodella* phycobilisome, agreed quite well with the value obtained for the morphologically similar WT6701 phycobilisome. The kinetic modelling of phycobilisomes is a function of structure (rod length, etc.) and because both *Rhodella* and *Nostoc* phycobilisomes are structurally indistinguishable from the WT6701 phycobilisomes, the kinetic model would indeed predict that the temporal values for the three phycobilisomes would be the same.

Gillbro and coworkers have performed comparative studies on the phycobilisomes from the cyanobacterium *Synechococcus* 6301 (WT6301) and a mutant strain, AN112 [52]. Their studies included both single-photon-timing emission measurements and absorption recovery data. The structures of the *Synechococcus* phycobilisomes have been characterized in great detail [53]. The WT6301 rods average three PC double disks in length and contain only PC complexes. The rods of WT6301 phycobilisomes exhibit greater variability in rod length than those of the WT6701 phycobilisomes that we chose for our comparative work. Within single preparations of WT6301 phycobilisomes, rod lengths of two to seven disks have been observed [53], while the WT6701 phycobilisomes have far greater homogeneity. WT6301 phycobilisomes and those of AN112 differ only in the rod substructures, in that the AN112 phycobilisomes have only a single PC complex in each rod. When excited with 620-nm pulses, recovery of absorption at 620 nm took 84 ± 8 ps for WT6301, and 43 ± 8 ps for the mutant. Taking into account the average change in rod length of two disks, the kinetic model requires that the disk-to-disk transfer time be 26 ± 8 ps to reproduce the experimentally determined 41 ± 16 ps difference in transfer

time. The disk-to-disk transfer time obtained for *Synechocystis* phycobilisomes was 24 ± 4 ps, in easy agreement with the results from the *Synechococcus* phycobilisomes.

In further work performed on WT6301 and AN112 phycobilisomes, Gillbro *et. al.* have reported some new results that seem at first inconsistent with our predictions [48]. For example, they have performed an experiment that is closely analogous to our UV16 measurement. Time-resolved emission from the terminal chromophores of AN112 phycobilisomes was monitored using a single-photon-timing instrument with an instrument-response-function of 130 ps (FWHM). Illumination of the AN112 phycobilisomes was with 660-nm pulses, resulting in excitation initially localized in the AP complexes of the phycobilisome core. (The PC rod complexes are partially spectrally bypassed by the long excitation wavelength making the experiment somewhat similar to the UV16 experiment described above.) The emission profile was fit to a sum of exponentials. The data require one component of the multiexponential fit to be a rise time; and the time constant of that growth term is 60 ps. In their interpretation of these data, Gillbro *et. al.* determine that the component of 60 ps corresponds to the time constant for energy migration from AP to TE chromophores. This result is clearly inconsistent with the instantaneous (≤ 6 ps) transfer time that we have determined for intracore transfer in the *Synechocystis* phycobilisomes. The inconsistency might indicate a difference between the *Synechococcus* and *Synechocystis* phycobilisomes.

However, a re-analysis of Gillbro's data shows that it is only their interpretation, not their emission profile, which is inconsistent with our predictions. The amplitude of the 60-ps rise time required to fit their data was 0.49, with the two other required decaying components having a total amplitude of 2.58. The amplitude of the 60-ps term relative to the amplitude of the instantaneously rising terms is $0.49/2.58 = 0.19$. The ratio indicates that less than 1/5 of the emitting population shows gradual growth. However, approximately 80 percent of the excitation is initially localized on the AP chromophores

and must transfer to the terminal chromophores [53]. The small relative amplitude of the 60-ps growth term indicates that it cannot be AP to TE transfer. For a reason that is not self-evident, and is not discussed in the Gillbro paper, only 20 percent of the population shows a slow rise even though 80 percent of the population must undergo that energy transfer process. We predict with certainty that Gillbro *et. al.* would get a much shorter rise time if the amplitude of the rising component were constrained to reflect the actual excitation distribution. We expect that the residuals would be of comparable quality. Although it is in some ways a loss of elegance to constrain the amplitudes of the components, this constraint results in physically significant time constants. A phycobilisome, even one as simple as AN112 or UV16, is a very complicated multi-chromophoric particle. The analysis of such a complicated system requires simplifying assumptions. If Gillbro *et. al.* were to re-analyze their data with realistic amplitude constraints, we are confident that their results would be consistent with ours.

The AN112 experiment just discussed is not the only measurement that Gillbro *et. al.* have made that seems to be inconsistent with our results. From measurements of time-resolved emission, they have reported that emission from WT6301 and AN112 phycobilisomes indicates that rod-to-core transfer takes ≈ 40 ps [48,52]. These measurements are, like the terminal chromophore measurements just discussed, subject to re-interpretation. For example, in AN112, a series of three time-resolved emission experiments was performed. The excitation wavelength was different in each of the three experiments, resulting in a different initial distribution of excited chromophores for each experiment. In a surprising result, the rise time of terminal chromophore emission was faster when the rods of AN112 were principally excited ($\lambda_{ex} = 620$ nm, $\tau_r = 51$ ps) than when the core was principally excited ($\lambda_{ex} = 660$ nm, $\tau_r = 60$ ps). In none of the three experiments was there correspondence between the amplitudes of the components and the initial chromophore distributions, clouding the interpretation of the temporal parameters.

We are confident that re-analysis of the temporal profiles with realistic constraints in amplitudes would bring their results into agreement with ours. Again, such constraints are necessary because of the great complexity of even simple phycobilisomes like AN112.

J. Conclusions

The results of the series of energy transfer rate determinations that have been described in this section can be summarized in a simple and concise way. Time-resolved emission measurements have allowed the rate-limiting steps in energy flow in phycobilisomes to be assigned as disk-to-disk and disk-to-core transfer. The time constant associated with inter-disk transfer is 24 ± 4 ps. Energy transfer within the disks and within the core of the phycobilisome occur on so fast a time scale (≤ 8 ps and ≤ 6 ps, respectively) as to be kinetically insignificant in terms of energy migration. We have been able to make these assignments on the basis of studies of isolated phycobiliprotein complexes and a comparative study of wild type and mutant phycobilisomes. Since disks are the only kinetically significant components of phycobilisomes, a simple kinetic model can be developed. The model is based only on structural data, and can successfully reproduce the experimental results, not only for *Synechocystis* phycobilisomes, but phycobilisomes of varying organismal origin and biliprotein content. The most surprising result of this study is the realization that the structure of the phycobilisome causes the assembly of 600+ chromophores to behave (with 8 ps resolution) like an assembly of only five chromophores. Energy flows so quickly through the phycobilisome that it appears to flow through only a linear array of five chromophores.

K. References for Chapter 4

1. R. R. Alfano, in *Biological Events Probed by Ultrafast Laser Spectroscopy*, R. R. Alfano, ed. (Academic Press, Inc., New York, 1983).
2. J. M. Friedman, *Science* **228**, (1985) 1273.
3. T. Tao, *Biopolymers* **8** (1969) 609.
4. R. M. Hochstrasser and D. K. Negus, *Proc. Natl. Acad. Sci. USA* **81**, (1984) 4399.
5. D. Magde, M. Zappala, W. H. Knox, and T. M. Nordlund, *J. Phys. Chem.* **87** (1983) 3286.
6. T. Yoshizawa, *Advances in Biophysics* **17** (1984) 5-67.
7. D. Wong, in *Biological Events Probed by Ultrafast Laser Spectroscopy*, R. R. Alfano, ed. (Academic Press, Inc., New York, 1983).
8. A. N. Glazer, S. W. Yeh, S. P. Webb, and J. H. Clark, *Science* **227** (1985) 419.
9. A. N. Glazer, C. Chan, R. C. Williams, S. W. Yeh, and J. H. Clark, *Science*, in press.
10. A. N. Glazer, *Ann. Rev. Biochem.* **52**, (1983) 125.
11. A. N. Glazer, *Ann. Rev. Biophys. Biophys. Chem.* **14** (1985) 47.
12. A. N. Glazer, *Ann. Rev. Microbiol.* **36** (1982) 173.
13. K. Sauer, in *Bioenergetics of Photosynthesis*, Govindjee, ed. (Academic, San Francisco, 1975), 115; A. Yu Borisov, in *The Photosynthetic Bacteria* R. K. Clayton and W. R. Sistrom, eds. (Plenum Press, New York, 1978) 323.
14. A. N. Glazer, *Biochim. Biophys. Acta* **768** (1984) 269.
15. A. N. Glazer, in *The Biochemistry of Plants*, M. D. Hatch and M. K. Boardman, eds. (Academic Press, New York, 1982), vol. **8**, pp. 51-96.
16. C. L. Renschler and L. R. Faulkner, *J. Am. Chem. Soc.* **104** (1982) 3315; A. A. Krasnovsky in *Topics in Photosynthesis*, J. Barber, ed. (1979) 281; M. Gratzel, *Pure Appl. Chem.* **54** (1982) 2369.
17. A. Yu Borisov, in *The Photosynthetic Bacteria* R. K. Clayton and W. R. Sistrom, eds. (Plenum Press, New York, 1978) 323.
18. R. C. Williams, J. C. Gingrich, and A. N. Glazer, *J. Cell Biol.* **85** (1980) 558.
19. J. C. Gingrich, R. C. Williams, and A. N. Glazer, *J. Cell Biol.* **95** (1982) 170.
20. L. K. Anderson, M. C. Rayner, and F. A. Eiserling, *Arch. Microbiol.* **138** (1984) 237.
21. J. C. Gingrich, L. K. Blaha, and A. N. Glazer, *J. Cell Biol.* **92** (1982) 261; J. C. Gingrich, R. C. Williams, and A. N. Glazer, *J. Cell. Biochem.* **22** (1983) 1; D. A.

- Bryant, G. Gulgielmi, N. Tandeau de Marsac, A. M. Castets, and G. Cohen-Bazire, *Arch. Microbiol.* **123** (1979) 113.
22. T. Schirmer, W. Bode, R. Huber, W. Sidler, and H. Zuber, *J. Mol. Biol.* **184** (1985) 257.
23. S. Braslavsky, A. R. Holzwarth, and K. Schaffner, *Angew. Chem. Int. Ed. Engl.* **22** (1983) 656.
24. W. Kufer, H. Scheer, and A. R. Holzwarth, *Isr. J. Chem.* **23** (1983) 233.
25. R. E. Dale and F. W. J. Teale, *Photochem. Photobiol.* **12** (1970) 99; F. W. J. Teale and R. E. Dale, *Biochem. J.* **116** (1970) 161; J. Grabowski and E. Gantt, *Photochem. Photobiol.* **28** (1978) 39.
26. J. Grabowski and E. Gantt, *Photochem. Photobiol.* **28** (1978) 47.
27. H. Nathel, D. M. Guthals, D. W. Anthon, and J. H. Clark, *J. Opt. Soc. Am.* **73** (1983) 1897; H. Nathel, D. M. Guthals, D. W. Anthon, and J. H. Clark, *Opt. Lett.*, to be submitted.
28. *CRC Handbook of Chemistry and Physics*, 55th ed., R. C. Weast, ed. (CRC Press, Cleveland, Ohio, 1975), p. F-195.
29. D. Wong, F. Pellegrino, R. R. Alfano, and B. A. Zilinskas, *Photochem. Photobiol.* **33** (1981) 651.
30. A. N. Glazer, J. A. West, and C. Chan, *Biochem. Syst. Ecol.* **10** (1982) 203.
31. C. E. Swenberg, N. E. Geacintov, and J. Breton, *Photochem. Photobiol.* **28** (1978) 999.
32. D. Mauzerall, *Photochem. Photobiol.* **28** (1978) 991.
33. A. J. Campillo and S. L. Shapiro, *Photochem. Photobiol.* **28** (1978) 975.
34. N. E. Geacintov and J. Breton, in *Biological Events Probed by Ultrafast Laser Spectroscopy*, R. R. Alfano, ed. (Academic Press, Inc., New York, 1982) pp. 157-191.
35. C. E. Swenberg, in *Biological Events Probed by Ultrafast Laser Spectroscopy*, R. R. Alfano, ed. (Academic Press, Inc., New York, 1982) pp. 193-214.
36. D. Mauzerall, in *Biological Events Probed by Ultrafast Laser Spectroscopy*, R. R. Alfano, ed. (Academic Press, Inc., New York, 1982) pp. 215-235.
37. G. S. Beddard, G. R. Fleming, G. Porter, G. F. W. Searle, and J. A. Synowiec, *Biochim. Biophys. Acta* **545** (1979) 165.
38. H. Kogelnik and T. Li, *Applied Optics* **5** (1966) 1550.
39. D. M. Guthals, H. Nathel, C. C. Hayden, D. W. Anthon, and J. H. Clark, *J. Opt. Soc. Am.* **73** (1983) 1896; D. M. Guthals, H. Nathel, C. C. Hayden, and J. H. Clark, *IEEE J. Quant. Electr.*, to be submitted.

40. C. V. Shank, E. P. Ippen and O. Teschke, *Chem. Phys. Lett.* **45** (1977) 291.
41. D. J. Lundell and A. N. Glazer, *J. Biol. Chem.* **258** (1983) 902.
42. D. R. Lutz, K. A. Nelson, C. R. Gochanour, and M. D. Fayer, *Chem. Phys.* **58** (1981) 325.
43. For an exciton interaction to occur, there must be π -electron cloud overlap; see M. Kasha, H. R. Rawls, and M. A. El-Bayoumi, *Pure Appl. Chem.* **11** (1965) 371.
44. M. Kasha, *Disc. Faraday Soc.* **9** (1950) 14.
45. F. Pellegrino, D. Wong, R. R. Alfano, and B. A. Zilinskas, *Photochem. Photobiol.* **34** (1981) 691.
46. A. R. Holzwarth, J. Wendler, and W. Wehrmeyer, *Photochem. Photobiol.* **36** (1982) 479.
47. Nile blue A laser dye has not yet been studied as thoroughly as Rhodamine B [33]. However, the two laser dyes are similar in size and molecular complexity, and it is reasonable to assume that the rates of vibrational relaxation in the electronically excited state would be comparable. The vibrational relaxation rates in Rho B in both methanol and glycerol solutions are fast enough that the emission rise time is less than 0.2 ps.
48. T. Gillbro, Å. Sandström, V. Sundström, J. Wendler, and A. R. Holzwarth, *Biochim. Biophys. Acta* **808** (1985) 52; T. Gillbro, Å. Sandström, V. Sundström, and A. R. Holzwarth, *FEBS Lett.* **162** (1983) 64.
49. S. C. Switalski and K. Sauer, *Photochem. Photobiol.* **40** (1985) 423.
50. R. J. Gulotty, L. Mets, R. S. Alberte, and G. R. Fleming, *Photochem. Photobiol.* **41** (1985) 487.
51. W. R. Ware and D. R. James, Am. Chem. Soc. 1985 Ann. Meet., Chicago, IL, Sept. 9-12, 1985, Abstr., Phys. Chem. 74.
52. T. Gillbro, Å. Sandström, V. Sundström, in *The Technical Digest from the 3rd Topical Meeting on Ultrafast Phenomena*, Optical Society of America, 1984; G. W. Suter, P. Mazzola, J. Wendler, and A. R. Holzwarth, *Biochim. Biophys. Acta* **766** (1984) 269.
53. D. J. Lundell and A. N. Glazer, *J. Biol. Chem.* **258** (1983) 902; G. Yamanaka, A. N. Glazer, and R. C. Williams, *J. Biol. Chem.* **255** (1980) 11004.

Chapter 5

Conclusions

The pages that have preceded this one have described in great detail the experiments that have produced some fundamentally new results on two different physical systems. The experiments were made possible by the construction of an ultrafast streak camera system. This final chapter will summarize the results that have been obtained so far, and suggest new directions that this work might take.

The streak camera system that has been constructed has superior temporal resolution and sensitivity. The streak camera system is composed of an amplified picosecond laser system, an ultrafast streak camera with an image intensifier, and an intensified linear photodiode array detector. The composite system allows the resolution of signals as short as 4 ps. The streak camera system has been interfaced to a microcomputer system, and independent data acquisition proceeds smoothly. Weakly luminescent samples can be detected with good time resolution because the automated data acquisition gives substantial signal averaging rates. The acquisition of even 1000 laser shots takes as little as six minutes. The streak camera system has been thoroughly calibrated and characterized, resulting in extremely reproducible data. The data-handling methods that allow temporal parameters to be obtained from the streak records have been described, in Chapter 2. The data is routinely reduced by an iterative convolute and compare technique (for short time scale data), or a semi-logarithmic method.

Parameters of emission profiles can be associated with physical processes, and that is the goal of the research described in Chapters 3 and 4 of this thesis. The experiments in Chapter 3 describe how the time-resolved emission profiles of a special class of solute molecules can be used to monitor in real-time the dynamics of solute-solvent interactions. The special molecules used in the study have electronically excited states

that have more dipolar character than the ground state. In polar solvents, the solute molecules show highly Stokes'-shifted steady-state emission profiles. When molecules of this sort in some solvents are excited with a picosecond light pulse the dynamics of the Stokes' shift can be resolved, even at room temperature. These Stokes' shifts are a result of solute-solvent interactions, indicating that the streak camera system can be used to monitor these dynamics in real-time. When the time constant of the relaxation process is measured in a wide range of solvents and under a wide range of temperatures, a strong correlation between the rate of relaxation and the dielectric relaxation rate is found. The correlation holds for solvent temperature change, isotopic substitution of the solvent, and even substitution of the probe chromophore with a structural isomer. The physical explanation of this phenomenon is that the same physical process that impedes dielectric relaxation impedes the solvents' reaction to the newly excited chromophore. Experiments of this sort have never before been carried out in such detail in room temperature solutions before, as it is the sensitivity and ease of operation of the streak camera system that makes these measurements possible. One expects that further temporally- and spectrally- resolved studies of solute-solvent interactions might lead to refinements in the results reported here.

In the work described in Chapter 4, experiments that elucidate the kinetics of energy transfer in a light-harvesting complex are described. The particular antenna studied is the phycobilisome, the macromolecular complex that serves as the principal photon-harvesting apparatus for red and blue-green algae. The wealth of structural information that is available for phycobilisomes and their constituent phycobiliproteins makes the phycobilisome the ideal antenna system for studies aimed at understanding the relationship between their structure and function. The phycobilisome, and even the constituent phycobiliproteins, are multichromophoric structures. Energy is transferred from chromophores of higher energy with extremely high efficiency to chromophores of lower energy. Time-

resolving the initial profile of emission from the lowest energy chromophores allows the rate of energy transfer to be determined. The reason for the high efficiency is clear from the time-resolved work: the rate of energy transfer is extremely fast so that transfer competes effectively with the rates of dissipative pathways. Comparative studies using structurally-deficient phycobilisomes from mutant strains of algae that lack specific chromophore complexes found in the wild-type phycobilisomes have allowed the rate of energy migration across various structural domains to be determined. Studies on isolated disks (of the phycoerythrin phycobiliprotein $(\alpha\beta)_6\gamma$ aggregates) showed that energy is transferred to the fluorescing chromophores faster than can be resolved with the streak camera (≤ 8 ps). This result had important ramifications on the comparative study involving phycobilisomes from mutant algae strains. Energy transfer through the cylindrical rods of phycobilisomes occurs between disks in the rods, and takes 24 ± 4 ps per disk. This delay is due to inter-disk transfer, because there are no long time scale components apparent in the isolated inter-disk transfer studies. A second comparative study determined that the rate of energy transfer within the core of the phycobilisome is also extremely rapid, with interchromophore energy transfer faster than the resolution of the streak camera. These data can yield a unified simple picture of the energy transfer process, and a kinetic model of energy transfer within phycobilisomes is included in Chapter 4. The results of a number of experiments can be shown to be consistent with the results that we have obtained. The Appendix which follows this chapter contains the mathematical details of the kinetic model.

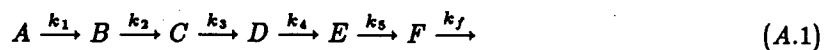
In conclusion, the results contained within this work all study the richness of the physics uniquely available to excited states. With short time scale resolution, dynamics on the time scale of solution phase chemistry can be obtained. For two systems where there is no final product that is any different than the starting material, physical interaction is monitored with the streak camera system. The pathways of energy dissipation compete in

these experiments, and the streak camera system monitors the competition. The dynamics of the competition provide invaluable information on the nature of the interactions that are occurring.

Appendix

A. Phycobilisome Modelling

Assuming that the only kinetically significant events in energy transfer in phycobilisomes is disk-to-disk transfer, the following mechanism is sufficient to describe energy transfer in WT6701 phycobilisomes:



For WT6701 phycobilisomes, A corresponds to the double-disk of C-PE bound with the linker polypeptide of 31.5 kDalton [C-PE(31.5K)], B to C-PE(30.5K), C to C-PC(33.5K), D to C-PC(27K), E to AP, and F to the terminal chromophores, TE. (See Figure 4.1 for more detail.) The constants k_1 through k_5 are energy transfer rate constants, and k_f gives the rate of decay of the terminal chromophores. While the particular energy transfer steps needed for the modelling of any particular phycobilisome depend on that phycobilisome's chromophore content and structure, the mathematical solution of the mechanism is independent of those details. Setting the initial conditions and evaluating the rate constants, which is required to complete the solution of the mechanism, is the part of the model which permits specification of the particular phycobilisome.

The above mechanism (A.1) gives the following time-dependent differential equations:

$$\frac{d[A]}{dt} = -k_1[A] \quad (\text{A.2})$$

$$\frac{d[B]}{dt} = -k_2[B] + k_1[A] \quad (\text{A.3})$$

$$\frac{d[C]}{dt} = -k_3[C] + k_2[B] \quad (\text{A.4})$$

$$\frac{d[D]}{dt} = -k_4[D] + k_3[C] \quad (\text{A.5})$$

$$\frac{d[E]}{dt} = -k_5[E] + k_4[D] \quad (\text{A.6})$$

$$\frac{d[F]}{dt} = -k_f[F] + k_5[E] \quad (\text{A.7})$$

These equations are coupled, but can be solved in a straightforward manner. Solutions that assume that the values of the k_i 's are never equal are used. In subsequent modelling, the k_i values are set nearly equal (within 5 percent) but are never mathematically identical. The solutions for the equations are naturally coupled. The solution for (A.2) is simple, and used in the solution to (A.3). The solutions are:

$$A(t) = A_0 e^{-k_1 t}, \text{ where } A_0 = A(t=0). \quad (\text{A.8})$$

$$B(t) = A'_0 e^{-k_1 t} + B'_0 e^{-k_2 t}, \quad (\text{A.9})$$

where

$$B'_0 = B_0 - A'_0,$$

$$A'_0 = \left(\frac{k_1}{k_2 - k_1} \right) A_0, \text{ and}$$

$$B_0 = B(t=0).$$

$$C(t) = A''_0 e^{-k_1 t} + B''_0 e^{-k_2 t} + C''_0 e^{-k_3 t}, \quad (\text{A.10})$$

where

$$C''_0 = C_0 - B''_0 - A''_0,$$

$$B''_0 = \left(\frac{k_2}{k_3 - k_2} \right) B'_0,$$

$$A''_0 = \left(\frac{k_2}{k_3 - k_1} \right) A'_0, \text{ and}$$

$$C_0 = C(t=0).$$

$$D(t) = A'''_0 e^{-k_1 t} + B'''_0 e^{-k_2 t} + C'''_0 e^{-k_3 t} + D'''_0 e^{-k_4 t}, \quad (\text{A.11})$$

where

$$D'''_0 = D_0 - C'''_0 - B'''_0 - A'''_0,$$

$$C'''_0 = \left(\frac{k_3}{k_4 - k_3} \right) C''_0,$$

$$B'''_0 = \left(\frac{k_3}{k_4 - k_2} \right) B''_0,$$

$$A'''_0 = \left(\frac{k_3}{k_4 - k_1} \right) A''_0, \text{ and}$$

$$D_0 = D(t=0).$$

$$E(t) = A_0'''' e^{-k_1 t} + B_0'''' e^{-k_2 t} + C_0'''' e^{-k_3 t} + D_0'''' e^{-k_4 t} + E_0'''' e^{-k_5 t}, \quad (\text{A.12})$$

where

$$E_0'''' = E_0 - D_0'''' - C_0'''' - B_0'''' - A_0'''' ,$$

$$D_0'''' = \left(\frac{k_4}{k_5 - k_4} \right) D_0''' ,$$

$$C_0'''' = \left(\frac{k_4}{k_5 - k_3} \right) C_0''' ,$$

$$B_0'''' = \left(\frac{k_4}{k_5 - k_2} \right) B_0''' ,$$

$$A_0'''' = \left(\frac{k_4}{k_5 - k_1} \right) A_0''' , \text{ and}$$

$$E_0 = E(t = 0).$$

$$F(t) = A_0''''' e^{-k_1 t} + B_0''''' e^{-k_2 t} + C_0''''' e^{-k_3 t} + D_0''''' e^{-k_4 t} + E_0''''' e^{-k_5 t} + F_0''''' e^{-k_f t}, \quad (\text{A.13})$$

where

$$F_0''''' = F_0 - E_0''''' - D_0''''' - C_0''''' - B_0''''' - A_0''''' ,$$

$$E_0''''' = \left(\frac{k_5}{k_f - k_5} \right) E_0'''' ,$$

$$D_0''''' = \left(\frac{k_5}{k_f - k_4} \right) D_0'''' ,$$

$$C_0''''' = \left(\frac{k_5}{k_f - k_3} \right) C_0'''' ,$$

$$B_0''''' = \left(\frac{k_5}{k_f - k_2} \right) B_0'''' ,$$

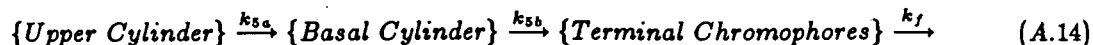
$$A_0''''' = \left(\frac{k_5}{k_f - k_1} \right) A_0'''' , \text{ and}$$

$$F_0 = F(t = 0).$$

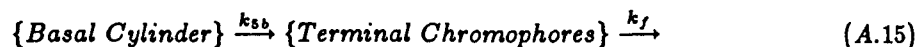
B. Modelling of the Phycobilisome Core

The core of the *Synechocystis* 6701 (WT6701) phycobilisome is as simple to model as the rods. The core is composed of three subdomains, as shown in Figure 4.1D. The two basal subdomains are identical, and contain terminal chromophores. The third subdomain, the upper cylinder, does not contain terminal chromophores. Excitation must migrate from

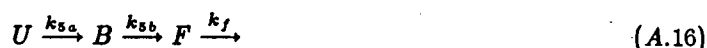
the upper cylinder to the lower cylinder, and then to the terminal chromophores:



For excitation initially localized in the lower cylinders, only a single energy transfer step is needed:



Simplifying the symbols, the energy transfer scheme can be represented by



where U represents the upper AP cylinder, B the basal AP cylinders, and F corresponds to the terminal chromophores. Solving the equations is again straightforward, resulting in three equations for the time-dependent population in each of the three subdomains. Only the terminal chromophore time-dependent population is used in the core kinetic analysis.

That equation is:

$$F(t) = U'_0 e^{-k_{5a}t} + B'_0 e^{-k_{5b}t} + F'_0 e^{-k_f t}, \quad (A.17)$$

where

$$U'_0 = \left(\frac{k_{5b}}{k_f - k_{5a}} \right) \left(\frac{k_{5a}}{k_{5b} - k_{5a}} \right) U_0, \text{ and}$$

$$U_0 = U(t=0);$$

$$B'_0 = \left(\frac{k_{5b}}{k_f - k_{5b}} \right) \left[B_0 - \left(\frac{k_{5a}}{k_{5b} - k_{5a}} \right) U_0 \right], \text{ and}$$

$$B_0 = B(t=0);$$

$$F'_0 = F_0 - B'_0 - U'_0, \text{ and}$$

$$F_0 = F(t=0).$$

This report was done with support from the Department of Energy. Any conclusions or opinions expressed in this report represent solely those of the author(s) and not necessarily those of The Regents of the University of California, the Lawrence Berkeley Laboratory or the Department of Energy.

Reference to a company or product name does not imply approval or recommendation of the product by the University of California or the U.S. Department of Energy to the exclusion of others that may be suitable.

TECHNICAL INFORMATION DEPARTMENT
LAWRENCE BERKELEY LABORATORY
UNIVERSITY OF CALIFORNIA
BERKELEY, CALIFORNIA 94720